Institute of Chemistry

Physical Chemistry

Förster resonance energy transfer (FRET)-based nanophotonics using DNA origami structures

---

Doctoral thesis (cumulative)

in fulfillment of the requirements for the degree

"doctor rerum naturalium"

(Dr. rer. nat.)

in the scientific discipline "Physical Chemistry"

submitted to the

Faculty of Science

of the University of Potsdam

by

Lydia Olejko

Potsdam, January 2017

Published online at the
Institutional Repository of the University of Potsdam:
URN urn:nbn:de:kobv:517-opus4-396747
http://nbn-resolving.de/urn:nbn:de:kobv:517-opus4-396747

Acknowledgement

Die vorliegende Arbeit wurde im Zeitraum Januar 2014 bis Januar 2017 am Institut für Chemie (Physikalische Chemie) der Universität Potsdam in der Arbeitsgruppe von Herrn JProf. Ilko Bald angefertigt.
Die Anfertigung dieser Arbeit wäre ohne die Unterstützung vieler Menschen nicht möglich gewesen. Ich möchte die Möglichkeit nutzen, um ihnen an dieser Stelle zu danken.
Als erstes möchte ich Ilko Bald für die Möglichkeit, meine Doktorarbeit auf diesem spannenden und interessanten Gebiet schreiben zu können und für die tolle Betreuung während der letzten Jahre, danken. Ich möchte ihm dafür danken, dass seine Tür immer offenstand und er mich während der gesamten Promotion immer motivierend begleitet hat.
Bei Dr. Michael Schlierf und Prof. Dr. Victoria Birkedal möchte ich mich für das Erstellen der Zweitgutachten bedanken.
Ich möchte der Graduiertenschule „SALSA - School of Analytical Sciences Adlershof“ (Humboldt-Universität zu Berlin) und der Bundesanstalt für Materialforschung und -prüfung (BAM) für die Finanzierung meiner Arbeit und die Unterstützung bei Reisekosten für verschiedene Tagungen danken.
Ein besonderer Dank gilt natürlich auch denjenigen, die mich und meine Arbeit durch das Bereitstellen von Chemikalien (zahlreiche Salze von der AG Strauch, mein Dank gilt hier insbesondere André) und Geräten (CD Spektroskopie in der AG Seckler, hier möchte ich Anja Thalhammer für die nette Einführung und Hilfe bei der Bedienung des Gerätes danken) unterstützt haben. Piotr möchte ich für die Zusammenarbeit in den letzten Jahren seit meiner Bachelorarbeit danken. Auch Tommy und Uschi danke ich herzlich für das Korrekturlesen meiner Doktorarbeit. Bei Jule bedanke ich mich für ihre Hilfe bei den technischen Schwierigkeiten, die es während des Zusammenschreibens zu überwinden galt.
Ein sehr großer Dank gilt natürlich der gesamten UPPC. Es war immer eine große Freude, in dieser Gruppe zu arbeiten.
Ich möchte mich bei Alex, Antonia, André, Christian, Eric, Jana, Janine, Jenny, Jule, Kenny, Philipp, Phillip, Robin, Sean, Steffi, Sven, Till, Tommy, Uschi und Youngeun für die schöne Atmosphäre beim täglichen Mittag (pünktlich um 11:00 Uhr ☺) oder

bei einem Kaffee zwischendurch danken. So war einem Arbeitstag auch in stressigen Zeiten immer etwas Schönes abzugewinnen.
I want to thank my lovely office (the ladies from 0.10) for the best working atmosphere one can think of. Besides fruitful discussions about our research we always eased the day with a pinch of fun. This becomes particularly clear on our whiteboard, where you can also find work-related things if you keep on looking long enough. Especially on Ppeppero-Day I will think of our office with a donut and "Mikado Stäbchen" in my hands.☺ Thank you so much, girls!
Natürlich möchte ich auch meinen Freunden außerhalb der Uni danken, die mich immer sehr gut von dem naturwissenschaftlichen Alltag ablenken konnten und gezeigt haben, dass sich nicht alles um DNA-Origamis dreht.
Der größte Dank gilt meiner gesamten Familie und Tim. Besonders meinen Eltern, ohne die ich niemals so weit gekommen wäre, möchte ich für ihre unendliche Unterstützung in allen möglichen Lebenslagen danken. Vom Finanziellen bis hin zum Daumendrücken für Klausuren, auf sie konnte ich immer zählen. Auch meiner Schwester möchte ich für ihre zahlreichen lieben und unterstützenden Worte in den letzten Jahren danken. Als letztes möchte ich Tim für die Freiheiten und unglaubliche Unterstützung während des gesamten Chemiestudiums und der Promotion danken. Unser Zuhause war für mich immer ein Ort, um die Batterien (und nicht nur die vom Handy) aufzuladen.
VIELEN DANK!

Contents

List of publications

Original publications

- **L. Olejko**, I. Bald "FRET Efficiency and Antenna Effect in Multi-Color DNA Origami-Based Light Harvesting Systems" *RSC Adv.* **2017**, 7, 23924-23934.[3]

- **L. Olejko**, P. J. Cywiński, I. Bald "An Ion-Controlled Four-Color Fluorescent Telomeric Switch on DNA Origami Structures" *Nanoscale* **2016**, 8 (19), 10339-10347.[2]

- P. J. Cywiński, **L. Olejko**, H.-G. Löhmannsröben "A Time-Resolved Luminescent Competitive Assay to Detect L-Selectin Using Aptamers as Recognition Elements" *Anal. Chim. Acta* **2015**, 887, 209-215.

- **L. Olejko**, P. J. Cywiński, I. Bald "Ion-Selective Formation of a Guanine Quadruplex on DNA Origami Structures" *Angew. Chem., Int. Ed.* **2015**, 54 (2), 673-677.[1a]

- **L. Olejko**, P. J. Cywiński, I. Bald "Ionenselektive Guanin-Quadruplex-Faltung auf DNA-Origami-Strukturen" *Angew. Chem.* **2015**, 127 (2), 683-687.[1b]

- C. Heck, **L. Olejko**, J. Prinz, R. Schürmann, I. Bald "Molekulare Prozesse im DNA-Nanolabor" *GIT Labor-Fachzeitschrift* **2014**, 11, 25-27.

- J. Prinz, B. Schreiber, **L. Olejko**, J. Oertel, J. Rackwitz, A. Keller, I. Bald "DNA Origami Substrates for Highly Sensitive Surface-Enhanced Raman Scattering" *J. Phys. Chem. Lett.* **2013**, 4 (23), 4140-4145.

Oral presentations

- L. Olejko, I. Bald "Artificial Light Harvesting on DNA Origami" *DNA Mitteldeutschland Workshop*, Potsdam, Germany, **2016**.

- L. Olejko, P. J. Cywiński, I. Bald "Switchable FRET-Based Photonic Wire on DNA Origami" *Functional DNA Nanotechnology*, Rome, Italy, **2016**.

- L. Olejko, P. J. Cywiński, I. Bald "Switchable Photonic Wires on DNA Origami" *DNA Mitteldeutschland Workshop*, Jena, Germany, **2016**.
- L. Olejko, P. J. Cywiński, I. Bald "Ion-Selective Telomeric FRET Switch on DNA Origami" *18th JCF Spring Symposium*, Kiel, Germany, **2016**.
- L. Olejko, P. J. Cywiński, I. Bald "G-Quadruplex Folding and Unfolding on DNA Origami Structures" *DNA Mitteldeutschland Workshop*, Dresden, Germany, **2015**.
- L. Olejko, P. J. Cywiński, I. Bald "Ion-Selective Formation of a Guanine Quadruplex on DNA Origami Structures" *17th JCF Spring Symposium*, Münster, Germany, **2015**.

Poster presentations

- L. Olejko, P. J. Cywiński, I. Bald "Ion-Controlled Three-Color Fluorescent Telomeric Switch on DNA Origami" *DNA-Nanotechnology*, Jena, Germany, **2016**.
- L. Olejko, P. J. Cywiński, H.-G. Löhmannsröben, I. Bald "G-Quadruplex Folding and Unfolding on DNA Origami" *SALSA Poster Session*, Berlin, Germany, **2015**.
- L. Olejko, P. J. Cywiński, I. Bald "Ion-Selective and Switchable Formation of Guanine Quadruplex Structures on DNA Origami Structures" *DNA21 - International Conference on DNA Computing and Molecular Programming*, Boston, U.S.A., **2015**.
- L. Olejko, P. J. Cywiński, I. Bald "Selective Potassium Sensing Using Human Telomeric DNA on DNA Origami Templates" *EuCheMS*, Istanbul, Turkey, **2014**.
- L. Olejko, P. J. Cywiński, I. Bald "Three-Color FRET Cascades and Selective Potassium Sensing on DNA Origami Templates" *113th Bunsentagung*, Hamburg, Germany, **2014**.

Awards

- Award for "Best Poster Content" at *SALSA Poster Session*, Berlin, Germany, **2015**.
- Award for "Best Oral Presentation" at the *17th JCF Spring Symposium*, Münster, Germany, **2015**.

Abstract

The field of nanophotonics focuses on the interaction between electromagnetic radiation and matter on the nanometer scale. The elements of nanoscale photonic devices can transfer excitation energy non-radiatively from an excited donor molecule to an acceptor molecule by Förster resonance energy transfer (FRET). The efficiency of this energy transfer is highly dependent on the donor-acceptor distance. Hence, in these nanoscale photonic devices it is of high importance to have a good control over the spatial assembly of used fluorophores. Based on molecular self-assembly processes, various nanostructures can be produced. Here, DNA nanotechnology and especially the DNA origami technique are auspicious self-assembling methods. By using DNA origami nanostructures different fluorophores can be introduced with a high local control to create a variety of nanoscale photonic objects. The applications of such nanostructures range from photonic wires and logic gates for molecular computing to artificial light harvesting systems for artificial photosynthesis.

In the present cumulative doctoral thesis, different FRET systems on DNA origami structures have been designed and thoroughly analyzed. Firstly, the formation of guanine (G) quadruplex structures from G rich DNA sequences has been studied based on a two-color FRET system (Fluorescein (FAM)/Cyanine3 (Cy3)). Here, the influences of different cations (Na^+ and K^+), of the DNA origami structure and of the DNA sequence on the G-quadruplex formation have been analyzed. In this study, an ion-selective K^+ sensing scheme based on the G-quadruplex formation on DNA origami structures has been developed. Subsequently, the reversibility of the G-quadruplex formation on DNA origami structures has been evaluated. This has been done for the simple two-color FRET system which has then been advanced to a switchable photonic wire by introducing additional fluorophores (FAM/Cy3/Cyanine5 (Cy5)/IRDye®700). In the last part, the emission intensity of the acceptor molecule (Cy5) in a three-color FRET cascade has been tuned by arranging multiple donor (FAM) and transmitter (Cy3) molecules around the central acceptor molecule. In such artificial light harvesting systems, the excitation energy is absorbed by several donor and transmitter molecules followed by an energy transfer to the acceptor leading to a brighter Cy5 emission. Furthermore, the range of possible excitation wavelengths is extended by using several different fluorophores (FAM/Cy3/Cy5). In this part of the thesis, the light harvesting efficiency (antenna effect) and the FRET efficiency of different donor/transmitter/

acceptor assemblies have been analyzed and the artificial light harvesting complex has been optimized in this respect.

Zusammenfassung

Nanotechnologie hat in den letzten Jahrzehnten durch die Herstellung von Materialien mit außergewöhnlichen Eigenschaften für Anwendungen im Bereich der Medizin und Materialwissenschaften immer mehr an Popularität gewonnen. Die Herstellungsmethoden von Nanostrukturen sind weit gefächert. Auch Desoxyribonukleinsäure (DNS bzw. *engl.* DNA, deoxyribonucleic acid) kann für die Herstellung von Strukturen im Nanometerbereich genutzt werden. Diese sogenannte DNA-Nanotechnologie wurde in den frühen 1980er Jahren von Nadrian C. Seeman begründet.[4,5] Ungefähr 30 Jahre später wurde eine neue Methodik für die Herstellung von DNA-Nanostrukturen von Paul W. K. Rothemund entwickelt, die er „scaffold DNA origami" (Gerüst-DNA-Origami) nannte.[6] DNA-Origami-Nanostrukturen können relativ einfach hergestellt werden und eignen sich perfekt für die Anordnung unterschiedlicher Moleküle (zum Beispiel Fluorophore) mit hoher räumlicher Kontrolle und Präzision. Daher können sie als Substrate genutzt werden, um verschiedene Förster-Resonanzenergietransfer (FRET) Systeme zu entwerfen und zu untersuchen. FRET ist ein strahlungsloser Energietransfer, bei dem die Anregungsenergie von einem Donor- auf ein Akzeptor-Molekül übertragen wird.

In dieser kumulativen Doktorarbeit wurden verschiedene FRET-Systeme auf DNA-Origami-Nanostrukturen entwickelt und mithilfe der Fluoreszenzspektroskopie untersucht. Hierbei wurde zuerst die durch einwertige Kationen (Kalium oder Natrium) induzierte Guanin-Quadruplex-Faltung von freier Telomer-DNA und Telomer-DNA auf DNA-Origami-Strukturen mittels FRET analysiert. Diese Untersuchungen haben gezeigt, dass die freie umgedrehte menschliche Telomer-Sequenz (RevHumTel, 5'-(GGG ATT)$_4$) generell sensitiver auf K^+ als auf Na^+ reagiert. Durch die Immobilisierung der Telomer-DNA auf DNA-Origami-Strukturen kann eine vollständige Selektivität für K^+ erreicht werden.[1] Interessanterweise wird die Ionenselektivität aufgehoben, wenn die menschliche Telomer-Sequenz (HumTel, 5'-(TTA GGG)$_4$) verwendet wird.

Basierend auf der G-Quadruplex-Faltung konnten schaltbare FRET-Systeme entwickelt werden, da sich die G-Quadruplexe wieder entfalten, wenn die Kationen mithilfe von zum Beispiel Kryptanden entfernt werden. In den hier untersuchten FRET-Systemen konnte zwischen hoher FRET-Effizienz (gefalteter G-Quadruplex) und niedriger FRET-Effizienz (entfalteter DNA Einzelstrang) durch Zugabe KCl bzw. cryptand gewechselt werden. Da sich DNA-Origami-Strukturen recht einfach modifizieren lassen, wurde

das ursprüngliche zwei-Farben-FRET-System durch Hinzufügen eines weiteren etwas rotverschobenen Farbstoffes erweitert (drei-Farben-FRET-Kaskade). Schließlich konnte ein schaltbarer photonischer Draht durch Einfügen eines vierten Farbstoffes entwickelt werden.[2]

Die Emissionsintensität des finalen Akzeptors ist in einer einfachen drei-Farben-FRET-Kaskade (ein Donor, ein Transmitter und ein Akzeptor) verhältnismäßig gering und kann durch das Anordnen von mehreren Donor- und Transmitter-Molekülen um ein zentrales Akzeptor-Molekül herum stark erhöht werden. In diesen sogenannten künstlichen Lichtsammelkomplexen absorbieren die Donor-Moleküle das Anregungslicht und übertragen dieses über mehrere FRET-Stufen zum Akzeptor-Molekül. Dadurch wird der Wellenlängenbereich der elektromagnetischen Strahlung, welcher vom Akzeptor absorbiert werden kann, vergrößert und die Emissionsintensität des Akzeptors verstärkt. In diesem Teil der Arbeit wurde die Anzahl der Farbstoffe und die Anordnung dieser unterschiedlichen Farbstoffe variiert und die Lichtsammeleffizienz und FRET-Effizienz bestimmt. Hierbei wurden diese Parameter optimiert und aufgrund der gefundenen Ergebnisse konnten Design-Regeln für solche künstlichen Lichtsammelkomplexe aufgestellt werden.[3]

Chapter 1

Introduction

Nanotechnology has gained more and more popularity over the last decades by developing materials with extraordinary properties for medical applications or material science. A variety of methods has been developed to create structures on the nanometer scale. These nanostructures have exceptional physical and chemical properties. The preparation of nanomaterials is basically done using two different processes called top-down and bottom-up. Top-down principally means that nanostructures are achieved by reducing the size of bulk material. Here, optical lithography or nanoimprint processes are often used to generate nano-objects with a great precision and reproducibility.[7] The main disadvantage of these top-down methods is that the needed equipment is of high cost.[8] The bottom-up process on the other hand is based on enlarging material starting from atoms, molecules or particles and is based on relatively simple chemistry which makes it a rather cost-effective method.[9] Here, the most attractive process for associating nanostructures is the self-assembly of for example nanoparticles or biomolecules. Self-assembly is the spontaneous formation of stable structures under equilibrium conditions held together by different interactions such as van-der-Waals forces, hydrogen bonds or electrostatic interactions.[8] Deoxyribonucleic acid (DNA) for example can be used to generate these self-assembled nanostructures with high precision and controllable conditions. The assembly of DNA nanostructures is based on the specific base pairing stabilized by hydrogen bonds. The idea for DNA nanotechnology was developed by Nadrian C. Seeman in 1982.[4] Seeman had the vision to generate larger highly ordered DNA lattices by linking certain smaller DNA building blocks (so called "DNA tiles") together. A variety of 2D and 3D nanostructures have been created based on this method.[10–13] Nevertheless, this DNA tile-based assembly has some limitations and the preparation of these DNA nanostructures is not necessarily straightforward.[14] In 2006, Paul W. K. Rothemund developed a new strategy to create DNA nanostructures which overcame the previous restrictions of DNA tile-based nanotechnology. In this approach ("scaffold DNA origami"), a long circular single DNA strand (so called "scaffold strand") is folded into arbitrary 2D and 3D structures with the help of short single

DNA strands (so called "staple strands", ca. 200 different single strands).[6] The main advantage of the DNA origami method is that each staple strand can be addressed individually and separately. This means, that up to 200 different modifications can be attached to one single DNA origami structure by modifying the staple strands with the desired moieties. Since the exact position of each staple strand of the DNA origami structure is known, these nanostructures can be used to arrange different molecules with a high spatial precision.[5] Hence, DNA origami structures are ideal to create different Förster resonance energy transfer (FRET)-based photonic assemblies with various fluorophores.[15,16] Such FRET-based nanoscale photonic devices have a variety of potential applications and can be used to create for example optical sensors for different molecules with high selectivity.[17,18] Furthermore, FRET-based photonic wires can be assembled to generate a signal transduction over a few nanometers with a high precision.[19] A photonic wire is created by a linear assembly of multiple fluorophores which transfer the light energy from one end to the other *via* multiple FRET steps.[20] To control the output signal of such photonic assemblies (fluorescence emission of the final acceptor molecule), molecular switches can be introduced. Molecular switches are based on the reversible switching between two conformations induced by different chemical inputs.[21] A prominent example for molecular switches is the conformational change of guanine rich DNA sequences between the random coil and the G-quadruplex conformation induced by certain cations.[22,23] By introducing or removing a certain input the molecular switch changes its conformation leading to an "on" and "off" state, respectively. When such a molecular switch is introduced in a photonic wire the signal transduction is either operative or interrupted. Furthermore, photonic assemblies on the nanometer scale can be used to create artificial light harvesting systems. In such systems, which are inspired by natural light harvesting systems found in photosynthesis, the light energy is collected by several molecules (donor) and funneled to a few or one single fluorophore (acceptor) in the center. Thus, the absorption of the acceptor is enhanced and the fluorescence emission becomes brighter.[24,25]

The aim of this work is to create different FRET-based photonic assemblies on DNA origami structures. In the first attempt, the conformational change of telomeric DNA is analyzed based on a two-color FRET system. Telomeric DNA is a guanine rich sequence which can change its conformation from a random coil to the G-quadruplex structure upon the addition of certain monovalent cations.[22,26] Here, the influence of different cations (K^+ *vs.* Na^+), the influence of the DNA origami structure (free telomeric DNA *vs.* telomeric DNA attached to DNA origami structures) and the influence of the DNA sequence itself (human telomeric DNA (HumTel) *vs.* reversed human telomeric DNA (RevHumTel)) are studied. By attaching RevHumTel to DNA origami structures a highly selective potassium sensing scheme is created (manuscript "ion-selective FRET"[1] in section 4.2). Furthermore, the reversibility of the G-quadruplex formation is investigated to generate switchable FRET systems on DNA origami structures.

This is done in a two-color FRET system which is extended to a more sophisticated three-color FRET cascade and finally to a switchable photonic wire by introducing additional acceptor molecules which emit further red shifted (manuscript "switchable photonic wire"[2] in section 4.3). In the last part, an artificial light harvesting system is created to enhance the overall emission intensity of the acceptor molecule. Here, a three-color FRET cascade is used to additionally increase the number of possible excitation wavelengths. The light harvesting efficiency expressed as antenna effect and the FRET efficiency are thoroughly analyzed for different donor/transmitter/acceptor assemblies. Based on these studies, design options for the optimal fluorophore arrangement and number can be derived (manuscript "artificial light harvesting"[3] in section 4.4).

Chapter 2

Theoretical background

2.1 DNA nanotechnology

The field of DNA (deoxyribonucleic acid) nanotechnology has developed in the last decades tremendously. It started all off in 1982 when Nadrian Seeman examined "branched immobile junctions" to build up highly ordered DNA constructs.[4,27] In this section the structural basics of DNA and the development of DNA nanotechnology starting with DNA tile-based structures and followed by the invention of the DNA origami method by Paul Rothemund in 2006 are discussed.[6]

2.1.1 Structural basics of DNA

Deoxyribonucleic acid is a polyelectrolyte which stores the genetic information. This polymer chain consists of repeating nucleotides (nt) which are composed of a nucleobase (nb), a sugar (deoxyribose) and a phosphate group (see figure 2.1a). The sugar-phosphate backbone provides the structural integrity and the order of the different bases contains the genetic information. There are four different nb, namely adenine (A), thymine (T), guanine (G) and cytosine (C) which can associate specifically and selectively *via* hydrogen bonds. Due to these specific interactions single stranded DNA (ssDNA) can hybridize and form a DNA double helix (figure 2.1).[28] The structure of the DNA double helix was first resolved by Watson and Crick in 1953.[29] Since then it is known that A pairs with T and G pairs with C (see figure 2.1b). As shown in figure 2.1b A and G are purine and T and C are pyrimidine derivatives. Additionally, A and T are connected *via* two hydrogen bonds whereas C and G are held together by three hydrogen bonds (Watson-Crick DNA pairing). Thus, DNA double strands containing many G and T bases are more stable compared to DNA double strands containing A and T bases. As depicted in figure 2.1b the hydrogen bonds are directed (schematically shown by an arrow pointing from the H-bond donor to the H-bond acceptor).

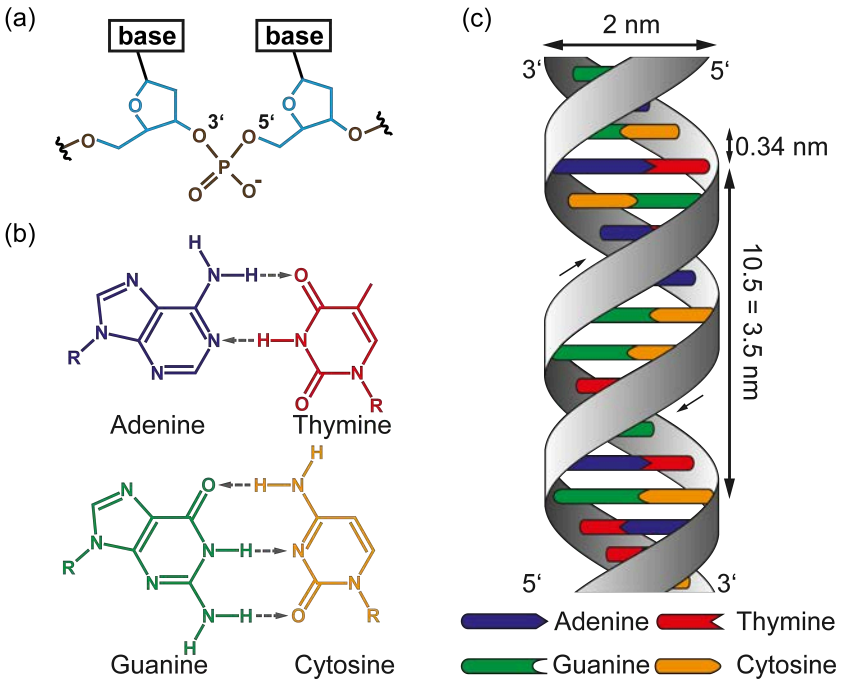

Figure 2.1: (a) Building blocks of the DNA: nucleobase (black), sugar (light blue) and phosphate group (brown). The sugar and the phosphate group represent the backbone of the DNA. (b) Pairing of DNA bases and arrangement of hydrogen bonds for Watson-Crick base pairing. (c) Schematic illustration of a DNA double helix in the B-form postulated by Watson and Crick. The sugar-phosphate backbone is depicted in gray together with the four different nb (blue: A, red: T, green: G, yellow: C). (Images are adapted from literature[28])

For the N–H – N bond in the base pair A/T, pyrimidine (T) is the proton donor and purine (A) the proton acceptor whereas for the base pair G/C it is the opposite. For the carboxylic hydrogen bond N–H – O in A/T, purine (A) is the proton donor and pyrimidine (T) the proton acceptor and again for G/C it is *vice versa*. This means, that in general A could pair with G and C with T because they would follow the same rules for hydrogen bonding. Here, the backbone of the DNA strand comes into play. It fixes the diameter of the DNA double helix so that only purine and pyrimidine bases match and only the hydrogen bonds shown in figure 2.1b are feasible. The combination of two purine or two pyrimidine bases lead to distortions of the DNA backbone resulting in an increase of the free energy.[5] The most common conformation of double stranded DNA (dsDNA) in biological media is the B-form but there are also the A- and Z-form which have different dimensions. In the B-form the distance between each nb is 0.34 nm, a whole turn of the DNA double helix appears every 10.5 nb and is 3.5 nm long and the diameter of the DNA double helix is 2 nm (figure 2.1c).[28] The DNA double helix is not only stabilized *via* the hydrogen bonds but also by stacking interactions between neighboring DNA bases. The hydrophobic DNA bases stack on top of each other to minimize the area of interaction with water molecules and they are associated by a combination of hydrophobic, electrostatic and van-der-Waals forces.[22,28] In addition

to the Watson-Crick DNA pairing there is the so called Hoogsteen base pairing. Here, the imidazole nitrogen of the purine bases form hydrogen bonds. In this conformation, self-pairing of for example G bases into planar G-tetrads (more detailed discussion in section 2.2) or the formation of hemi-protonated C duplexes are possible.[5]

2.1.2 The beginning of DNA nanotechnology - DNA tiles

Because of the unique properties of ssDNA to hybridize to a complementary single strand it can be used to generate well-defined DNA nanostructures on the nanometer scale. The field of DNA nanotechnology started off in 1982 when Nadrian Seeman constructed ordered DNA arrays (DNA tiles) based on branched immobile junctions which can be linked together to create larger DNA networks.[4,27] Since then different DNA tiles have been created to form multiple DNA nanostructures with different shapes and dimensions. The principles of the DNA tiles and their structural properties are discussed in this section.[5,30]

In 1993, Fu and Seeman showed for the first time the possibility to arrange and link DNA double helices in a parallel and coplanar manner together.[10] These DNA double helices are held together *via* immobile crossover junctions and are called double crossover tiles (DX tiles, figure 2.2). By introducing sticky ends (unpaired DNA strands) at the end of such a DNA tile larger arrays and lattices can be formed.[11] In this way many more DNA tiles have been constructed and the field of DNA nanotechnology gained more and more popularity. In 2000, the triple crossover tile (TX tile, figure 2.2) has been introduced in which three DNA double helices have a parallel arrangement and are linked together *via* crossover junctions.[31] Yan *et al.* introduced a multi-armed DNA tile called "4 x 4 tile" (see figure 2.2) which gave the possibility to enlarge DNA nanostructures independently and equally in the x- and y-direction by introducing sticky ends on both DNA double helices in every arm of the four-arm junction.[32] Similar multi-armed DNA tiles have been introduced to form large self-assembling DNA arrays based on three-[33], four-[34] and six-armed DNA tiles.[35] Another way of arranging DNA into DNA nanostructures is to link DNA double helices in a parallel but not coplanar manner together. In this way "DNA helix bundle tiles" have been created consisting of three[36], four[37] and six DNA double helices.[38] By connecting these DNA tiles (*e.g.* by introducing sticky ends) micrometer long DNA fibers can be created. In 2010, Hansen *et al.* introduced another DNA tile design called "weave tile" shown in figure 2.2.[39] Here, only two DNA strands are needed for one DNA tile (other DNA tiles are created from four to nine DNA strands). The DNA strands weave back and forth creating weave-like DNA tiles with rigid double helices tethered together *via* single-stranded T_4 loops. In these tiles, crossover junctions are avoided and a higher structural flexibility of the DNA nanostructure is provided.[30] DNA origami structures discussed in section 2.1.3 are principally formed based on this strand routing but with

crossover junctions. Already in 1991, Chen and Seeman showed the immense potential of DNA tile-based nanostructures and created a three-dimensional DNA nanocube.[12] Three years later Zhang and Seeman designed a DNA-truncated octahedron which was at that time hard to visualize. Thus, it was difficult to confirm the formation of such structures.[13] Only in 2004, Shih and co-workers showed and proved the formation of a DNA octahedron using cryo-electron microscopy.[40] In 2009, Seeman was finally able to obtain a three-dimensional self-assembled DNA crystal based on tensegrity triangles.[41]

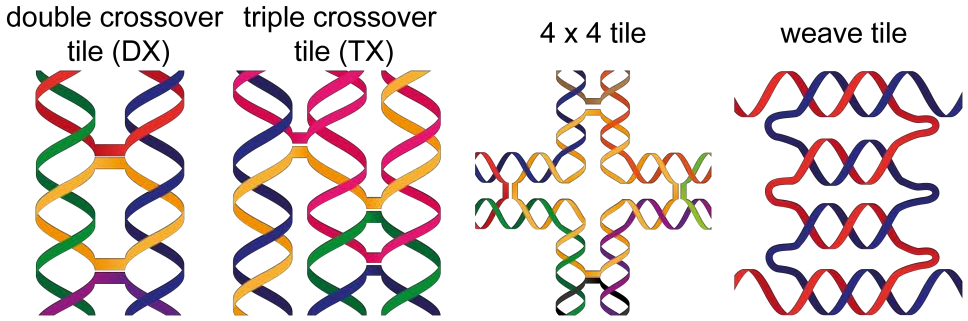

Figure 2.2: Schematic illustration of different possible DNA tiles. DNA tiles can be connected to each other using sticky ends to create larger DNA nanostructures. The images are adapted from literature.[30]

To design DNA tiles, one has to carefully construct the geometric structure (free energy and strain minimization) and the DNA sequence (sequence-symmetry minimization to avoid formation of other structures). Seeman developed a computer program called "SEQUIN" to help designing DNA sequences for the DNA tile construction.[30] To prepare DNA tile-based nanostructures, one has to ensure the purity and correct stoichiometry of used DNA strands. Impure DNA strands and wrong stoichiometry can lead to an alteration of the DNA tile and therefore prevent the formation of larger 2D and 3D lattices. Furthermore, the formation of DNA tiles is highly dependent on the presence of positively charged counterions. Magnesium ions are commonly used to prepare DNA nanostructures in aqueous solutions because they minimize the electrostatic repulsion of the negatively charged phosphate backbone of the DNA strand. Divalent cations are able to bridge the neighboring phosphate groups inter- and intrahelically. Once the right experimental conditions are found, the DNA strands and the buffer are mixed together and the mixture is exposed to denaturing conditions. Thus, secondary structures are destroyed and by reducing the denaturing conditions continuously Watson-Crick base pairing is maximized. The self-assembling process can be done with thermal annealing (heating of the sample followed by a slow cool down process) or at isothermal conditions with a denaturing agent such as urea or formamide[42] (first high concentration of the denaturing agent followed by a reduction of the concentration). The right denaturing conditions (time, temperature, denaturing agent concentration, combination of temperature and denaturing agent) highly depend

on the DNA structure itself.[30]

2.1.3 DNA origami structures

As written above the field of DNA nanotechnology started more than 30 years ago. The invention of DNA tiles gave the opportunity to build up nanostructures made of DNA. Still these DNA tile-based nanostructures have some constraints. To create larger 2D and 3D structures, a variety of short DNA strands is required which need to be of high purity and a certain stoichiometry of oligonucleotides is necessary. Furthermore, multiple reaction and purification steps are needed. To overcome these restrictions, Paul Rothemund introduced the DNA origami technique in 2006.[6] The principles and the potential for different applications of this method are discussed in this section.

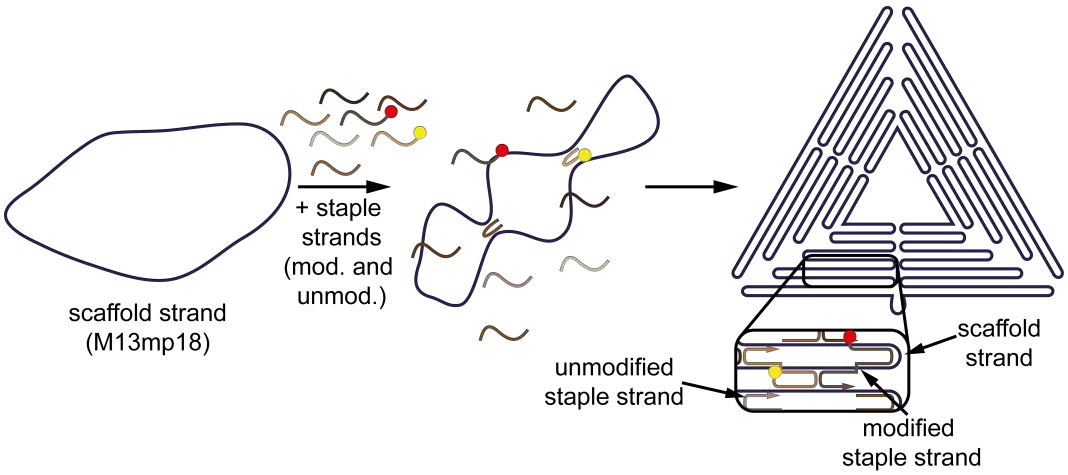

Figure 2.3: Schematic illustration of the DNA origami nanostructure self-assembling process. A circular "scaffold strand" is folded into arbitrary shapes with the help of short "staple strands". The DNA origami structures self-assemble during an annealing process. Modifications of the DNA origami structure can be introduced by modifying certain staple strands. The image is adapted from Bald *et al.*[43]

In this DNA origami approach, a long single stranded "scaffold" DNA is folded into arbitrary shapes with the help of short DNA single strands ("staple strands", 200 - 250 different strands) as schematically shown in figure 2.3. As a scaffold strand the M13mp18 bacteriophage is often used which consists of 7249 nt and has a known sequence.[6] The advantage of this method is that the short staple strands are commercially available and relatively inexpensive. Additionally, the long scaffold strand is easily extracted from virus DNA and is also rather inexpensive compared to long synthetic oligonucleotides. Furthermore, a known scaffold DNA sequence omits the need of complicated algorithms to generate randomized DNA sequences.[30] In the original paper by Paul Rothemund, it was shown that with the same scaffold DNA strand (M13mp18) and different sets of staple strands a variety of DNA nanostructures of different shapes can be prepared. He was able to prepare rectangles, triangles and even a five-pointed star

and smiley-face-shaped DNA nanostructures.[6] The size of these DNA nanostructures is approximately 100 nm x 100 nm and the preparation of such structures is relatively easy. To assemble the DNA origami structures, the scaffold strand is mixed with an excess of staple strands (5 - 20 fold excess compared to the scaffold strand) together with a Mg^{2+} containing buffer (*e.g.* Tris acetate-EDTA (TAE) buffer + $MgCl_2$, exact $MgCl_2$ concentration can depend on the DNA manufacturer because of different residues from various purification methods[44]) and followed by a thermal annealing step (from 90 °C to 20 °C in 2 hours). The DNA nanostructures self-assemble during this annealing process. Advantageously, the exact stoichiometry of staple and scaffold strands is of minor importance.[6] The exact shape of the DNA origami structure is determined by the used staple strands and can be altered by changing the sequences and number of staple strands. The packing distance between neighboring helices inside the DNA origami structure can be controlled by the space between crossovers. The inter-helical gap size depends on the number of half-turns (an integer number of half turns is needed for planar structures, 1.5 turns $\rightarrow$ 1 nm, 2.5 turns $\rightarrow$ 1.5 nm).[6,30]

The field of DNA origami structures grew quite fast in the last years. Researchers started to design and successfully built up three-dimensional DNA origami structures. The first example of such a 3D construct has been presented in 2009. Andersen *et al.* connected rectangles made from the M13mp18 scaffold strand to form a hollow 3D DNA origami box with a flexible lid showing the possibility of controlled unloading of nanocargo.[45] Ke *et al.* showed in the same year the successful assembly of a 3D tetrahedron from just one scaffold strand.[46] These 3D DNA origami structures are examples for hollow structures. Douglas *et al.* constructed the first solid 3D DNA origami nanostructure also in 2009 by changing the space and thus the angle between crossovers. It has to be noted that the yield of intact 3D DNA origami structures is lower than for 2D DNA origami structures and longer annealing times are needed. This is ascribed to the fact that the staple strands have difficulties to migrate to the center of the 3D DNA nanostructure.[47] Douglas *et al.* also designed a new scaffold strand to form DNA origami structures and found out that the yield of correctly formed DNA origami structures was lower than with M13mp18. They attributed this to a higher amount of G/C in the new scaffold strand showing that a certain balance of nt is necessary for DNA origami formation.[47] Furthermore, curvatures were introduced to construct even more complex DNA origami structures.[48,49] Because the formation of DNA origami structures is based on folding of a scaffold strand the final size of the DNA nanostructure highly depends on the used scaffold strand. Therefore, the size of such structures is limited and several works have been conducted to increase the size of these DNA nanostructures. In this sense, a new method called "DNA bricks" has been introduced. Here, DNA nanostructures are formed from many short single DNA strands. Each DNA strand can be seen as a pixel (3 nm x 7 nm in size) and the shape of the DNA nanostructure can be modified by including or omitting certain

DNA strands. 2D and 3D DNA nanostructures have been created using this DNA brick-based self-assembling method.[50,51]

To design DNA origami structures and to generate staple strand sequences, several computer programs have been developed. For designing 2D DNA origami structures "Tiamat" together with "SARSE" are generally used.[52–54] One of the most prominent programs is "caDNAno" (open-source software, http://cadnano.org/) which was developed by Shih and co-workers in 2009 and can also be used to design 3D structures.[55] In such programs, the user chooses a shape for the DNA origami structure and in the case of "SARSE" one can even import a bitmap of the desired shape followed by putting in DNA double helices (or single DNA molecules), joining them together (along the DNA backbone or with crossovers) and finally adding the desired scaffold strand. Then the program calculates the corresponding sequences for the DNA staple strands.[30]

The main advantage of DNA origami structures is that they are approximately 10,000 nm^2 in size and possess ca. 200 addressable positions (staple strands).[5] Each staple strand in the DNA origami structure can be addressed separately and individually. Since the exact position of each staple strand in the DNA origami structure is known different modifications can be introduced with a high local control. Rothemund showed in his initial paper that he was able to actually write on DNA origami structures by introducing "dumbbell hairpins" in the middle of the staple strands and visualize these "DNA letters" using atomic force microscopy (AFM).[6] Nowadays, modified nucleoside phosphoramidite building blocks containing for example fluorophores, biotin and other functional groups (NH_2, SH, alkyne etc.) are commercially available giving the opportunity to modify DNA origami nanostructures in a huge variety. Furthermore, DNA origami structures give the possibility to do spectroscopy in solution and on the single-molecule level without changing the nano-environment of the studied molecules.[56] Numerous review papers show the potential and possibilities of functionalizing DNA origami structures with different moieties.[43,57–66] The modifications range from gold[67–77] and silver nanoparticles[76,78] over quantum dots[72,73,79] and rods[80], fluorophores[19,56,70,73,81–86], aptamers[87], RNA[88] and DNA strands[89–92] to proteins such as streptavidin[93–96] and other organic molecules such as cholesterol.[97,98] The applications of these DNA origami arrays are also numerous and only a few of them are mentioned here. Gold nanoparticles (AuNPs) have been arranged on DNA origami structures to develop highly sensitive substrates for surface-enhanced Raman scattering (SERS).[67,68] This has further been improved by making DNA-graphene hybrid structures to improve the overall stability of the DNA origami structures.[99,100] Furthermore, AuNPs have been coupled to hollow DNA origami structures to generate a directional nanoparticle growth inside the DNA origami structure.[69] Streptavidin is often bound to DNA origami structures to analyze structural changes and chemical reactions exploiting the capability to visualize streptavidin molecules with AFM. For this, the highly specific streptavidin-biotin interaction is used to evaluate for exam-

ple DNA single strand breaks induced by low-energy electrons or UV photons using AFM.[89–92] Fluorescent labeled DNA origami structures can be used as nanoscopic rulers and standards for high resolution microscopy.[84–86] Due to the high local control of the spatial assembly of molecules fluorophores can be arranged precisely to create FRET arrays. Such FRET arrays can be used to monitor conformational changes of the DNA origami structure itself[45,70,101] or conformational dynamics of DNA strands attached to the DNA origami platform.[102,103] Furthermore, FRET arrays on DNA origami structures have been studied to create nanoscopic FRET rulers[81], artificial light harvesting systems[82,104] and photonic wire-like systems with controllable energy transfer pathways.[19]

2.2 G-quadruplex structures

DNA cannot only associate into a double strand but also into higher order structures as mentioned above. G-quadruplexes are such structures and can form from G rich sequences which occur for example naturally in telomere sequences which are located at the end of eukaryotic chromosomes to stabilize and protect the genome[105,106], in immunoglobulin switch regions[107] and promoter regions.[23,108,109] In 2005, two different surveys have been conducted to analyze the human genome regarding possible G-quadruplex forming sequences. Both investigations have found a similar number of such sequences (375,157[110] and 376,446[111]) showing the significance of G-quadruplexes in nature. In 1962, Gellert *et al.* analyzed concentrated solutions of guanosine monophosphate (GMP) which have been known to form gels since 1910[26,112] with X-ray fiber diffraction. In this study, it was shown that four G bases can be associated *via* eight Hoogsteen hydrogen bonds to form planar G-tetrads which are the structural basis of G-quadruplex structures.[113] In the following section an overview of G-quadruplex topology, thermodynamics, kinetics and potential applications is given.

2.2.1 G-quadruplex topology

As mentioned above, planar G-tetrads are four associated G bases which are stabilized by eight hydrogen bonds and a cation in the middle of the G-tetrad (see figure 2.4). The cation coordinates with the four central oxygen atoms of the G bases shown in figure 2.4. Due to the coordination of the cation the electronic repulsion between the oxygen atoms is weakened resulting in stronger hydrogen bonds and therefore a stabilization of the G-tetrad.[22] G-quadruplexes are generally two or more stacked G-tetrads as shown in figure 2.4 and can be folded from DNA sequences which contain tracts of repeated G bases. These G-quadruplexes can be classified according to the number of DNA strands involved in the G-quadruplex formation. G-quadruplex structures can be folded from four (tetramolecular or intermolecular), two (bimolecular or intermolecu-

lar) and one (unimolecular or intramolecular) DNA strands as schematically shown in figure 2.4. Generally, a tetramolecular G-quadruplex can be folded from four identical DNA strands with the following sequence $X_nG_mX_n$ (X_n: any nt of length n, G_m: any number of G bases of length m) and bimolecular G-quadruplexes are folded from two identical sequences $X_nG_mX_oG_mX_n$ (X_o: any nt of length o). It has to be noted that G-quadruplexes can be formed from non-identical sequences but just a few have been studied in detail so far. Unimolecular G-quadruplexes are folded from DNA strands with the following sequences $X_nG_mX_oG_mX_oG_mX_oG_mX_n$.[22,23]

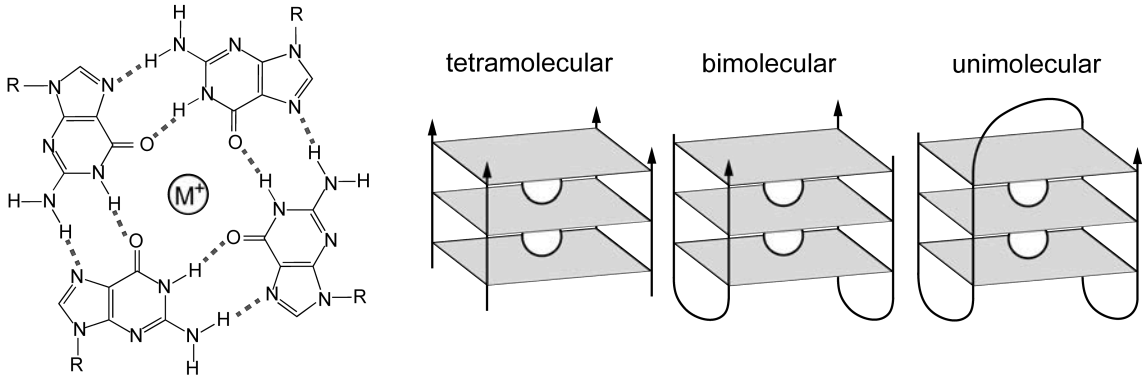

Figure 2.4: Schematic depiction of the G-quadruplex topology. Four G bases are associated by eight hydrogen bonds to a planar G-tetrad and stabilized by a cation in the center (left). G-quadruplexes are stacked G-tetrads (illustrated as gray flat rectangles) and can be formed from four (tetramolecular), two (bimolecular) or one (unimolecular) DNA strands (the shown assemblies represent only examples for such structures (see text)). The 3'-end of the DNA strand is visualized with an arrow. The images are adapted from Burge *et al.*[23]

Depending on the DNA strand orientation the G-quadruplex structure can be divided into anti-parallel (opposite strand orientations) and parallel (same strand orientation) structures. The DNA strands for most tetramolecular G-quadruplexes are aligned in a parallel manner.[22,23,26] In the case of bimolecular and unimolecular G-quadruplexes the top and bottom G-tetrads are connected *via* loops which can have different orientations. The G-tetrads can be connected with lateral and diagonal loops leading to so called "basket-type" or "chair-type" G-quadruplexes (anti-parallel) or with external loops leading to "propeller-type" G-quadruplexes (parallel). A combination of lateral and/or diagonal loops with external loops lead to "hybrid-type" G-quadruplexes (combination of anti-parallel and parallel). A mixture of all loop orientations is possible and some examples for different loop orientations are shown in figure 2.5a-f (examples for unimolecular G-quadruplexes).[22,23,26] The orientation of the loops for bimolecular G-quadruplexes depends on the loop length. Balagurumoorthy *et al.* for example showed that the G-quadruplex structure changes depending on the loop length (parallel: $G_4\mathbf{T}G_4$, parallel/anti-parallel: $G_4\mathbf{TT}G_4$, anti-parallel: $G_4\mathbf{TTT}G_4$/$G_4\mathbf{TTTT}G_4$).[114] Depending on the strand orientation the glycosidic angle (orientation of nb and sugar)

is either *syn* or *anti* (see figure 2.5g). For the anti-parallel strand orientation, the glycosidic angle alternates between *syn* and *anti*. For the parallel strand orientation the glycosidic angle is either *syn* or *anti* for all G bases (see also figure 2.5a-f).[22,23] As mentioned above, the cation (usually monovalent cations, some G-quadruplexes are stabilized by divalent cations[115,116]) in the core of the G-quadruplex stabilizes the structure. The precise position of the stabilizing cation within the G-quadruplex depends on the cation itself. Sodium ions for example can be located in plane with the G-tetrad (relatively small ion radius of Na^+) or sandwiched between two G-tetrads. Since potassium has a larger ion radius, K^+ is always located between two G-tetrads with an equal distance to each G-tetrad (symmetric tetragonal bipyramidal configuration).[23] Not only the exact position of the cation varies but also the stability of the overall G-quadruplex is influenced by different cations. The exact stabilization effect of the cation depends on the specific DNA sequence. Nevertheless, a general trend for some monovalent ions has been found ($K^+ > Na^+ > Rb^+ > NH_4^+ > Cs^+ > Li^+$). Please note that this trend might not be valid for all DNA sequences forming G-quadruplexes.[22,23]

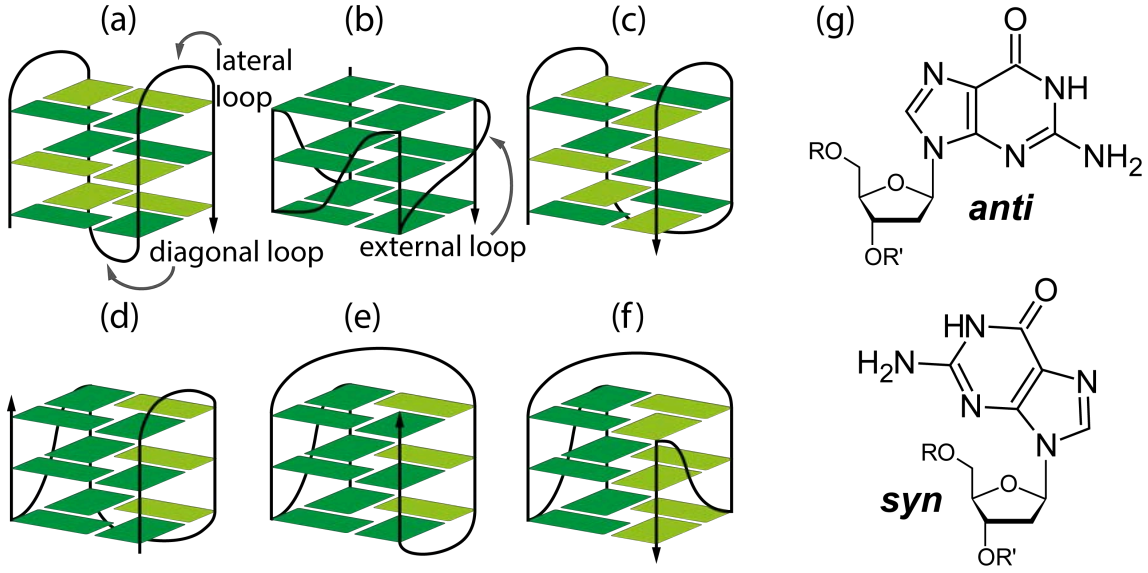

Figure 2.5: (a-f) Illustration of different possible unimolecular G-quadruplex configurations (single G bases depicted as green flat rectangles) showing the combination of different loop orientations (lateral, diagonal and external). Different glycosidic angles are represented by different colored G bases (dark green: *anti*, light green: *syn*). The illustrations are adapted from literature.[22] (g) Possible nb orientations for *syn* and *anti* glycosidic angles.

The G-quadruplex structures are additionally stabilized by the base-stacking effect through hydrophobic, electrostatic and van-der-Waals forces. Furthermore, the G bases cannot sit directly on top of each other resulting in a slight twist of the G-quadruplex structure.[22] As mentioned above G-quadruplexes take on a variety of specific structures. Especially for bimolecular and even more for unimolecular G-quadruplexes a

huge variety of different conformations is known and so far universal series of rules have not been found.[23] Some of the possible configurations for unimolecular G-quadruplexes are shown in figure 2.5a-f. The specific G-quadruplex structures and properties can be influenced by for example changing the loop sequence ($(G_3\mathbf{TTT})_3G_3$, $(G_3\mathbf{TTA})_3G_3$, $(G_3\mathbf{TAA})_3G_3$ and $(G_3\mathbf{AAA})_3G_3$: fraction of parallel/anti-parallel G-quadruplex structures changes)[117] and length ($G_3\mathbf{T}(G_3T)_2G_3$, $G_3\mathbf{TT}(G_3T)_2G_3$, $G_3\mathbf{TTT}(G_3T)_2G_3$, $G_3\mathbf{TTTT}(G_3T)_2G_3$ and $G_3\mathbf{TTTTT}(G_3T)_2G_3$: fraction of parallel/anti-parallel G-quadruplex structures changes)[117] or even by changing the directionality of the G rich DNA strand (*e.g.* $G_3TAG_3CAG_4ACACAG_3TAG_3$ *vs.* $G_3ATG_3ACACAG_4ACG_3ATG_3$: different melting temperatures).[118] Especially for the human telomeric DNA (HumTel, $(TTA\ GGG)_n$) a wide variety of structural conformations has been found making it hard to predict exact G-quadruplex structures for certain sequences. Many studies revealed that a variety of changes both within the DNA sequence and external conditions influence the specific G-quadruplex structure. The G-quadruplex structure is different for telomeric DNA and telomeric RNA[119], it is altered by changing the number of flanking nt ($\mathbf{A}G_3(T_2AG_3)_3$, $\mathbf{TA}G_3(T_2AG_3)_3$, $\mathbf{TA}G_3(T_2A\ G_3)_3\mathbf{T_2}$ and $\mathbf{A_3}G_3(T_2AG_3)_3\mathbf{A_2}$)[120,121] or the number of involved repeating units ($(TTA\ GGG)_\mathbf{2}$ *vs.* $(TTA\ GGG)_\mathbf{4}$).[122] When experimental conditions such as the cation itself (Na^+, K^+ and divalent cations)[123–126], the cation concentration[127], the DNA concentration[120], crowding agents (addition of polyethylene glycol to mimic molecular crowding in cells)[128] or the temperature[129] are changed alterations of the G-quadruplex structure are expected.[26] To determine the G-quadruplex structure of certain DNA sequences, a variety of experimental methods are used such as X-ray crystallography[123], NMR spectroscopy (nuclear magnetic resonance)[124,126], circular dichroism (CD) spectroscopy[130,131], Raman spectroscopy[132] and FRET experiments.[117,129,133]

2.2.2 G-quadruplex thermodynamics and kinetics

The overall G-quadruplex formation is enthalpy driven and the enthalpy values per G-tetrad are between -60 to -105 $\frac{kJ}{mol}$. Nevertheless, the exact enthalpy depends on different parameters such as the DNA sequence, DNA length, number of DNA strands involved in the G-quadruplex formation (tetramolecular, bimolecular and unimolecular), the cation and the specific G-quadruplex conformation (parallel, anti-parallel) as shown in table 2.1.[22] This favorable enthalpy is partly compensated by an unfavorable entropy (negative values). Again, the entropy values differ also depending on various parameters and are in the range from -0.4 to -1.3 $\frac{kJ}{mol\,K}$ (table 2.1).[22] Despite the unfavorable entropy most G-quadruplexes are stable under physiological conditions having negative Gibbs energies (exergonic process). Thus, under physiological conditions some G-quadruplex structures are the predominant configuration.[22] An overview of experimentally determined thermodynamic data found in literature for HumTel showing the

influence of DNA length, DNA sequence and cations are given in table 2.1.[134,135]

Table 2.1: Thermodynamic data reported in literature[134,135] for different G-quadruplex forming DNA sequences (enthalpy (ΔH), entropy (ΔS) and Gibbs energy (ΔG)). The values are all given for the complete G-quadruplex (not for a single G-tetrad).

DNA sequence	**cation**	$\boldsymbol{\Delta H}\left[\frac{kJ}{mol}\right]$	$\boldsymbol{\Delta S}\left[\frac{kJ}{mol\,K}\right]$	$\boldsymbol{\Delta G}$**(37 °C)** $\left[\frac{kJ}{mol}\right]$
TG_3T[134]	K^+	-262.1	-0.78	-28.9 (25 °C)
$T(G_3)_2T$[134]	K^+	-553.5	-1.45	-84.6 (25 °C)
$(G_3TTA)_3G_3$[135]	Na^+	-213.5	-0.65	-12.6
	K^+	-253.3	-0.75	-21.4
$A(G_3TTA)_3G_3$[135]	Na^+	-226.1	-0.68	-14.7
	K^+	-238.6	-0.71	-19.3
$TTTAA(G_3TTA)_3G_3$[135]	Na^+	-161.2	-0.51	-4.2
	K^+	-263.8	-0.81	-13.4

Another interesting aspect of G-quadruplexes is the kinetics of their formation. The question of how the G-quadruplex structures are folded has been addressed by different research groups.[121,133,136–138] The formation of a "hybrid-type" G-quadruplex structure (combination of anti-parallel and parallel strand orientations, an example of such structure is shown in figure 2.5d) is discussed in this section to show the variety of intermediate steps which are adopted during the folding process. Several studies have been conducted for this "hybrid-type" structure which can be folded by HumTel in presence of K^+ to resolve the folding process.[133,136–138] Generally, three different folding pathways have been proposed for this G-quadruplex formation (all three folding pathways are shown in figure 2.6). The folding pathway proposed by Mashimo *et al.* in 2007 involves the formation of an intermediate hairpin structure (formation of Hoogsteen H-bonds between G bases) followed by the formation of a "chair-type" G-quadruplex. This anti-parallel G-quadruplex transforms into the "hybrid-type" G-quadruplex as shown in figure 2.6 (red folding pathway).[136] In the second pathway also proposed by Mashimo *et al.* in 2008, the "hybrid-type" G-quadruplex is folded by firstly adopting a hairpin followed by a triplex intermediate structure as shown in figure 2.6 (brown folding pathway). Afterwards, the "hybrid-type" G-quadruplex forms directly from the triplex intermediate state.[137] In 2014, Gray *et al.* proposed a third folding pathway which is a combination of the earlier works. Here, the folding of a "hybrid-type" G-quadruplex takes place *via* a hairpin formation followed by the transition to an anti-parallel "chair-type" G-quadruplex which then transforms into a triplex intermediate (figure 2.6, blue folding pathway). This triplex intermediate finally transforms into the "hybrid-type" G-quadruplex as shown in figure 2.6 (blue folding pathway).[133] Gray *et al.* also proposed that the first step (transition from the unfolded structure to the hairpin intermediate) is a fast transformation and happens in less than 5 ms. The formation of the anti-parallel G-quadruplex intermediate is slower and happens

within 1 s. Subsequently, the transition from the G-quadruplex to the triplex intermediate state is rather slow (up to 3700 s) and is the rate-determining step. The last transition from the triplex intermediate to the final "hybrid-type" G-quadruplex takes around 750 s.[133] These results have been determined with a variety of methods (CD spectroscopy, fluorescence and UV stopped-flow kinetic measurements, FRET measurements (steady-state and time-resolved) and molecular modeling) showing the difficulties one faces when resolving a folding pathway for G-quadruplexes.

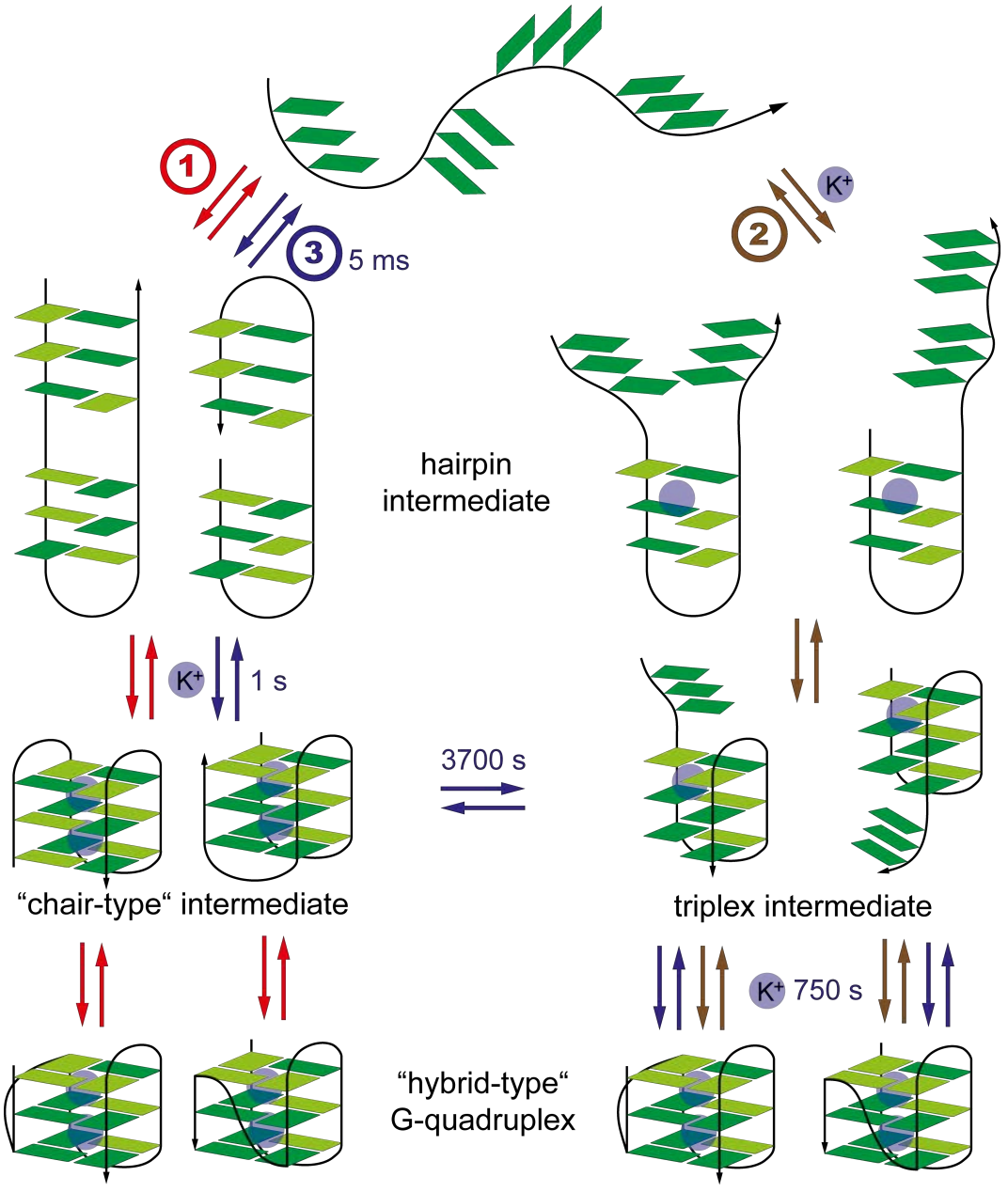

Figure 2.6: Proposed folding pathways based on different intermediate states (hairpin, triplex and anti-parallel G-quadruplex structure). The first (red) and second folding pathway (brown) have been proposed by Mashimo *et al.*[136,137] The third folding pathway (blue) is a combination of the other two folding pathways and has been presented by Gray *et al.*[133]

2.2.3 Applications for G-quadruplexes

In this section a few potential applications for G-quadruplex structures are discussed.

Telomere sequences which are located at the end of chromosomes are shortened during each cell division until they reach a critical length. At this point, the "Hayflick limit", the cells stop to replicate which can lead to cell death (apoptosis).[26,139] In 1985, an enzyme named telomerase was discovered which can extend telomeric DNA by adding telomeric repeating units.[140] Thus, the telomerase inhibits telomeric shortening and can prolong the cell activity. It has been found out that the telomerase is only expressed to a low amount in normal human somatic cells. For cancerous cells on the other hand, telomerase is expressed significantly.[26] When the telomerase activity is inhibited the telomeric DNA is shortened leading to apoptosis of the cancer cell in the end. G-quadruplexes for example are promising structures to inhibit the telomerase activity.[141] Thus, G-quadruplex stabilizing molecules are explored for anti-cancer therapeutics.[26,142]

Furthermore, G-quadruplex structures have been studied to be used as molecular switches with a variety of potential applications. Molecular switches or more precisely DNA switches are based on the reversible switching between two conformations (G-quadruplex and random coil/DNA duplex).[21,143,144] The switching phenomenon is generally based on the addition of "fuel" to fold the G-quadruplex structure followed by the addition of an "anti-fuel" to unfold the G-quadruplex structure subsequently. Repeated and alternating addition of "fuel" and "anti-fuel" leads to a cyclic folding and unfolding of the G-quadruplex (molecular switch, see figure 2.7).[21] Different mechanisms for the switching of G-quadruplex structures have been designed so far. Since G-quadruplex structures are stabilized by cations, switching can be achieved by removing the cation from the core of the G-quadruplex with the help of certain ligand molecules (see figure 2.7, yellow). Li *et al.* for example introduced lead ions to fold the G-quadruplex and removed them subsequently with the help of 1,4,7,10-tetraazacyclododecane-1,4,7,10-tetraacetic acid (DOTA, chelating agent).[115] K^+ stabilized G-quadruplex structures can be unfolded with the help of crown ethers such as 18-crown-6.[145,146] Switching between the folded and unfolded G-quadruplex can also be realized electrochemically by repeated reduction and oxidation of the metal ion (figure 2.7, red).[116] Furthermore, photoinduced switching is an elegant method to change the DNA conformation between G-quadruplex and random coil (figure 2.7, green). Here, the ability of certain *trans* azobenzene derivatives to stabilize certain G-quadruplexes is exploited. The *trans* azobenzene derivative isomerizes into the *cis* configuration under UV light leading to a destabilization of the G-quadruplex followed by unfolding. The G-quadruplex folds again after treating the system with visible light (*trans* azobenzene emerges). The advantage of this method is that no waste products are generated which could hamper the reproducibility of the switching cycle (figure 2.7, green).[147]

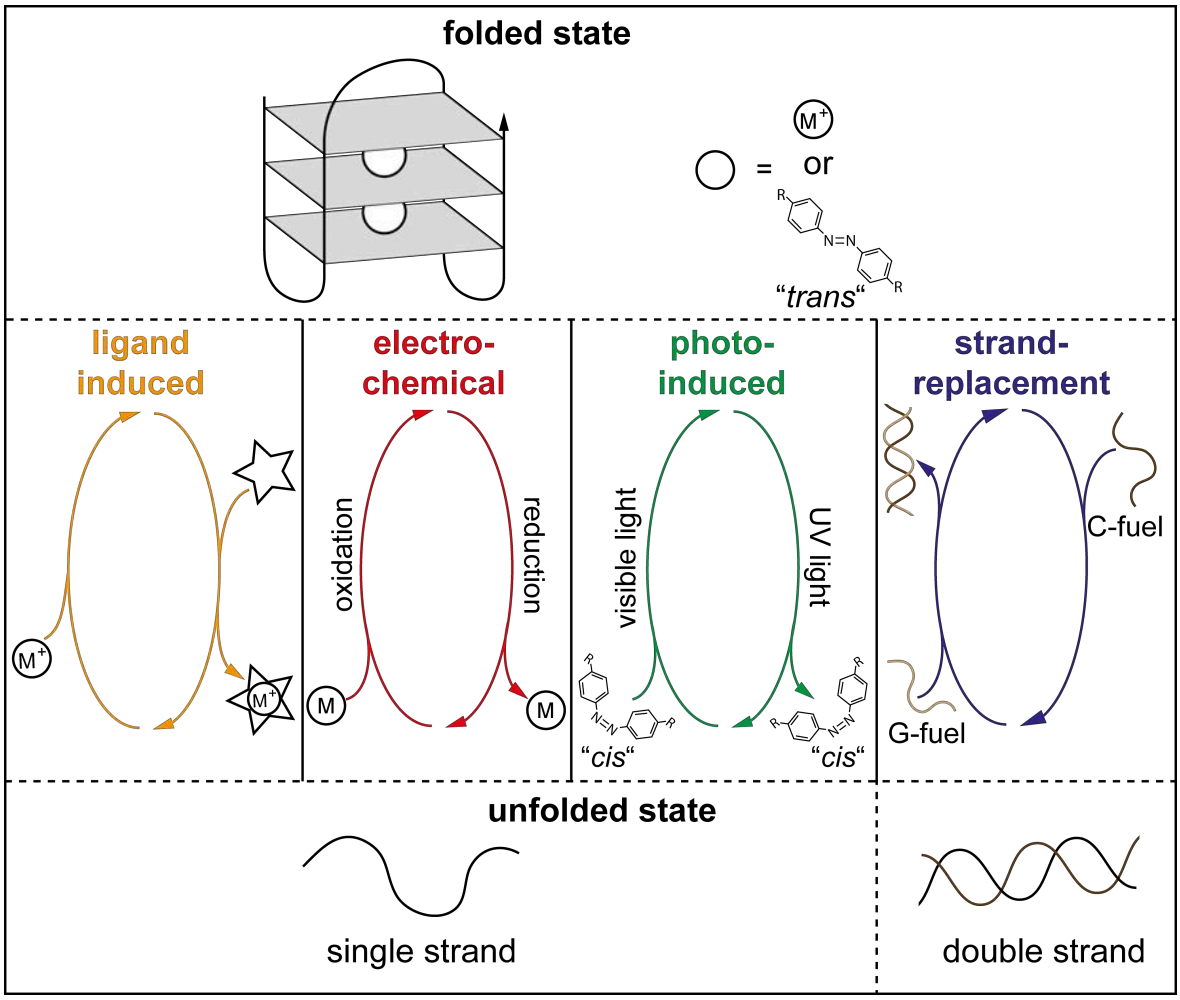

Figure 2.7: Schematic illustration of different switching pathways. The switching between folded and unfolded G-quadruplex can be achieved with the addition of certain ligands (yellow, the ligand is represented by the star), electrochemically (red), photoinduced (green, for G-quadruplexes which are stabilized by *trans* azobenzene derivatives) or by strand replacement (blue, here: switching between G-quadruplex and DNA double strand).[21,143]

Another prominent mechanism for the conformational switching of G-quadruplexes is based on strand replacement reactions (figure 2.7, blue). Here, the G-quadruplex is unfolded by introducing a complementary DNA strand ("C-fuel") which forms a duplex with the G rich sequence. Afterwards, this fuel strand is removed by the addition of another DNA strand ("G-fuel") resulting in a double stranded waste product.[143,148] Different experimental methods have been used to study the switching process of G-quadruplex structures *e.g.* high-speed AFM[138,149–152], FRET[17,153,154], fluorescence intensity of intercalating fluorophores[116,155] and voltammetric measurements.[156] There are a variety of potential applications for such switchable systems. Since some G-quadruplex structures are selective for certain cations, these systems can be used as sensing devices.[17,115,154,157–159] Furthermore, switching of G-quadruplex structures can be used to control enzyme cascades[146], design switchable DNA hydrogels[160,161] or to generate a controlled release of certain molecules.[162]

2.3 Förster resonance energy transfer

In the following section the basics of fluorescence and Förster resonance energy transfer (FRET) are explained including potential applications for FRET.

2.3.1 Fluorescence

Matter can interact with electromagnetic radiation in different ways. An overview of different matter-light interactions is presented in figure 2.8. The interaction between light and matter can result in scattering, absorption and ionization processes. In the following section the process of absorption and more precisely the process of photoluminescence are discussed.[163,164]

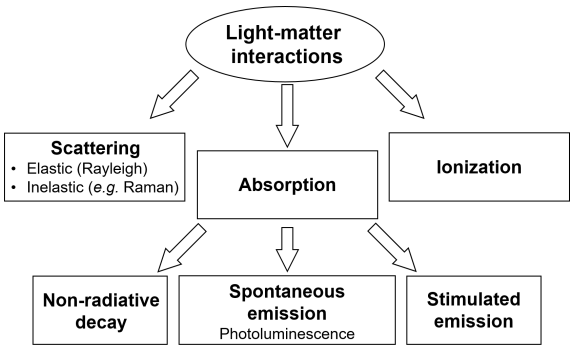

Figure 2.8: Overview of different interactions between electromagnetic radiation and matter. Image is adapted from literature.[164]

The photon absorption of electromagnetic radiation in the UV and visible range can lead to electronic transitions. In this sense, a molecule can be excited from its electronic ground state S_0 to higher electronic states such as S_1 or S_2. Such an excitation process is shown in the Jablonski diagram in figure 2.9.[165] The absorption of electromagnetic radiation follows the Beer-Lambert law (equation 2.1).

$$A = \varepsilon \cdot l \cdot c \tag{2.1}$$

Where A is the absorbance, ε the extinction coefficient, l is the absorption path length and c is the concentration of the sample.[163,164] Two selection rules are valid for electronic transitions - the spin-multiplicity (electronic transitions between electronic states with different spin-multiplicities are forbidden) and the Laporte rule (electronic transitions are only allowed if the parity changes).[163,164,166] Intersystem crossing (ISC) - which is for example a transition from a singlet excited state to a triplet excited state (spin-multiplicity changes) - becomes more likely in heavy atoms due to stronger spin-orbit coupling. The electronic transition of molecules behaves according to the Franck-Condon principle. This means that because of the high mass difference between the nucleus and the electron an electron transition proceeds always vertically.

Since light absorption is such a fast process ($< 10^{-15}$ s) the nucleus does not change significantly its position during this process.[163,164]

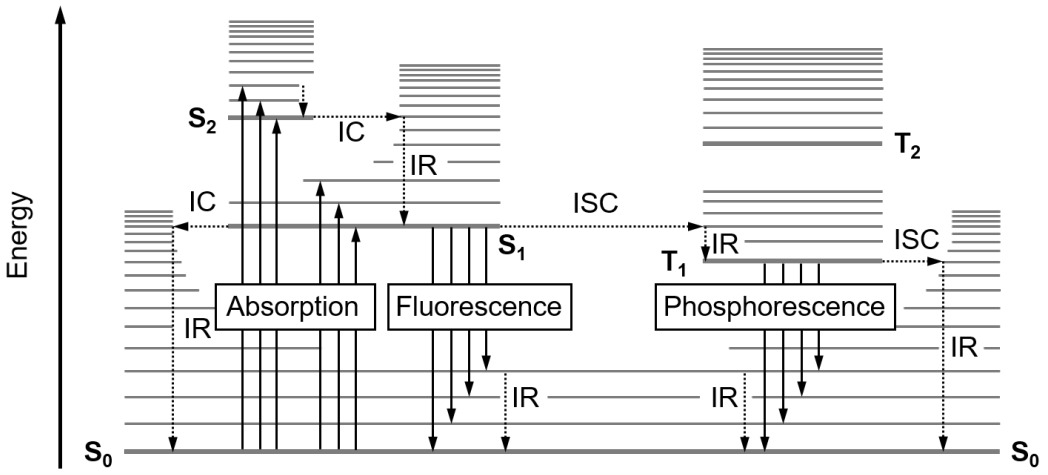

Figure 2.9: Jablonski diagram (adapted from literature[164]) showing possible electronic transitions (S_0 = singlet ground state; S_1, S_2 = singlet excited state; T_1, T_2 = triplet excited state). Solid arrows illustrate radiative processes (absorption, fluorescence and phosphorescence) and dashed arrows represent non-radiative processes (internal relaxation (IR), internal conversion (IC) and intersystem crossing (ISC)).

After the absorption of one or more photons different radiative and non-radiative processes can follow as shown in figure 2.9. When a molecule is excited to a higher excited state than S_1 such as S_2 non-radiative relaxation (internal relaxation (IR)) to the vibrational ground state of S_2 follows, from which transitions to the S_1 state (higher vibrational states) *via* internal conversion (IC) take place. From these higher vibrational states of S_1, IR to the vibrational ground state of S_1 follows. Now, the molecule can be deactivated by different steps. From the vibrational ground state of S_1 non-radiative transitions *via* IC to a higher vibrational state of S_0 are possible followed by IR to the vibrational ground state of S_0. This IC is less efficient compared to the IC from S_2 to S_1 because the energy gap between S_1 and S_0 is larger. When the deactivation from S_1 is accompanied with light emission the process is called fluorescence. According to Kasha's rule fluorescence is mainly happening from the vibrational ground state of S_1 (emission spectrum is independent from the excitation wavelength). The molecule either translates to higher vibrational states of S_0 followed by IR or directly to the vibrational ground state of S_0. As explained above the molecule can also undergo an ISC which is a transition from a singlet state (S_1) to a triplet state (T_1). From higher vibrational states of T_1, IR to the vibrational ground state of T_1 follows from which radiative transitions to S_0 can take place. This phenomenon is called phosphorescence (figure 2.9). It has to be noted that fluorescence occurs at higher wavelength compared to the light absorption process because of energy loss in the excited state (due to for example interaction with solvent molecules, Stokes shift). Only a small fraction appears

at smaller wavelength (overlap between absorption and emission spectra) because a few molecules are at a higher vibrational state of S_0 at room temperature (RT) according to the Boltzmann equation.[163,164] The time a molecule is located in the excited state is called fluorescence decay time τ_F and is defined as follows,

$$\tau_F = \frac{1}{k_r + k_{nr}} \tag{2.2}$$

where k_r is the rate constant for radiative and k_{nr} for non-radiative deactivation. For organic molecules the fluorescence decay time is in the range of tens of picoseconds to hundreds of nanoseconds. The fluorescence decay time can be experimentally measured using time-resolved spectroscopy (*e.g.* TCSPC, see section 3.4.4). The ratio of emitted photons to absorbed photons is called fluorescence quantum yield Φ_F and can be expressed using equation 2.3.[163,164]

$$\Phi_F = \frac{k_r}{k_r + k_{nr}} = k_r \cdot \tau_F \tag{2.3}$$

2.3.2 Theory of FRET

The energy of an excited molecule can be released in different ways. Luminescence as described above is one way. Another de-excitation process is the energy transfer from one molecule (donor) to another molecule (acceptor) given that the donor's emission overlaps with the acceptor's absorption spectrum. This energy transfer can occur based on different mechanisms. An overview of these mechanisms is shown in figure 2.10. Förster resonance energy transfer (short: FRET) is a non-radiative energy transfer and the theory of it is explained in this section.

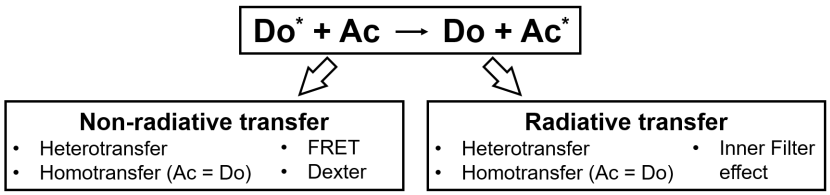

Figure 2.10: Possible energy transfer processes from an excited donor (Do^*) to an acceptor molecule (Ac).

FRET is an energy transfer from an excited donor (Do) to an acceptor (Ac) *via* long-range dipole-dipole interactions. Based on these coulombic interactions the excited Do molecule returns to its ground state and at the same time the Ac molecule is excited from its HOMO (highest occupied molecular orbital) to its LUMO (lowest unoccupied molecular orbital) (see figure 2.11a). For FRET to take place the Do and Ac molecules need to be in resonance (energy differences between HOMO and LUMO of Ac and Do are identical). This is fulfilled when the Do's emission spectrum overlaps with the Ac's absorption spectrum as mentioned above (figure 2.11b). Furthermore, the Do-Ac pair

needs to be in close proximity for an efficient energy transfer process. Efficient FRET is usually observed for distances ranging from 2 to 10 nm for organic chromophores.[163,164]

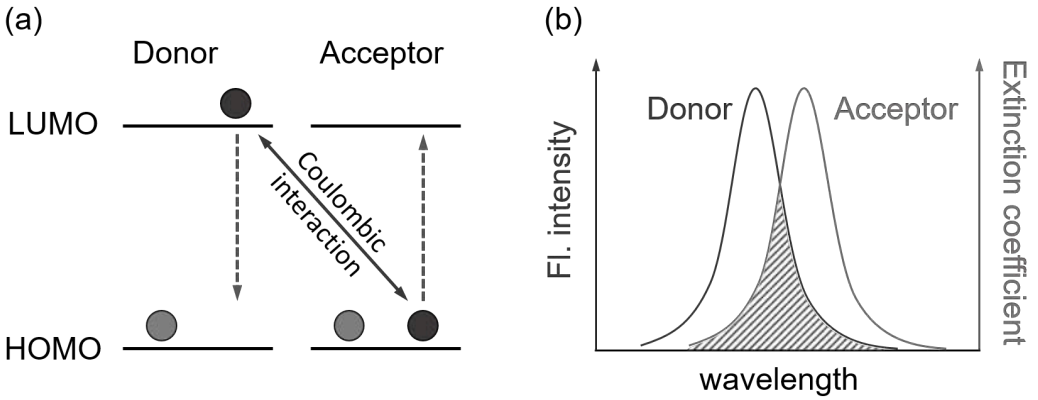

Figure 2.11: (a) During the FRET process the energy of the excited Do is transferred *via* coulombic interactions to the Ac (LUMO = lowest unoccupied molecular orbital, HOMO = highest occupied molecular orbital). (b) Schematic illustration of the spectral overlap between the emission spectrum of the Do and the absorption spectrum of the Ac. (Illustrations are adapted from literature[164])

As FRET is based on a dipole-dipole interaction the rate constant for FRET k_{FRET} is as follows,

$$k_{FRET} = k_D \left(\frac{R_0}{R}\right)^6 = \frac{1}{\tau_D}\left(\frac{R_0}{R}\right)^6 \tag{2.4}$$

with k_D being the emission rate constant of the Do, τ_D the Do's fluorescence decay time in the absence of the Ac molecule, R_0 the Förster distance and R the physical Do-Ac distance. The Förster distance is the Do-Ac distance at which spontaneous decay of the Do and FRET are equally probable. The FRET efficiency is equal to 50 % at this distance. R_0 is a FRET pair specific parameter and it can be calculated based on the spectral properties of the Do and Ac molecules. The Förster distance is typically in the range from 1 to 8 nm for organic fluorophores.[163,164] It can be calculated with the following equation 2.5.

$$R_0^6 = \frac{9(ln10)\kappa^2 \Phi_D J(\lambda)}{128\pi^5 n^4 N_{AV}} \tag{2.5}$$

Here, κ^2 is the dipole orientation factor, Φ_D is the Do's quantum yield in absence of the Ac molecule, $J(\lambda)$ is the spectral overlap integral, n is the medium's refractive index and N_{AV} is Avogadro's constant ($6.02 \cdot 10^{23}$ mol^{-1}). The dipole orientation factor depends on the orientation of the Do's emission transition moment $\vec{r}_D$ and the Ac's absorption transition moment $\vec{r}_A$. It is expressed as follows,

$$\kappa^2 = (cos\alpha - 3 \cdot cos\beta \cdot cos\gamma)^2 \tag{2.6}$$

where α is the angle between Do's emission and Ac's absorption transition moments, β and γ are the angles between Do-Ac linkage and Do's emission and Ac's absorption transition moment, respectively (see figure 2.12a). The dipole orientation factor can have values ranging from 0 to 4 (collinear: $\kappa^2 = 4$, parallel: $\kappa^2 = 1$, perpendicular: $\kappa^2 = 0$). For freely oriented molecules which rotate with a faster rate than the de-excitation rate of the Do κ^2 is $\frac{2}{3}$.[163,164]

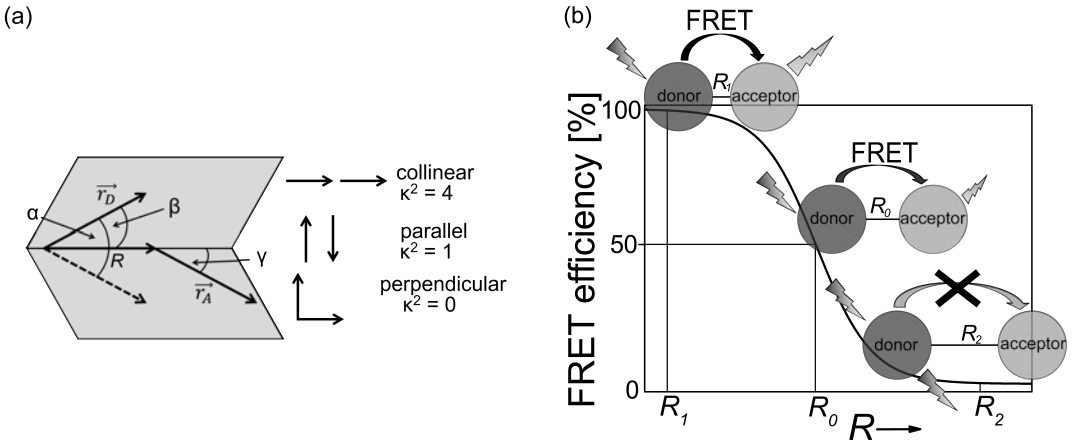

Figure 2.12: Fundamentals of Förster resonance energy transfer. (a) Influence of the orientation of the Do emission transition moment $\vec{r}_D$ and the Ac absorption transition moment $\vec{r}_A$ on κ^2 with the Do-Ac linkage R. The figure is adapted from literature.[164] (b) FRET efficiency as a function of Do-Ac distance (R) with R_0 being the Förster distance at which the FRET efficiency is 50 %.

The overlap integral expresses the degree of spectral overlap between Do's emission and Ac's absorption spectra and can be calculated as follows,

$$J(\lambda) = \frac{\int_0^\infty F_D(\lambda)\varepsilon_A(\lambda)\lambda^4 d\lambda}{\int_0^\infty F_D(\lambda)d\lambda} \tag{2.7}$$

where $F_D(\lambda)$ is the Do's emission spectrum at particular wavelengths λ and $\varepsilon(\lambda)$ is the Ac's extinction coefficient spectrum. The spectral overlap integral can be expressed in terms of $[M^{-1}cm^{-1}nm^4]$ or $[M^{-1}cm^3]$. Depending on the unit of the spectral overlap integral R_0 can be calculated with the following equations 2.8 and 2.9 where all of the constants from equation 2.5 are combined. The values of the Förster distance using either equation 2.8 or equation 2.9 are in $[\mathring{A}]$.[163,164]

$$[M^{-1}cm^{-1}nm^4]: \; R_0 = 0.211 \left(\frac{\kappa^2 \Phi_D J(\lambda)}{n^4}\right)^{\frac{1}{6}} \tag{2.8}$$

$$[M^{-1}cm^3]: \; R_0 = 9.79 \cdot 10^3 \left(\frac{\kappa^2 \Phi_D J(\lambda)}{n^4}\right)^{\frac{1}{6}} \tag{2.9}$$

The FRET efficiency E as mentioned above is highly distance dependent and behaves

according to equation 2.10.

$$E = \frac{R_0^6}{R_0^6 + R^6} \tag{2.10}$$

The FRET efficiency is high at short distances and low at long distances. It changes barely at short and long distances and rapidly around the Förster distance resulting in a sigmoidal behavior of the FRET efficiency plot as shown in figure 2.12b. The FRET efficiency can be calculated based on the Do's emission intensity (E_I, equation 2.11). Since the emission intensity is highly dependent on the overall sample concentration the FRET efficiency can also be calculated using the Do's fluorescence decay time (E_τ, equation 2.12).[163,164]

$$E_I = 1 - \frac{I_{DA}}{I_D} \tag{2.11}$$

$$E_\tau = 1 - \frac{\tau_{DA}}{\tau_D} \tag{2.12}$$

The index DA denotes the system when the Ac molecule is present and D when only the Do molecule is present.[163,164]

2.3.3 DNA-based photonic wires and light harvesting systems

FRET has numerous applications in the field of life sciences and nanotechnology. It is used for example to transfer light energy either in a linear manner over a cascade of fluorophores for several nanometers (photonic wires) or to funnel the excitation energy into a reaction center (light harvesting systems). These two applications are discussed in the following section.

A FRET-based photonic wire can be regarded as an optical waveguide in which the light energy is transferred along a certain pathway. In these photonic wires, multiple fluorophores are linearly assembled and they transfer the energy from one to another. This fluorophore alignment can be prepared by directly linking the fluorophores together or by arranging them on a molecular scaffold such as DNA.[20,24,25] The first photonic wire was constructed by Wagner *et al.* in 1994 by linking porphyrin molecules directly together.[167] Generally, there are two different approaches to transfer the light energy along a linear alignment of fluorophores. Firstly, the energy transfer process can be based on homo-FRET (figure 2.13). Here, the light energy is transferred between identical fluorophores given that the fluorophore has a small Stokes shift (large spectral overlap between absorption and emission spectra). In this case, the energy transfer has no direction and it is also referred to as statistical diffusion.[20] Ohya *et al.* designed a photonic assembly on DNA based on homo-FRET. In this study different organic molecules (eosin, Texas Red, tetramethylrhodamine (TAMRA)) have been used to transfer the energy along the DNA scaffold (based on homo-FRET of

TAMRA).[168] In another study, light energy was transferred from Fluorescein (FAM) over TAMRA to Cyanine5 (Cy5) (again, all fluorophores have been assembled on a DNA scaffold). Here, TAMRA acted as a transmitter dye to transfer the energy *via* homo-FRET from FAM to Cy5.[169] In these examples the organic fluorophores have all been bound covalently to DNA strands. Another approach for homo-FRET-based photonic wires is the use of intercalating fluorophores which transfer the light energy along the DNA double helix.[170,171]

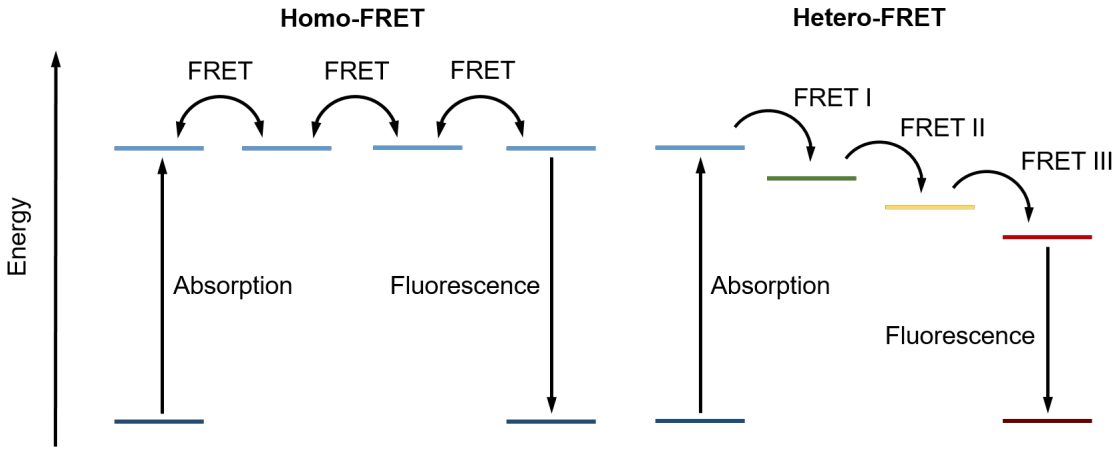

Figure 2.13: Schematic illustration of homo-FRET- (left) and hetero-FRET-based (right) photonic wires. For homo-FRET, the energy passes between the same type of fluorophore without any directionality. For hetero-FRET, the energy is passed from one fluorophore to another with directionality and loss in energy. The illustration is adapted from Albinsson *et al.*[20]

Additionally, the light energy cannot only be transmitted based on homo-FRET but also using multiple hetero-FRET steps. Here, an energy gradient is created from one end (high energy) to the other end (low energy) by choosing matching fluorophores (see figure 2.13). In such systems, a Do molecule transfers its energy to an Ac molecule given that the Do's emission spectrum overlaps with the Ac's absorption spectrum. Then the Ac molecule becomes a Do molecule and transfers the light energy to the next Ac (again, spectral overlap between Do's emission and Ac's absorption spectra is necessary). Here, the energy cascade creates a pronounced directionality involving an energy loss due to the red-shifted emission of the fluorophores.[20] There are numerous examples for such systems on different DNA platforms.[25] Heilemann *et al.* for example coupled five different fluorophores to a DNA double helix and achieved a photonic wire with a length of 13.6 nm and a spectral range of 200 nm.[172,173] Medintz and co-workers have created plenty of photonic wires combining different fluorophores such as organic dyes (up to seven different organic dyes in one photonic wire[174]), quantum dots or lanthanide complexes.[174–179] In all of these studies the light energy propagates in just one direction. With the use of DNA origami structures two-dimensional energy transfer pathways can be created which has been shown by Stein *et al.* In this study, they used

a so called "jumper" dye which depending on its position changed the direction of the energy transfer cascade.[19]

Artificial light harvesting systems are inspired by biological light harvesting complexes found in natural photosynthesis. Here, light is absorbed by many pigment molecules (antenna units) and the light energy is then funneled into a reaction center where the optical energy is converted into chemical energy (figure 2.14).[180–184]

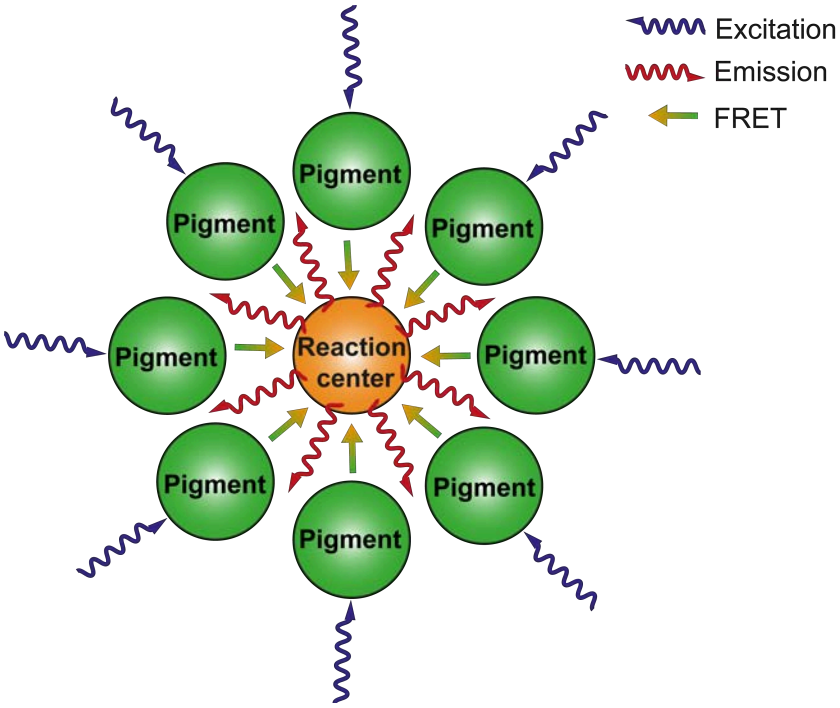

Figure 2.14: Illustration of a light harvesting system. The pigment molecules (Do molecules) absorb the light energy and transfer it to a reaction center for example another fluorophore (Ac molecule). Image is adapted from Mayr *et al.*[185]

The light harvesting efficiency is often expressed using the antenna effect (AE). The antenna effect in this manner is the Ac intensity ratio of Ac emission generated due to the FRET process (sensitized emission) and Ac emission upon direct excitation (equation 2.13).

$$AE = \frac{I(A,\, \lambda_{ex}(D))}{I(A,\, \lambda_{ex}(A))} \tag{2.13}$$

Here, $I(A, \lambda_{ex}(D))$ is the Ac emission intensity due to FRET (Do direct excitation) and $I(A, \lambda_{ex}(A))$ is the Ac emission intensity of the same sample when directly excited.[24] It has to be noted that the antenna effect is highly dependent on the chosen wavelength for direct Ac excitation and can only be compared when the same experimental settings are used.[82,104,176] Many artificial light harvesting systems have been created in which the energy is transferred based on FRET from multiple Do molecules to just a few or one single Ac molecule.[20,186,187] These photonic assemblies have been generated in one[188], two[189] and three dimensions.[190] Different light harvesting systems have been created using DNA as a scaffold and intercalating dyes as energy transmitting

units.[188,191–193] Medintz and co-workers analyzed the effect of different geometries and number of chromophores on the light harvesting efficiency (linear assembly, Holliday junction and star-like assembly).[176] With the introduction of DNA origami structures well-defined three-dimensional light harvesting systems have been created. Dutta *et al.* used a seven-helix DNA bundle to study the light harvesting efficiency and FRET efficiency of a three-color FRET system carefully using steady-state and time-resolved fluorescence spectroscopy. They used pyrene as a Do, Cyanine3 (Cy3) as a transmitter and Alexa Fluor 647 as the final Ac molecule and studied different Do/transmitter/ Ac ratios.[104] Recently, Hemmig *et al.* analyzed the light harvesting efficiency of a two-color FRET system (Do: Cy3; Ac: Cy5) on rectangular DNA origami structures. The Ac molecule was surrounded by a maximum number of six Do molecules. In this study, they analyzed thoroughly the antenna effect of different Do/Ac ratios starting from 1:1 to 6:1 (Do:Ac). They showed that the antenna effect increases linearly with an increasing number of Do molecules.[82]

Chapter 3

Experiments and Methods

3.1 Materials and chemicals

In this work, unmodified oligonucleotides used as staple strands (sequences shown in the appendix in table A.1) have been purchased from Integrated DNA Technologies (Leuven, Belgium). The DNA strands have been purified by standard desalting procedures and dissolved in RNase-free water by the manufacturer and have been used as delivered. The viral genome M13mp18 has been purchased from tilibit nanosystems GmbH (Garching, Germany). The DNA has been dissolved in buffer containing 10 mM Tris (tris(hydroxymethyl)aminomethane) and 1 mM EDTA (ethylenediaminetetraacetic acid) by the manufacturer (quality control by agarose gel electrophoresis) and used as delivered. The oligonucleotides modified with the organic dyes (Fluorescein (FAM), Cyanine3 (Cy3), Cyanine5 (Cy5) and IRDye®700 (IRDye700)) have been acquired from Metabion International AG (Planegg/Steinkirchen, Germany). The modified oligonucleotides have been purified by the manufacturer using HPLC (high-performance liquid chromatography) and have been used as delivered. An overview of used fluorophores showing their structural and spectroscopic properties are shown in table 3.1. Magnesium chloride ($MgCl_2$, $\geq$ 98 %), sodium chloride (NaCl), cryptand (4,7,13,16,21,24-hexaoxa-1,10-diazabicyclo[8.8.8]hexacosane, $\geq$ 98 %) and TAE buffer (10x concentrated) have been acquired from Sigma Aldrich (Taufkirchen, Germany). Diluted TAE buffer (1x concentrated) (pH = 8.2) contains 40 mM Tris-acetate and 1 mM EDTA. Ammonium chloride (NH_4Cl, $\geq$ 99.5 %) and calcium chloride ($CaCl_2$, $\geq$ 98 %) have been acquired from Carl Roth (Karlsruhe, Germany), potassium chloride (KCl) from VWR Prolabo (Darmstadt, Germany), lithium chloride (LiCl, $\geq$ 99 %) from Acros organics (Fisher Scientific GmbH, Schwerte, Germany) and cesium chloride (CsCl, $\geq$ 99 %) from chemPUR (Karlsruhe, Germany). 18-crown-6 (1,4,7,10,13,16-hexaoxacyclooctadecane) and 100 kDa and 10 kDa molecular weight cut-off centrifugal filters have been used from Merck Millipore (Darmstadt, Germany). Diluted DNA solutions, TAE buffer and salt stock solutions have been prepared in ultrapure water

(Merck Millipore). Mica has been purchased from Plano GmbH (Wetzlar, Germany). For the DNA origami assembly, a Thermocycler "advanced primus25" from PEQLAB/ VWR (Erlangen, Germany) and for the sample filtration a centrifuge 5804 from Eppendorf (Hamburg, Germany) have been used.

Table 3.1: Overview of used fluorophores showing the chemical structures of each fluorophore (FAM, Cy3, Cy5 and IRDye700) and spectral properties (absorption maximum (λ_{abs}), emission maximum (λ'_{em}) and fluorescence decay time (τ_F)). All values have been measured on DNA origami structures. The variations are due to different dye positions on the DNA origami structure. The blue circle in the chemical structures of the fluorophores resembles the attachment point for DNA which is shown in detail in the appendix in figure A.1.

fluorophore	**abbreviation**	**chemical structure**	**λ_{abs} [nm]**	**λ'_{em} [nm]**	**τ_F [ns]**
Fluorescein	FAM	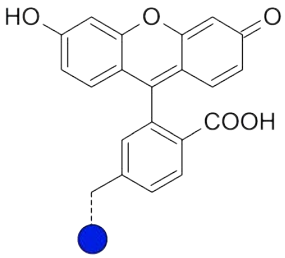	455 - 460	515 - 522	4.1 - 4.6
Cyanine3	Cy3	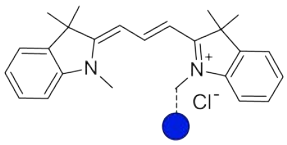	548 - 550	564 - 567	2.2 - 2,6
Cyanine5	Cy5	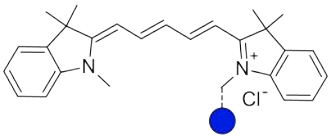	645 - 650	663 - 668	1.8 - 2.0
IRDye®700	IRDye700	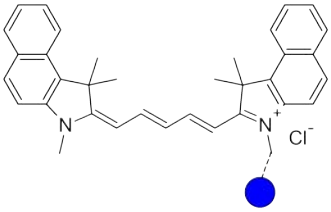	690	710	1.1

3.2 Sample preparation

3.2.1 Preparation of DNA origami structures

The DNA origami structures have been prepared by mixing the circular, single stranded viral genome M13mp18 (5 nM) with 208 short single DNA strands (modified and unmodified staple strand sequences can be found in the appendix tables A.1 and A.2) (150 nM), TAE buffer (10x concentrated) containing 100 mM $MgCl_2$ and ultrapure water (Merck Millipore). The solution has been heated up to 80 °C and then slowly cooled down to 8 °C in 2 hours with a defined temperature program (80 °C - 66 °C:

1 °C every 30 s, 66 °C - 25 °C: 1 °C every 2 min, 25 °C - 8 °C: 1 °C every minute) using a thermal cycler. Afterwards, the self-assembled DNA origami structures have been purified using 100 kDa molecular weight cut-off centrifugal filters to remove the excess of staple strands. For this, the samples have been washed four times with TAE buffer (1x concentrated) containing 10 mM $MgCl_2$ at 2655×g for 10 min. After the preparation of DNA origami structures, each sample has been analyzed using AFM to verify the correctly formed structures followed by fluorescence spectroscopy analysis.

3.2.2 G-quadruplex folding and unfolding

The folding of G-quadruplexes has been analyzed for free telomeric DNA and for telomeric DNA on DNA origami structures. For the free telomeric DNA KCl (c = 20 mM, 200 mM, 2 M) has been added to the solution and incubated for 15 min at RT. After the incubation, the samples have been analyzed using steady-state and time-resolved fluorescence spectroscopy at a DNA concentration of ca. 5 nM.
For telomeric DNA on DNA origami structures, KCl (c = 20 mM, 200 mM, 2 M) has been added to the samples followed by shaking at 40 °C for 15 min. To unfold the G-quadruplex subsequently, an aqueous cryptand solution has been added (c = 200 mM, 2 M) and the samples have been incubated at 40 °C for 15 min. To remove KCl and cryptand from the samples, they have been washed three times with TAE buffer (1x concentrated) containing 10 mM $MgCl_2$ using centrifugal filters (10 kDa molecular weight cut-off filter) at 3824×g for 7 min. The samples have been analyzed after each KCl and cryptand addition and after each filtration step using steady-state and time-resolved spectroscopy at a DNA concentration of ca. 5 nM.

3.3 FRET systems on DNA origami structures

Different FRET systems with different fluorophores and different fluorophore orientations on DNA origami structures have been analyzed in this work.[1–3] In the following section the fluorophore positions and orientations and the intermolecular distances of the fluorophores in the different FRET systems are discussed. For all systems triangular shaped DNA origami structures based on the original Rothemund design[6] have been used to arrange the fluorophores at certain positions. A detailed map of the whole DNA origami structure is shown in the appendix in figure A.2. The distances discussed in this section are based on a rigid and idealized geometry and are only rough values to give an overview of the size ranges of the analyzed FRET systems. Here, certain assumptions for the distance calculations have been made based on the structural properties of dsDNA (dsDNA: 0.34 nm/nb, 10.5 nb = 3.5 nm, DNA double helix diameter: 2 nm) and the DNA origami design (inter-helical gap size: 0.5 nm (crossover every 16 nb)). For ssDNA, the DNA strand length is also calculated based on the struc-

tural properties of dsDNA and can therefore differ from the actual length because of a higher flexibility in ssDNA.[28] The exact sequences for the modified staple strands mentioned in this section can be found in table A.2 in the appendix. This section is divided according to the manuscripts discussed in this work.

3.3.1 Ion-selective formation of a guanine quadruplex on DNA origami structures

The formation of G-quadruplex structures has been analyzed for free telomeric DNA and for telomeric DNA on DNA origami structures (using the reversed human telomeric DNA (RevHumTel)).[1] For the free telomeric DNA the 5'- and 3'-end of the DNA strand are modified with an acceptor and a donor dye, respectively. Here, FAM is the donor and Cy3 the acceptor dye. The fluorophores are separated by 26 nb (Cy3-RevHumTel-FAM, 5'-Cy3-TT (GGG ATT)$_4$-FAM) which corresponds to a length of approximately 8.6 nm (see figure 3.1).

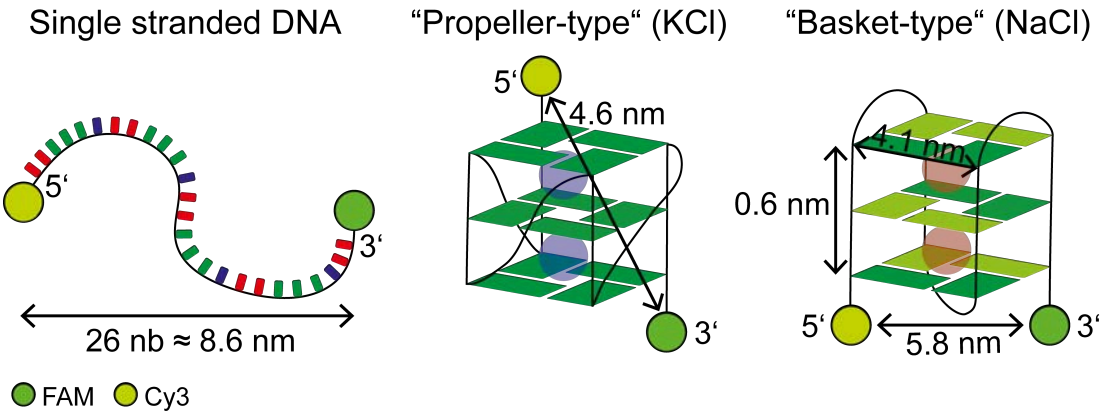

Figure 3.1: Estimated donor-acceptor distances (green: donor, FAM; yellow: acceptor, Cy3) for the single stranded telomeric DNA (red: T, green: G, blue: A), "propeller-type" G-quadruplex in presence of KCl and "basket-type" G-quadruplex in presence of NaCl (dark green: *anti*, light green: *syn*). The distances have been determined based on X-ray crystallography, NMR and molecular dynamics data reported in literature for the human telomeric DNA.[123,124]

The donor-acceptor distance decreases due to the G-quadruplex formation in presence of sodium and potassium ions. The distance between Cy3 and FAM in the G-quadruplex conformation is estimated based on the X-ray crystallography, NMR and molecular dynamics data reported in literature for HumTel (5'-(TTA GGG)$_4$) in presence of Na^+ and K^+.[123,124] The donor-acceptor distances range from approximately 4.6 nm ("propeller-type", KCl) to 5.8 nm ("basket-type", NaCl) as shown in figure 3.1. Here, a linker length of 0.7 nm between fluorophore and DNA strand has been taken into account. Please note, that these distances are only estimations because in this work RevHumTel has been used to achieve an ion-selectivity on DNA origami structures. The exact G-quadruplex structures for RevHumTel in presence of Na^+ and K^+

are not known. Thus, the actual donor-acceptor distances present in the G-quadruplex structures can differ from the theoretical values.

For the telomeric DNA attached to DNA origami structures one staple strand ("t1s6i") is prolonged at its 5'-end with RevHumTel and modified with Cy3 (Cy3-RevHumTel-t1s6i, exact DNA sequence is shown in table A.2). FAM is placed 10 nb away from the telomeric DNA directly on the DNA origami structure resulting in a distance of approximately 3.3 nm (figure 3.2). A distance of 10 nb makes sure that the fluorophores are positioned on the same side of the DNA origami structure (distance corresponds to one whole helical turn) and increases the potential FRET efficiency.[20,194] FAM has been internally introduced in the "t-1s6i" staple strand (FAM-t-1s6i, table A.2). The maximum donor-acceptor distance in absence of K^+ is estimated to be 9.2 nm (see figure 3.2). The donor-acceptor distance decreases to approximately 7.4 nm in the compact G-quadruplex structures as shown in figure 3.2. Please note that the distances determined here are estimations and can differ from the actual distances because the single stranded telomeric DNA and the G-quadruplex can rotate on the DNA origami platform.

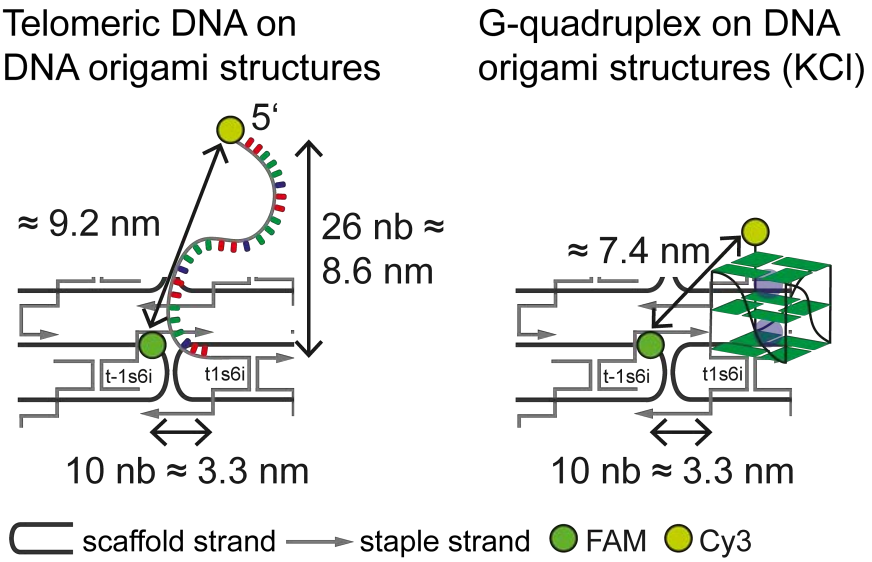

Figure 3.2: Donor-acceptor distances (green: donor, FAM; yellow: acceptor, Cy3) for telomeric DNA (red: T, green: G, blue: A) on DNA origami structures in the unfolded (left) and folded state in presence of KCl (right). The images represent only a small section of the triangular shaped DNA origami structure for a better visualization.

3.3.2 An ion-controlled four-color fluorescent telomeric switch on DNA origami structures

To create larger switchable FRET systems on DNA origami structures, further fluorophores are introduced to the two-color FRET system shown in figure 3.2.[2] For this, Cy5 is introduced directly on the DNA origami structure again 10 nb (ca. 3.3 nm) away from the telomeric DNA by modifying a staple strand ("t2s7f") internally (see

figure 3.3, Cy5-t2s7f, exact DNA sequence can be found in table A.2). This results in a Cy3/Cy5 distance of approximately 9.2 nm in the unfolded state (see figure 3.3). When the G-quadruplex folds in presence of KCl the Cy3/Cy5 distance decreases to ca. 7.4 nm. The distance between the initial donor FAM and the final acceptor Cy5 is 20 nb (ca. 6.6 nm, figure 3.3).

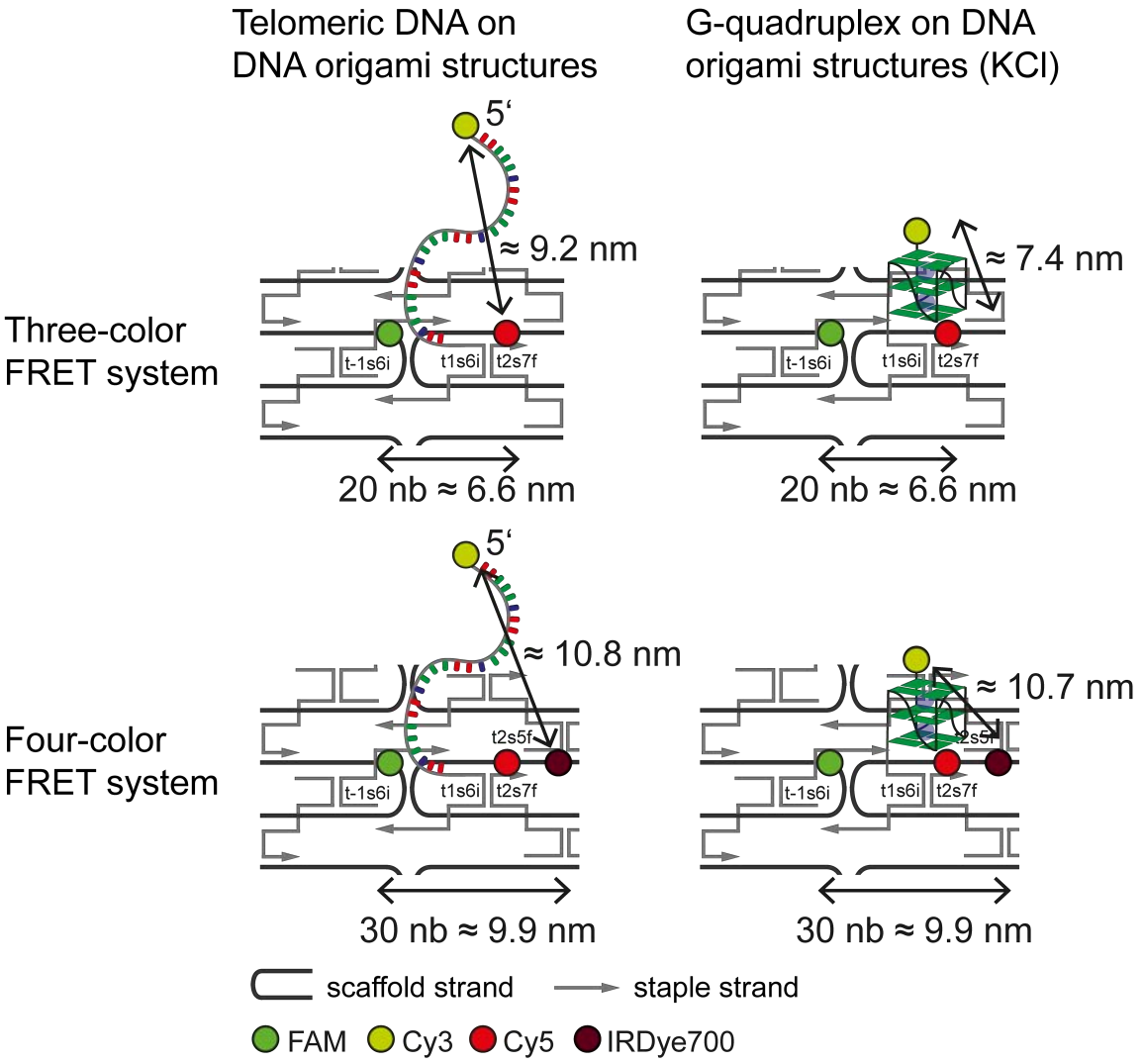

Figure 3.3: Determined nominal distances between fluorophores (green: donor, FAM; yellow: transmitter1, Cy3; red: transmitter2, Cy5; dark red: acceptor, IRDye700) in the three-color FRET cascade and the four-color photonic wire on triangular shaped DNA origami structures (for better visualization only a small section of the DNA origami structure is shown, (telomeric DNA: red: T, green: G, blue: A)). The FRET-pairs (FAM/RevHumTel-Cy3, RevHumTel-Cy3/Cy5 and Cy5/IRDye700) are separated by 10 nb (ca. 3.3 nm) leading to the same orientation of the fluorophores on the DNA origami structure.

A photonic wire-like system consisting of four fluorophores is created by extending the three-color FRET system even more. For this, the organic dye IRDye700 is introduced as the final acceptor. Again, IRDye700 is placed 10 nb (ca. 3.3 nm) away from Cy5 directly on the DNA origami structure by modifying a staple strand (“t2s5f”)

internally (figure 3.3, IRDye700-t2s5f, exact DNA sequence is shown in table A.2 in the appendix). This design results in a FAM/IRDye700 distance of approximately 10 nm. The intermolecular distance of Cy3 and IRDye700 in the unfolded state is maximal 10.8 nm and does not significantly change in the folded conformation (10.7 nm, figure 3.3). All distances determined here are the average distances and can vary due to rotation of the unfolded telomeric DNA and the G-quadruplex on the DNA origami structure. Here, all fluorophores have the same orientation on the DNA origami structure because each fluorophore is introduced after one whole helical turn. The determined distances are calculated by taking a linker length of 0.7 nm into account.

3.3.3 FRET efficiency and antenna effect in multi-color DNA origami-based light harvesting systems

An artificial light harvesting system with three different fluorophores has been created on DNA origami structures.[3] For this, an acceptor dye (Cy5) is placed in the center of the light harvesting complex. This acceptor dye is surrounded by a maximum number of four transmitter molecules (Cy3). These transmitter molecules can be either placed on a neighboring double helix (T1 and T3, paths I and III) or along the same double helix (T2 and T4, paths II and IV) as shown in figure 3.4. The distance between Cy3 and Cy5 on neighboring DNA double helices is 4.2 nm when the fluorophore orientation and a linker length of 0.7 nm is taken into account (figure 3.4). The fluorophores are positioned on opposite sides of the DNA origami structure. The Cy3/Cy5 distance along the same DNA double helix is 9 nb resulting in a nominal distance of 3.4 nm (figure 3.4). Again, the fluorophore orientation and the linker length are taken into account. Next to each Cy3, one FAM molecule is placed. Again, the fluorophores are either placed on neighboring DNA double helices (D1 and D3, paths I and III) or along the same DNA double helix (D2 and D4, paths II and IV) as shown in figure 3.4. The FAM/Cy3 distances are similar to the previously discussed Cy3/Cy5 distances (see figure 3.4). The distance between FAM and Cy5 on different DNA double helices (paths I and III) is 5 nm (FAM and Cy5 are positioned on the same side of the DNA origami structure). The distance between FAM and Cy5 along the same DNA double helix (paths II and IV) is 18 nb corresponding to a distance of 6.5 nm when the fluorophore orientation and linker length are taken into account (figure 3.4).
Additionally, FAM is placed shifted such that it can serve as a donor for two Cy3 molecules (D5 - D8, see figure 3.4). In this way a maximum number of eight FAM molecules can be used as donor molecules. The FAM position has been chosen in such a way that the FAM/Cy3 distance is nearly the same for all four Cy3 molecules (R(T1/D5) = R(T1/D8) = R(T2/D5) = R(T2/D6) = R(T3/D6) = R(T3/D7) = R(T4/D7) = R(T4/D8)). The FAM/Cy3 distance is approximately 3.3 nm for all these positions (see figure 3.4). Please note that for the positions T1 and T3 Cy3 and FAM are on

the same side of the DNA origami structure (R = 10 nb, one whole helical turn) and for T2 and T4 the orientation of the fluorophores is slightly twisted. The FAM/Cy5 distance is approximately 5.4 nm (figure 3.4). Again, Cy5 and FAM are on opposite sides of the DNA origami structure. All modified DNA sequences used for the artificial light harvesting system are listed in table A.2. With such a FRET array the number of overall fluorophores, the number of each fluorophore (Cy5, Cy3 and FAM) and the donor-transmitter-acceptor ratio can be varied and the light harvesting efficiency and FRET efficiency can be analyzed.

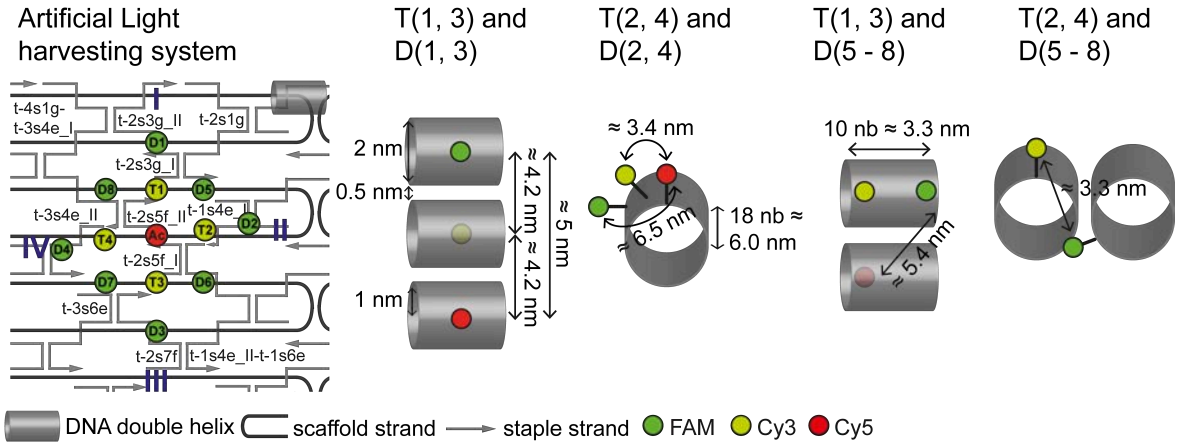

Figure 3.4: Intermolecular donor-transmitter-acceptor distances and fluorophore orientations in the artificial light harvesting system on DNA origami structures (green: donor, FAM; yellow: transmitter, Cy3; red: acceptor, Cy5). Only a small section of the DNA origami triangle is shown for better visualization.

3.4 Analytical methods

3.4.1 Atomic force microscopy

To investigate the correctly formed DNA origami structures, AFM has been performed for each sample after the assembly process. AFM imaging has been done using a Flex atomic force microscope from Nanosurf GmbH (Liestal, Switzerland). A Tap150 Al-G cantilever from Budget Sensors (Sofia, Bulgaria) with a resonance frequency of (125 - 160) kHz and a spring constant of 5 Nm^{-1} has been used to visualize the DNA origami structures. The samples have been prepared on freshly cleaved mica. For this, 2 µL of the sample (ca. 20 nM) and 33 µL of TAE buffer (1x concentrated) containing 10 mM $MgCl_2$ have been incubated for 30 s and subsequently washed twice with 1 mL of ultrapure water (Merck Millipore). Afterwards, the fluid has been removed with compressed air. The measurements have been performed in air using the tapping mode. The AFM images have been analyzed and visualized using the Gwyddion 2.44 open-source software. The measured triangles have a length of (100 - 150) nm and a height of (1 - 2) nm (see figure 3.5).

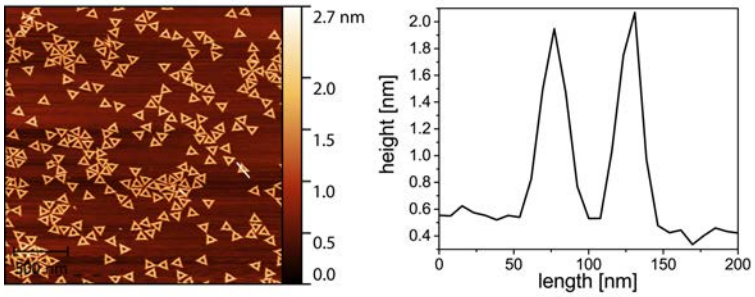

Figure 3.5: Typical AFM image of adsorbed DNA origami nanostructures on freshly cleaved mica (left) together with a height profile of one DNA origami structure (right). The DNA origami structures measure a height of (1 - 2) nm and a length of (100 - 150) nm.

3.4.2 UV/Vis absorption spectroscopy

To determine the concentration of the DNA origami nanostructures, UV/Vis absorption spectra have been measured on a NanoDrop2000 Spectrophotometer from Thermo Scientific (Waltham, U.S.A.). For this, 2 µL of the sample have been given on the NanoDrop2000 and the UV/Vis spectrum has been recorded in the range from 200 to 800 nm. Prior to the sample, the solvent (TAE buffer (1x concentrated) containing 10 mM $MgCl_2$) has been recorded and automatically subtracted from the sample's spectrum. To determine the DNA origami concentration, the Beer-Lambert law (equation 2.1) is used. According to the manufacturer the extinction coefficient at 260 nm of dsDNA is $\varepsilon = 0.02\ \frac{\mu L}{ng \cdot cm}$ and the absorption path length is $l = 0.1\ cm$. Now, the DNA concentration can be calculated with equation 3.1 when the absorbance at 260 nm ($A(260\ nm)$) is known.

$$c' = 500\ \frac{ng}{\mu L} \cdot A(260\ nm) \tag{3.1}$$

The DNA origami concentration c' based on equation 3.1 is given in $[\frac{ng}{\mu L}]$ and by using the molecular mass of the DNA origami structure ($M \approx 4.4 \cdot 10^6\ \frac{g}{mol}$) a conversion factor can be determined to calculate the DNA origami concentration c in $[nM]$ (equation 3.2).

$$c = 0.2272\ \frac{nM \cdot \mu L}{ng} \cdot c' \tag{3.2}$$

3.4.3 Steady-state fluorescence spectroscopy

Steady-state fluorescence spectroscopy measurements have been performed using a FluoromaxP fluorescence spectrophotometer from HORIBA Jobin Yvon GmbH (Bensheim, Germany) with 3 mm quartz cuvettes from Hellma Analytics (Müllheim, Germany). The measurements have been performed in a 90° angle acquisition using

the system-internal quantum correction. For emission spectra, the excitation wavelength has been chosen according to the fluorophore which is directly excited (FAM: λ_{ex} = 450 nm, Cy3: λ_{ex} = 500 nm, Cy5: λ_{ex} = 600 nm, IRDye700: λ_{ex} = 650 nm). To record excitation spectra, the emission wavelength has been set to λ_{em} = 540 nm (FAM), λ_{em} = 640 nm (Cy3), λ_{em} = 680 nm (Cy5) and λ_{em} = 740 nm (IRDye700), respectively. For all measurements an increment of 1 nm and an integration time of 0.2 s have been set and the bandpass has been fixed to 5 nm for both emission and excitation.

3.4.4 Time-correlated single photon counting

Time-correlated single photon counting (TCSPC) experiments have been carried out to determine the fluorescence decay time of fluorophores. The basic principles of the method are shortly discussed in this section.[163] For TCSPC the sample is excited with a laser pulse followed by the detection of a single photon. A typical setup of such a TCSPC instrument is shown in figure 3.6. After the excitation pulse a signal is sent to a constant function discriminator (CFD) which measures the starting point of the excitation pulse. Afterwards, this signal passes through a time-to-amplitude converter (TAC) which starts to generate a voltage ramp with a linear increase on the nanosecond scale. After the sample excitation, the pulse of a photon is detected in a second channel with another CFD. Consequently, the voltage ramp is stopped. The measured voltage is proportional to the time delay between sample excitation and photon emission. With a programmable gain amplifier (PGA) the voltage can be enhanced if necessary followed by the signal transfer to a multichannel analyzer (MCA). A window discriminator (WD) is introduced to reduce errors. Here, the voltage is limited to a certain range and if the voltage is not within this range the single measurement is omitted. This process is repeated numerous times (10^5 - 10^7 times) to create a histogram consisting of counted photons (y-axis) at certain time delays (x-axis) which is schematically shown in figure 3.6. This histogram represents the fluorescence decay of the sample under certain conditions. For this, it is important that only one photon is detected per laser pulse otherwise the data can be distorted especially at high counting rates. Thus, the detection rate is usually relatively low (one photon is detected every 100 excitation pulses). Furthermore, the dead time of the instrument (time in which a photon cannot be detected by the detector) has to be taken into account and the time between two excitation pulses has to be adjusted accordingly. When measuring TCSPC one has to keep in mind that the excitation pulse is not infinitely short. Therefore, the impulse response function (IRF) is measured using a scattering sample representing the shortest time profile which can be measured with the used instrument (the width of the IRF depends on the light source, detector and timing of electronics). This IRF curve has to be taken into account when analyzing and fitting the fluorescence decay curves.[163] In this work, TCSPC measurements have been carried out on a FLS920 fluorescence

spectrophotometer from Edinburgh Instruments Ltd (Livingston, UK) with the F900 (Edinburgh Instruments Ltd) software using 3 mm quartz cuvettes (Hellma Analytics). The samples have been measured in a 90° setup using a supercontinuum white light source SC-400-PP from Fianium/NKT Photonics A/S (Birkerød, Denmark) as the excitation source ((0.5 - 20) MHz, 400 nm $< \lambda <$ 24 000 nm, pulse width: ca. 30 ps). As a detector a multi-channel-plate ELDY EM1-132/300 from Europhoton GmbH (Neusalza-Spremberg, Germany) has been used. The excitation and emission wavelengths have been set according to the fluorophore which is excited (FAM: $\lambda_{ex} = (490 \pm 1)$ nm, $\lambda_{em} = (520 \pm 1)$ nm; Cy3: $\lambda_{ex} = (545 \pm 1)$ nm, $\lambda_{em} = (565 \pm 1)$ nm; Cy5: $\lambda_{ex} = (645 \pm 1)$ nm, $\lambda_{em} = (665 \pm 1)$ nm; IRDye700: $\lambda_{ex} = (690 \pm 1)$ nm, $\lambda_{em} = (710 \pm 1)$ nm).

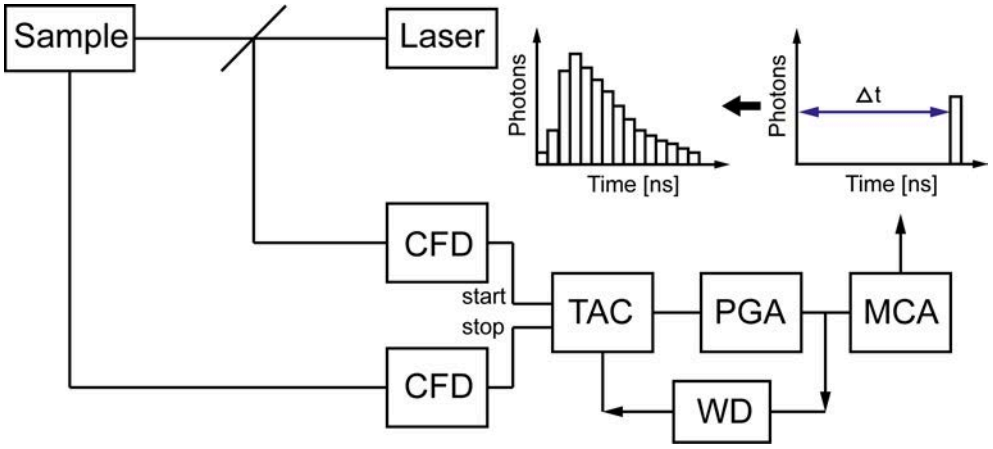

Figure 3.6: Schematic illustration of a typical TCSPC setup with constant function discriminator (CFD), time-to-amplitude converter (TAC), programmable gain amplifier (PGA), window discriminator (WD) and multichannel analyzer (MCA). The image is adapted from literature.[163]

The fluorescence decay curves (intensity-time-function $I(t)$) have been fitted with mono-exponential or multi-exponential functions (bi- or tri-exponential, equation 3.3) depending on the sample using the FAST software (Edinburgh Instruments, UK).

$$I(t) = \sum_{i=1}^{n} A_i e^{\frac{-t}{\tau_i}} \tag{3.3}$$

Here, τ_i is the decay time component and A_i is the amplitude characteristic for each decay time component. The amplitude averaged fluorescence decay time $\overline{\tau}_{DA}$ is then calculated with equation 3.4.

$$\overline{\tau}_{DA} = \frac{\sum_{i=1}^{n} A_i \tau_i}{\sum_{i=1}^{n} A_i} \tag{3.4}$$

3.4.5 CD spectroscopy

Circular dichroism spectroscopy is based on the effect that chiral (optically active) molecules absorb right- and left-handed circularly polarized light differently. Therefore, CD spectroscopy can be used for structural investigations of biomolecules such as DNA. In this sense, it can be used to analyze the different structures of certain G-quadruplexes. Different G-quadruplex structures lead to different CD spectra. This effect is ascribed to the different stacking interactions due to different glycosidic angles and strand orientations.[195,196] An overview of certain CD signals induced by different G-quadruplex structures is given in table 3.2.

Table 3.2: Overview of different CD signals induced by different G-quadruplex structures. The peak assignment is based on previously reported peak positions.[118,126]

type	**positive peak**	**negative peak**	**example**
parallel	(260 - 265) nm	240 nm	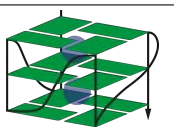
hybrid	290 nm (260 - 270) nm (shoulder)	240 nm	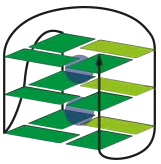
anti- parallel	(290 - 295) nm (240 - 250) nm	(240 - 275) nm	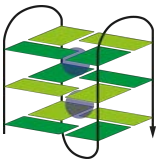

CD spectroscopy has been performed on a JASCO J-815 CD spectrometer (JASCO Labor- und Datentechnik GmbH, Gross-Umstadt, Germany) with 1 mm quartz cuvettes from Hellma Analytics. For this, the DNA strands (unmodified RevHumTel (5'-TT (GGG ATT)$_4$) and HumTel (5'-TT (GGG TTA)$_3$ GGG TTT), c = 100 µM) have been diluted in TAE buffer (1x concentrated) to a concentration of 8.5 µM. KCl and NaCl, respectively (c = 200 mM, 2 M) have been added to the sample to induce the G-quadruplex formation (incubation for 15 min at RT). Each sample has been prepared separately for each salt concentration ranging from 0 to 500 mM (c = (2, 10, 20, 200, 500) mM). The pure TAE buffer has been measured individually and subtracted from the sample's CD spectrum. The CD spectra have been recorded from 200 to 320 nm with the following settings: digital integration time: 4 s, sensitivity: standard, spectral bandwidth: 1 nm, data pitch: 1 nm, start mode: immediately, scanning mode: continuous, scanning speed: 50 $\frac{nm}{min}$, accumulation: 3.

Chapter 4

Manuscripts

4.1 Contributions to the manuscripts

L. Olejko, P. J. Cywiński, I. Bald "Ion-Selective Formation of a Guanine Quadruplex on DNA Origami Structures" *Angewandte Chemie International Edition* **2015**, 54 (2), 673-677:[1a]

The design and orientation of fluorophores on DNA origami structures was discussed between Ilko Bald and me. I did all of the experimental sample preparation and measurements (steady-state and time-resolved fluorescence spectroscopy, AFM). I did the whole data analysis (analysis of emission spectra and fluorescence decay curves) and wrote the manuscript together with Ilko Bald and Piotr J. Cywiński. I prepared the images which are published in the manuscript and supporting information.

L. Olejko, P. J. Cywiński, I. Bald "Ionenselektive Guanin-Quadruplex-Faltung auf DNA-Origami-Strukturen" *Angewandte Chemie* **2015**, 127 (2), 683-687:[1b]

I translated the manuscript "Ion-Selective Formation of a Guanine Quadruplex on DNA Origami Structures" into German together with Ilko Bald.

L. Olejko, P. J. Cywiński, I. Bald "An Ion-Controlled Four-Color Fluorescent Telomeric Switch on DNA Origami Structures" *Nanoscale* **2016**, 8 (19), 10339-10347:[2]

Together with Ilko Bald I designed the fluorescence array on DNA origami structures and planned the experiments. I did all of the experimental sample preparation and performed all of the measurements (steady-state and time-resolved fluorescence spectroscopy, AFM). I analyzed the fluorescence data and prepared the images for the manuscript and supporting information. I wrote the manuscript together with Ilko Bald and Piotr J. Cywiński.

L. Olejko, I. Bald "FRET Efficiency and Antenna Effect in Multi-Color DNA Origami-Based Light Harvesting Systems" *RSC Adv.* **2017**, 7, 23924-23934:[3]

I designed the FRET array on DNA origami structures together with Ilko Bald. I planned and performed all of the experiments (steady-state and time-resolved fluorescence spectroscopy, AFM). I analyzed the fluorescence data and prepared the images for the manuscript and supporting information. I wrote the manuscript together with Ilko Bald.

4.2 Ion-selective FRET

"Ion-Selective Formation of a Guanine Quadruplex on DNA Origami Structures"

Angewandte Chemie International Edition **2015**, 54 (2), 673-677[1a]

"Ionenselektive Guanin-Quadruplex-Faltung auf DNA-Origami-Strukturen"

Angewandte Chemie **2015**, 127 (2), 683-687[1b]

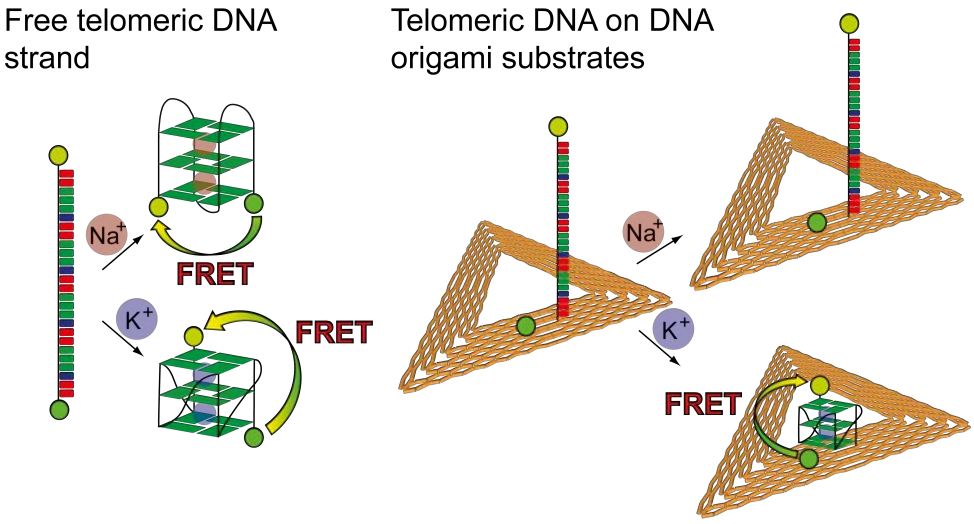

Angewandte International Edition Chemie

DNA Nanotechnology

DOI: 10.1002/anie.201409278

Ion-Selective Formation of a Guanine Quadruplex on DNA Origami Structures**

Lydia Olejko, Piotr J. Cywinski, and Ilko Bald**

Abstract: *DNA origami nanostructures are a versatile tool that can be used to arrange functionalities with high local control to study molecular processes at a single-molecule level. Here, we demonstrate that DNA origami substrates can be used to suppress the formation of specific guanine (G) quadruplex structures from telomeric DNA. The folding of telomeres into G-quadruplex structures in the presence of monovalent cations (e.g. Na^+ and K^+) is currently used for the detection of K^+ ions, however, with insufficient selectivity towards Na^+. By means of FRET between two suitable dyes attached to the 3′- and 5′-ends of telomeric DNA we demonstrate that the formation of G-quadruplexes on DNA origami templates in the presence of sodium ions is suppressed due to steric hindrance. Hence, telomeric DNA attached to DNA origami structures represents a highly sensitive and selective detection tool for potassium ions even in the presence of high concentrations of sodium ions.*

DNA can be folded into almost any 2D and 3D shape by using the DNA origami technique.[1] DNA nanostructures can be decorated with proteins, nanoparticles, fluorescent dyes, and higher-order DNA structures with nanometer precision, and thus they can serve as a versatile tool in analytical science.[2] DNA origami structures can be used as a platform to detect RNA sequences[3] and other molecular species through atomic force microscopy,[4] for few-molecule detection using surface-enhanced Raman scattering (SERS),[5] and to determine the yield of sequence-specific DNA damage.[6] The formation of guanine (G) quadruplex structures from telomeric DNA sequences was also extensively studied using a DNA origami frame and high-speed AFM.[7] Telomeres are located at the ends of eukaryotic chromosomes, and stabilize and protect the genome.[8] The G-rich, single-stranded mammalian telomeres have the sequence 5′-$(TTAGGG)_n$[9] and they can form nonduplex structures in the presence of monovalent cations. In the nonduplex structure four G bases are associated with eight stable hydrogen bonds to form a G-tetrad. Two or more G-tetrads are stacked to form a G-quadruplex. Since the association constant for G-quadruplex formation is lower for Na^+ than for K^+ ions,[10,11] telomere sequences have been suggested as selective K^+ sensors using Förster resonance energy transfer (FRET).[10–12] However, Na^+ induces G-quadruplex formation from free human telomeric DNA in a concentration range from 10–205 mM. Under physiological conditions (ca. 145 mM Na^+) this can lead to considerable errors in the determination of K^+ concentration. As we demonstrate here, by using telomeric DNA attached to DNA origami platforms, the formation of G-quadruplexes by Na^+ is completely suppressed, whereas the K^+-induced G-quadruplex formation is not influenced.

In the present study, we have used FRET to investigate in detail the K^+- and Na^+-induced folding of G-quadruplexes from both free telomere sequences and telomere sequences attached to triangular DNA origami platforms. FRET refers to a nonradiative energy transfer from an excited donor to an acceptor through dipole–dipole interactions. The FRET efficiency η is strongly distance-dependent according to Equation (1).

$$\eta = \frac{R_0^6}{R_0^6 + R^6} \tag{1}$$

Here, R is the donor–acceptor distance and R_0 the Förster radius at which the FRET efficiency is 50%. The FRET efficiency can also be calculated based on the donor's decay time [Eq. (2)].

$$\eta = 1 - \frac{\tau_{DA}}{\tau_D} \tag{2}$$

Here, τ_D is the donor's decay time in the absence of the acceptor and τ_{DA} is the decay time in the presence of the acceptor.[13]

In the present study, free human telomeric DNA was used as a reference system modified with cyanine 3 (Cy3) at the 5′-end and fluorescein (FAM) at the 3′-end (5′-Cy3-TTG GGA TTG GGA TTG GGA TTG GGA TT-FAM). When K^+ or Na^+ is added to the solution, the conformation changes from

[*] L. Olejko, Prof. Dr. I. Bald
Department of Chemistry, University of Potsdam
Karl-Liebknecht-Strasse 24–25, 14476 Potsdam (Germany)
E-mail: bald@uni-potsdam.de
Dr. P. J. Cywinski
NanoPolyPhotonics, Fraunhofer IAP
Geiselbergstrasse 69, 14476 Potsdam (Germany)
E-mail: piotr.cywinski@iap.fraunhofer.de
Prof. Dr. I. Bald
BAM Federal Institute of Materials Research and Testing
Richard-Willstätter Strasse 11, 12489 Berlin (Germany)
L. Olejko
School of Analytical Sciences Adlershof
Humboldt-Universität zu Berlin
Unter den Linden 6, 10099 Berlin (Germany)

[**] We are grateful to Prof. Michael Kumke for discussions and for providing access to fluorescence spectroscopy equipment. We also thank A. Keller for carefully reading the manuscript. This research was supported by a Marie Curie FP7 Integration Grant within the 7th European Union Framework Programme, the Deutsche Forschungsgemeinschaft (DFG), the University of Potsdam, and the DFG project GSC 1013 (SALSA).

Supporting information for this article is available on the WWW under http://dx.doi.org/10.1002/anie.201409278.

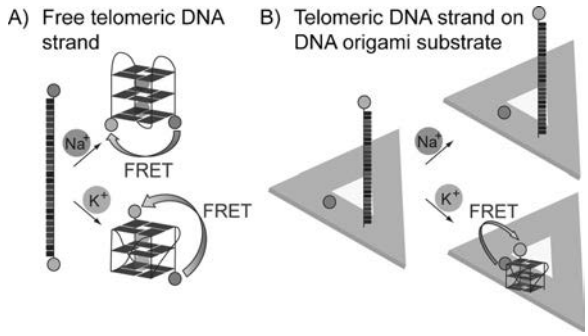

Figure 1. Scheme of the telomere-based potassium-sensing systems. A) Free telomeric DNA strand (5′-Cy3-TT(GGGA)$_4$TT-FAM, T = black, G = dark gray, A = light grey) with fluorescein (FAM, dark gray) as the donor dye and cyanine3 (Cy3, light gray) as the acceptor dye. The DNA strand folds into G-quadruplex structures when monovalent cations such as K^+ and Na^+ are present. The different cations induce the formation of different G-quadruplex structures. When the free telomeric DNA strands are used, both G-quadruplexes can be formed and K^+ and Na^+ are detected using FRET. B) The telomeric DNA strand is immobilized on the DNA origami structure as a protruding strand attached to one staple strand. The telomeric DNA strand is placed 3.3 nm away from FAM on the DNA origami structure. The G-quadruplex can only be folded in the presence of potassium ions.

a single-stranded random coil to a compact G-quadruplex structure, in which the donor–acceptor distance is 4.6 nm in the presence of K^+ and 5.8 nm in the presence of Na^+ (see Figure 1 A and Figure S1 in the Supporting Information (SI) for details). In the second system, in which triangular DNA origami templates are used (AFM image is shown in Figure S2), FAM was placed 3.3 nm away from the 3′-end of the protruding telomeric DNA. The latter is modified with Cy3 at its 5′-end (Figure 1 B and Figure S1). In the compact G-quadruplex structure the donor–acceptor distance has a maximum value of 7.5 nm.

Steady-state emission spectra were recorded at a DNA concentration of 5 nM with an excitation wavelength of 450 nm and are shown in Figure 2. Figure 2 A and B show the fluorescence emission spectra for the free telomeric DNA sequence upon addition of KCl (A) and NaCl (B). In Figure 2 C and D the respective spectra are shown for the telomeric DNA attached to DNA origami triangles. When no FRET occurs, the emission of FAM at 515 nm is dominant. Since in the random-coil conformation the organic dyes are already close enough for FRET to occur, weak Cy3 emission at 565 nm can be observed in the steady-state spectra (Figure 2 A,B) also when no salt is present. When either KCl or NaCl is added to the free telomeric DNA (Figure 2 A,B), the dyes are brought closer together due to G-quadruplex formation and more efficient FRET can be observed. FAM fluorescence is quenched and simultaneously Cy3 emission increases. The addition of 1 mM KCl (Figure 2 A) is sufficient to change the emission properties. As the association constant for Na^+ [11] is lower than that for K^+, a clear change in the fluorescence emission is observed upon addition of about 25 mM NaCl (Figure 2 B). However, this distinction is insufficient under biologically relevant conditions, since in extracellular liquids the Na^+ concentration is roughly 145 mM and the K^+ concentration is as low as 4 mM. As can be seen in Figure 2 B the single telomeric DNA strand shows high sensitivity for Na^+ in a concentration range of 25–205 mM. Thus, the use of free telomeric DNA as a selective potassium sensor in biological media is not feasible. In order to overcome this problem, the telomeric DNA was immobilized on DNA origami structures to construct the DNA origami/telomere FRET sensing system. Figure 2 C shows the response of the DNA origami/telomere system to increasing amounts of KCl. Overall, the FRET efficiencies are lower since the donor–acceptor distance in the DNA origami design is larger than that in the free telomeric system (Figure 1). Nevertheless, a clear change both in the donor and acceptor emission is observed in the concentration range between 5 mM and 110 mM KCl. The Cy3 emission intensity decreases slightly at 0.1–2.5 mM KCl owing to moderate heating to 40 °C with the first KCl addition, which might increase the average distance between the dyes in the nonfolded telomeres. Starting at a concentration of 5 mM KCl the FRET efficiency increases clearly. The situation is completely different when NaCl is added to the DNA origami/telomere structures (Figure 2 D). The steady-state fluorescence emission spectra are unaffected by Na^+ ions even at concentrations as high as 205 mM. That is, the average donor–acceptor distance does not change with increasing NaCl concentration, indicating that the G-quadruplex formation does not take place on DNA origami structures in the presence of Na^+ ions. In Figure 2 E it is demonstrated that the high sensitivity for K^+ is preserved even in the presence of 145 mM NaCl. It should be noted that FRET is also not observed upon addition of NaCl to the DNA origami/telomere system when one of the dyes is placed directly beside the 3′-end of the telomere sequence to mimic the free-telomeric DNA FRET system (see Figure S3 (SI)).

Based on the fluorescence intensity of FAM and Cy3, the association constants are calculated for the free telomeric DNA system to be $1.5 \times 10^4\,M^{-2}$ for K^+ and $33.7\,M^{-2}$ for Na^+ (see Figure S4 (SI)). The association constant for the DNA origami/telomere system is determined to be $2.6 \times 10^4\,M^{-2}$ for K^+ (Figure S4 (SI)), which is very close to the value obtained for the free telomeric DNA with KCl addition. In the presence of 145 mM NaCl, an association constant of $1.4 \times 10^4\,M^{-2}$ in the presence of KCl was obtained (Figure S4 (SI)). This indicates that the formation of the G-quadruplex, and therefore, the sensitivity towards K^+ is virtually unaffected by the DNA origami platform and the presence of Na^+.

Since the steady-state measurements depend on the absolute DNA concentration, the FRET efficiencies have also been determined using time-resolved fluorescence spectroscopy. The fluorescence decay times determined for the donor are summarized in Table 1 (decay curves are shown in Figure S5), and the FRET efficiency is determined using Equation (2). In Figure 3 the FRET efficiencies are plotted *versus* the different salt concentrations.

For free telomeric DNA, the donor decay time decreases with the increase in KCl and NaCl concentration. Accordingly, the FRET efficiency increases with an increase in KCl and NaCl concentration. The dynamic range in the FRET efficiency for K^+ is from about 0.5 mM to 50 mM. On the other

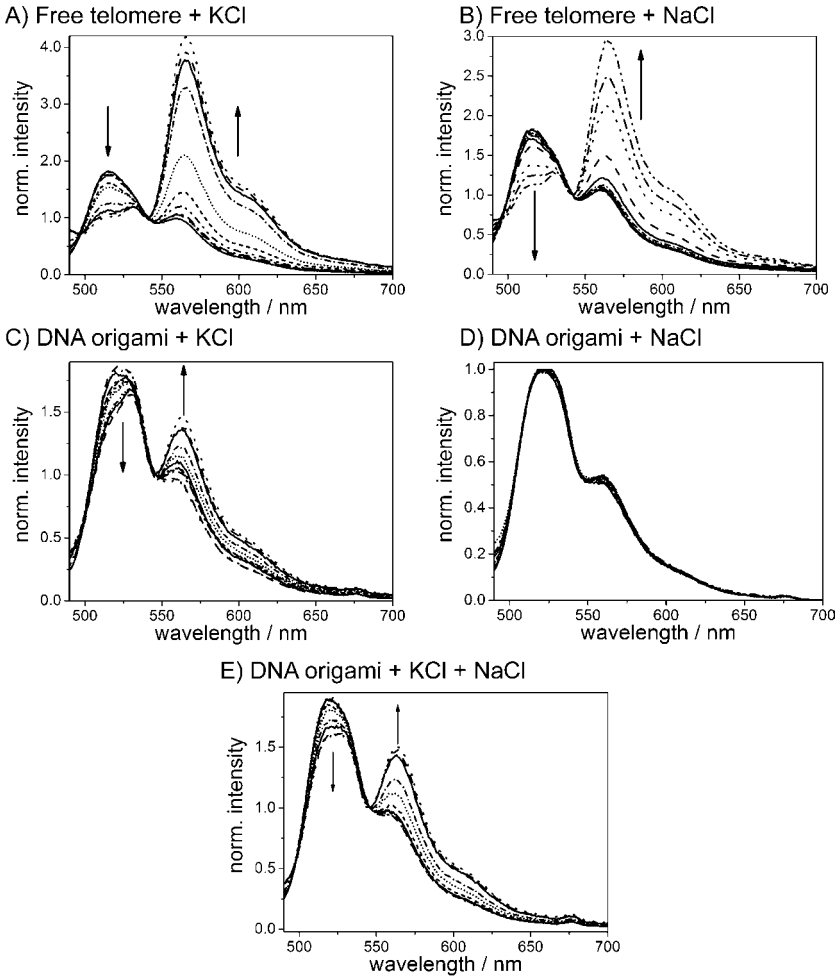

Figure 2. Normalized emission spectra (λ_{ex} = 450 nm) of free telomeric DNA (c = 5 nM) (A,B) and telomeric DNA on DNA origami structures (C,D,E) for various salt concentrations (KCl and NaCl). A,B) Addition of KCl (A; c = 0–110 mM) and NaCl (B; c = 0–205 mM) results in a decrease of the emission intensity of the donor dye FAM (515 nm) and an increase of the emission intensity of the acceptor dye Cy3 (565 nm) with increasing salt concentration due to FRET. Thus, free telomeric DNA is folded into G-quadruplex structures in the presence of both potassium and sodium ions. C,D,E) With the telomeric DNA on DNA origami structures, only KCl addition (C; c = 0–110 mM) leads to a change of the fluorescence emission due to FRET, even in presence of 145 mM NaCl (E; c = 0–110 mM). When NaCl is added (D; c = 0–205 mM), the G-quadruplex structure is not formed on DNA origami substrates and the fluorescence emission of FAM and Cy3 does not change.

hand, for Na^+ the FRET efficiency changes strongly within a wide concentration range from 5 mM to more than 165 mM.

Similar to the case for free telomeric DNA, the FRET efficiency also increases for the DNA origami/telomere system upon the addition of KCl. The differences between the FRET efficiencies of the free telomeric DNA and the DNA origami system (free telomeric DNA: 0.56–0.91; DNA origami substrate: 0.28–0.57) are due to the different donor acceptor–distances in the two systems (Figure 1). When NaCl is added, the FRET efficiency remains unaffected (Figure 3) indicating again that G-quadruplex formation in the presence of Na^+ is suppressed on the DNA origami structures. Consequently, K^+ sensing is also operative at a concentration of 145 mM NaCl (Figure 3).

The formation of G-quadruplexes in the presence of K^+ and the suppression of its formation in the presence of Na^+ with the DNA origami/telomere system can be explained by the specific G-quadruplex structures. Apart from the telomere sequence and the strand polarization, the G-quadruplex structure depends critically on the central metal ion.[14] According to X-ray crystallographic and NMR analysis, Na^+ ions induce a "basket-type" G-quadruplex, whereas in the presence of K^+, a "propeller-type" structure is formed (Figure 1 A).[15,16] The basket-type G-quadruplex has a diagonal loop at the end and therefore its formation is sterically hindered by the DNA origami surface.[15] In contrast, the propeller-type G-quadruplex can still be formed on DNA origami platforms in the presence of K^+ . The formation of the different G-quadruplex structures in the presence of K^+ and Na^+ ions is confirmed by the slightly different donor–acceptor dye distances, which can be determined from the FRET efficiencies for the free telomeric DNA system. The donor–acceptor distances are determined using Equation (1) and the Förster radius R_0 for the FAM–Cy3 FRET pair. R_0 has been calculated to be 6.7 nm based on the spectral overlap (see Figure S6 (SI)). Accordingly, the donor–acceptor distance in the free telomere sequence without the addition of NaCl or KCl is 6.4 nm. Upon the addition of 165 mM KCl the donor–acceptor distance decreases to 4.6 nm indicating the folding of the G-quadruplex. This agrees very well with the expected distance (4.6 nm, Figure S1) based on the X-ray crystallography data[16] and taking into account the length of the linker between the organic dyes and DNA strand (0.7 nm). For 165 mM NaCl the donor–acceptor distance determined from the FRET efficiency is 5.1 nm, which is shorter than the expected distance of 5.8 nm (ΔR(NaCl) = 0.7 nm, Figure S1 (SI)). Here, it should be noted that in the G-quadruplex structures induced by Na^+ (Figure 1 A) the organic dyes are located at the same end of the G-quadruplex. Due to the linker between the organic dyes and the DNA

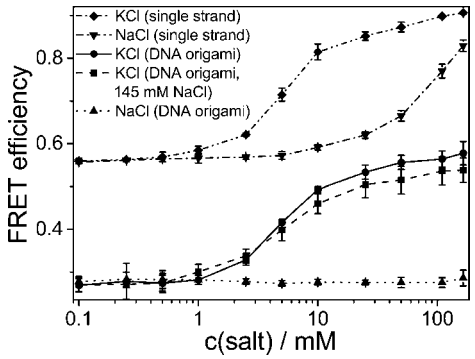

Figure 3. FRET efficiencies based on FAM decay times are plotted versus salt concentrations (KCl (diamonds, circles, squares) and NaCl (triangles pointed down, triangles pointed up)) for the free telomeric DNA ($c = 5$ nM) (diamonds, triangles pointed down) and for telomeric DNA immobilized on DNA origami templates (circles, squares, and triangles pointed up). The FRET efficiency increases with increasing KCl concentration for both systems, even in the presence of 145 mM NaCl (squares). With increasing NaCl concentration only the FRET efficiency of the free telomeric DNA increases. When the telomeric DNA strand is attached to the DNA origami substrate, NaCl is not detectable.

Table 1: Overview of FAM decay times τ for the different systems studied in this work.[a]

c(salt) [mM]	τ (ssDNA, KCl) [ns]	τ (ssDNA, NaCl) [ns]	τ (DNA origami, KCl) [ns]	τ (DNA origami, NaCl) [ns]	τ (DNA origami, KCl in 145 mM NaCl) [ns]
0	1.87	1.89	3.56	3.47	3.47
0.1	1.89	1.90	3.55	3.47	3.50
0.25	1.88	1.89	3.58	3.44	3.50
0.5	1.85	1.87	3.54	3.44	3.48
1	1.79	1.87	3.50	3.45	3.35
2.5	1.63	1.85	3.31	3.47	3.18
5	1.23	1.84	2.96	4.49	2.89
10	0.80	1.76	2.66	3.47	2.59
25	0.64	1.63	2.50	3.48	2.38
50	0.55	1.44	2.40	3.48	2.33
110	0.44	0.99	2.36	3.48	2.23
165	0.40	0.73	2.30	3.43	2.22

[a] Due to FRET the decay time decreases for the free telomeric DNA (ssDNA) after addition of KCl and NaCl, and for the telomeric DNA immobilized on DNA origami substrate (DNA origami) upon addition of KCl and even in presence of 145 mM NaCl. For telomeric DNA on DNA origami structures the decay time is not influenced by the presence of NaCl. τ_D(ssDNA, FAM) = 4.3 ns; τ_D(DNA origami, FAM) = 4.8 ns.

strand, the average distance between FAM and Cy3 might be shorter than expected based on only the G-quadruplex structure.

For the DNA origami/telomere system the donor–acceptor distance decreases from 7.8 nm without added salt to 6.4 nm upon addition of 165 mM KCl due to the formation of G-quadruplexes. The expected maximum distance in this G-quadruplex system in the presence of KCl is 7.4 nm (Figure S1 (SI)). Here it is assumed that the rigid G-quadruplex structure is rotated such that the donor–acceptor distance has a maximum value. The value determined here is an average of all possible rotational conformers and thus is clearly lower than the maximum distance of 7.4 nm.

The sensing system presented in this work is based on "FAM-to-Cy3" FRET on DNA origami substrates and enables selective potassium sensing at concentrations from about 0.5 mM to 50 mM even in the presence of high sodium concentrations (145 mM). To demonstrate this selectivity, we compare the G-quadruplex folding of free telomeric DNA with that of telomeric DNA attached to DNA origami templates. The free telomeric DNA strand shows sensitivity towards both NaCl and KCl, but with different association constants. When telomeric DNA attached to DNA origami structures is used, high selectivity for potassium ions is achieved and the sensitivity of the free telomeric DNA strand is maintained. G-quadruplex formation is completely suppressed on DNA origami structures in the presence of sodium ions due to steric hindrance arising from the the DNA origami surface.

Received: September 19, 2014
Published online: November 20, 2014

Keywords: DNA nanotechnology · FRET · G-quadruplexes · nanostructures · self-assembly

[1] P. W. K. Rothemund, *Nature* **2006**, *440*, 297 – 302.
[2] a) G. P. Acuna, F. M. Möller, P. Holzmeister, S. Beater, B. Lalkens, P. Tinnefeld, *Science* **2012**, *338*, 506 – 510; b) J. Fu, M. Liu, Y. Liu, N. W. Woodbury, H. Yan, *J. Am. Chem. Soc.* **2012**, *134*, 5516 – 5519; c) A. Kuzyk, R. Schreiber, Z. Fan, G. Pardatscher, E.-M. Roller, A. Högele, F. C. Simmel, A. O. Govorov, T. Liedl, *Nature* **2012**, *483*, 311 – 314; d) I. Bald, A. Keller, *Molecules* **2014**, *19*, 13803 – 13823.
[3] Y. Ke, S. Lindsay, Y. Chang, Y. Liu, H. Yan, *Science* **2008**, *319*, 180 – 183.
[4] A. Kuzuya, Y. Sakai, T. Yamazaki, Y. Xu, M. Komiyama, *Nat. Commun.* **2011**, *2*, 449.
[5] J. Prinz, B. Schreiber, L. Olejko, J. Oertel, J. Rackwitz, A. Keller, I. Bald, *J. Phys. Chem. Lett.* **2013**, *4*, 4140 – 4145.
[6] A. Keller, I. Bald, A. Rotaru, E. Cauët, K. V. Gothelf, F. Besenbacher, *ACS Nano* **2012**, *6*, 4392 – 4399.
[7] a) Y. Sannohe, M. Endo, Y. Katsuda, K. Hidaka, H. Sugiyama, *J. Am. Chem. Soc.* **2010**, *132*, 16311 – 16313; b) A. Rajendran, M. Endo, K. Hidaka, P. Lan Thao Tran, J.-L. Mergny, H. Sugiyama, *Nucleic Acids Res.* **2013**, *41*, 8738 – 8747; c) A. Rajendran, M. Endo, K. Hidaka, H. Sugiyama, *Angew. Chem. Int. Ed.* **2014**, *53*, 4107 – 4112; *Angew. Chem.* **2014**, *126*, 4191 – 4196.
[8] S. Neidle, G. N. Parkinson, *Curr. Opin. Struct. Biol.* **2003**, *13*, 275 – 283.
[9] a) T. R. Cech, *Angew. Chem. Int. Ed.* **2000**, *39*, 34 – 43; *Angew. Chem.* **2000**, *112*, 34 – 44; b) R. K. Moyzis, J. M. Buckingham, L. S. Cram, M. Dani, L. L. Deaven, M. D. Jones, J. Meyne, R. L. Ratliff, J. R. Wu, *Proc. Natl. Acad. Sci. USA* **1988**, *85*, 6622 – 6626.
[10] H. Ueyama, M. Takagi, S. Takenaka, *J. Am. Chem. Soc.* **2002**, *124*, 14286 – 14287.
[11] S. Takenaka, B. Juskowiak, *Anal. Sci.* **2011**, *27*, 1167 – 1172.
[12] a) L.-D. Li, X.-Q. Huang, L. Guo, *Rare Met.* **2013**, *32*, 369 – 374; b) S. Nagatoishi, T. Nojima, E. Galezowska, A. Gluszynska, B.

Juskowiak, S. Takenaka, *Anal. Chim. Acta* **2007**, *581*, 125 – 131; c) F. He, Y. Tang, S. Wang, Y. Li, D. Zhu, *J. Am. Chem. Soc.* **2005**, *127*, 12343 – 12346; d) B. Kim, I. H. Jung, M. Kang, H.-K. Shim, H. Y. Woo, *J. Am. Chem. Soc.* **2012**, *134*, 3133 – 3138.

[13] a) J. R. Lakowicz, *Principles of Fluorescence Spectroscopy*, Springer, Boston, **2006**; b) T. Förster, *Naturwissenschaften* **1946**, *33*, 166 – 175; c) T. Förster, *Ann. Phys.* **1948**, *437*, 55 – 75.

[14] a) D. Sen, W. Gilbert, *Nature* **1988**, *334*, 364 – 366; b) T. Simonsson, *Biol. Chem.* **2001**, *382*, 621 – 628; c) S. Neidle, S. Balasubramanian, *Quadruplex Nucleic Acids*, RSC, Cambridge, **2006**.

[15] Y. Wang, D. J. Patel, *Structure* **1993**, *1*, 263 – 282.

[16] G. N. Parkinson, M. P. H. Lee, S. Neidle, *Nature* **2002**, *417*, 876 – 880.

Angewandte Chemie

DOI: 10.1002/ange.201409278

DNA-Nanotechnologie

Ionenselektive Guanin-Quadruplex-Faltung auf DNA-Origami-Strukturen**

Lydia Olejko, Piotr J. Cywinski und Ilko Bald**

Abstract: *DNA-Origami-Nanostrukturen sind vielseitig anwendbare Hilfsmittel, die genutzt werden können, um Funktionalitäten mit hoher lokaler Kontrolle anzuordnen. Hier zeigen wir, dass DNA-Origami-Substrate genutzt werden können, um die Faltung bestimmter Guanin(G)-Quadruplex-Strukturen zu unterdrücken. Die Faltung von Telomer-DNA zu G-Quadruplexen in Gegenwart einwertiger Kationen (z. B. Na^+ und K^+) wird derzeit zur Detektion von K^+-Ionen genutzt, allerdings mit ungenügender Selektivität gegenüber Na^+. Mithilfe von FRET zwischen zwei organischen Farbstoffen, die am 3′- und 5′-Ende der Telomer-DNA immobilisiert werden, zeigen wir, dass die G-Quadruplex-Faltung auf DNA-Origami-Strukturen in Gegenwart von Natriumionen sterisch gehindert wird. Dadurch stellt die an DNA-Origami-Strukturen gebundene Telomer-DNA ein hochempfindliches und selektives Detektionssystem für Kaliumionen dar, sogar in Gegenwart hoher Natriumionenkonzentration.*

DNA kann in fast jede beliebige 2D- und 3D-Form mithilfe der DNA-Origami-Technik gefaltet werden.[1] DNA-Nanostrukturen lassen sich mit den unterschiedlichsten Molekülen mit hoher Präzision modifizieren, z. B. mit Proteinen, Nanopartikeln, fluoreszierenden Farbstoffen und anderen DNA-Strukturen. Daher eignen sie sich sehr gut für analytische Untersuchungen.[2] DNA-Origami-Strukturen können als Substrat genutzt werden, um RNA-Sequenzen[3] und andere Moleküle mithilfe der Rasterkraftmikroskopie (AFM) zu detektieren,[4] um einzelne Moleküle durch oberflächenverstärkte Raman-Streuung zu identifizieren[5] oder die Strangbruchausbeute verschiedener DNA-Sequenzen zu bestimmen.[6] Die Faltung von Guanin(G)-Quadruplexen wurde umfangreich auf DNA-Origami-Gerüsten mittels Hochgeschwindigkeits-AFM untersucht.[7] Telomer-DNA befindet sich an den Enden von eukaryotischen Chromosomen und stabilisiert und schützt das Genom.[8] Die G-reiche einzelsträngige Säugetier-Telomer-DNA hat die Sequenz 5′-$(TTAGGG)_n$[9] und kann G-Quadruplexe in Gegenwart von einwertigen Kationen bilden. In diesen Komplexen werden vier G-Basen durch Ausbildung von acht Wasserstoffbrücken zu G-Tetraden assoziiert. Zwei oder mehr gestapelte G-Tetraden bilden einen G-Quadruplex. Da die Assoziationskonstante der G-Quadruplexe für Na^+ kleiner als die für K^+ ist,[10,11] wurden Telomersequenzen als selektive K^+-Sensoren basierend auf FRET (resonanter Energietransfer nach Förster) vorgeschlagen.[10–12] Allerdings induziert Na^+ die G-Quadruplex-Faltung von menschlicher Telomer-DNA in einem Konzentrationsbereich von 10–205 mM. Dies kann unter physiologischen Bedingungen (ca. 145 mM Na^+) zu beträchtlichen Fehlern in der K^+-Bestimmung führen. Wie wir hier zeigen, wird die G-Quadruplex-Bildung aus Telomer-DNA, welche an DNA-Origami-Strukturen gebunden ist, in Gegenwart von Na^+ komplett unterdrückt, wohingegen die Faltung der G-Quadruplexe in Gegenwart von K^+ unbeeinflusst bleibt.

In unserer Studie haben wir FRET genutzt, um die durch Na^+ und K^+ induzierte G-Quadruplex-Faltung aus freien Telomersequenzen und an DNA-Origami-Dreiecken gebundenen Sequenzen detailliert zu untersuchen. FRET ist ein strahlungsloser Energietransfer, bei dem die Energie von einem angeregten Donor auf einen Akzeptor durch Dipol-Dipol-Wechselwirkungen übertragen wird. Die FRET-Effizienz η hängt sehr stark von dem Donor-Akzeptor-Abstand nach folgender Gleichung ab:

$$\eta = \frac{R_0^6}{R_0^6 + R^6}, \quad (1)$$

wobei R der Donor-Akzeptor-Abstand ist und R_0 der Förster-Abstand, bei dem die FRET-Effizienz 50 % beträgt. Die FRET-Effizienz kann basierend auf der Donor-Abklingzeit mit folgender Gleichung berechnet werden:

$$\eta = 1 - \frac{\tau_{DA}}{\tau_D}, \quad (2)$$

wobei τ_D die Donor-Abklingzeit in Abwesenheit des Akzeptors ist und τ_{DA} die Abklingzeit in Gegenwart des Akzeptors.[13]

[*] L. Olejko, Prof. Dr. I. Bald
Institut für Chemie, Universität Potsdam
Karl-Liebknecht-Straße 24–25, 14476 Potsdam (Deutschland)
E-Mail: bald@uni-potsdam.de
Dr. P. J. Cywinski
NanoPolyPhotonics, Fraunhofer IAP
Geiselbergstraße 69, 14476 Potsdam (Deutschland)
E-Mail: piotr.cywinski@iap.fraunhofer.de
Prof. Dr. I. Bald
Bundesanstalt für Materialforschung und -prüfung
Richard-Willstätter Straße 11, 12489 Berlin (Deutschland)
L. Olejko
School of Analytical Sciences Adlershof
Humboldt-Universität zu Berlin
Unter den Linden 6, 10099 Berlin (Deutschland)

[**] Wir danken Prof. Michael Kumke für Diskussionen und Zugang zum Fluoreszenzspektrometer sowie A. Keller für das Korrekturlesen des Manuskripts. Unsere Forschungen wurden durch einen Marie Curie FP7 Integration Grant im Rahmen des 7th European Union Framework Programme, die Deutsche Forschungsgemeinschaft (DFG), die Universität Potsdam und das DFG-Projekt GSC 1013 (SALSA) unterstützt.

Hintergrundinformationen zu diesem Beitrag sind im WWW unter http://dx.doi.org/10.1002/ange.201409278 zu finden.

Wir nutzten freie Telomer-DNA als Referenzsystem, wobei das 5′-Ende mit Cyanin 3 (Cy3) und das 3′-Ende mit Fluorescein (FAM) modifiziert wurden (5′-Cy3-TTG GGA TTG GGA TTG GGA TTG GA TT-FAM). Wird K^+ oder Na^+ zu solch einer Lösung hinzugegeben, so ändert sich die Konformation des DNA-Stranges von einer Random-Coil-Struktur zu einer G-Quadruplex-Struktur. Hierbei ist der Donor-Akzeptor-Abstand in Gegenwart von K^+ 4.6 nm und von Na^+ 5.8 nm (siehe Abbildung 1 A und Abbildung S1 in den Hintergrundinformationen (SI)). Im zweiten System, in dem dreieckige DNA-Origami-Strukturen verwendet werden (AFM-Bild ist in Abbildung S2 in den SI gezeigt), wurde FAM 3.3 nm entfernt vom 3′-Ende des verlängerten Telomerstrangs platziert. Die Sequenz wurde am 5′-Ende mit Cy3 modifiziert (Abbildung 1 B und Abbildung S1 in den SI). In der gefalteten G-Quadruplex-Struktur beträgt der Donor-Akzeptor-Abstand maximal 7.5 nm.

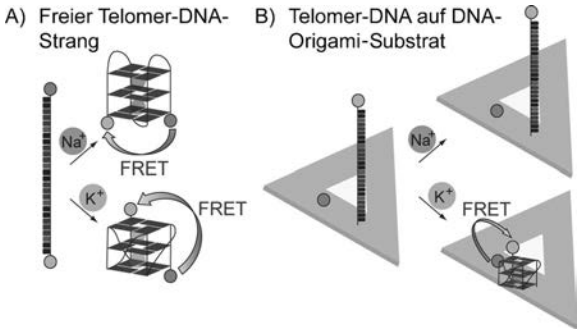

Abbildung 1. Prinzip des Kaliumdetektionssystems basierend auf Telomer-DNA. A) Freier Telomer-DNA-Strang (5′-Cy3-TT$(GGGA)_4$TT-FAM, T = schwarz, G = dunkelgrau, A = hellgrau) mit Fluorescein (FAM, dunkelgrau) als Donorfarbstoff und Cyanin 3 (Cy3, hellgrau) als Akzeptorfarbstoff. Sind einwertige Kationen wie K^+ und Na^+ in Lösung vorhanden, faltet sich der DNA-Strang in eine G-Quadruplex-Struktur. Die unterschiedlichen Kationen bewirken die Bildung von verschiedenen G-Quadruplex-Strukturen. Mithilfe des freien Telomer-DNA-Stranges können beide G-Quadruplexe gebildet und K^+ und Na^+ mittels FRET detektiert werden. B) Der Telomer-DNA-Strang ist als Verlängerung eines Helferstrangs auf dem DNA-Origami-Substrat immobilisiert. Der Telomer-DNA-Strang wurde 3.3 nm von FAM auf der DNA-Origami-Struktur entfernt platziert. Der G-Quadruplex kann nun nur in Gegenwart von Kalium gebildet werden.

Emissionsspektren wurden bei einer DNA-Konzentration von 5 nM mit einer Anregungswellenlänge von 450 nm aufgenommen und sind in Abbildung 2 gezeigt. Abbildung 2 A und B zeigen die Fluoreszenzemissionsspektren der freien Telomer-DNA-Sequenz in Abhängigkeit der KCl- (A) und NaCl-Konzentration (B). In Abbildung 2 C und B sind die Emissionsspektren für das Telomer-DNA-Origami-System dargestellt. Findet kein FRET statt, ist die Emission von FAM bei 515 nm dominant. Da die organischen Farbstoffe in der Random-Coil-Struktur schon so nahe beieinander sind, dass FRET stattfinden kann, ist das Cy3-Emissionsmaximum bei 565 nm in den Emissionsspektren (Abbildung 2 A,B) auch ohne Salzzugabe sichtbar. Wird entweder KCl oder NaCl zu den freien Telomer-DNA-Strängen gegeben (Abbildung 2 A,B), kommen sich die organischen Farbstoffe aufgrund der G-Quadruplex-Faltung immer näher, sodass die FRET-Effizienz steigt. Die Fluoreszenz von FAM wird gelöscht, und gleichzeitig wird die Emission von Cy3 verstärkt. Die Zugabe von 1 mM KCl (Abbildung 2 A) ist ausreichend, um eine Änderung der Emissionseigenschaften des Systems zu bewirken. Wegen der kleineren Assoziationskonstante von Na^+[11] im Vergleich zu der von K^+, wird eine Änderung des Emissionsspektrums erst nach Zugabe von 25 mM NaCl sichtbar (Abbildung 2 B). Jedoch ist diese Unterscheidung für biologisch relevante Bedingungen nicht ausreichend, da in extrazellulären Flüssigkeiten die Konzentration von Na^+ ca. 145 mM und von K^+ nur 4 mM beträgt. Der freie Telomer-DNA-Strang zeigt eine hohe Sensitivität für Na^+ in einem Bereich von 25–205 mM, wie in Abbildung 2 B zu sehen ist. Demnach ist ein Kalium-Sensor unter Verwendung von freier Telomer-DNA in biologischen Medien nicht realisierbar. Um dieses Problem zu überwinden, wurde die Telomer-Sequenz auf DNA-Origami-Substraten immobilisiert, um das DNA-Origami-Telomer-FRET-Sensorsystem zu erhalten. In Abbildung 2 C sind die Emissionsspektren des Telomer-DNA-Origami-Systems in Abhängigkeit der KCl-Konzentration gezeigt. Im Allgemeinen sind die FRET-Effizienzen dieses Systems geringer, da der Donor-Akzeptor-Abstand größer als im freien Telomerstrang ist (Abbildung 1). Dennoch wird eine klare Änderung der Donor- und Akzeptoremission in einem Konzentrationsbereich von 5–110 mM KCl beobachtet. Die Emission von Cy3 nimmt von 0.1 bis 2.5 mM KCl leicht ab, was auf ein mäßiges Erwärmen auf 40 °C zurückgeführt wird, welches den durchschnittlichen Abstand zwischen den Farbstoffen im ungefalteten Telomer erhöhen könnte. Ab einer Konzentration von 5 mM KCl nimmt die FRET-Effizienz deutlich zu. Bei Zugabe von NaCl zu den Telomer-DNA-Origami-Strukturen zeigt sich ein vollständig anderes Verhalten (Abbildung 2 D). Die Emissionsspektren bleiben durch Na^+ unbeeinflusst, sogar bei einer Konzentration von 205 mM NaCl. Das zeigt, dass sich der durchschnittliche Donor-Akzeptor-Abstand mit Erhöhung der NaCl-Konzentration nicht ändert. Dies deutet darauf hin, dass sich die G-Quadruplexe auf DNA-Origami-Strukturen in Gegenwart von Na^+ nicht ausbilden können. In Abbildung 2 E ist gezeigt, dass die hohe Selektivität für K^+ auch in Gegenwart von 145 mM NaCl erhalten bleibt. Außerdem ist zu erwähnen, dass ebenfalls kein FRET durch Na^+-Zugabe zu dem DNA-Origami-Substrat beobachtet wird, wenn ein Farbstoff direkt neben dem 3′-Ende der Telomersequenz platziert wird, um das freie Telomersystem nachzuahmen, (Abbildung S3 in den SI).

Basierend auf den Fluoreszenzintensitäten von FAM und Cy3 wurden die Assoziationskonstanten für den freien Telomer-DNA-Strang mit $1.5 \times 10^4\,M^{-2}$ für K^+ und $33.7\,M^{-2}$ für Na^+ berechnet (Abbildung S4 in den SI). Die Assoziationskonstante des Telomer-DNA-Origami-Systems beträgt $2.6 \times 10^4\,M^{-2}$ für K^+ (Abbildung S4 in den SI), was dem Wert des freien Telomer-DNA-Strangs sehr nahe kommt. In Gegenwart von 145 mM NaCl beträgt die Assoziationskonstante für die KCl-Zugabe $1.4 \times 10^4\,M^{-2}$ (Abbildung S4 in den SI). Das

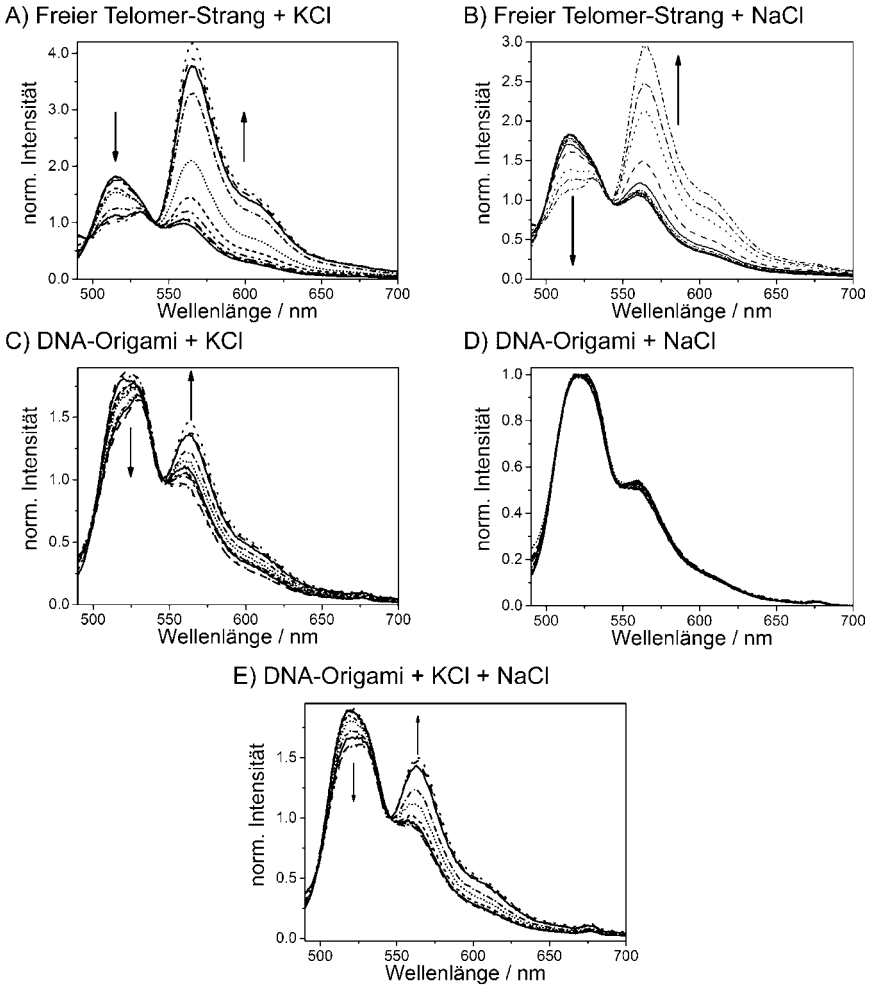

Abbildung 2. Normierte Emissionsspektren (λ_{ex} = 450 nm) der freien Telomer-DNA (c = 5 nM) (A,B) und von Telomer-DNA auf DNA-Origami-Strukturen (C,D,E) für unterschiedliche Salzkonzentrationen (KCl und NaCl). A,B) Zugabe von KCl (A; c = 0–110 mM) und NaCl (B; c = 0–205 mM) resultiert in einer Abnahme der Emissionsintensität des Donorfarbstoffs FAM (515 nm) und einer Zunahme der Emissionsintensität des Akzeptors Cy3 (565 nm) aufgrund des verstärkten FRET-Prozesses. Das zeigt, dass freie Telomer-DNA in Gegenwart von K^+ und Na^+ in G-Quadruplexe gefaltet wird. C,D,E) Ist die Telomer-DNA auf dem DNA-Origami-Substrat immobilisiert, führt nur eine KCl-Zugabe (C; c = 0–110 mM) zu einer Änderung der Emissionseigenschaften aufgrund von FRET, sogar in Gegenwart von 145 mM NaCl (E, c = 0–110 mM). Durch Zugabe von NaCl (D, c = 0–205 mM) wird der G-Quadruplex auf DNA-Origami-Strukturen nicht gebildet und die Emission von FAM und Cy3 sind unbeeinflusst.

zeigt, dass die Faltung von G-Quadruplexen und die Sensitivität gegenüber K^+ durch die DNA-Origami-Strukturen und Na^+ unbeeinflusst sind.

Da die intensitätsbasierten Messungen von der DNA-Konzentration abhängig sind, wurden die FRET-Effizienzen mit zeitaufgelöster Fluoreszenzspektroskopie bestimmt. Die Fluoreszenzabklingzeiten des Donorfarbstoffs sind in Tabelle 1 zusammengefasst (die Abklingkurven sind in Abbildung S5 in den SI dargestellt), und die FRET-Effizienzen wurden mit Gleichung 2 berechnet. In Abbildung 3 sind die FRET-Effizienzen gegen die Salzkonzentration aufgetragen.

Im Falle des freien Telomer-DNA-Stranges nimmt die Abklingzeit des Donors mit zunehmender KCl- und NaCl-Konzentration ab. Folglich nimmt die FRET-Effizienz mit zunehmender KCl- und NaCl-Konzentration zu. Der dynamische Bereich in der FRET-Effizienz liegt für K^+ zwischen 0.5 mM und 50 mM. Auf der anderen Seite kommt es für Na^+ zu einer starken Änderung der FRET-Effizienz im Konzentrationsbereich von 5 mM bis über 165 mM.

Ähnlich wie bei dem freien Telomer-DNA-Strang ändert sich die FRET-Effizienz für das Telomer-DNA-Origami-System durch Zugabe von KCl. Die Unterschiede in den FRET-Effizienzen des freien Telomer-DNA-Stranges und des DNA-Origami-Systems (freie Telomer-DNA: 0.56–0.91; DNA-Origami-Substrat: 0.28–0.57) kommen durch die unterschiedlichen Donor-Akzeptor-Abstände zustande (Abbildung 1). Wird NaCl hinzugegeben, bleibt die FRET-Effizienz unbeeinflusst (Abbildung 3), was wiederum auf eine Hinderung der G-Quadruplex-Faltung auf DNA-Origami-Strukturen hinweist. Dementsprechend wird K^+ auch in Gegenwart von hohen Na^+-Konzentrationen detektiert (145 mM, Abbildung 3).

Die Bildung von G-Quadruplexen in Gegenwart von K^+ und die Unterdrückung der G-Quadruplex-Bildung in Gegenwart von Na^+ auf DNA-Origami-Substraten ist durch die spezifische Struktur der G-Quadruplexe zu erklären. Neben der Telomersequenz und der Strangpolarisation hängt die G-Quadruplex-Struktur auch vom zentralen Metallion ab.[14] Entsprechend Röntgenkristallstruktur- und NMR-Analysen bewirkt Na^+ die Bildung eines „Basket-Typs“ und K^+ die eines „Propeller-Typs“ (Abbildung 1 A).[15,16] Der „Basket-Typ“ hat eine diagonale Schlaufe am Ende des G-Quadruplexes, wodurch die Faltung durch die DNA-Origami-Oberfläche sterisch behindert wird.[15] Im Gegensatz dazu kann der „Propeller-Typ“, mit den Schlaufen an den Seiten, in Gegenwart von K^+ auf der DNA-Origami-Plattform gebildet werden. Die Bildung der

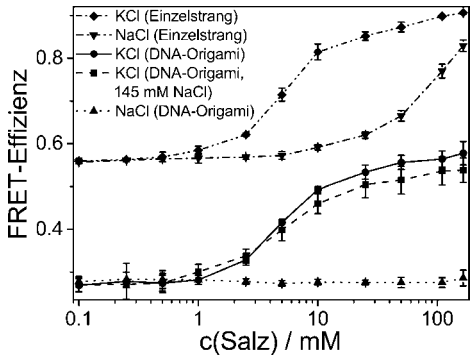

Abbildung 3. FRET-Effizienzen basierend auf FAM-Abklingkurven, aufgetragen gegen Salzkonzentrationen (KCl (Karos, Kreise, Quadrate) und NaCl (Dreiecke nach unten, Dreiecke nach oben)) für das freie Telomer-DNA-System ($c = 5$ nM) (Karos, Dreiecke nach unten) und für das Telomer-DNA-Origami-System (Kreise, Quadrate, Dreiecke nach oben). Die FRET-Effizienz nimmt für beide Systeme mit zunehmender KCl-Konzentration zu, sogar in Gegenwart von 145 mM NaCl (Quadrat). Durch Zunahme der NaCl-Konzentration nimmt nur die FRET-Effizienz des freien Telomer-DNA-Stranges zu. Ist die Telomer-DNA auf dem DNA-Origami-Substrat immobilisiert, kann NaCl nicht detektiert werden.

Tabelle 1: FAM-Abklingzeiten τ der hier behandelten Systeme.[a]

c(Salz) [mM]	τ (ssDNA, KCl) [ns]	τ (ssDNA, NaCl) [ns]	τ (DNA-Origami, KCl) [ns]	τ (DNA-Origami, NaCl) [ns]	τ (DNA-Origami, KCl in 145 mM NaCl) [ns]
0	1.87	1.89	3.56	3.47	3.47
0.1	1.89	1.90	3.55	3.47	3.50
0.25	1.88	1.89	3.58	3.44	3.50
0.5	1.85	1.87	3.54	3.44	3.48
1	1.79	1.87	3.50	3.45	3.35
2.5	1.63	1.85	3.31	3.47	3.18
5	1.23	1.84	2.96	4.49	2.89
10	0.80	1.76	2.66	3.47	2.59
25	0.64	1.63	2.50	3.48	2.38
50	0.55	1.44	2.40	3.48	2.33
110	0.44	0.99	2.36	3.48	2.23
165	0.40	0.73	2.30	3.43	2.22

[a] Aufgrund von FRET nimmt die Abklingzeit für das freie Telomer-DNA-System (ssDNA) nach KCl- und NaCl-Zugabe und für das Telomer-DNA-Origami-System (DNA-Origami) nach Zugabe von KCl auch in Gegenwart von 145 mM NaCl ab. Die Abklingzeit wird durch NaCl im Telomer-DNA-Origami-System nicht beeinflusst. τ_D(ssDNA, FAM) = 4.3 ns; τ_D(DNA-Origami, FAM) = 4.8 ns.

unterschiedlichen G-Quadruplex-Strukturen in Gegenwart von K^+ und Na^+ wird durch die unterschiedlichen Donor-Akzeptor-Abstände bestätigt, welche mittels der FRET-Effizienzen des freien Telomersystems bestimmt werden können. Die Donor-Akzeptor-Abstände werden mit Gleichung (1) und dem Förster-Abstand R_0 für das FAM-Cy3-FRET-Paar berechnet. Basierend auf dem spektralen Überlapp wurde R_0 zu 6.7 nm berechnet (Abbildung S6 in den SI). Dementsprechend ist der Donor-Akzeptor-Abstand im freien Telomerstrang ohne Zugabe von NaCl oder KCl 6.4 nm. Durch Zugabe von 165 mM KCl nimmt der Donor-Akzeptor-Abstand bis auf 4.6 nm ab, was darauf hindeutet, dass der G-Quadruplex gefaltet wird. Dieses Ergebnis stimmt mit dem erwarteten Abstand von 4.6 nm (Abbildung S1 in den SI) basierend auf den Kristallstrukturdaten[16] und den Linkerlängen zwischen Farbstoffen und DNA (0.7 nm) überein. Für 165 mM NaCl beträgt der aus den FRET-Effizienzen berechnete Donor-Akzeptor-Abstand 5.1 nm, was kürzer ist als der erwartete Abstand von 5.8 nm (ΔR(NaCl) = 0.7 nm, Abbildung S1 in den SI). Hier muss beachtet werden, dass sich bei der durch Na^+ induzierten G-Quadruplex-Struktur (Abbildung 1) die organischen Farbstoffe am gleichen Ende des G-Quadruplexes befinden. Durch die Linker zwischen den organischen Farbstoffen und der DNA kann der durchschnittliche Abstand zwischen FAM und Cy3 etwas kürzer als der Erwartungswert sein. In dem Telomer-DNA-Origami-System nimmt der Donor-Akzeptor-Abstand von 7.8 nm (ohne Zugabe von Salz) auf 6.4 nm durch Zugabe von 165 mM KCl aufgrund der G-Quadruplex-Faltung ab. Der maximal erwartete Abstand dieses G-Quadruplex-Systems in Gegenwart von KCl beträgt 7.4 nm (Abbildung S1 in den SI). Hierbei wurde angenommen, dass die starre G-Quadruplex-Struktur so gedreht ist, dass der Donor-Akzeptor-Abstand maximal ist. Der experimentell bestimmte Abstand ist ein Durchschnitt aller möglichen gedrehten Konformere und ist daher kürzer als der maximal zu erwartende Abstand.

Das hier vorgestellte Nachweissystem basiert auf dem „FAM-zu-Cy3"-FRET-Prozess auf DNA-Origami-Substraten und ermöglicht die Detektion von Kalium im Bereich von 0.5–50 mM, sogar in Gegenwart von hohen Na^+-Konzentrationen (145 mM). Um diese Selektivität zu demonstrieren, haben wir die G-Quadruplex-Faltung von freien Telomer-DNA-Strängen mit der von Telomersträngen gebunden an DNA-Origami-Strukturen verglichen. Der freie Telomerstrang zeigt eine Sensitivität gegenüber beiden Ionen (Na^+ und K^+) mit unterschiedlichen Assoziationskonstanten. Wird die Telomer-DNA an DNA-Origami-Substrate gebunden, wird eine hohe Selektivität für Kalium erzielt, ohne die Sensitivität im Vergleich zum freien DNA-Strang zu verlieren. Die G-Quadruplex-Faltung durch Natriumionen wird auf DNA-Origami-Strukturen aufgrund der sterischen Hinderung durch die DNA-Origami-Oberfläche komplett unterdrückt.

Eingegangen am 19. September 2014
Online veröffentlicht am 24. November 2014

Stichwörter: DNA-Nanotechnologie · FRET · G-Quadruplexe · DNA-Origami

[1] P. W. K. Rothemund, *Nature* **2006**, *440*, 297 – 302.
[2] a) G. P. Acuna, F. M. Möller, P. Holzmeister, S. Beater, B. Lalkens, P. Tinnefeld, *Science* **2012**, *338*, 506 – 510; b) J. Fu, M. Liu, Y. Liu, N. W. Woodbury, H. Yan, *J. Am. Chem. Soc.* **2012**, *134*, 5516 – 5519; c) A. Kuzyk, R. Schreiber, Z. Fan, G. Pardatscher, E.-M. Roller, A. Högele, F. C. Simmel, A. O. Govorov, T. Liedl, *Nature* **2012**, *483*, 311 – 314; d) I. Bald, A. Keller, *Molecules* **2014**, *19*, 13803 – 13823.
[3] Y. Ke, S. Lindsay, Y. Chang, Y. Liu, H. Yan, *Science* **2008**, *319*, 180 – 183.

[4] A. Kuzuya, Y. Sakai, T. Yamazaki, Y. Xu, M. Komiyama, *Nat. Commun.* **2011**, *2*, 449.
[5] J. Prinz, B. Schreiber, L. Olejko, J. Oertel, J. Rackwitz, A. Keller, I. Bald, *J. Phys. Chem. Lett.* **2013**, *4*, 4140 – 4145.
[6] A. Keller, I. Bald, A. Rotaru, E. Cauët, K. V. Gothelf, F. Besenbacher, *ACS Nano* **2012**, *6*, 4392 – 4399.
[7] a) Y. Sannohe, M. Endo, Y. Katsuda, K. Hidaka, H. Sugiyama, *J. Am. Chem. Soc.* **2010**, *132*, 16311 – 16313; b) A. Rajendran, M. Endo, K. Hidaka, H. Sugiyama, *Angew. Chem. Int. Ed.* **2014**, *53*, 4107 – 4112; *Angew. Chem.* **2014**, *126*, 4191 – 4196; c) A. Rajendran, M. Endo, K. Hidaka, P. Lan Thao Tran, J.-L. Mergny, H. Sugiyama, *Nucleic Acids Res.* **2013**, *41*, 8738 – 8747.
[8] S. Neidle, G. N. Parkinson, *Curr. Opin. Struct. Biol.* **2003**, *13*, 275 – 283.
[9] a) T. R. Cech, *Angew. Chem. Int. Ed.* **2000**, *39*, 34 – 43; *Angew. Chem.* **2000**, *112*, 34 – 44; b) R. K. Moyzis, J. M. Buckingham, L. S. Cram, M. Dani, L. L. Deaven, M. D. Jones, J. Meyne, R. L. Ratliff, J. R. Wu, *Proc. Natl. Acad. Sci. USA* **1988**, *85*, 6622 – 6626.
[10] H. Ueyama, M. Takagi, S. Takenaka, *J. Am. Chem. Soc.* **2002**, *124*, 14286 – 14287.
[11] S. Takenaka, B. Juskowiak, *Anal. Sci.* **2011**, *27*, 1167 – 1172.
[12] a) L.-D. Li, X.-Q. Huang, L. Guo, *Rare Met.* **2013**, *32*, 369 – 374; b) S. Nagatoishi, T. Nojima, E. Galezowska, A. Gluszynska, B. Juskowiak, S. Takenaka, *Anal. Chim. Acta* **2007**, *581*, 125 – 131; c) F. He, Y. Tang, S. Wang, Y. Li, D. Zhu, *J. Am. Chem. Soc.* **2005**, *127*, 12343 – 12346; d) B. Kim, I. H. Jung, M. Kang, H.-K. Shim, H. Y. Woo, *J. Am. Chem. Soc.* **2012**, *134*, 3133 – 3138.
[13] a) J. R. Lakowicz, *Principles of Fluorescence Spectroscopy*, Springer, Boston, **2006**; b) T. Förster, *Ann. Phys.* **1948**, *437*, 55 – 75; c) T. Forster, *Naturwissenschaften* **1946**, *33*, 166 – 175.
[14] a) D. Sen, W. Gilbert, *Nature* **1988**, *334*, 364 – 366; b) T. Simonsson, *Biol. Chem.* **2001**, *382*, 621 – 628; c) S. Neidle, S. Balasubramanian, *Quadruplex Nucleic Acids*, RSC, Cambridge **2006**.
[15] Y. Wang, D. J. Patel, *Structure* **1993**, *1*, 263 – 282.
[16] G. N. Parkinson, M. P. H. Lee, S. Neidle, *Nature* **2002**, *417*, 876 – 880.

Angewandte Chemie
Eine Zeitschrift der Gesellschaft Deutscher Chemiker

Supporting Information

69451 Weinheim, Germany

Ion-Selective Formation of a Guanine Quadruplex on DNA Origami Structures**

Lydia Olejko, Piotr J. Cywinski, and Ilko Bald**

anie_201409278_sm_miscellaneous_information.pdf

Supporting information

Table of contents

1. Experimental Section

DNA origami preparation

The DNA origami structures were prepared by mixing the staple strands (150 nM) with the single stranded M13mp18 viral genome (5 nM) in TAE buffer (10x) containing 100 mM $MgCl_2$ and ultrapure water (Millipore). This mixture was heated up to 80 °C and then slowly cooled down to 8 °C in 2 h using a thermal cycler (PEQLAB, Germany). After the annealing process, the solutions were purified *via* a 100 kDa molecular weight cut-off centrifugal filter (Millipore) with TAE buffer (1x) containing 10 mM $MgCl_2$ (2x 3214 g for 10 min). The purified samples were first imaged with a Flex AFM (Nanosurf, Germany) to confirm the successful formation of the DNA origami structures. Afterwards, fluorescence spectroscopic measurements were performed to study the photophysical properties.

G-quadruplex formation

To analyse the G-quadruplex formation with the free telomeric DNA strand containing Fluorescein and Cyanine3 (5nM in 1xTAE buffer to match the concentration of the DNA origami telomere system) a KCl or NaCl solution (c = 20 mM, 200 mM, 2 M in ultrapure water) was added step by step. Afterwards, the samples were left at RT for 15 min. Fluorescence steady-state and time-resolved spectra were recorded after each salt addition.

After the preparation of DNA origami triangles a KCl and NaCl solution, respectively (c = 20 mM, 200 mM, 2 M in ultrapure water), was added and for the formation of the G-quadruplexes a moderate heating to 40 °C was required while shaking the samples for 20 min. Fluorescence emission and time-resolved spectra were measured after each salt addition.

Steady-state fluorescence spectroscopy

Steady-state Fluorescence spectroscopy measurements were done using a FluoromaxP Fluorescence spectrophotometer (HORIBA Jobin Yvon GmbH, Germany) with 3 mm quartz cuvettes. The measurements were performed in a 90° angle acquisition using the system-internal quantum correction. An increment of 1 nm, an integration time of 0.2 s and slits of 5 nm were set for the measurements.

Time-correlated single photon counting (TCSPC)

Time-correlated single photon counting measurements were done on a FLS920 Fluorescence spectrophotometer (Edinburgh Instruments, UK) using 3 mm quartz cuvettes. The samples were measured in a 90° setup using a white light source (SC-400-PP supercontinuum-source, Fianium: 0,5-20 MHz, 400 nm < l < 24000 nm, pulse width: ca. 30 ps) as excitation source and a Multi-Channel-Plate (ELDY EM1-132/300, Europhoton GmbH, Berlin) as detector. The excitation wavelength was set to 490 nm and the emission wavelength was set to 530 nm. The Fluorescence decays were fitted with biexponential function using the FAST software:

$$I(t) = A_0 + A_1 e^{\frac{-t}{\tau_1}} + A_2 e^{\frac{-t}{\tau_2}} , \qquad (1)$$

where A_0 is the background or dark current, τ_1 and τ_2 are the decay times and A_1 and A_2 are the amplitudes characteristic for each decay time. Each set of concentration-dependent measurements was repeated three times and the error bars in Figure 3 are the standard deviations from mean FRET efficiencies.

2. Distance calculations

The nominal donor-acceptor distances were calculated based on the G-quadruplex geometry determined previously by X-ray diffraction [1]. Accordingly, the height of the G-quadruplex is 0.6 nm and the length is 4.1 nm. The linker length between the organic dye and DNA strand is 0.77 nm according to the manufacturer (Glen Research, Sterling, Virginia, USA) and has to be taken into account. In our estimation, we assumed that the linkers are stiff and point away from the G quadruplex. The estimated distances of the G-quadruplex structures in the presence of Na^+ and K^+ and on the DNA origami structure are shown in Figure S1.

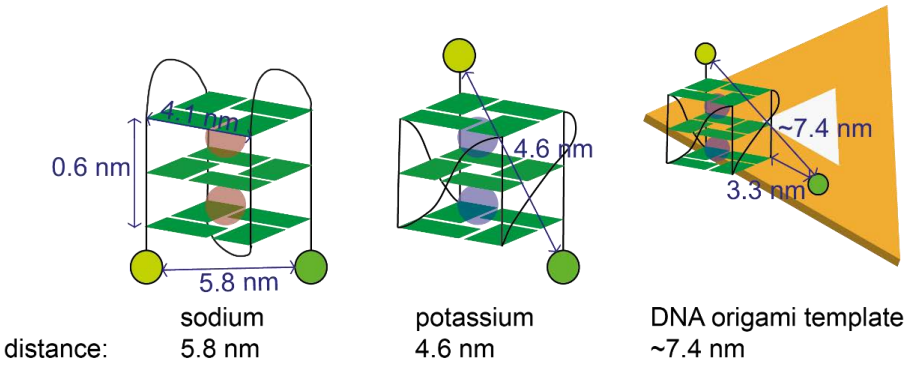

Figure S1. Determination of distances between FAM (green) and Cy3 (yellow) in different systems based on structural properties of the G-quadruplex, DNA strand and DNA origami template (height: 0.6 nm, length: 4.1 nm, linker length: 0.77 nm, distance between FAM and telomeric DNA on DNA origami structure: 3.3 nm).

3. Chemicals

Unmodified oligonucleotides (used as staple strands) were purchased from Integrated DNA Technologies (Leuven, Belgium). The DNA strands were dissolved in ultra-pure water (Merck Millipore, Germany) prior to use. The viral genome M13mp18 (scaffold strand) was purchased from New England BioLabs (Frankfurt am Main, Germany). The oligonucleotides modified with the organic dyes (Cy3, Fluorescein) were acquired from Metabion International AG (Planegg, Germany). The modified oligonucleotides have been purified by the manufacturer using HPLC and have been used as delivered. Magnesium chloride, potassium chloride, sodium chloride and Tris acetate-EDTA buffer (TAE buffer) were acquired from Sigma Aldrich (Taufkirchen bei München, Germany). Diluted TAE buffer (pH = 8.3) contained 40 mM Tris-acetate and 1 mM EDTA. Mica was purchased from Plano GmbH (Wetzlar, Germany).

4. Atomic force microscopy (AFM)

AFM imaging was performed with a Flex AFM (Nanosurf, Germany). A Multi75Al-G cantilever (Budget Sensors, Sofia, Bulgaria) with a resonance frequency of (75 - 15) kHz and a spring constant of 3 N/m was used to study DNA origami structures. The samples were prepared on freshly cleaved mica. For this, 2 µl of the sample and 33 µl of TAE (1x) containing 10 mM $MgCl_2$ were incubated for 30 sec and subsequently washed twice using 1 ml of ultrapure water. Afterwards, the fluid was removed with compressed air. The measurements were performed in air using the phase contrast mode. The measured triangles have a length of 100-150 nm and a height of 1-2 nm. A typical AFM image of DNA origami triangles is shown in Figure S2.

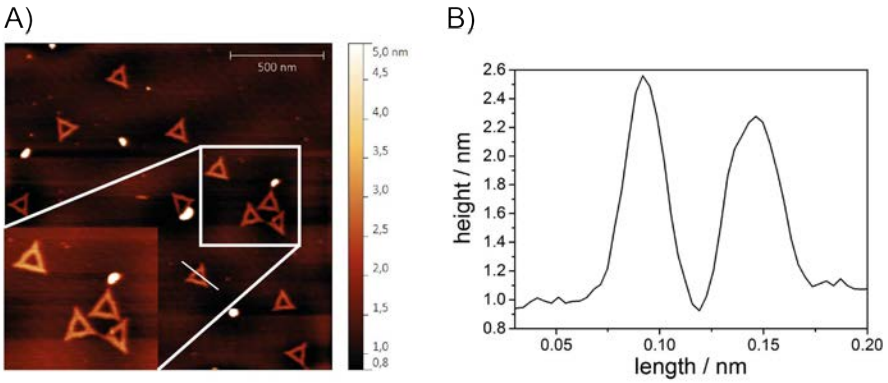

Figure S2. A) AFM image showing DNA origami structures on mica. B) Profile of one DNA origami triangle with a height of 1.6 nm and a length of 110 nm.

5. Association constants

Calculations of the associations constants K_{ass} for free telomeric DNA (KCl, NaCl) and DNA origami system (KCl) were done based on the following equation[2]:

$$\Delta F = \frac{\Delta F_{\infty} \cdot K_{ass} \cdot [M^+]^2}{1 + K_{ass} \cdot [M^+]^2} \quad (4)$$

$$\Delta F = \frac{I_{565}}{I_{515}} - \frac{I_{565,0}}{I_{515,0}} \quad (5)$$

Where I_{565} and I_{515} are the emission intensities of Cy3 and FAM, respectively at their emission maximum with salt being present and $I_{565,0}$ and $I_{515,0}$ are the emission intensity with salt being absent. The association constant was determined by fitting equation (4) to the plot ΔF versus KCl and NaCl concentrations as shown in Figure S3.

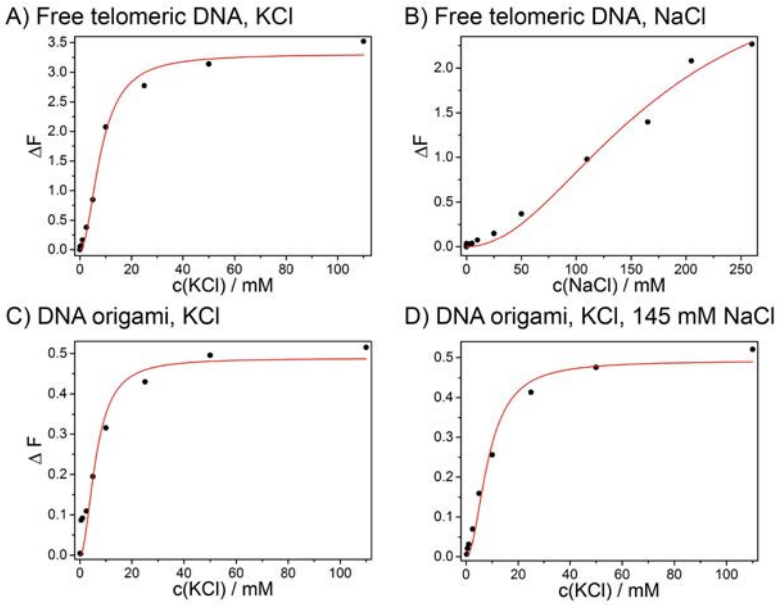

Figure S3. ΔF plotted against different salt concentrations (KCl: 0 – 110 mM, NaCl: 0 – 205 mM) for the different systems to determine K_{ass}. A) free telomeric DNA with increasing KCl, K_{ass} = 1.5 · 10^4 M^{-2} and B) NaCl concentration, K_{ass} = 33.7 M^{-2}. C) Telomeric DNA attached to DNA origami with increasing KCl concentration, K_{ass} = 2.6 · 10^4 M^{-2}. D) Telomeric DNA attached to DNA origami with increasing KCl concentration in the presence of 145 mM NaCl, K_{ass} = 1.4 · 10^4 M^{-2}. Data was fitted with $\Delta F = \frac{\Delta F_{\infty} \cdot K_{ass} \cdot [M^+]^2}{1 + K_{ass}[M^+]^2}$ (red line).

6. DNA origami-telomere system with dyes at the 3'- and 5'-ends of the telomere

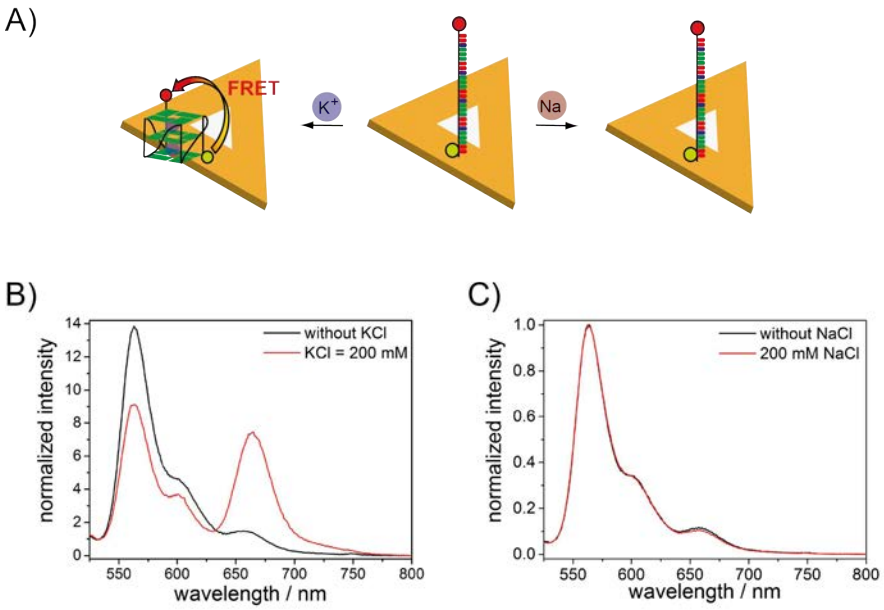

Figure S4. DNA origami-telomere system with dyes at the 3'- and 5'-end of the telomere sequence. This system mimics the situation in the free telomeric DNA. Here, Cy3 acts as a donor dye and Cy5 as an acceptor dye (λ_{em} = 665 nm). Upon addition of 200 mM KCl the emission of Cy5 is strong due to FRET, which occurs upon folding of the G quadruplex on the DNA origami structure. Upon addition of 200 mM NaCl the emission of Cy5 does not increase, since the G quadruplex can't form with Na^+ on the DNA origami structure.

7. FAM decay times

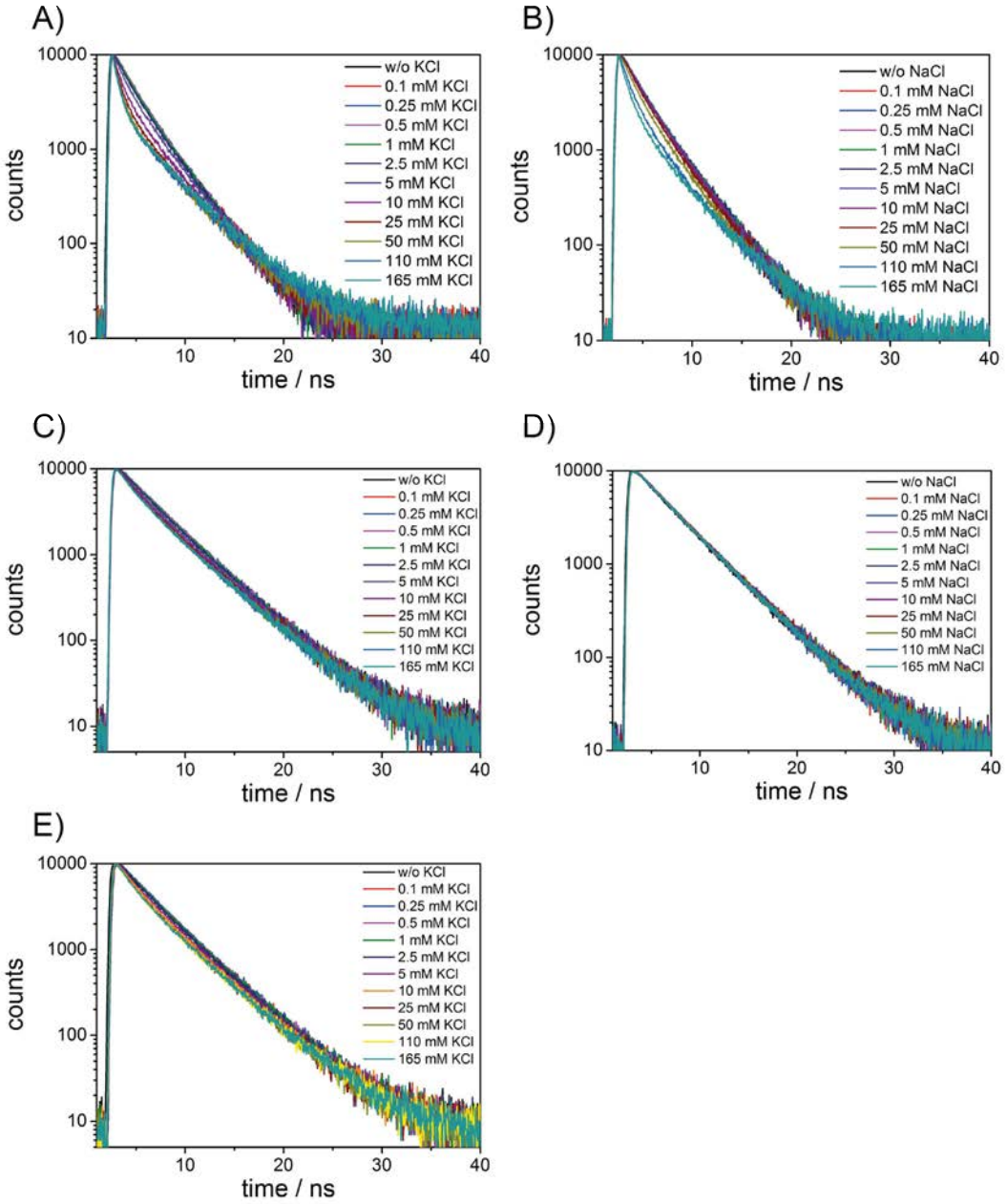

Figure S5. Different decay times with λ_{ex} = 490 nm and λ_{em} = 530 nm with increasing salt concentrations (0 – 165 mM). A) free telomeric DNA with increasing KCl concentration, B) free telomeric DNA with increasing NaCl concentration, C) telomeric DNA on DNA origami structure with increasing KCl concentration, D) telomeric DNA on DNA origami with increasing NaCl concentration, E) telomeric DNA on DNA origami with increasing NaCl concentration.

8. Calculation of spectral overlap integral and Förster radius

To calculate the spectral overlap integrals J and the Förster radius R_0 the software PhotochemCAD 2.1 was used. The desired spectra for the FRET pair (donor's emission spectrum and acceptor's absorption spectrum in terms of extinction coefficient, Figure S) were imported and the dipole orientation factor ($\kappa^2 = 2/3$), the refraction index (n = 1.33) and the specific quantum yield of FAM ($Q_D =$ 0.90) were used as inputs in the software.

$$R_0^6 = \frac{9(\ln 10)\kappa^2 Q_D J}{128\pi^5 n^4 N_{AV}} = 6.7 \text{ nm} \quad (2)$$

$$J(\lambda) = \frac{\int F_D(\lambda)\cdot\varepsilon(\lambda)\cdot\lambda^4 \, d\lambda}{\int F_D(\lambda) \, d\lambda} = 5.6 \cdot 10^{15} \text{ nm}^4 \cdot \text{l} \cdot \text{mol}^{-1} \cdot \text{cm}^{-1} \quad (3)$$

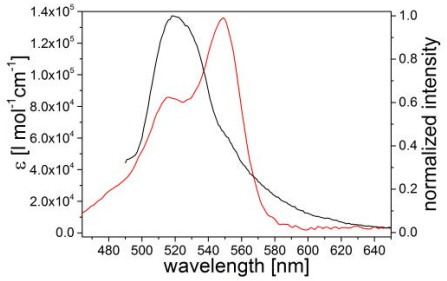

Figure S6. Cy3-DNA-origami absorption spectrum (red) and FAM-DNA-origami emission spectrum (black; λ_{ex} = 450 nm).

9. References:

[1] G. N. Parkinson, Lee, Michael P H, S. Neidle, *Nature* **2002**, *417*, 876–880.
[2] H. Ueyama, M. Takagi, S. Takenaka, *J Am Chem Soc* **2002**, *124*, 14286–14287.

4.3 Switchable photonic wire

"An Ion-Controlled Four-Color Fluorescent Telomeric Switch on DNA Origami Structures"

Nanoscale **2016**, 8 (19), 10339-10347[2]

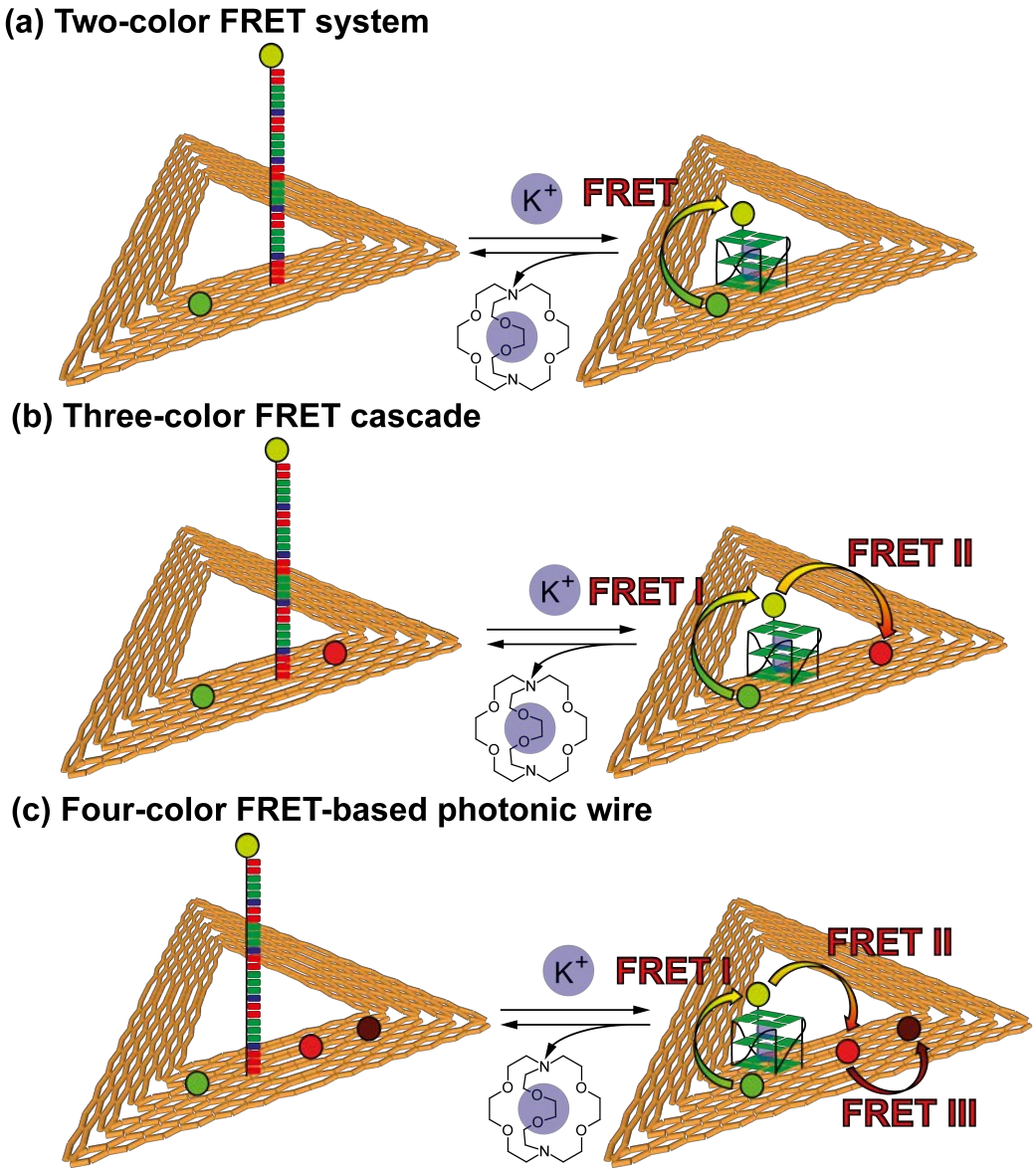

Nanoscale

PAPER

View Article Online
View Journal | View Issue

Cite this: *Nanoscale*, 2016, **8**, 10339

An ion-controlled four-color fluorescent telomeric switch on DNA origami structures†

L. Olejko,[a,b,c] P. J. Cywiński[d,e] and I. Bald*[a,c]

Received 6th January 2016,
Accepted 12th April 2016

DOI: 10.1039/c6nr00119j

www.rsc.org/nanoscale

The folding of single-stranded telomeric DNA into guanine (G) quadruplexes is a conformational change that plays a major role in sensing and drug targeting. The telomeric DNA can be placed on DNA origami nanostructures to make the folding process extremely selective for K^+ ions even in the presence of high Na^+ concentrations. Here, we demonstrate that the K^+-selective G-quadruplex formation is reversible when using a cryptand to remove K^+ from the G-quadruplex. We present a full characterization of the reversible switching between single-stranded telomeric DNA and G-quadruplex structures using Förster resonance energy transfer (FRET) between the dyes fluorescein (FAM) and cyanine3 (Cy3). When attached to the DNA origami platform, the G-quadruplex switch can be incorporated into more complex photonic networks, which is demonstrated for a three-color and a four-color FRET cascade from FAM over Cy3 and Cy5 to IRDye700 with G-quadruplex-Cy3 acting as a switchable transmitter.

1. Introduction

The specific Watson–Crick base pairing and possibility for rather simple functionalization makes DNA an extremely versatile material, which can adopt virtually any nanoscale shape and simultaneously can be functionalized with different chemical entities such as metal nanoparticles or fluorophores.[1–7] In such systems the optically-active functionalities act as signal reporters providing information about events occurring at the microscale and allow for detection, structure analysis and precise localization in sensing and imaging applications. Particularly interesting are nanophotonic programmable photonic networks or multifluorophoric cascades based on Förster resonance energy transfer (FRET) to control system functionality, readout or characterization. In such systems, excitons are transferred down in an array of fluorophores possessing successively lower excitation energies.[8,9] DNA nanostructures enable the controlled arrangement of multiple fluorophores,[10] which can be used for light harvesting, energy conversion, artificial photosynthesis, excitonic wires, switches, logic gates and optical communication.[11,12]

By exploiting the dynamic function of DNA sequences, switchable systems can be designed, which further extend the potential applications of functional DNA nanostructures to more sophisticated excitonic systems such as DNA micromachines and bio-computers.[13]

Very prominent switchable DNA structures are guanine (G) quadruplexes. Linear G-rich telomeric DNA strands can fold into G-quadruplex structures in the presence of monovalent cations such as K^+ or Na^+. G-quadruplex structures consist of two or more stacked planar G-tetrads, which are formed from four G nucleobases assembled and stabilized by Hoogsteen-type hydrogen bonds.[14] Basically, the G-quadruplex can unfold into single-stranded telomeric DNA when the central cation is removed from the G-quadruplex. Thus, G-quadruplex structures can be used to design DNA-nanoswitches sensitive to different chemical triggers.[13,15] An electrochemical switch based on a K^+ stabilized G-quadruplex structure has recently been developed.[16] Fluorescent switches based on reversible folding and unfolding have also been reported for Pb^{2+}-stabilized G-quadruplex structures[17] as well as for Na^+/K^+ induced G-quadruplex structures.[18–20] We have recently demonstrated ion-selective G-quadruplex folding on DNA origami structures using Förster resonance energy transfer (FRET), which can be used for selective K^+ recognition even in the presence of 145 mM Na^+.[21]

FRET is a non-radiative energy transfer, in which the energy is transferred from an excited donor molecule to an acceptor molecule through dipole–dipole interactions. Due to its

[a]Department of Chemistry, Physical Chemistry, University of Potsdam, Karl-Liebknecht Str. 24-25, 14476 Potsdam, Germany. E-mail: olejko@uni-potsdam.de, bald@uni-potsdam.de
[b]School of Analytical Sciences Adlershof, Humboldt-Universität zu Berlin, Unter den Linden 6, 10099, Germany
[c]BAM Federal Institute for Materials Research and Testing, Richard-Willstätter Str. 11, 12489 Berlin, Germany
[d]Fraunhofer IAP, Geiselbergstrasse 69, 14476 Potsdam, Germany. E-mail: piotrcyw@interia.pl
[e]Institute of Physical Chemistry, Polish Academy of Sciences, Kasprzaka 44/53, 01-224 Warsaw, Poland

†Electronic supplementary information (ESI) available. See DOI: 10.1039/c6nr00119j

View Article Online
Paper Nanoscale

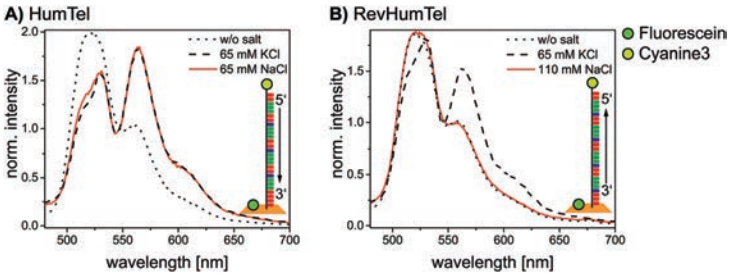

Fig. 1 Normalized emission spectra (λ_{ex} = 450 nm) of DNA origami triangles modified with two different telomeric DNA sequences (red = thymine, green = guanine, blue = adenine). (A) Human telomeric DNA (5′-GGG(TTA GGG)$_3$) folds into G-quadruplex structures in the presence of KCl (dashed line) and NaCl (red line). (B) Reversed human telomeric DNA (5′-(GGG ATT)$_4$) enables selective potassium sensing on DNA origami nanostructures. The G-quadruplex folds only in the presence of K^+ (dashed line). The emission properties do not change after NaCl addition (red line) meaning that the G-quadruplex does not fold. Note that for both sequences two T bases are introduced as a spacer at the 5′-end and four T bases (HumTel) or one T base (RevHumTel), respectively, at the 3′-end. In this way, four bases are located on the 3′-end in-between the DNA origami platform and the first G-tetrad.

prominent efficiencies of energy transfer at the corresponding distances, FRET is a process used in artificial photosynthesis and photonic wires or networks with different fluorophores attached *e.g.* to DNA.[10,22,23] Furthermore, FRET plays an important role as a sensing tool for a variety of biologically relevant molecules such as antibodies, proteins, aptamers and even nanoparticles,[24–27] and for structure elucidation of macromolecules such as double stranded DNA and DNA nanostructures.[28–30] Especially for the study of macromolecular structures multi-color FRET plays a crucial role due to the possibility of modulating the optical signal over longer distances, *i.e.* beyond $2R_0$.[31–34]

Since FRET is a highly distance-dependent process, it is important to arrange the donor and acceptor molecules in a controlled way at well-defined distances. DNA origami nanostructures are excellent substrates to arrange and analyze different modifications with a high local control.[35–37] DNA origami structures can adopt various 2D and 3D shapes by folding a circular single stranded virus DNA (scaffold strand, here: M13mp18) through hybridization with a suitable set of short single DNA strands (staple strands, about 200 different strands).[1,35–37] Since every staple strand can be addressed separately and individually different modifications with predetermined distances can be introduced. Based on this property, DNA origami nanostructures have been used to investigate single-molecule chemical reactions,[38,39] radiation induced DNA strand breaks in different DNA sequences[40–43] and few-molecule detection using surface-enhanced Raman scattering (SERS).[44,45] DNA origami frames have also been used to study the folding and unfolding events of G-quadruplex structures *via* atomic force microscopy (AFM).[46–49]

Here, we present the preparation and characterization of a reversibly switchable three and four-color FRET cascade realized on DNA origami nanostructures. The telomeric DNA 5′-(GGG ATT)$_4$ is the middle element in the wire, and as already demonstrated, it assures reversible folding selective for K^+.[21] We also demonstrate that the ion-selectivity for K^+ depends strongly on the DNA sequence. To this end we investigate the G-quadruplex formation in human telomeric DNA (5′-(GGG TTA)$_4$, HumTel) and the reversed human telomeric DNA with the sequence 5′-(GGG ATT)$_4$ (RevHumTel) both attached to DNA origami nanostructures.

2. Results and discussion

2.1. The importance of the telomere sequence for ion-selectivity

The telomeric DNA sequences (HumTel or RevHumTel) are functionalized with an acceptor molecule (here: cyanine3, Cy3) at their 5′-end and prolonged with a staple strand to place them on DNA origami triangles. The donor molecule fluorescein (FAM) is placed 3.3 nm away from the 5′-end of the telomeric DNA by modifying one staple strand internally. Fluorescence measurements have been carried out in solution using steady-state and time-resolved spectroscopy (fluorescence decays and the corresponding decay times are shown in ESI Fig. S1†). The steady-state fluorescence spectroscopy results for both sequences are shown in Fig. 1. The emission spectra of HumTel are shown in Fig. 1A without salt (dotted line) and after KCl (dashed line) and NaCl (red line) addition. The fluorescence emission spectrum before salt addition (dotted line) exhibits high intensity at 515 nm (FAM) and a weak shoulder at 565 nm (Cy3). After salt addition (KCl or NaCl) the emission at 515 nm drops and the emission at 565 nm rises as a consequence of FRET. The FRET efficiency increases because of a decrease in the distance between the fluorophores due to a conformational change of the telomeric DNA from a random coil to the compact G-quadruplex structure. When HumTel is used, the G-quadruplex formation is observed in the presence of both K^+ and Na^+; however, for the reversed sequence RevHumTel, the observed effect is remarkably different. As the fluorescence emission spectra in Fig. 1B indicate, the FRET process, and thus the G-quadruplex

View Article Online
Nanoscale Paper

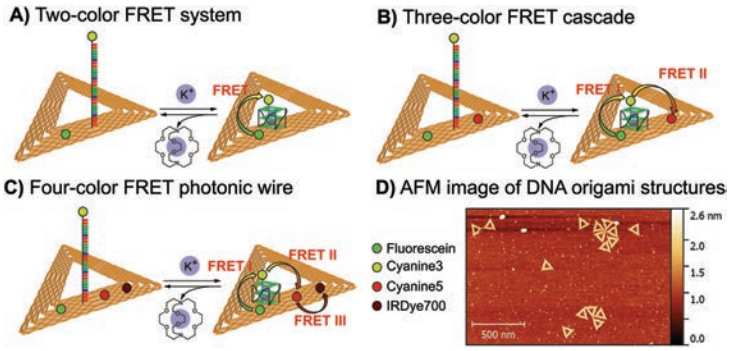

Fig. 2 Switchable FRET systems described in this work. (A) Two-color FRET system on DNA origami triangles with FAM (green circle) as the donor attached directly to the DNA origami structure and Cy3 (yellow circle) as the acceptor molecule attached to 5′-end of the telomeric DNA (5′-Cy3-TT $(GGG\ ATT)_4$T-staple strand, red = thymine, green = guanine, blue = adenine). The FRET process is turned on due to G-quadruplex formation induced by potassium ions. When [2.2.2]cryptand is added the G-quadruplex unfolds resulting in a decrease in FRET signals. (B) Three-color FRET cascade on DNA origami structures with FAM (green), Cy3 (yellow) and Cy5 (red) as donor, transmitter and acceptor molecules, respectively. Again, the G-quadruplex folds and unfolds by adding potassium ions and [2.2.2]cryptand, respectively. (C) Four-color FRET photonic wire on DNA origami structures with IRDye700 (dark red) as the final acceptor. Due to G-quadruplex formation the energy can be transferred from FAM to Cy3 to Cy5 and finally to IRDye700 with a total distance of 10 nm. The FRET cascade is turned off when the G-quadruplex is unfolded. (D) Typical AFM image of DNA origami structures on freshly cleaved mica.

folding, is only turned on after KCl addition (dashed line, see also Fig. S2†), but not after NaCl addition (red line). That is, only for RevHumTel on DNA origami platforms, the G-quadruplex folding is K^+ selective, whereas the HumTel sequence is sensitive for both Na^+ and K^+. The different selectivities can be ascribed to different 3D structures of the folded G-quadruplexes adopted by the two different sequences. Recently, it was demonstrated that subtle differences in the G-quadruplex forming sequence such as the sequence inversion from 5′–3′ to 3′–5′ can result in different G-quadruplex structures.[50] Some of these structures might be suppressed on DNA origami substrates. Selective K^+ sensing can be achieved even in solutions containing Na^+ at a concentration as high as 145 mM, which represents the concentration usually occurring under physiological conditions.[21] In the following experiments only RevHumTel is used. Other monovalent cations such as Na^+, Li^+, Cs^+ and NH_4^+ do not influence the FRET efficiency and therefore do not induce G-quadruplex formation (Fig. S2†). Divalent cations such as Mg^{2+} and Ca^{2+} can basically influence the FRET efficiency (Fig. S2†) and stabilize G-quadruplex structures.[51,52] However, since the $MgCl_2$ concentration for the DNA origami preparation is as low as 10 mM in the present case and does not increase throughout the experiments, only a small constant number of Mg^{2+} induced G-quadruplexes should be present.

2.2. Two-color FRET system

In order to explore the potential of RevHumTel to become a switch for a photonic cascade, the reversibility of G-quadruplex formation is extensively studied using fluorescence spectroscopy. To demonstrate that the G-quadruplex formation is reversible as shown in Fig. 2 we used a complexing agent, which has a higher affinity towards the central ion (here: K^+) rather than towards the G-quadruplex. When the agent is added the G-quadruplex unfolds and returns to its initial conformation. Typical complexing agents are for example crown ethers or cryptands. 18-Crown-6 is a well-known substance which can encapsulate K^+ (see ESI Fig. S3†). Since cryptands have a stronger binding to cations 4,7,13,16,21,24-hexaoxa-1,10-diazabicyclo[8.8.8]hexaco-sane, also known as [2.2.2] cryptand and in the following referred to as "cryptand", is used in our study. Cryptands are bi- and oligocyclic multidentate ligands, which can bind specific ions. In general, they are three dimensional molecules similar to crown ethers, but containing additionally two nitrogen atoms connected *via* ethyleneoxy bridges. These compounds can encapsulate metal ions with high selectivity.[53–55] The cryptand-induced switching phenomenon is analyzed in solution with steady-state (λ_{ex} = 450 nm) and time-resolved fluorescence spectroscopy (λ_{ex} = 490 nm, λ_{em} = 520 nm). The results for the two-color FRET system are shown in Fig. 3. In Fig. 3A the fluorescence emission spectra of the sample before and after KCl or cryptand addition are shown. The emission spectrum of the initial sample (blue spectrum, Fig. 3A) exhibits a strong peak at 515 nm from FAM. A very weak shoulder at 565 nm arising from Cy3 emission is also visible indicating that energy transfer occurs although the G-quadruplex is not folded, as the donor–acceptor distance is short enough for low-efficient FRET to occur. When 22 mM KCl is added to the sample the FAM emission is quenched, and at the same time the Cy3 emission is highly intensified (black spectrum, Fig. 3A) due to a shorter donor–acceptor distance resulting in a higher FRET efficiency. After adding 47 mM cryptand Cy3 emission decreases drastically and FAM emission increases slightly

View Article Online
Paper Nanoscale

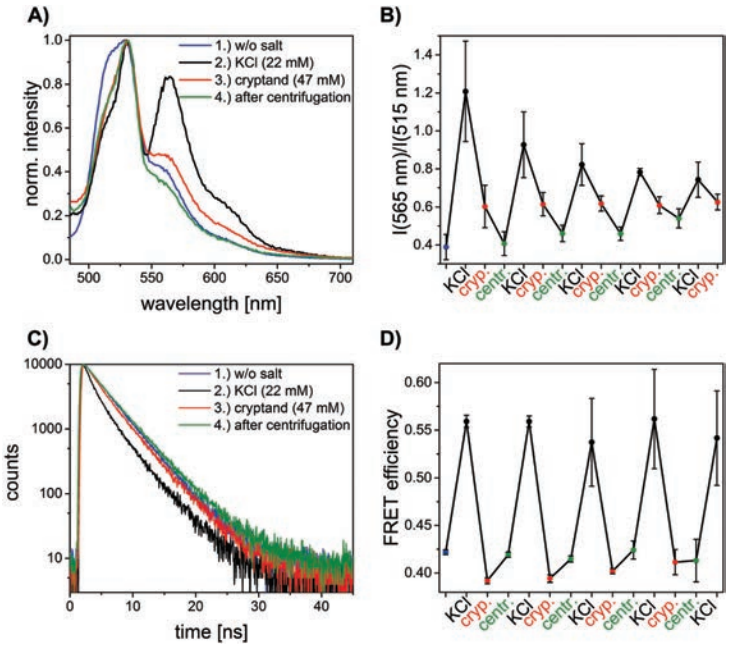

Fig. 3 Results for the two-color FRET system with FAM and Cy3 as donor and acceptor molecules (color code: blue = initial sample, black = after KCl addition, red = after cryptand addition, green = after centrifugation). (A) Normalized emission spectra excited at 450 nm. The emission intensity of FAM at 515 nm decreases and at the same time Cy3 emission at 565 nm increases after KCl addition due to G-quadruplex formation. After cryptand addition the FAM emission increases and Cy3 emission decreases again due to unfolding of the G-quadruplex. After centrifugation the emission properties of the sample are similar when compared to the starting point but the overall intensity is lower (Raman peak of water becomes more dominant at 530 nm). The decay associated spectra of the first switching cycle are shown in ESI Fig. S7 and S8.† (B) Acceptor–donor intensity ratio for one sample after subsequent KCl and cryptand addition. The ratio rises after KCl addition and drops after cryptand addition. The FRET process is turned on and off due to folding and unfolding of the G-quadruplex. (C) FAM fluorescence decay time (λ_{ex} = 490 nm, λ_{em} = 520 nm) decreases after KCl addition due to G-quadruplex formation. After cryptand addition the decay time increases again because the FRET process is turned off. The system is restored after centrifugation. (D) FRET efficiencies calculated with average FAM fluorescence decay times for one sample with subsequent KCl and cryptand addition. The switchable FRET system is based on G-quadruplex folding and unfolding. The G-quadruplex formation can be repeated 5 times on DNA origami structures.

(red spectrum, Fig. 3A). The FRET process is weakened or rather switched off due to G-quadruplex unfolding. The FAM emission does not return to its initial intensity because the cryptand quenches the FAM fluorescence (see ESI Fig. S4†). To repeat the folding of the G-quadruplex on DNA origami structures potassium chloride and cryptand are removed using 10 kDa molecular weight cut-off centrifugal filters and washing three times with TAE (1×) buffer containing 10 mM $MgCl_2$. The fluorescence spectrum of the sample after centrifugation is shown in Fig. 3A (green spectrum). The overall fluorescence intensity is lower because the total sample concentration decreases after centrifugation. It has to be noted that the peak at 530 nm is due to the Raman peak of water, which becomes visible due to the overall low fluorescence intensity of the sample. Decay associated spectra of the first switching cycle are shown in ESI Fig. S7 and S8.† The ratio of acceptor emission intensity (at 565 nm) to donor emission intensity (at 515 nm) changes due to the FRET process and can be used to monitor the changes occurring in the system (Fig. 3B). It increases due to G-quadruplex folding after the addition of KCl (black dots, Fig. 3B) and decreases due to G-quadruplex unfolding after cryptand addition (red dots, Fig. 3B). Because the cryptand quenches the FAM fluorescence, the acceptor–donor ratio does not return to its initial value after cryptand addition. Lower FAM emission intensity when compared to the initial point results in a higher ratio. After centrifugation KCl and cryptand are removed from the solution and the value virtually returns to its initial value. We demonstrate that the switching between the folded and unfolded state can be repeated 5 times on DNA origami structures in the two-color FRET system. The acceptor–donor ratio decreases step by step after each KCl/cryptand addition. This is attributed to a partial unfolding of the DNA origami structure induced by the cryptand, which might also capture Mg^{2+}. The removal of Mg^{2+} ions from the DNA structure results in a destabilization of the DNA origami triangles and thus to more free FAM labeled DNA strands in solution, which do not participate in the FRET process (see ESI, Fig. S5†). Since the emission intensity is highly dependent on the total sample concentration, time-resolved measurements were carried out

View Article Online
Nanoscale Paper

to overcome this drawback and to calculate the FRET efficiencies. Fluorescence decays are shown in Fig. 3C for a sample before (blue decay) and after KCl (black decay) and cryptand (red decay) addition. The FAM fluorescence decay time decreases drastically after KCl addition (black decay, Fig. 3C) due to higher FRET efficiencies and it increases again after cryptand addition (red decay, Fig. 3C). After centrifugation the fluorescence decay time is the same as the initial sample (green decay, Fig. 3C). The fluorescence decays have been fitted with a tri-exponential function with fixed τ-values (see ESI Table S1†). The decay time τ_1 is set to 1.6 ns and is attributed to FAM fluorescence in the folded species ($R_{\text{fold.}}$ = 6.0 nm), while τ_2 is set to 2.7 ns assigned to FAM fluorescence in the unfolded species ($R_{\text{unfold.}}$ = 7.2 nm). The donor–acceptor distance in the unfolded state is still short enough for FRET to take place with a low efficiency. The decay time τ_3 is equal to 4.4 ns and is due to the unquenched FAM, which does not take part in the FRET process (free strands or missing acceptor molecules on the DNA origami structure). The physical acceptor–donor distances R are determined using eqn (1) and (2).

$$E = 1 - \frac{\tau_{DA}}{\tau_D} \quad (1)$$

$$R = R_0 \sqrt[6]{\frac{1}{E} - 1} \quad (2)$$

τ_{DA} is the (average) FAM fluorescence decay time when FRET occurs and τ_D is the unquenched FAM fluorescence decay time. To calculate R, the Förster radius R_0 for the FRET pair is needed. The Förster radius is a FRET pair-specific physical donor–acceptor distance at which the FRET efficiency is equal to 50%. It depends on the spectral properties of donor and acceptor molecules.[56] For FAM and Cy3 the Förster radius is equal to 6.7 nm (see also ESI Table S2 and Fig. S5†). The determined donor–acceptor distances ($R_{\text{fold.}}$ = 6.0 nm; $R_{\text{unfold.}}$ = 7.2 nm) represent average values because the telomeric DNA and the G-quadruplex can rotate freely on the DNA origami structure. The amplitudes for each decay time component and the average fluorescence decay times for each step (KCl addition, cryptand addition and centrifugation) are shown in Table S1 in the ESI.† The amplitude of τ_3 increases continuously throughout repeating folding/unfolding cycles because the amount of free FAM–DNA-sequences increases as mentioned above (see also ESI Fig. S6†). Therefore, only the first two decay time components are taken into account to calculate the average decay time. Based on the average FAM fluorescence decay times the FRET efficiency is calculated using eqn (1). In Fig. 3D the FRET efficiencies are plotted *vs.* KCl and cryptand addition. In accordance with the experiments described above the FRET efficiency rises due to the G-quadruplex formation after the addition of KCl (black dots, Fig. 3D), and after cryptand addition the G-quadruplex unfolds and the FRET process is switched off (red dots, Fig. 3D). After centrifugation the initial FRET efficiency is reached and the FRET system is restored (green dots, Fig. 3D). The G-quadruplex folding–unfolding cycle is again repeated 5 times on DNA origami structures.

2.3. Switchable three-color FRET cascade

In the next step we introduced a third dye to realize a three-color FRET cascade, which can be switched on and off using the reversible G-quadruplex folding and unfolding. In this three-color FRET cascade FAM, Cy3 and cyanine5 (Cy5) are used as a donor, a transmitter and an acceptor, respectively (Fig. 2B). Cy3 is attached to the 5′-end of the telomeric DNA and FAM and Cy5 are placed 3.3 nm away from it on opposite sides (Fig. 2B). Since the spectral overlap between FAM and Cy5 is very small (see ESI Fig. S9†) FRET is unlikely to take place between these two dyes. Additionally, the donor–acceptor distance is around 7 nm, which makes FRET highly inefficient (see ESI Fig. S10A†). For FRET to take place, a third molecule (transmitter molecule) has to be introduced (here: Cy3). Because FAM/Cy3 and Cy3/Cy5 FRET pairs have larger spectral overlaps, FRET can take place from FAM to Cy3 followed by an energy transfer from Cy3 to Cy5 (see ESI Fig. S9†). This results in a FRET cascade, which can be excited at 450 nm (excitation wavelength for FAM) and can emit at 665 nm (Cy5). With such a FRET cascade longer inter-molecular distances (here: FAM-Cy5 $\approx$ 7 nm) can be achieved and a larger spectral range can be screened.

The results for the three-color FRET cascade on DNA origami structures are depicted in Fig. 4. In Fig. 4A the emission spectra of one sample before and after KCl and cryptand addition are shown. For the initial sample (without KCl), the FAM emission at 515 nm is rather strong and the Cy3 at 565 nm and Cy5 at 665 nm emissions are very weak (blue spectrum, Fig. 4A). After KCl addition (black spectrum, Fig. 4A) the FAM emission is quenched and the Cy3 and Cy5 emissions strongly increase due to FAM-to-Cy3 and Cy3-to-Cy5 FRET. Since the G-quadruplex is formed, the distance between each FRET pair decreases resulting in higher energy transfer efficiency. After cryptand addition the emission of Cy3 and Cy5 is clearly turned off (red spectrum, Fig. 4A) and the FAM emission becomes stronger. As observed for the two-color system, the FAM emission does not return to the initial value because of the quenching effect induced by the cryptand. After a centrifugation step (green spectrum, Fig. 4A) KCl and cryptand are removed and the system is restored, but the overall fluorescence intensity decreases. As was described before for the two-color FRET system the water Raman peak becomes more pronounced at 530 nm because the overall sample concentration is very low and the fluorescence emission intensity is weaker. In Fig. 4B the acceptor–donor intensity ratios determined for each FRET pair are shown (Cy3/FAM (squares) = I(565 nm)/I(515 nm); Cy5/Cy3 (circles) = I(665 nm)/I(565 nm); Cy5/FAM (triangles) = I(665 nm)/I(515 nm)). The different FRET pair curves exhibit a similar tendency. After the addition of 22 mM KCl (black points, Fig. 4B) the ratio increases drastically due to an increase in FRET efficiency. After the addition of 47 mM cryptand (red points, Fig. 4B) the ratio decreases because of the G-quadruplex unfolding. Similar to what was

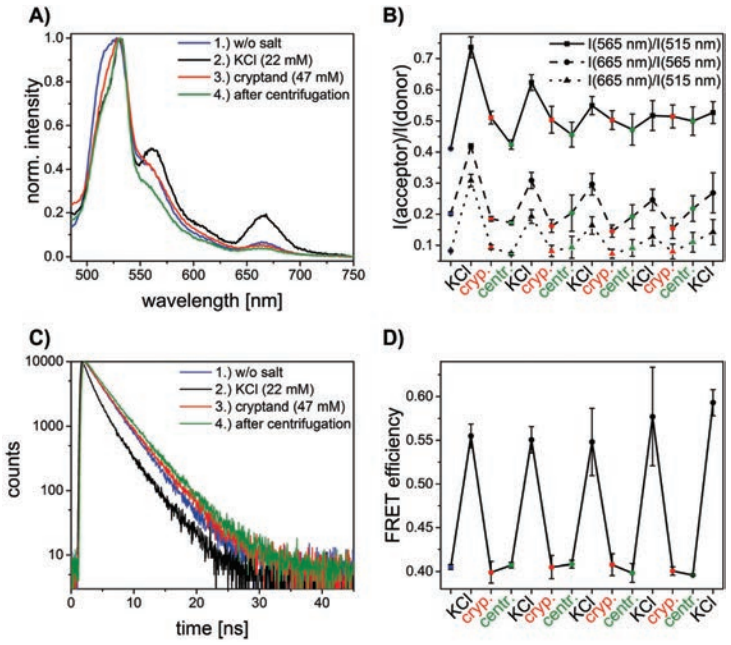

Fig. 4 Results of the three-color FRET system (donor: FAM, transmitter: Cy3, acceptor: Cy5) on DNA origami structures (color code: blue: initial sample, black: after KCl addition, red: after cryptand addition, green: after centrifugation). (A) Steady state emission spectra excited at 450 nm. The emissions of Cy3 at 565 nm and Cy5 at 665 nm increase and the FAM emission intensity at 515 nm decreases after KCl addition. After cryptand addition Cy3 and Cy5 emissions decrease and FAM emission increases again. The FRET cascade is switched off. After centrifugation the system is restored. The overall intensity decreases due to decreased sample concentration after the centrifugation step (Raman peak of water at 530 nm appears). (B) Repeated cycles of FRET switching represented with acceptor–donor intensity ratios (Cy3/FAM: *I*(565 nm)/*I*(515 nm) squares, Cy5/Cy3: *I*(665 nm)/*I*(565 nm) circles, Cy5/FAM: *I*(665 nm)/(515 nm) triangles). The acceptor–donor intensity ratios decrease after KCl addition due to G-quadruplex formation followed by an increase after cryptand addition due to G-quadruplex unfolding. After centrifugation the system is restored. (C) FAM decay time (λ_{ex} = 490 nm, λ_{em} = 520 nm) decreases after KCl addition due to G-quadruplex folding. After adding the cryptand, the decay time increases again because the FRET process is turned off. After centrifugation the system is restored. (D) FRET efficiencies calculated with average FAM fluorescence decay times. After the addition of KCl the FRET efficiency increases and it decreases again after cryptand addition. The system can be restored by centrifugation. The G-quadruplex formation can be repeated 5 times in a three-color FRET cascade on DNA origami structures.

described before for the two-color FRET system, the intensity ratio for all FRET pairs does not return to its initial value after cryptand addition. The FAM fluorescence decays for one folding–unfolding cycle are depicted in Fig. 4C. The fluorescence decay time decreases after the addition of KCl (black decay, Fig. 4C) compared to the fluorescence decay time of the initial sample (blue decay, Fig. 4C). After cryptand addition the fluorescence decay time increases again (red decay, Fig. 4C) because of G-quadruplex unfolding and increasing donor–transmitter–acceptor distances. The FAM fluorescence decay curves were fitted just as the two-color FRET system and the amplitudes for each decay time and the average decay times are shown in Table S1 in the ESI.† The Cy3 fluorescence decay times are shown in Fig. S11 of the ESI.† The FRET efficiencies were calculated using eqn (1) and are shown in Fig. 4D. The FRET efficiency rises after the addition of KCl (black dots, Fig. 4D) and the FRET cascade is turned off after the addition of cryptand (red dots, Fig. 4D) since the transmitter dye is moved away from the acceptor. The three color FRET cascade is again turned on 5 times.

2.4. Four-color FRET photonic wire

Finally, we introduce a fourth dye to the FRET cascade to exploit the full potential of the telomeric FRET switch on DNA origami structures. The design of the four-color FRET photonic wire is basically the same as the three-color FRET cascade but with IRDye700 as an additional acceptor molecule placed 3.3 nm away from Cy5 (see Fig. 2). In this photonic wire the energy is transferred from FAM to Cy3 followed by an energy transfer to Cy5 and finally to IRDye700 (see also ESI Fig. S12 and S13†). With such a photonic wire an inter-molecular distance of *ca.* 10 nm is achieved. This system is excited at 450 nm (FAM excitation) and it emits at 710 nm (IRDye700 emission) when the G-quadruplex is folded.

The results of one switching cycle based on the four-color FRET photonic wire are shown in Fig. 5 and S12† to show the basic mechanism. For the initial sample, FAM emission at 515 nm is dominant and the emission intensities of Cy3 at 565 nm, Cy5 at 665 nm and IRDye700 at 710 nm are rather weak (blue spectrum, Fig. 5). The FRET cascade is turned on

View Article Online
Nanoscale Paper

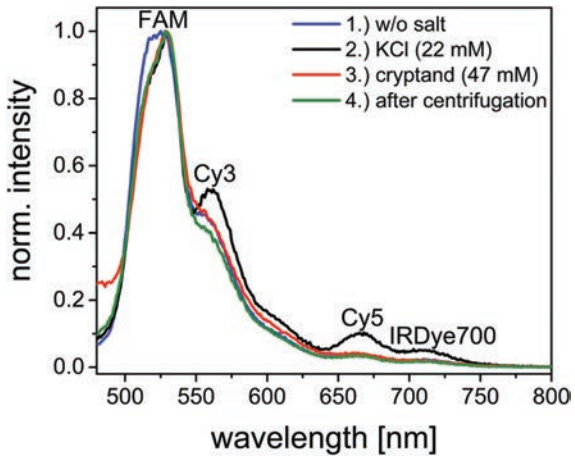

Fig. 5 One switching cycle for the four-color photonic wire (donor: FAM, transmitter1: Cy3, transmitter2: Cy5, acceptor: IRDye700, λ_{ex} = 450 nm) on DNA origami structures (color code: blue: initial sample, black: after KCl addition, red: after cryptand addition, green: after centrifugation). After KCl addition the emissions of Cy3 (565 nm), Cy5 (665 nm) and IRDye700 (710 nm) increase and FAM emission (515 nm) decreases because of the G-quadruplex formation. This photonic wire can be turned off after cryptand addition (G-quadruplex unfolds).

after KCl addition leading to a decrease of FAM emission and at the same time an increase in Cy3, Cy5 and IRDye700 emissions (black spectrum, Fig. 5). The distances between each FRET pair are reduced resulting in higher FRET efficiencies. The energy transfer cascade is turned off again after cryptand addition due to unfolding of the G-quadruplex. Thus, the Cy3, Cy5 and IRDye700 emissions are turned off. The FAM emission does not return to its initial value (as already observed for the two- and three-color FRET systems) because the cryptand quenches the FAM emission (red spectrum, Fig. 5). The system is restored after a centrifugation step (green spectrum, Fig. 5). Again, the water Raman peak becomes visible at 530 nm because the overall sample concentration decreases after centrifugation and therefore the overall fluorescence intensity decreases.

3. Conclusions

In this paper, we present a comprehensive comparison of two different telomeric DNA strands (HumTel and RevHumTel) with respect to their ion-selective G-quadruplex formation using FRET. We have shown that HumTel, when immobilized on DNA origami structures, folds into G-quadruplex structures both in the presence of Na^+ and K^+. RevHumTel on the other hand is selective for K^+ only when attached to DNA origami triangles. Furthermore, we have analyzed the switching between folded and unfolded G-quadruplex structures for RevHumTel. We have realized a highly ion-selective and restorable, reversible nanophotonic FRET switch on DNA origami structures based on a two-color FRET system (FAM–Cy3–FRET). Additionally, we developed a switchable photonic wire on DNA origami structures using three and four different fluorophores (FAM-to-Cy3-to-Cy5-to-IRDye700 FRET cascade). We have shown that the G-quadruplex formation can be repeated up to 5 times. The unique properties of telomeric DNA (conformational switching and ion-selectivity) combined with the excellent possibilities of DNA origami structures to assemble different moieties at defined distances give the opportunity to design and further extend the applications of functional DNA nanostructures towards new nanophotonic systems such as light harvesting antennae, photonic wires and networks and chemically triggered logic gates or nanosensors with an optical readout.

4. Experimental section

4.1. Chemicals

Unmodified oligonucleotides (used as staple strands) were purchased from Integrated DNA Technologies (Leuven, Belgium). The viral genome M13mp18 (scaffold strand) was purchased from tilbit nanosystems GmbH (Garching, Germany). The oligonucleotides modified with the organic dyes (fluorescein, cyanine3, cyanine5) were acquired from Metabion International AG (Planegg/Steinkirchen, Germany). The modified oligonucleotides have been purified by the manufacturer using HPLC and have been used as delivered. Magnesium chloride, potassium chloride, sodium chloride, 4,7,13,16,21,24-hexaoxa-1,10-diazabicyclo[8.8.8]hexacosane and Tris acetate-EDTA buffer (TAE buffer) were acquired from Sigma Aldrich (Taufkirchen, Germany). Diluted TAE buffer (1×) (pH = 8.2) contained 40 mM Tris-acetate and 1 mM EDTA.

4.2. DNA origami preparation

The DNA origami structures were prepared by mixing the staple strands (150 nM) with the single stranded M13mp18 viral genome (5 nM) in TAE buffer (10×) containing 100 mM $MgCl_2$ and ultrapure water (Millipore). This mixture was heated up to 80 °C and then slowly cooled down to 8 °C in 2 h (80 °C–66 °C: 1 °C every 30 s; 66 °C–25 °C: 1 °C every 2 min, 25 °C–8 °C: 1 °C every 1 min) using a thermal cycler (PEQLAB, Germany). After the annealing process, the solutions were purified *via* a 100 kDa molecular weight cut-off centrifugal filter (Millipore) with TAE buffer (1×) containing 10 mM $MgCl_2$ (4 × 3214*g* for 10 min).

4.3. G-quadruplex folding/unfolding

After the preparation of DNA origami triangles a KCl, NaCl or cryptand solution (c = 200 mM, 2 M in ultrapure water (Millipore)) was added and the samples were shaken for 15 min at 40 °C to fold (KCl, NaCl) and unfold (cryptand) the G-quadruplexes on DNA origami structures. After KCl/cryptand addition the sample was purified *via* a 10 kDa molecular weight cut-off centrifugal filter (Millipore) with TAE buffer (1×) containing 10 mM $MgCl_2$ (3 × 3800*g* for 7 min) to remove KCl and cryptand. Steady-state and time-resolved fluorescence

View Article Online
Paper Nanoscale

spectroscopy was performed after each KCl and cryptand addition and centrifugation step at DNA origami concentration of *ca*. 5 nM.

4.4. Atomic force microscopy (AFM)

To investigate the correctly formed DNA origami structures, AFM was performed for each sample after the preparation. AFM imaging was done with a Flex AFM (Nanosurf, Germany). A Tap150 Al-G cantilever (Budget Sensors, Sofia, Bulgaria) with a resonance frequency of (125–160) kHz and a spring constant of 5 N m^{-1} was used to visualize the DNA origami structures. The samples were prepared on freshly cleaved mica (Plano GmbH, Germany). For this, 2 µl of the sample (*ca*. 20 nM) and 33 µl of TAE (1×) containing 10 mM $MgCl_2$ were incubated for 30 s and subsequently washed twice with 1 ml of ultrapure water (Millipore). Afterwards, the fluid was removed with compressed air. The measurements were performed in air using the phase contrast mode. The measured triangles have a length of 100–150 nm and a height of 1–2 nm (see Fig. 2). The yield of correctly formed DNA origami structures has been determined from AFM images to be about 95%.

4.5. Steady-state fluorescence spectroscopy

Steady-state fluorescence spectroscopy measurements were done using a FluoromaxP fluorescence spectrophotometer (HORIBA Jobin Yvon GmbH, Germany) with 3 mm quartz cuvettes. The measurements were performed in a 90° angle acquisition using the system-internal quantum correction. The excitation wavelength for all emission spectra was set to 450 nm. For the measurements an increment of 1 nm and integration time of 0.2 s were chosen and the bandpass was set to 5 nm for both emission and excitation.

4.6. Time-resolved fluorescence spectroscopy

Time-correlated single photon counting (TCSPC) measurements were performed on a FLS920 Fluorescence spectrophotometer (Edinburgh Instruments, UK) using 3 mm quartz cuvettes. The samples were measured in a 90° setup using a white light source (SC-400-PP supercontinuum-source, Fianium: 0.5–20 MHz, 400 nm < l < 24 000 nm, pulse width: *ca*. 30 ps) as the excitation source and a Multi-Channel-Plate (ELDY EM1-132/300, Europhoton GmbH, Berlin) as the detector. The excitation wavelength was set to 490 nm and the emission wavelength was set to 520 nm. The fluorescence decay curves were fitted with a tri-exponential function (eqn (3)) using FAST software (Edinburgh Instruments, UK).

$$I(t) = A_0 + A_1 e^{\frac{-t}{\tau_1}} + A_2 e^{\frac{-t}{\tau_2}} + A_3 e^{\frac{-t}{\tau_3}} \quad (3)$$

A_0 is the background or dark current, τ_1, τ_2 and τ_3 are the decay times and A_1, A_2 and A_3 are the amplitudes characteristic for each decay time. The different decay time components were set to specific values for different species. τ_1 is equal to 1.4 ns and belongs to the folded state, τ_2 is set to 2.7 ns and belongs to the unfolded G-quadruplex and τ_3 is equal to 4.4 ns belonging to the unquenched donor dye. The average fluorescence decay time $\bar{\tau}_{DA}$ was calculated with eqn (4).

$$\bar{\tau}_{DA} = \frac{\tau_1 \cdot A_1 + \tau_2 \cdot A_2}{A_1 + A_2} \quad (4)$$

Acknowledgements

This research was supported by the Deutsche Forschungsgemeinschaft (DFG), a Marie Curie FP7 Integration Grant within the 7th European Union Framework Programme, by the University of Potsdam, the Federal Institute for Materials Research (BAM), and the DFG project GSC 1013 (SALSA).

References

1 W. K. P. Rothemund, *Nature*, 2006, **440**, 297–302.
2 Z.-G. Wang and B. Ding, *Acc. Chem. Res.*, 2014, **47**, 1654–1662.
3 T. Tørring, N. V. Voigt, J. Nangreave, H. Yan and K. V. Gothelf, *Chem. Soc. Rev.*, 2011, **40**, 5636–5646.
4 Y. R. Yang, Y. Liu and H. Yan, *Bioconjugate Chem.*, 2015, **26**, 1381–1395.
5 R. Schreiber, J. Do, E.-M. Roller, T. Zhang, V. J. Schüller, P. C. Nickels, J. Feldmann and T. Liedl, *Nat. Nanotechnol.*, 2014, **9**, 74–78.
6 Z. Deng, A. Samanta, J. Nangreave, H. Yan and Y. Liu, *J. Am. Chem. Soc.*, 2012, **134**, 17424–17427.
7 T. L. Doane, R. Alam and M. M. Maye, *Nanoscale*, 2015, **7**, 2883–2888.
8 C. M. Spillmann, M. G. Ancona, S. Buckhout-White, W. R. Algar, M. H. Stewart, K. Susumu, A. L. Huston, E. R. Goldman and I. L. Medintz, *ACS Nano*, 2013, **7**, 7101–7118.
9 C. M. Spillmann, S. Buckhout-White, E. Oh, E. R. Goldman, M. G. Ancona and I. L. Medintz, *Chem. Commun.*, 2014, **50**, 7246.
10 S. Buckhout-White, C. M. Spillmann, W. R. Algar, A. Khachatrian, J. S. Melinger, E. R. Goldman, M. G. Ancona and I. L. Medintz, *Nat. Commun.*, 2014, **5**, 5615.
11 W. Su, V. Bonnard and G. A. Burley, *Chem. – Eur. J.*, 2011, **17**, 7982–7991.
12 B. Albinsson, J. K. Hannestad and K. Börjesson, *Coord. Chem. Rev.*, 2012, **256**, 2399–2413.
13 F. Wang, X. Liu and I. Willner, *Angew. Chem., Int. Ed.*, 2015, **54**, 1098–1129.
14 S. Neidle and G. N. Parkinson, *Curr. Opin. Struct. Biol.*, 2003, **13**, 275–283.
15 Y. Krishnan and F. C. Simmel, *Angew. Chem., Int. Ed.*, 2011, **50**, 3124–3156.
16 B. Ge, Y. C. Huang, D. Sen and H.-Z. Yu, *Angew. Chem., Int. Ed.*, 2010, **49**, 9965–9967.

17 T. Li, S. Dong and E. Wang, *J. Am. Chem. Soc.*, 2010, **132**, 13156–13157.
18 B. Saccà, B. Siebers, R. Meyer, M. Bayer and C. M. Niemeyer, *Small*, 2012, **8**, 3000–3008.
19 Y. Hu, F. Wang, C.-H. Lu, J. Girsh, E. Golub and I. Willner, *Chem. – Eur. J.*, 2014, **20**, 16203–16209.
20 L. Hu, X. Liu, A. Cecconello and I. Willner, *Nano Lett.*, 2014, **14**, 6030–6035.
21 L. Olejko, P. J. Cywinski and I. Bald, *Angew. Chem. Int. Ed.*, 2015, **54**, 673–677.
22 P. D. Cunningham, A. Khachatrian, S. Buckhout-White, J. R. Deschamps, E. R. Goldman, I. L. Medintz and J. S. Melinger, *J. Phys. Chem. B*, 2014, **118**, 14555–14565.
23 P. K. Dutta, R. Varghese, J. Nangreave, S. Lin, H. Yan and Y. Liu, *J. Am. Chem. Soc.*, 2011, **133**, 11985–11993.
24 P. J. Cywiński, L. Olejko and H.-G. Löhmannsröben, *Anal. Chim. Acta*, 2015, **887**, 209–215.
25 P. J. Cywinski, T. Hammann, D. Hühn, W. J. Parak, N. Hildebrandt and H.-G. Löhmannsröben, *J. Biomed. Opt.*, 2014, **19**, 101506.
26 P. J. Cywiński, K. Nchimi Nono, L. J. Charbonnière, T. Hammann and H.-G. Löhmannsröben, *Phys. Chem. Chem. Phys.*, 2014, **16**, 6060–6067.
27 H. Härmä, S. Pihlasalo, P. J. Cywinski, P. Mikkonen, T. Hammann, H.-G. Löhmannsröben and P. Hänninen, *Anal. Chem.*, 2013, **85**, 2921–2926.
28 S. Kalinin, T. Peulen, S. Sindbert, P. J. Rothwell, S. Berger, T. Restle, R. S. Goody, H. Gohlke and C. A. M. Seidel, *Nat. Methods*, 2012, **9**, 1218–1225.
29 I. H. Stein, V. Schüller, P. Böhm, P. Tinnefeld and T. Liedl, *ChemPhysChem*, 2011, **12**, 689–695.
30 E. S. Andersen, M. Dong, M. M. Nielsen, K. Jahn, R. Subramani, W. Mamdouh, M. M. Golas, B. Sander, H. Stark, L. P. C Oliveira, J. S. Pedersen, V. Birkedal, F. Besenbacher, K. V. Gothelf and J. Kjems, *Nature*, 2009, **459**, 73–76.
31 S. Hohng, C. Joo and T. Ha, *Biophys. J.*, 2004, **87**, 1328–1337.
32 A. Kienzler, R. Flehr, R. A. Kramer, S. Gehne, M. U. Kumke and W. Bannwarth, *Bioconjugate Chem.*, 2011, **22**, 1852–1863.
33 S. Gehne, R. Flehr, A. Altevogt, M. Berg, W. Bannwarth and M. U. Kumke, *J. Phys. Chem. B*, 2012, **116**, 10798–10806.
34 I. H. Stein, C. Steinhauer and P. Tinnefeld, *J. Am. Chem. Soc.*, 2011, **133**, 4193–4195.
35 M. Endo, Y. Yang and H. Sugiyama, *Biomater. Sci.*, 2013, **1**, 347.
36 A. Rajendran, M. Endo and H. Sugiyama, *Angew. Chem. Int. Ed.*, 2012, **51**, 874–890.
37 I. Bald and A. Keller, *Molecules*, 2014, **19**, 13803–13823.
38 S. Helmig, A. Rotaru, D. Arian, L. Kovbasyuk, J. Arnbjerg, P. R. Ogilby, J. Kjems, A. Mokhir, F. Besenbacher and K. V. Gothelf, *ACS Nano*, 2010, **4**, 7475–7480.
39 N. V. Voigt, T. Tørring, A. Rotaru, M. F. Jacobsen, J. B. Ravnsbaek, R. Subramani, W. Mamdouh, J. Kjems, A. Mokhir, F. Besenbacher and K. V. Gothelf, *Nat. Nanotechnol.*, 2010, **5**, 200–203.
40 S. Vogel, J. Rackwitz, R. Schürmann, J. Prinz, A. R. Milosavljevic, M. Refregiers, A. Giuliani and I. Bald, *J. Phys. Chem. Lett.*, 2015, **6**, 4589–4593.
41 A. Keller, J. Rackwitz, E. Cauët, J. Liévin, T. Körzdörfer, A. Rotaru, K. V. Gothelf, F. Besenbacher and I. Bald, *Sci. Rep.*, 2014, **4**, 7391.
42 A. Keller, J. Kopyra, K. V. Gothelf and I. Bald, *New J. Phys.*, 2013, **15**, 83045.
43 A. Keller, I. Bald, A. Rotaru, E. Cauët, K. V. Gothelf and F. Besenbacher, *ACS Nano*, 2012, **6**, 4392–4399.
44 J. Prinz, C. Heck, L. Ellerik, V. Merk and I. Bald, *Nanoscale*, 2016, **8**, 5612–5620.
45 J. Prinz, B. Schreiber, L. Olejko, J. Oertel, J. Rackwitz, A. Keller and I. Bald, *J. Phys. Chem. Lett.*, 2013, **4**, 4140–4145.
46 Y. Sannohe, M. Endo, Y. Katsuda, K. Hidaka and H. Sugiyama, *J. Am. Chem. Soc.*, 2010, **132**, 16311–16313.
47 A. Rajendran, M. Endo, K. Hidaka, P. L. T. Tran, J.-L. Mergny, R. J. Gorelick and H. Sugiyama, *J. Am. Chem. Soc.*, 2013, **135**, 18575–18585.
48 A. Rajendran, M. Endo, K. Hidaka and H. Sugiyama, *Angew. Chem.*, 2014, **126**, 4191–4196.
49 A. Rajendran, M. Endo, K. Hidaka, P. L. T. Tran, M.-P. Teulade-Fichou, J.-L. Mergny and H. Sugiyama, *RSC Adv.*, 2014, **4**, 6346.
50 M. Marušič and J. Plavec, *Angew. Chem., Int. Ed.*, 2015, **54**, 11716.
51 Y.-Y. Yan, J. Lin, T.-M. Ou, J.-H. Tan, D. Li, L.-Q. Gu and Z.-S. Huang, *Biochem. Biophys. Res. Commun.*, 2010, **402**, 614–618.
52 B. Kankia, *Sci. Rep.*, 2015, **5**, 12996.
53 K. E. Krakowiak, J. S. Bradshaw, H.-Y. An and R. M. Izatt, *Pure Appl. Chem.*, 1993, **65**, 511–516.
54 P. Müller, *Pure Appl. Chem.*, 1994, **66**, 1077–1184.
55 *IUPAC Compendium of Chemical Terminology*, ed. M. Nič *et al.*, IUPAC, Research Triangle Park, NC, 2009.
56 T. Förster, *Ann. Phys.*, 1948, **437**, 55–75.

Electronic Supplementary Information (ESI)

Ion-controlled three-color fluorescent telomeric switch on DNA origami

L. Olejko[a, b, c], P. J.Cywiński[d, e] and I. Bald[a, c]

[a.] Department of Chemistry, Physical Chemistry, University of Potsdam, Karl-Liebknecht Str. 24-25, 14476 Potsdam, Germany

[b.] School of Analytical Sciences Adlershof, Humboldt-Universität zu Berlin, Unter den Linden 6, 10099, Germany

[c.] BAM Federal Institute for Materials Research and Testing, Richard-Willstätter Str. 11, 12489 Berlin, Germany

[d.] Fraunhofer IAP, Geiselbergstrasse 69, 14476 Potsdam, Germany

[e.] Institute of Physical Chemistry, Polish Academy of Sciences, Kasprzaka 44/53, 01-224 Warsaw, Poland

HumTel and RevHumTel on DNA origami structures

FAM fluorescence decays for HumTel and RevHumTel on DNA origami structures are shown in Fig. S1. The fluorescence decay time for HumTel (blue decay, τ = 3.2 ns) decreases after KCl (black decay, τ = 1.5 ns) and NaCl (brown decay, τ = 1.6 ns) addition (Fig. S1 A). The G-quadruplex folds in presence of both salts. For RevHumTel on the other hand the fluorescence decay time is only influenced by KCl (without salt: blue decay, τ = 3.1 ns; KCl: black decay, τ = 1.8 ns; NaCl: brown decay, τ = 2.9 ns, (Fig. S1 B)). RevHumTel attached to DNA origami structures is selective for K^+. The G-quadruplex cannot fold in presence of Na^+ on DNA origami structures.

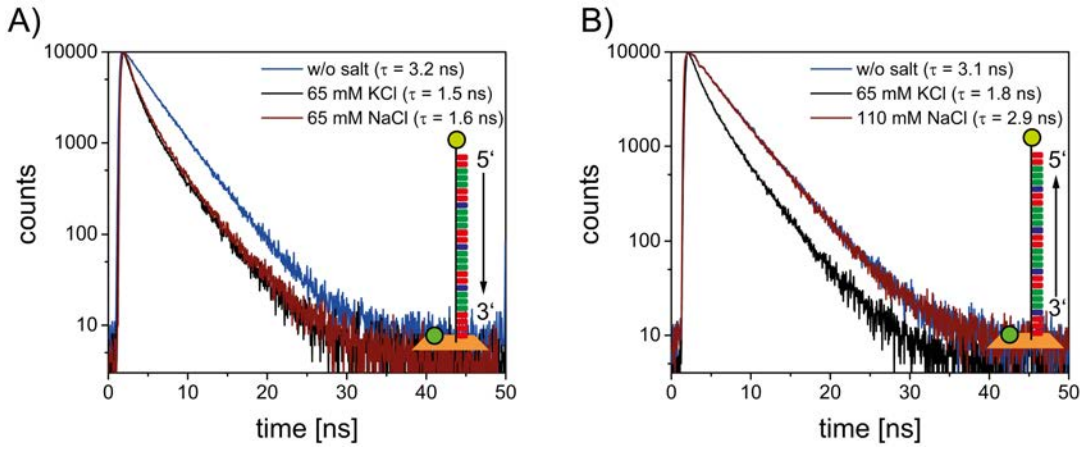

Fig. S 1 *FAM fluorescence decays (λ_{ex} = 490 nm, λ_{em} = 520 nm) for DNA origami triangles modified with two different telomeric DNA sequences: HumTel (A) and RevHumTel (B) before (blue) and after KCl (black) and NaCl (brown) addition. RevHumTel folds into G-quadruplex structures only in presence of KCl (NaCl does not influence FAM fluorescence decay time).*

Ion-selectivity of RevHumTel on DNA origami structures

The reversed human telomere shows a high selectivity only for KCl. Other monovalent cations such as Na^+, Li^+, Cs^+ and NH_4^+ do not influence the FRET efficiency and therefore do not induce G-quadruplex formation (Fig. S2). Divalent cations such as Mg^{2+} and Ca^{2+} influence the FRET efficiency (Fig. S2) and stabilize G-quadruplex structures.[1,2] Since the $MgCl_2$ concentration for the DNA origami preparation is as low as 10 mM in the present case and does not increase throughout the experiments, only a small constant number of Mg^{2+}-induced G-quadruplexes is present.

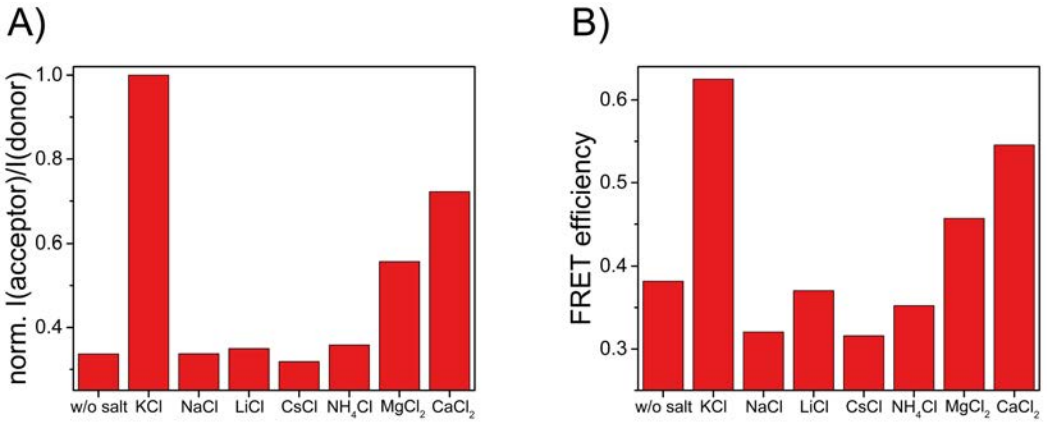

Fig. S 2 *RevHumTel shows a high selectivity towards potassium. The FRET process is only turned on after KCl addition. Other monovalent cations (Na^+, Li^+, Cs^+ and NH_4^+) do not induce a G-quadruplex formation. Only divalent cations such as Mg^{2+} and Ca^{2+} have an influence on the FRET process. A) Results for steady state fluorescence measurements (λ_{ex} = 450 nm). Normalized donor-acceptor-ratios (I(565 nm/I(515 nm) after the addition of 110 mM salt (except $MgCl_2$: 120 mM). B) FRET efficiencies calculated with FAM decay times after salt addition (c = 110 mM, except $MgCl_2$: c = 120 mM).*

G-quadruplex unfolding using 18-crown-6

In this study, we use cryptand to remove K^+ and unfold the G-quadruplex. Other complexing agents can also be used such as 18-crown-6. This crown ether can also encapsulate K^+ and therefore unfold the G-quadruplex. Steady state and time-resolved fluorescence data for one switching cycle using 18-crown-6 in the two-color FRET system are shown in Fig. S3. To unfold the G-quadruplex and turn off the energy transfer from FAM to Cy3 comparatively high amounts of 18-crown-6 are needed (for 22 mM KCl 130 mM 18-crown-6). Therefore, cryptand is used in this study to unfold the G-quadruplex.

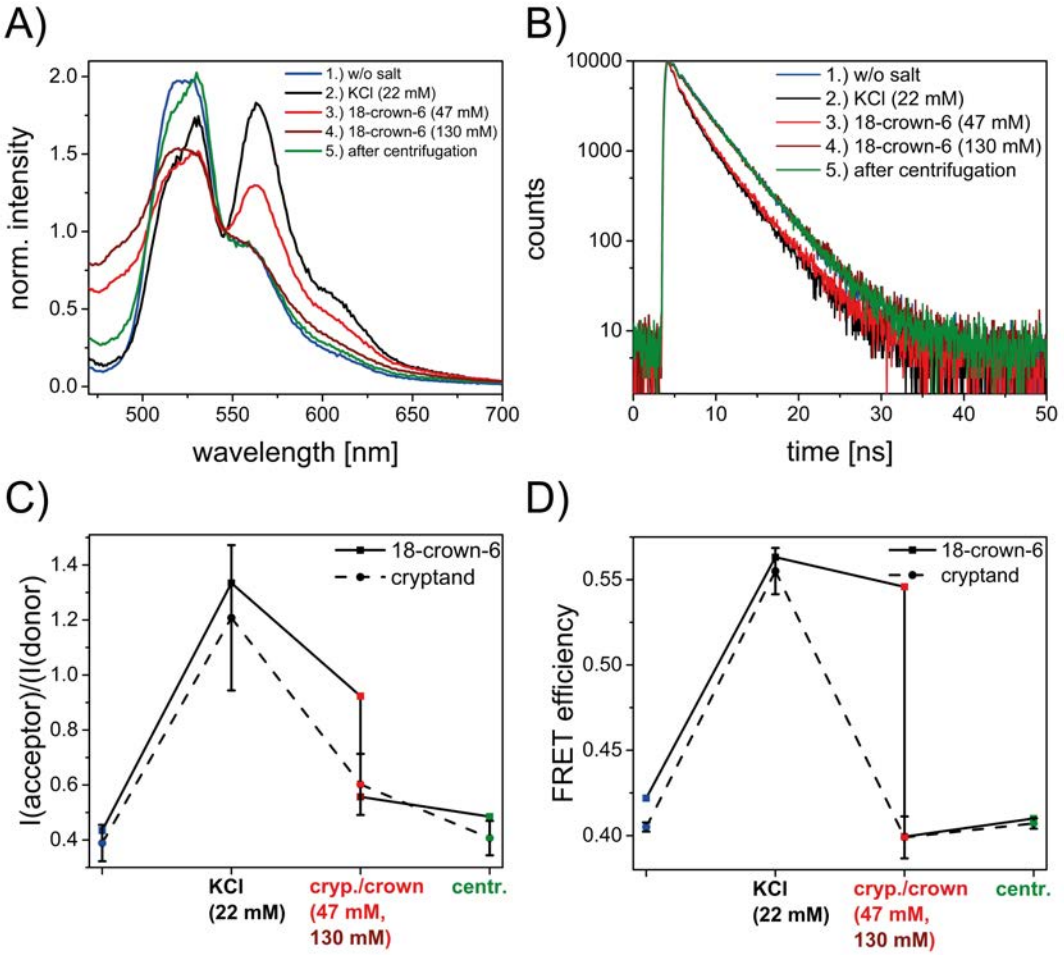

Fig. S 3 *FRET switching of two-color FRET system using 18-crown-6. A) Normalized emission spectra (λ_{ex} = 450 nm) before (blue), after KCl (black) and after 18-crown-6 (47 mM: red; 130 mM: brown) addition and after centrifugation (green). The G-quadruplex unfolds after 18-crown-6 addition and the FRET process is turned off. A high concentration of 18-crown-6 is needed to unfold the G-quadruplex. B) Fluorescence decays (λ_{ex} = 490 nm, λ_{em} = 520 nm) before (blue), after KCl (black) and after 18-crown-6 (47 mM: red, 130 mM: brown) addition and after centrifugation (green). C) Comparison of donor-acceptor ratios (I(565 nm)/I(515 nm)) after cryptand and 18-crown-6 addition. A lower concentration of cryptand is needed to unfold the G-quadruplex. D) FRET efficiencies calculated with FAM fluorescence decay times. Again, a lower concentration of cryptand is needed to unfold the G-quadruplex. Therefore, cryptand is used to perform further experiments.*

Influence of cryptand on FAM fluorescence

DNA origami structures modified only with FAM are analyzed after one cycle of KCl/cryptand addition. The fluorescence emission spectra and decays (Fig. S4) show that the FAM fluorescence is quenched after cryptand addition. The FAM emission intensity drops (Fig. S4 A, red) and the FAM fluorescence decay time decreases from 4.4 ns to 4.0 ns after cryptand addition (Fig. S4 B).

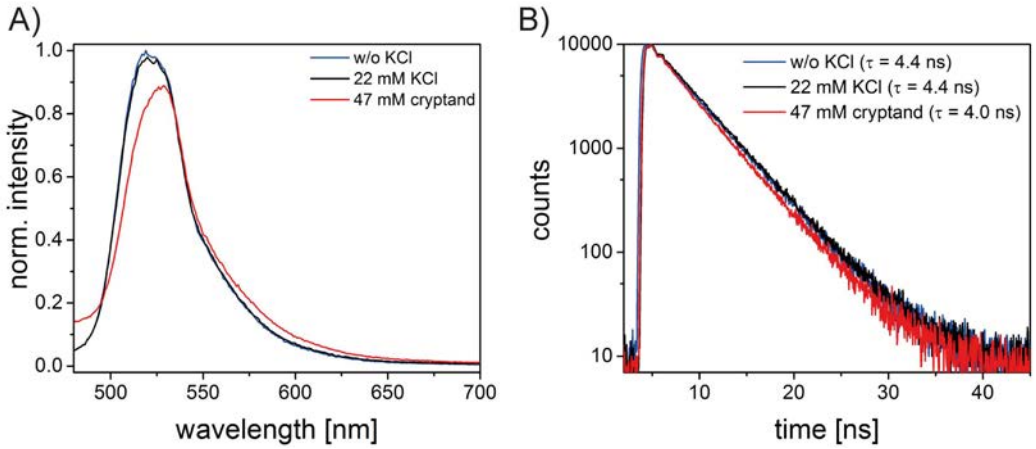

Fig. S 4 *Influence of cryptand on FAM fluorescence properties. A) Normalized emission spectra (λ_{ex} = 450 nm) of one sample before (blue), after KCl addition (black) and cryptand addition (red). The emission intensity decreases after cryptand addition. B) FAM fluorescence decays of one sample before (blue), after KCl (black) and after cryptand addition (red).*

Influence of cryptand on stability of DNA origami structures

For one sample the centrifugation step was carried out with a 100 kDa molecular weight cut-off filter instead of a 10 kDa molecular weight cut-off filter. The average fluorescence decay times of FAM and amplitudes of each decay time component are shown in Fig. S5. By using a 100 kDa molecular weight cut-off filter free DNA staple strands are removed from the solution (this is not the case when a 10 kDa molecular weight cut-off filter is used, 10 kDa < M(staple DNA) < 100 kDa). This can be confirmed with the time-resolved measurements. In Fig. S5 A the average FAM fluorescence decay time using all three decay time components is plotted.

$$\bar{\tau} = \frac{A_1 \cdot \tau_1 + A_2 \cdot \tau_2 + A_3 \cdot \tau_3}{A_1 + A_2 + A_3} \qquad (1)$$

The average fluorescence decay time decreases after KCl addition and it increases after cryptand addition. Furthermore, the amplitude of each decay time component is plotted in Fig. S5 B. It shows that the amplitude of the third decay time does not increase throughout repeating folding and unfolding cycles. In case of centrifugation steps using 10 kDa molecular weight cut-off filters the amplitude of the third decay time component increases continuously throughout the folding/unfolding experiments (see Fig. S6).

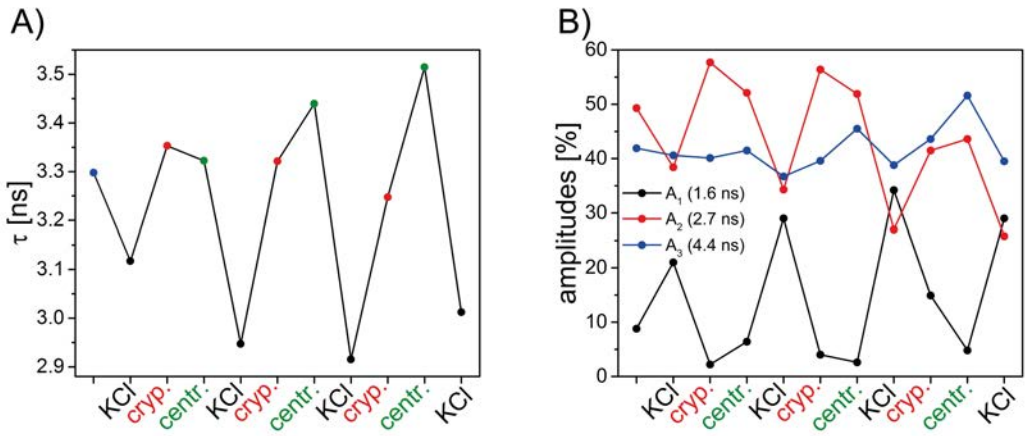

Fig. S 5 *Time-resolved measurements for centrifugation steps using 100 kDa molecular weight cut-off filter. A) Average fluorescence decay time calculated using all three decay time components. B) Amplitudes of each decay time component ($A_1 \rightarrow \tau_1$ (black); $A_2 \rightarrow \tau_2$ (red); $A_3 \rightarrow \tau_3$ (blue)).*

FAM fluorescence decay time

An overview of all determined fluorescence decay times and amplitudes for the two-color and three-color FRET systems are shown in Table S1. Additionally, the amplitudes for each fluorescence decay time component (two-color and three-color FRET systems) are plotted in Fig. S6. The diagrams show that the amplitude for the third decay time component (unquenched FAM) increases continuously throughout repeated folding-unfolding-cycles. This indicates that the DNA origami structures might dissociate and more free FAM labeled DNA strands are present.

Table S 1 *Overview of measured FAM fluorescence decay times. The fluorescence decay curves were fitted tri-exponentially with fixed τ values. The amplitudes for each decay time (A_1: τ_1 = 1.6 ns; A_2: τ_2 = 2.7 ns; A_3: τ_3 = 4.4 ns) and the average decay times calculated with the first two decay time components $\left(\bar{\tau} = \frac{A_1\tau_1 + A_2\tau_2}{A_1 + A_2}\right)$ for the two-color FRET system and three-color FRET cascade are depicted (with standard deviation of three separate measurements). The fluorescence decay times were measured at a KCl concentration of 22 mM and cryptand concentration of 47 mM.*

	Two-color FRET system				Three-color FRET cascade			
	A_1 [%]	**A_2 [%]**	**A_3 [%]**	**$\bar{\tau}$ [ns]**	**A_1 [%]**	**A_2 [%]**	**A_3 [%]**	**$\bar{\tau}$ [ns]**
	8.2 ± 0.9	49.6 ± 0.9	42.1 ± 1.8	2.54 ± 0.01	6.0 ± 0.9	74.3 ± 0.3	19.7 ± 1.2	2.62 ± 0.01
KCl	43.5 ± 3.1	19.4 ± 1.1	37.1 ± 2.4	1.94 ± 0.03	53.2 ± 4.4	25.6 ± 4.2	21.2 ±0.3	1.96 ± 0.06
crypt.	1.2 ± 0.6	52.3 ± 1.3	46.5 ± 1.6	2.68 ± 0.01	3.2 ± 3.2	59.8 ± 2.6	37.0 ±1.5	2.64 ± 0.05
centri.	6.0 ± 0.8	39.6 ± 3.9	54.4 ± 4.5	2.56 ± 0.01	4.8 ± 0.7	52.6 ± 0.5	42.7 ± 0.2	2.61 ± 0.01
KCl	28.5 ± 2.8	12.8 ± 2.0	58.6 ± 4.5	1.94 ± 0.03	28.1 ± 1.6	15.1 ± 4.5	56.8 ± 6.1	1.98 ± 0.07
crypt.	1.3 ± 0.6	39.8 ± 4.2	58.9 ± 4.1	2.67 ± 0.02	3.3 ± 2.3	41.5 ± 4.5	55.1 ± 4.1	2.62 ± 0.06
centri.	4.2 ± 0.9	33.2 ± 5.9	62.6 ± 6.7	2.58 ± 0.01	3.4 ± 1.0	35.3 ± 4.2	61.2 ± 5.1	2.60 ± 0.02
KCl	13.9 ± 7.2	8.2 ± 2.5	77.9 ± 5.6	2.04 ± 0.20	16.6 ± 2.8	9.3 ± 4.6	74.1 ± 3.1	1.99 ± 0.17
crypt.	2.2 ± 0.6	33.1 ± 2.1	64.7 ± 2.7	2.63 ± 0.01	3.5 ± 2.4	35.5 ± 3.8	61.0 ± 6.2	2.61 ± 0.05
centri.	4.3 ± 0.8	25.3 ± 8.4	70.4 ± 8.6	2.53 ± 0.04	1.3 ± 1.2	24.7 ± 5.9	74.1 ± 6.2	2.65 ± 0.04
KCl	13.2 ± 9.5	4.5 ± 3.1	82.3 ± 8.0	1.93 ± 0.22	13.2 ± 5.5	3.7 ± 3.5	83.1 ± 2.2	1.86 ± 0.25
crypt.	3.5 ± 2.3	30.0 ± 2.1	66.5 ± 4.3	2.59 ± 0.06	1.6 ± 0.6	26.6 ± 0.1	71.8 ± 0.5	2.64 ± 0.02
centri.	2.1 ± 1.8	19.8 ± 6.6	78.1 ± 5.8	2.58 ± 0.10	0.5 ± 0.1	12.7 ± 1.3	86.8 ± 1.4	2.66 ± 0.01
KCl	10.4 ± 9.5	5.3 ± 2.8	84.3 ± 11.2	2.02 ± 0.22	12.6 ± 3.1	2.8 ± 1.8	84.6 ± 4.8	1.79 ± 0.06

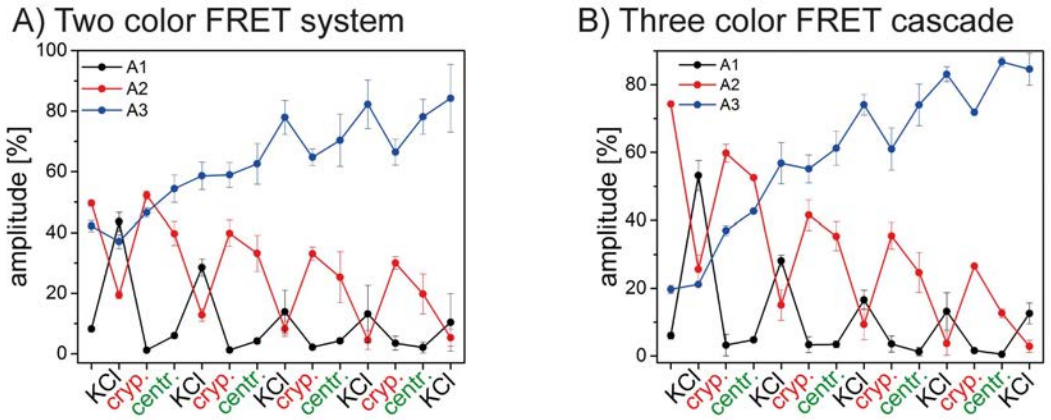

Fig. S 6 *Amplitudes of each fluorescence decay time component (A_1→ τ_1 (black); A_2→ τ_2 (red); A_3→ τ_3 (blue)) for the two-color FRET system (A) and three-color FRET cascade (B). The amplitude of A_3 increases throughout repeated folding and unfolding due to increasing amounts of free FAM labeled DNA strands.*

Decay associated spectra

Decay associated spectra are determined for the two-color FRET system to resolve the different contributions of the fluorescence emission spectra. The data are shown in Fig. S7 and Fig. S8. Fluorescence decay times have been measured at different emission wavelengths with an excitation

wavelength of 490 nm. The fluorescence decays are fitted tri-exponentially with fixed τ values for specific fluorescence decay times of FAM and Cy3, respectively. Since theses fluorescence decay times vary depending on KCl/cryptand concentration the fluorescence decays were fitted with different fixed decay time components (w/o salt/after centrifugation: τ_1(Cy3) = 1.9 ns, τ_2(FAM) = 2.7 ns, τ_3(FAM) = 4.4 ns; KCl: τ_1(FAM) = 1.6 ns, τ_2(Cy3) = 2.5 ns, τ_3(FAM) = 4.4 ns; cryptand: τ_1(Cy3) = 2.3 ns, τ_2(FAM) = 2.7 ns, τ_3(FAM) = 4.4 ns). The amplitudes for each decay time component are plotted in Fig. S7. The amplitudes of each decay time component are then multiplied with the normalized steady state emission spectra to obtain the deconvolved emission spectra (see Fig. S8). The acceptor-donor fluorescence intensity ratios are calculated based on the deconvolved data (Fig S8 D). The absolute values differ slightly from the raw data but the overall behavior stays the same. Thus, all other ratios are calculated based on raw data.

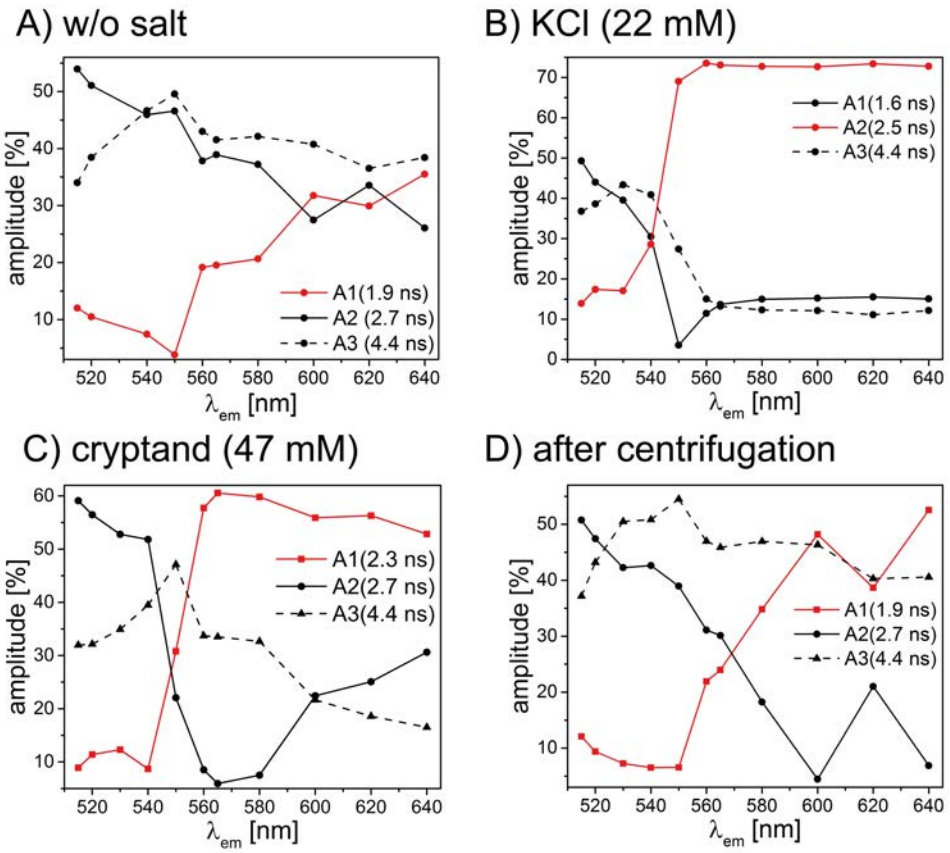

Fig. S 7 *Decay associated spectra of two-color FRET system of initial sample (A), after KCl addition (B), after cryptand addition (C) and after centrifugation (D). Amplitudes plotted for different decay time components (black: FAM: initial sample/cryptand/after centrifugation (unfolded telomere): τ_1 = 2.7 ns; KCl (folded G-quadruplex): τ_1 = 1.6 ns; unquenched FAM: τ_3 = 4.4 ns; red: Cy3: initial sample/after centrifugation: τ_1 = 1.9 ns; after KCl: τ_2 = 2.5 ns; after cryptand: τ_1 = 2.3 ns).*

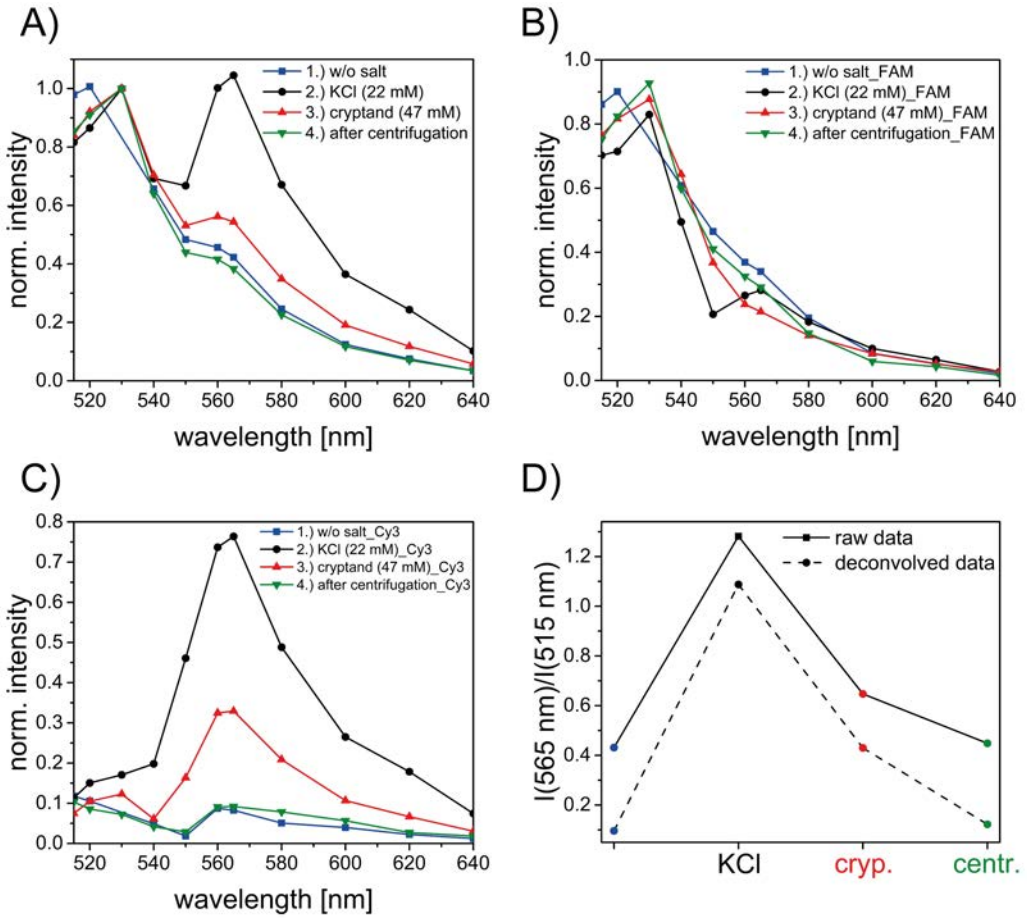

Fig. S 8 *Deconvolved emission spectra of two-color FRET system for one folding/unfolding cycle. Color code: blue: initial sample, black: after KCl addition, red: after cryptand addition, green: after centrifugation. A) Normalized steady state emission spectra without deconvolution. B) Deconvolved emission spectra for FAM. In the black spectrum a shoulder belonging to Cy3 is still visible. Peak at 530 nm belongs to the water Raman peak. C) Deconvolved Cy3 emission spectra. Emission belonging to Cy3 only is visible. D) Acceptor-donor ratios calculated with raw data (solid line) and deconvolved data (dashed line). Only the total values differ but not the overall behavior.*

FRET calculations

FRET is a non-radiative energy transfer from an excited donor to an acceptor molecule through dipole-dipole interactions. For FRET to take place two main conditions need to be fulfilled. Firstly, the donor's emission spectrum has to overlap with the acceptor's absorption spectrum (resonance condition, see Fig. S9). Secondly, the FRET pair needs to be in close proximity for FRET to take place. The FRET efficiency *E* is highly distance dependent and behaves according to the following equation.

$$E = \frac{R_0^6}{R_0^6 + R^6} \tag{2}$$

Here, *R* is the donor-acceptor distance and R_0 the Förster radius. The Förster radius is a FRET pair specific parameter at which the FRET efficiency is equal to 50 %. It depends on the spectral properties of donor and acceptor molecule and can be calculated using the following equations 3 and 4.

$$R_0^6 = \frac{9(ln10)\kappa^2 Q_D J}{128\pi^5 n^4 N_{AV}} \tag{3}$$

Where κ^2 is the dipole orientation factor, Q_D is the fluorescence quantum yield of the donor molecule when the acceptor is absent, N_{AV} is Avogadro's number, *n* is the medium's refractive index and *J* is the

spectral overlap integral representing the overlap of donor's emission and acceptor's absorption spectra. The spectral overlap integral is calculated using the following equation 4.

$$J(\lambda) = \int F_D(\lambda) \cdot \varepsilon(\lambda) \cdot \lambda^4 \, d\lambda \quad (4)$$

Here, $F_D(\lambda)$ is the normalized fluorescence emission spectrum of the donor at particular wavelength, $\epsilon(\lambda)$ is the acceptor's extinction coefficient spectrum in $l \cdot mol^{-1} \cdot cm^{-1}$ and λ is the wavelength in nm. The dipole orientation factor κ^2 takes on values between 0 and 4. For freely rotating molecules with a rotation rate much faster than the donor's de-excitation rate, κ^2 is equal to 2/3. [3–6]

The software PhotochemCAD 2.1 is used to calculate the spectral overlap integrals *J* and the Förster radius R_0 for each FRET pair (FAM-Cy3, Cy3-Cy5, FAM-Cy5, FAM-IRDye700, Cy3-IRDye700, Cy5-IRDye700). The desired spectra for the different FRET pairs (donor's emission spectrum and acceptor's absorption spectrum in terms of extinction coefficient, Fig. S9 A-F) are imported and the dipole orientation factor ($\kappa^2 = 2/3$), the refraction index (n = 1.33) and the specific quantum yield of the donor molecule ($Q(FAM)$ = 0.90; $Q(Cy3)$ = 0.15; Q(Cy5) = 0.30)[7] are used as inputs in the software. The calculated Förster radii are listed in Table S2.

FRET between FAM and Cy5 at a distance of ~7 nm is highly inefficient as shown in Fig. S10 (blue). Thus, Cy3 has to be introduced as a transmitter dye so that the energy is transferred from FAM to Cy3 followed by an energy transfer from Cy3 to Cy5.

Table S 2 *Overview of donor's quantum yield (Q_D), spectral overlap integral ($J(\lambda)$) and Förster radii (R_0) for the different FRET pairs.*

FRET-pair	Q_D[7]	$J(\lambda)$ **[nm⁴ · l · mol⁻¹]**	R_0 **[nm]**
FAM-Cy3	0.90	$5.6 \cdot 10^{15}$	6.7
Cy3-Cy5	0.15	$7.4 \cdot 10^{15}$	5.2
FAM-Cy5	0.90	$3.1 \cdot 10^{15}$	6.1
FAM-IRDye700	0.90	$0.9 \cdot 10^{15}$	5.0
Cy3-IRDye700	0.15	$3.3 \cdot 10^{15}$	4.6
Cy5-IRDye700	0.30	$21.2 \cdot 10^{15}$	7.2

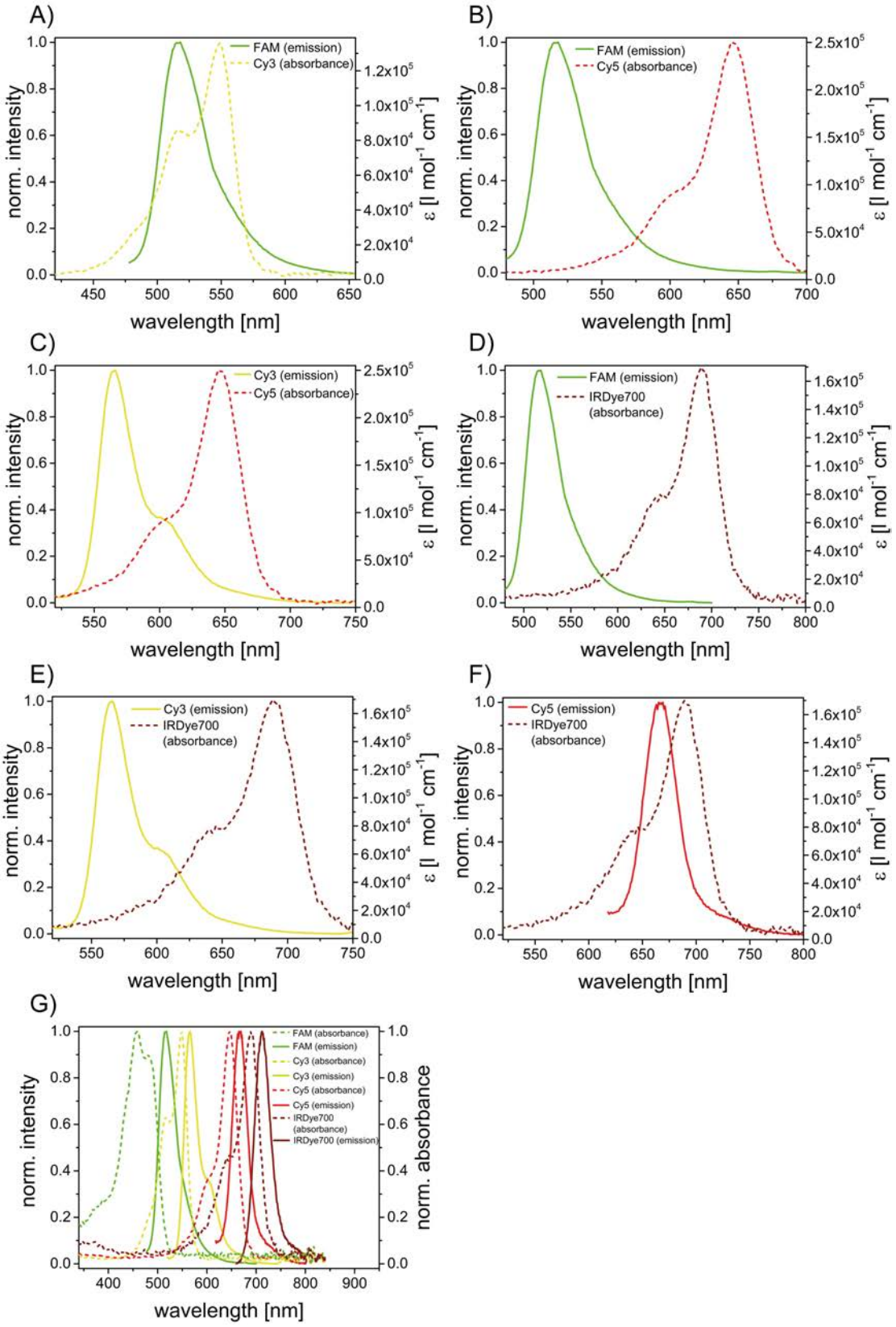

Fig. S 9 *Spectral overlap for each FRET pair (emission spectrum: solid line, absorption spectrum: dashed line). A) Large spectral overlap between FAM emission (donor, green) and Cy3 absorption spectra (acceptor, yellow). B) Small spectral overlap between FAM emission (donor, green) and Cy5 absorption spectra (acceptor, red). C) Large spectral overlap between Cy3*

emission (donor, yellow) and Cy5 absorption spectra (acceptor, red). D) Small spectral overlap between FAM emission (donor, green) and IRDye700 absorption spectra (acceptor, dark red). E) Small spectral overlap between Cy3 emission (donor, yellow) and IRDye700 absorption spectra (acceptor, dark red). F) Large spectral overlap between Cy5 emission (donor, red) and IRDye700 absorption spectra (acceptor, dark red). G) Spectral overlap of organic dyes used for the different FRET systems. Absorption (dashed line) and emission (solid line) spectra for donor molecule FAM (green), acceptor/transmitter molecule Cy3 (yellow), acceptor/transmitter molecule Cy5 (red) and acceptor molecule IRDye700 (dark red).

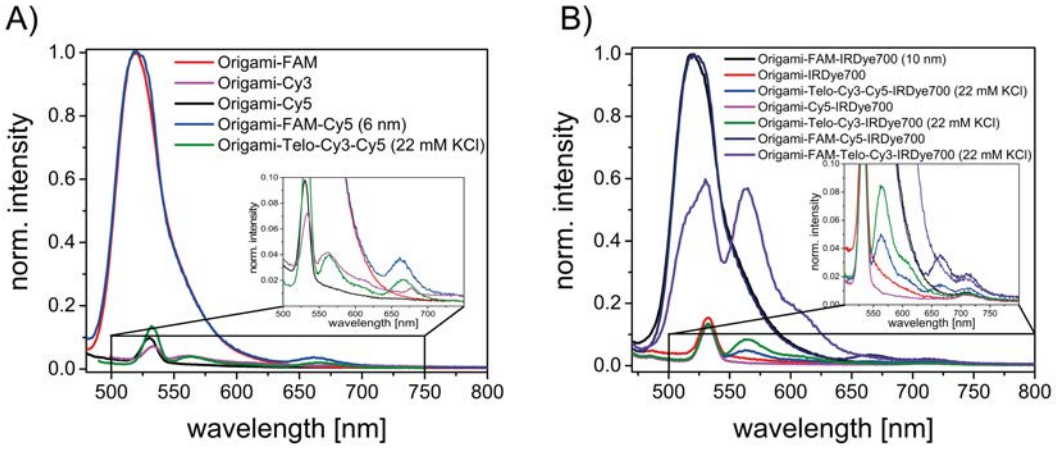

Fig. S 10 *Normalized emission spectra (λ_{ex} = 450 nm) for DNA origami structures modified with different organic dyes. A) Control experiments for two- and three-color FRET cascade for DNA origami structures modified with FAM (red), Cy3 (pink), Cy5 (black), FAM-Cy5 (blue) and RevHumTel-Cy3-Cy5 (green). Direct excitation of organic dyes other than FAM is neglectable. Weak emission of Cy5 at 665 nm in FAM-Cy5-sytsem (blue) is visible due to low energy transfer efficiency from FAM to Cy5. B) Control experiments for four-color FRET system. FAM-IRDye700 (black), IRDye700 (red), RevHumTel-Cy3-Cy5-IRDye700 (blue), Cy5-IRDye700 (pink), RevHumTel-Cy3-IRDye700 (green), FAM-Cy5-IRDye700 (dark blue), FAM-RevHumTel-Cy3-IRDye700 (violet). Direct excitation at 450 nm of organic dyes other than FAM is neglectable.*

Cy3 fluorescence decay time (three-color FRET cascade)

The Cy3 fluorescence decay time is analyzed in the three-color FRET cascade. The analysis of Cy3 fluorescence decay time is not trivial because it is influenced by many factors (G-quadruplex, FRET (enhancement by FAM, quenching by Cy5)). The fluorescence decay time of only Cy3 attached to the telomeric DNA on DNA origami structures increases significantly after KCl addition and decreases again after cryptand addition and centrifugation. The Cy3 fluorescence is known to be influenced by G-quadruplex structures due to association with the G-quadruplex.[8] The fluorescence decays of Cy3 are fitted bi-exponentially (τ_1 = 1.17 ns; τ_2 = 2.72 ns) and an average decay time based on the amplitudes is calculated. The decay curves and fluorescence decay times of origami structures only modified with Cy3 are plotted in Fig. S11 A-B. The fluorescence decay curves of Cy3 in the three-color FRET cascade are fitted tri-exponentially (τ_1 = 0.57 ns (FRET-component); τ_2 = 1.17 ns (Cy3); τ_3 = 2.72 ns (Cy3)) and the average fluorescence decay time is calculated based on the amplitudes. The fluorescence decay times are plotted in Fig. S11. The FRET efficiencies are calculated using equation 5.

$$E = 1 - \frac{\tau_{DA}}{\tau_D}, \qquad (5)$$

where τ_{DA} is the average fluorescence decay time when FRET occurs and τ_D is the Cy3 fluorescence decay time without FAM and Cy5 being present. Since τ_D depends strongly on KCl and cryptand the FRET efficiencies are calculated with the Cy3 fluorescence decay times measured in presence of KCl/cryptand (τ_D(KCl) = 2.6 ns; τ_D(cryptand) = 2.3 ns; τ_D(before/after centrifugation) = 1.9 ns) assuming that the Cy3 fluorescence decay time does not change throughout repeated folding/unfolding cycles. The calculated FRET efficiencies are plotted in Fig. S11 D. It has to be noted that since the Cy3 fluorescence decay time is highly influenced by KCl/cryptand addition and Cy3 and

Cy5 fluorescence decay times are quite similar (τ(Cy3) ≈ 2.2 ns, τ(Cy5) = 2.0 ns) the determined FRET efficiencies are somewhat error prone.

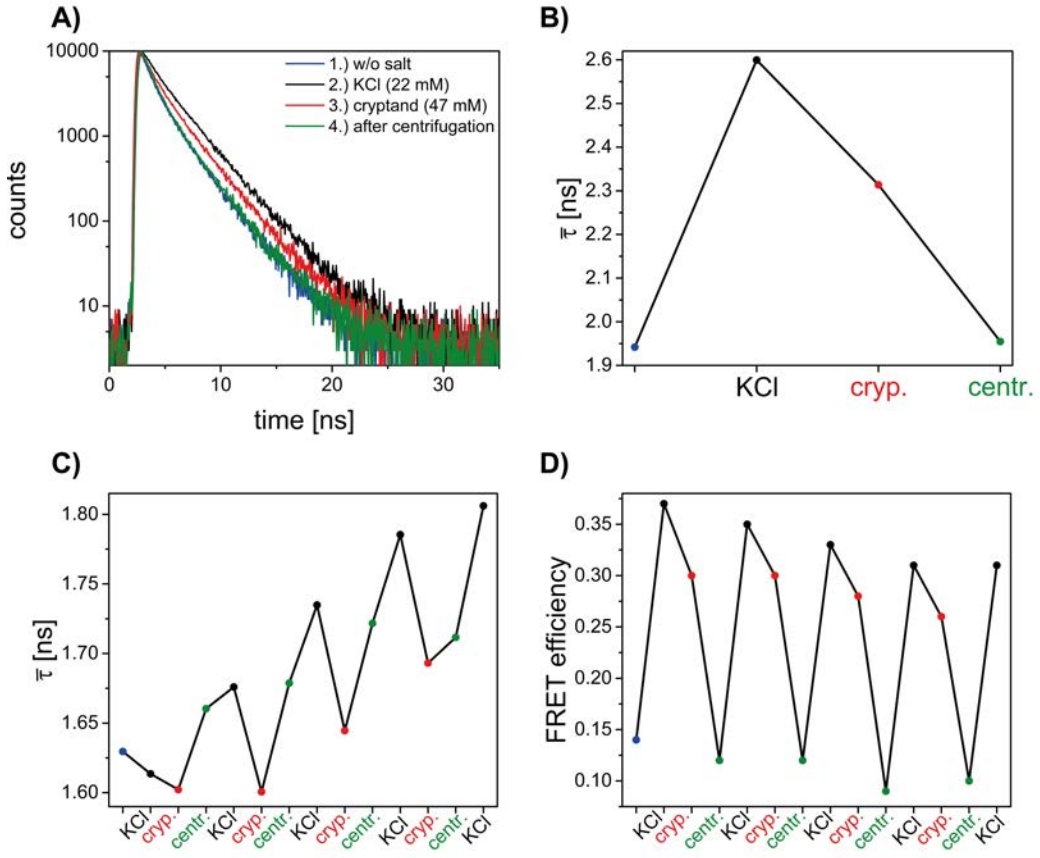

Fig. S 11 *Determination of Cy3 fluorescence decay times (λ_{ex} = 545 nm; λ_{em} = 565 nm). A) Fluorescence decays of DNA origami structures modified with Cy3 attached to RevHumTel. B) Determined fluorescence decay times of Cy3 attached to RevHumTel and immobilized on DNA origami structures. The Cy3 fluorescence decay time is highly influenced by KCl/cryptand addition. C) Average Cy3 fluorescence decay time of Cy3 in the three-color FRET cascade. D) FRET efficiencies calculated based on Cy3 fluorescence decay times.*

Four-color FRET photonic wire

To generally show the switching behavior of the four-color photonic wire two switching cycles are performed and shown in Fig. S12. The donor-acceptor ratios of each FRET pair (I(Cy3)/I(FAM); I(Cy5)/I(Cy3); I(Cy5)/I(FAM); I(IRDye700)/I(Cy5); I(IRDye700)/I(Cy3) and I(IRDye700)/I(FAM)) are shown in Fig. S12 B. Similar to the two- and three-color FRET systems they increase after KCl addition because of G-quadruplex formation and decrease after cryptand addition. The folding of the G-quadruplex can be repeated after centrifugation. It has to be noted that the IRDye700-Cy5-ratio behaves different than the others. This is because the distance between IRDye700 and Cy5 does not change during the G-quadruplex folding and unfolding process. Therefore, the overall FRET efficiency between these two dyes stays the same and only the Cy5 emission increases more strongly. FAM and Cy3 fluorescence decay times behave similarly compared to the three-color FRET system. The FAM fluorescence decay times and the FRET efficiencies based on FAM fluorescence decay times are exemplary shown in Fig. S12 C-D. Control experiments are shown in Fig. S13 to show that the FRET cascade is only efficient if all four organic dyes are present.

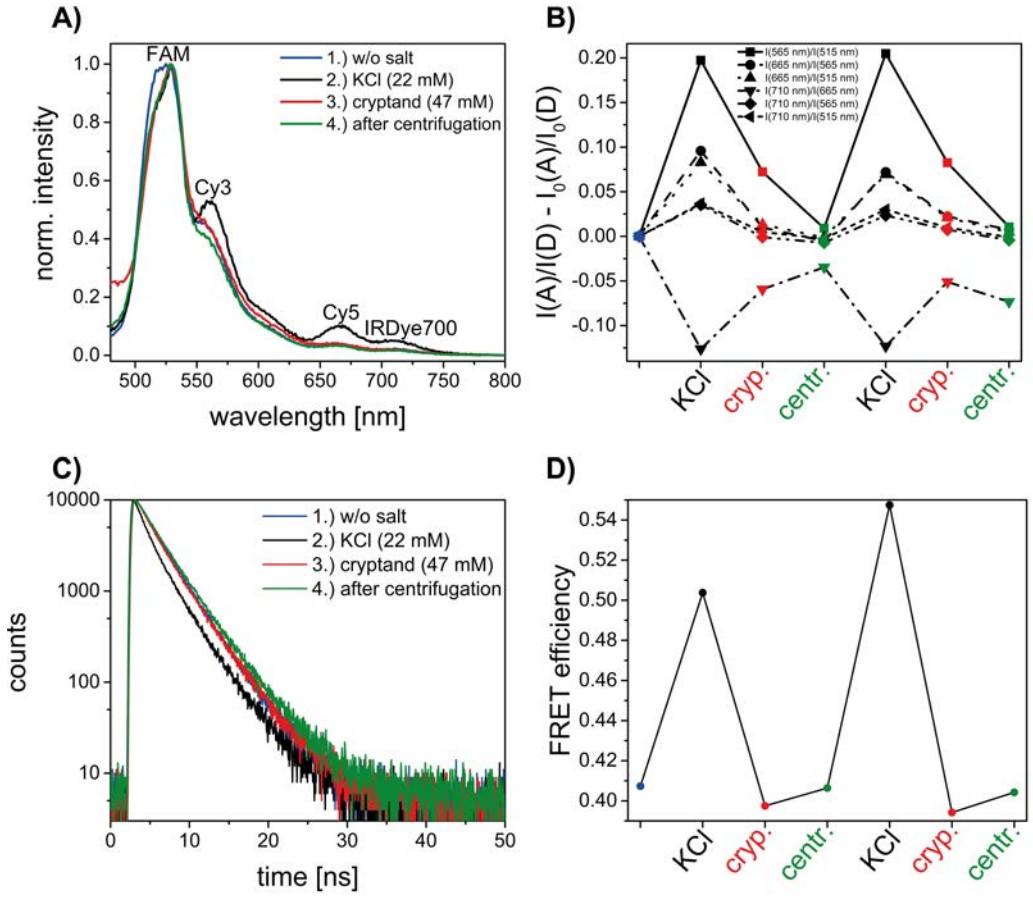

Fig. S 12 *Results for the four-color FRET photonic wire on DNA origami structures. A) emission spectra excited at 450 nm for one switching cycle (blue: initial sample, black: KCl, red: cryptand, green: after centrifugation). B) Calculated acceptor-donor ratios for each dye-pair. The ratios increase after KCl addition due to G-quadruplex formation and they decrease after cryptand addition due to G-quadruplex unfolding. The switching can be repeated. C) FAM fluorescence decay curves (λ_{ex} = 490 nm, λ_{em} = 520 nm) (blue: initial sample, black: KCl, red: cryptand, green: after centrifugation). D) FRET efficiencies based on FAM fluorescence decay times. The FRET efficiencies increase and decrease after KCl and cryptand addition, respectively*

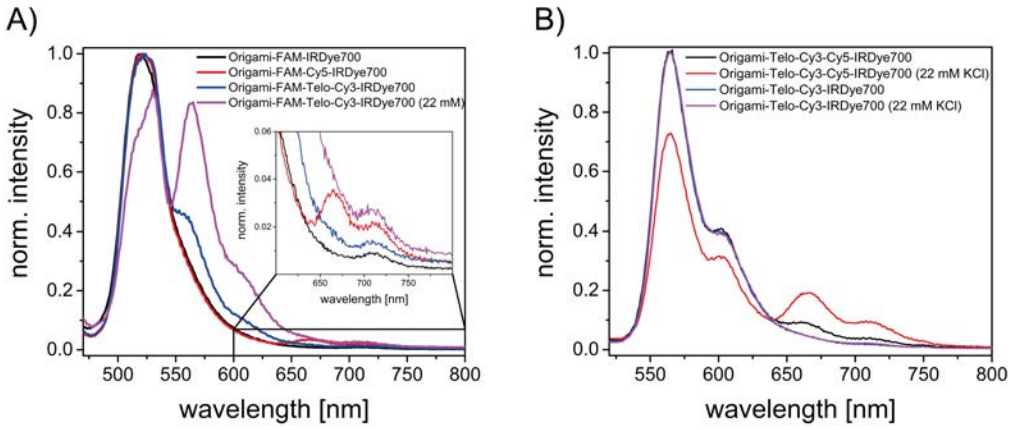

Fig. S 13 *Control experiments for the four-color FRET photonic wire. A) Steady state emission spectra with an excitation wavelength of 450 nm. Direct FRET from FAM to IRDye700 is very weak (black). FRET cascade is not working well if the first*

transmitter dye Cy3 is missing (red). If Cy5 is missing, the FRET cascade is also not working very efficient from FAM to Cy3 to IRDye700 (blue (w/o KCl), violet (KCl)). B) Switchable three-color FRET cascade (black) with Cy3 (donor), Cy5 (transmitter) and IRDye700 (acceptor). The FRET cascade is turned on after KCl addition (blue). FRET cascade is inefficient when Cy5 is missing (blue (w/o salt), violet (KCl)).

References

1 Kankia B., *Sci. Rep.*, 2015, **5**, 12996.
2 Yan Y.-Y., Lin J., Ou T.-M., Tan J.-H., Li D., Gu L.-Q. and Huang Z.-S., *Biochem. Biophys. Res. Commun.*, 2010, **402**, 614-618.
3 Förster T., *Naturwissenschaften*, 1946, **33**, 166-175.
4 Förster T., *Ann. Phys.*, 1948, **437**, 55-75.
5 Lakowicz J. R. *Principles of fluorescence spectroscopy.* 3rd ed. New York: Springer; 2006
6 Valeur B. and Berberan-Santos M. N. *Molecular Fluorescence: Principles and applications.* 2nd ed. Weinheim: Wiley-VCH; 2013
7 http://www.glenresearch.com//Technical/Extinctions.html
8 Søndergaard S., Aznauryan M., Haustrup E. K., Schiøtt B., Birkedal V. and Corry B., *Chemphyschem : a European journal of chemical physics and physical chemistry*, 2015, **16**, 2562-2570.

4.4 Artificial light harvesting system

"FRET Efficiency and Antenna Effect in Multi-Color DNA Origami-Based Light Harvesting Systems"

RSC Advances **2017**, 7, 23924-23934[3]

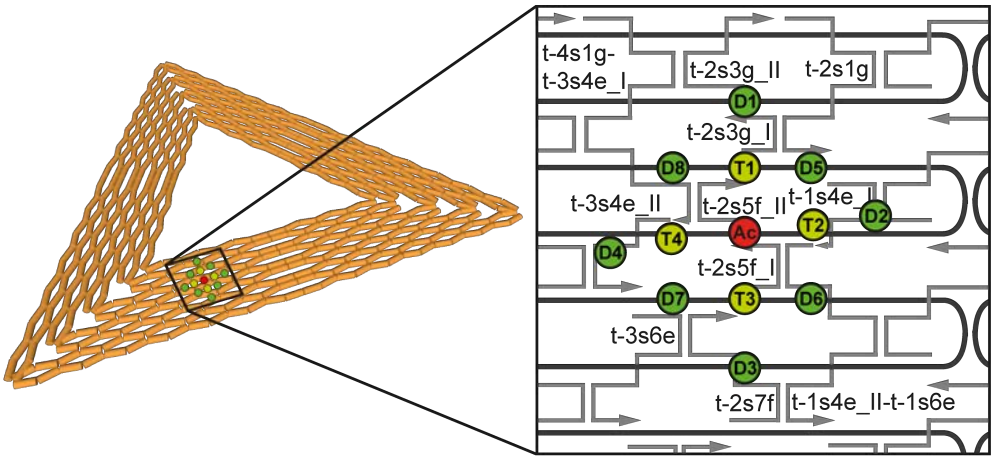

RSC Advances

PAPER

Cite this: *RSC Adv.*, 2017, **7**, 23924

FRET efficiency and antenna effect in multi-color DNA origami-based light harvesting systems†

L. Olejko[abc] and I. Bald *[ab]

Artificial light harvesting complexes find applications in artificial photosynthesis, photovoltaics and light harvesting chemical sensors. They are used to enhance the absorption of light of a reaction center which is often represented by a single acceptor. Here, we present different light harvesting systems on DNA origami structures and analyze systematically the light harvesting efficiency. By changing the number and arrangement of different fluorophores (FAM as donor, Cy3 as transmitter and Cy5 as acceptor molecules) the light harvesting efficiency is optimized to create a broadband absorption and to improve the antenna effect 1 (including two energy transfer steps) from 0.02 to 1.58, and the antenna effect 2 (including a single energy transfer step) from 0.04 to 8.7, *i.e.* the fluorescence emission of the acceptor is significantly higher when the light-harvesting antenna is excited at lower wavelength compared to direct excitation of the acceptor. The channeling of photo energy to the acceptor proceeds by Förster Resonance Energy Transfer (FRET) and we carefully analyze also the FRET efficiency of the different light harvesting systems. Accordingly, the antenna effect can be tuned by modifying the stoichiometry of donor, transmitter and acceptor dyes, whereas the FRET efficiency is mainly governed by the spectroscopic properties of dyes and their distances.

Received 20th February 2017
Accepted 25th April 2017

DOI: 10.1039/c7ra02114c

rsc.li/rsc-advances

Introduction

In natural photosynthesis light energy is absorbed by large networks of accurately positioned chromophores and converted into chemical energy in a reaction center.[1–4] These light harvesting complexes consist of many pigment molecules such as chlorophyll, which absorb the light energy and funnel the excitation energy to a reaction center *via* Förster resonance energy transfer (FRET). As a consequence, the absorption of the reaction center is amplified.[1–5] In the endeavor to harvest the sun light by mimicking the natural photosynthesis, artificial light harvesting systems have been created, in which the excitation energy is channeled from multiple donor molecules to just a few or a single acceptor.[6–10] These artificial light harvesting systems have been designed in one,[11] two[12] and three[13] dimensions. Apart from photosynthesis the concept of light harvesting is also exploited for analytical purposes to enhance the fluorescence emission of luminescent probes and in this way improve the sensitivity of sensors.[14] To improve the functionality of artificial light harvesting complexes, a higher variety of chromophores can be combined and multi-color photonic networks can be assembled. Here, the principle of photonic wires is exploited. Photonic wires are optical waveguides, in which the light energy is controlled on the nanoscale by transferring it linearly along multiple fluorophores from one end to the other end based on FRET.[6,15–19] Several FRET cascades can be combined in a star-like arrangement to transfer the light energy from the outside (donor molecules) to the center of the photonic network (acceptor dye). By combing these two photonic assemblies (light harvesting complexes with FRET cascades) larger end-to-end distances can be achieved and, above all, a broader range of wavelengths from the electromagnetic spectrum can be absorbed to a higher extent leading to a better light harvesting efficiency for several wavelengths. Additionally, the light harvesting efficiency of such systems can be improved on the one hand by optimizing the parameters determining the FRET process, *i.e.* through a larger spectral overlap of donor (D) and acceptor (A) molecules and shorter D–A distances. On the other hand, the number and spatial arrangement of D and A molecules can be varied. The distance and number of D and A dyes can be accurately controlled by using DNA scaffolds. This has been demonstrated *e.g.* with different star-like DNA nanostructures,[16] however, the relative flexibility of the arms of these DNA structures is rather high. DNA origami nanostructures[20] offer a higher control over the arrangement of a larger number of dye molecules without changing the geometry of the DNA substrate. These DNA nanostructures which are assembled by molecular self-

[a]*Department of Chemistry, Physical Chemistry, University of Potsdam, Karl-Liebknecht Str. 24-25, 14476 Potsdam, Germany. E-mail: olejko@uni-potsdam.de*

[b]*BAM Federal Institute for Materials Research and Testing, Richard-Willstätter Str. 11, 12489 Berlin, Germany. E-mail: bald@uni-potsdam.de*

[c]*School of Analytical Sciences Adlershof, Humboldt-Universität zu Berlin, Unter den Linden 6, 10099 Berlin, Germany*

† Electronic supplementary information (ESI) available. See DOI: 10.1039/c7ra02114c

assembly using a circular virus DNA strand called "scaffold strand" (here: M13mp18, 7249 nucleobases (nb)) and many short single DNA strands called "staple strands" (208 different staple strands, 32 nb)[20] are a versatile tool to arrange and analyze different molecules with a high local control and a variety of applications.[21,22] Since every staple strand can be addressed and modified individually and separately, different moieties can be arranged with a high local control since the exact position of each staple strand in the DNA origami structure is known. DNA origami structures have been used to create highly sensitive SERS substrates by attaching gold nanoparticle dimers,[23–25] to analyze DNA strand breaks induced by low energy electrons[26,27] and UV photons[28] and to arrange different fluorophores[29,29,30] at precise distances to create nanoscale photonic devices which can be used for example as photonic wires,[15,18] to resolve conformational changes of biomolecules,[31–34] as logic gates[35,36] and artificial light harvesting complexes.[8,10,18] The light harvesting efficiency is in this context typically expressed as an antenna effect (AE), *i.e.* the intensity of A emission when D is excited compared to the A intensity when it is directly excited.[6,8,10,16,37,38] An antenna is therefore formed when AE is higher than 1, *i.e.* A is getting brighter by collecting light at lower wavelength compared to the direct excitation wavelength. Very recently, it has been demonstrated by using a DNA origami template that AE can be increased to higher values than 1 by increasing the number of D molecules (up to six).[8] However, to screen a broader range of possible excitation wavelengths another energy transfer step, *i.e.* a third dye needs to be introduced. Here, we design and analyze different light harvesting systems on DNA origami structures using three different fluorophores. We focus in particular on the question how the stoichiometry of D and transmitter (T) molecules affect both the AE and the FRET efficiency in the two-step energy transfer with up to eight D molecules. In general, the FRET efficiency characterizes the energy transfer with respect to the donor fluorescence, whereas the antenna effect is determined from the acceptor properties. Due to the presence of the third dye we also study the effect of the relative positioning of D, T and A, *i.e.* the difference between a linear, cross-like arrangement and a snowflake arrangement (in which the donors are rotated by 90°). For all arrangements we carefully determine antenna effects and the three-color FRET efficiencies.

Results and discussion

Design of the artificial light harvesting system

In this study, we have designed light harvesting antennas on triangularly shaped DNA origami structures (AFM image shown in the ESI Fig. S1†). For this, one acceptor molecule (Cyanine5, Cy5) is placed in the center of the light harvesting system. This acceptor molecule is surrounded by a maximum number of four transmitter molecules (Cyanine3, Cy3) (see also Fig. 1). The transmitter molecules are either placed on a neighboring DNA double helix (Fig. 1: paths I and III, T1 and T3) resulting in a nominal T–A distance of *ca.* 4 nm (the fluorophores are on opposite sides of the DNA origami structure, detailed fluorophore orientation is shown in the ESI in Fig. S2†) or they are

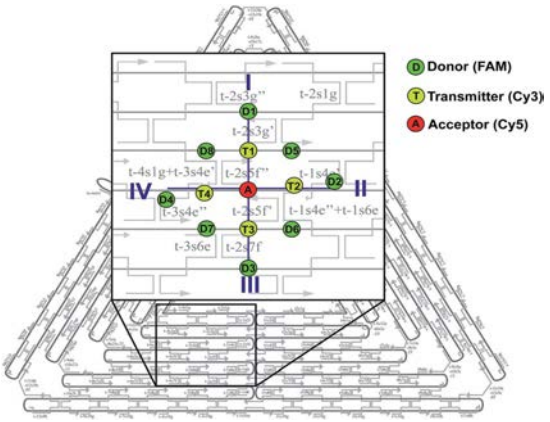

Fig. 1 Illustration of the artificial, FRET-based light harvesting complex on DNA origami structures with three different chromophores (donor: fluorescein (FAM), transmitter: Cyanine3 (Cy3), acceptor: Cyanine5 (Cy5)). The acceptor dye Cy5 (red) is placed in the middle of the light harvesting complex. A maximum number of four transmitter dyes (yellow) is placed around Cy5 (two on neighboring DNA double helices (gap size = 0.5 nm; Cy5-Cy3-distance: *ca.* 4 nm; path: I, III; T1 and T3) and two along the same DNA double helix (9 nb away from Cy5 on opposite sides; Cy5-Cy3-distance: *ca.* 3 nm, path: II, IV; T2 and T4)). One donor molecule (green) is placed next to each transmitter molecule. Again, either on a neighboring DNA double helix (Cy3-FAM-distance: *ca.* 4 nm; path: I, III; D1 and D3) or along the same DNA double helix (Cy3-FAM-distance: *ca.* 3 nm; path: II, IV; D2 and D4). Additionally, FAM is placed between two Cy3 molecules having similar distances to each Cy3 (R = 3.3 nm, D5–D8). The light harvesting efficiency is influenced by the amount of donor and transmitter dyes around the central acceptor dye.

placed along the same DNA double helix with a distance of 9 nb between Cy5 and Cy3 (9 nb ≈ 3 nm) (Fig. 1: paths II and IV, T2 and T4). Next to each transmitter molecule a donor molecule (fluorescein, FAM) is placed. Again, the fluorophores are either placed on a neighboring DNA double helix (Fig. 1: paths I and III, D1 and D3) or along the same DNA double helix (distance = 9 nb, Fig. 1: paths II and IV, D2 and D4). In addition to these four FAM molecules, FAM can be placed at equal distance to two Cy3 molecules (such that FAM, two Cy3 molecules and Cy5 form a square, *e.g.* A-T1-D5-T2). Here, every FAM molecule (Fig. 1, D5–D8) has a similar distance to the two neighboring Cy3 molecules (≈3.3 nm). In such a fluorophore arrangement high FRET efficiencies are expected because the intermolecular distances are shorter than the corresponding Förster distances (R_0(Cy3/Cy5)) = 5.2 nm; R_0(FAM/Cy3) = 6.7 nm; see Table S1 in the ESI†). In this study, artificial light harvesting systems with a maximum number of eight FAM molecules can be created. This nanoscale photonic array can be excited at 450 nm (direct excitation of FAM) and due to an energy transfer from FAM over Cy3 to Cy5 it emits at 665 nm. The emission intensity and therefore the light harvesting efficiency of the system can be tuned by changing the combination of used fluorophores and donor/transmitter/acceptor ratios.

The light harvesting efficiency can be expressed in different ways. On the one hand, the light harvesting efficiency can be

determined by comparing the absorption spectrum with the fluorescence excitation spectrum recorded at the emission wavelength of the central acceptor dye. The decrease in intensity of the donor excitation peak compared to the donor's absorption maximum (normalizing of the absorption and excitation spectra is necessary) represents the transfer efficiency.[40,41] However, in the present experiments the concentrations of the dyes are in the range of nM, which prevents the detection of absorption spectra. On the other hand, the AE is understood as the relative emission intensity of the acceptor when the donor or the acceptor is excited, respectively. Hence, to characterize the light harvesting efficiency the AE is used as defined below. The AE resembles the acceptor emission generated by neighboring donors (sensitized emission) relative to the acceptor emission upon direct excitation.[6,8,10,16,37–39] The overall antenna effect (AE1, FAM-Cy3-Cy5-FRET) is calculated using the following eqn (1).

$$\mathrm{AE1} = \frac{I_{\mathrm{A(450\ nm)}}}{I_{\mathrm{A(600\ nm)}}} \quad (1)$$

Thus, it is the ratio of the acceptor emission intensity due to FRET $I_{\mathrm{A(450\ nm)}}$ (number in brackets denotes the excitation wavelength) and the acceptor emission intensity upon direct excitation at 600 nm $I_{\mathrm{A(600\ nm)}}$ of the same sample (both emission intensities are corrected for equal photon fluxes).[8,10,16,42] For the three-color FRET cascade an antenna effect for the second FRET step (AE2, Cy3-Cy5-FRET) can be determined based on the direct excitation of the transmitter dye (here: Cy3; excitation wavelength = 500 nm; $I_{\mathrm{A(500\ nm)}}$).

$$\mathrm{AE2} = \frac{I_{\mathrm{A(500\ nm)}}}{I_{\mathrm{A(600\ nm)}}} \quad (2)$$

It has to be noted that the exact value of the antenna effect depends strongly on the wavelength chosen for direct acceptor excitation, which has been intensively studied by Hemmig *et al.*[8] Therefore, when comparing AE values one has to carefully use the same wavelengths and measurement settings for every sample. In the present study, an excitation wavelength is chosen that allows to record the whole emission spectrum of Cy5 (thus, the excitation wavelength is not necessarily the absorption maximum).

The FRET efficiency E is calculated based on the donor's fluorescence decay time using eqn (3).[43,44]

$$E = 1 - \frac{\bar{\tau}_{\mathrm{DA}}}{\tau_{\mathrm{D}}} \quad (3)$$

Here, $\bar{\tau}_{\mathrm{DA}}$ is the donor's fluorescence decay time when FRET takes place (amplitude averaged fluorescence decay time) and τ_{D} is the donor's fluorescence decay time with the acceptor being absent. To analyze the overall FRET efficiency and to take the contributions of all species (different donor–transmitter–acceptor distances, unquenched FAM *etc.*) into account the amplitude averaged decay has been used to calculate the FRET efficiency. The donor's decay curves in absence and presence of the acceptor/transmitter molecules have been recorded using time-correlated single photon counting.

Antenna effect

We have analyzed different fluorophore assemblies and determined the antenna effects AE1 and AE2 and the FRET efficiencies for each system (AE2 is shown in the ESI, Fig. S3†). The determination of all these quantities yields a complete description of the energy transfer pathways in such light harvesting antennas.

Firstly, we have characterized the two-color FRET system using FAM as the donor and Cy5 as the acceptor molecule. Since the spectral overlap between these two organic dyes (see ESI, Fig. S4A†) is rather small and the distance between FAM and Cy5 (≈5–6 nm) is relatively long the light harvesting efficiency is expected to be rather small for this system. Nevertheless, the light harvesting efficiency of such a two-color FRET pair can be improved by increasing the number of donor molecules $((\mathrm{Cy5})_1\ (\mathrm{Cy3})_0\ (\mathrm{FAM})_{1-4}$, Fig. 2A, fluorophore which is increased is written in bold letters) which has also been shown in other studies.[8,12,13] The emission intensity of Cy5 (665 nm) increases with additional donor molecules as shown in the normalized emission spectra in Fig. 2A (normalized to Cy5 emission intensity when Cy5 is directly excited; normalized emission spectra represent the overall functionality of the light harvesting system because emission of Cy5 in not correctly formed light harvesting systems is also taken into account). Please note that the peak at 533 nm in the emission spectrum of $(\mathrm{Cy5})_1\ (\mathrm{Cy3})_0\ (\mathrm{FAM})_0$ is the water Raman peak, which is also present in other emission spectra. Since the number of FAM molecules increases and FRET is rather weak, the emission intensity of FAM (520 nm) also increases stepwise (Fig. 2A). As depicted in Fig. 2D (black curve) the overall light harvesting efficiency increases with the addition of donor molecules. Please note that the AE1 values are mean values for each path and path combination (1× FAM: I, II, III, IV; 2× FAM: I + II, I + III, I + IV, II + III, II + IV, III + IV; 3× FAM: I + II + III, I + II + IV, I + III + IV, II + III + IV; see ESI Fig. S5A† for further information). The error bars in Fig. 2D are the standard deviations of different paths and path combination and for systems with only one combination possibility $((\mathrm{Cy5})_1\ (\mathrm{Cy3})_0\ (\mathrm{FAM})_0$, $(\mathrm{Cy5})_1\ (\mathrm{Cy3})_0\ (\mathrm{FAM})_4$ and $(\mathrm{Cy5})_1\ (\mathrm{Cy3})_4\ (\mathrm{FAM})_4)$ they are the standard deviation of three independent measurements. The overall antenna effect is rather small due to weak FRET between FAM and Cy5 as explained above (AE1 range: 0.02 ± 0.01 to 0.32 ± 0.01). Since the antenna effect cannot be tuned arbitrarily using this two-color FRET system a transmitter molecule (Cy3) is introduced (Fig. 1). The normalized emission spectra for the stepwise addition of Cy3 to the two-color FRET system with the highest antenna effect $((\mathrm{Cy5})_1\ (\mathrm{Cy3})_0\ (\mathrm{FAM})_4)$ is shown in Fig. 2B. Here, the emission intensity of Cy3 (565 nm) increases with an increasing number of Cy3 molecules. This is on the one hand due to the raising amount of Cy3 molecules (see also ESI, Fig S6†), and on the other hand the FRET efficiency from FAM to Cy3 increases, which is also visible by a drop in the FAM emission intensity at 520 nm (Fig. 2B). Please note that the emission peak of FAM for

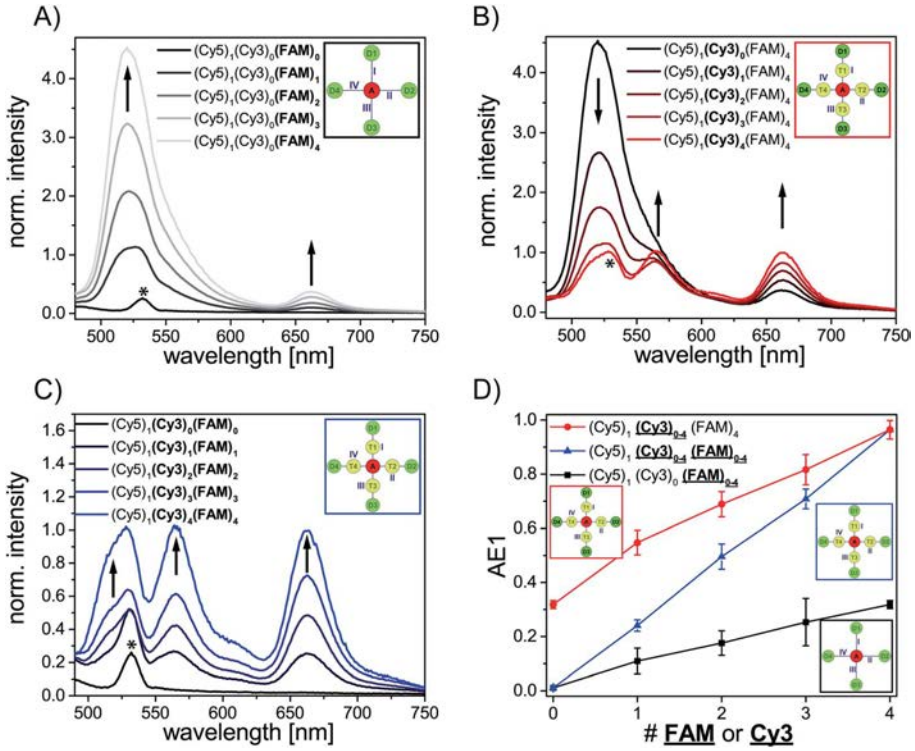

Fig. 2 Normalized emission spectra (λ_{ex} = 450 nm, water Raman peak labelled with a star) and calculated antenna effect (AE1) for different light harvesting systems (mean values of different paths and path combinations). (A) Normalized emission spectra of the two-color FRET system ($(Cy5)_1$ $(Cy3)_0$ $(FAM)_{0-4}$) with increasing FAM molecules. The emission intensities of both FAM (520 nm) and Cy5 (665 nm) increase with increasing number of FAM molecules. (B) Light harvesting system with a fixed number of Cy5 and FAM molecules and increasing number of Cy3 molecules ($(Cy5)_1$ $(Cy3)_{0-4}$ $(FAM)_4$). Emission intensities of Cy3 and Cy5 increase and at the same time FAM emission intensity decreases due to higher FRET efficiencies. (C) Light harvesting system with increasing number of Cy3 and FAM ($(Cy5)_1$ $(Cy3)_{0-4}$ $(FAM)_{0-4}$). The emission intensities of all three dyes increase due to a higher amount of molecules (FAM, Cy3) and therefore more light energy is transferred to Cy5. (D) The antenna effect increases for all systems with an increasing number of FAM and/or Cy3 molecules indicated in bold letters in the respective system. The overall AE1 of $(Cy5)_1$ $(Cy3)_0$ $(FAM)_{0-4}$ (black) is rather small due to weak FRET between FAM and Cy5. The increase in AE1 for $(Cy5)_1$ $(Cy3)_{0-4}$ $(FAM)_{0-4}$ (blue) is steeper because two effects lead to an increase in AE1 in this light harvesting system. Namely, direct FAM-Cy5-FRET (stays the same for $(Cy5)_1$ $(Cy3)_{0-4}$ $(FAM)_4$ (red)) increases and three-color FRET increases. Please note that the number of FAM or Cy3 on the *x*-axis refers to the number of fluorophores which are increased as indicated by highlighted letters in the caption.

the system $(Cy5)_1$ $(Cy3)_4$ $(FAM)_4$ is altered due to the underlying water Raman peak at 533 nm. The overall emission intensity of Cy5 increases as well due to better energy transfer from FAM over Cy3 to Cy5. Furthermore, the antenna effect increases linearly with an increasing number of Cy3 molecules as shown in Fig. 2D (red curve). Here, the antenna effect can be further tuned from 0.32 ± 0.01 to 0.96 ± 0.03. This is very close to a value of 1, which means that the light harvesting system is good enough to provide the same emission of A when excited at 450 nm as for direct A excitation at 600 nm, although two energy transfer steps are required. Due to larger spectral overlaps between FAM/Cy3 and Cy3/Cy5 (see ESI, Fig. S4A–D, Table S1†) and shorter intermolecular distances the energy transfer becomes more efficient and therefore the sensitized emission of Cy5 is intensified. Again, the values of the antenna effect represent mean values of different paths and pathway combinations as mentioned above (see also ESI, Fig. S5C†). The AE2 values for these systems also increase linearly and are shown in the ESI (Fig. S3A and C†). The AE2 values range from 3.0 ± 0.2 to 5.7 ± 0.4 showing that the brightness of the light harvesting complex also depends on the overall excitation wavelength (λ_{ex} = 450 nm (AE1) *vs.* λ_{ex} = 500 nm (AE2)). Interestingly, the AE2 values are significantly higher than 1 meaning that the light harvesting system can be very efficiently excited at 500 nm. This can be attributed to the fact, that at 500 nm both FAM and Cy3 are excited. Thus, more light energy is transferred to the final acceptor Cy5. This shows that by using a three-color FRET cascade for a light-harvesting complex a broader range of wavelengths can be used to efficiently generate acceptor emission.

We have also analyzed the light harvesting system with an increasing number of both Cy3 and FAM. The amount of both fluorophores has been increased to the same extent ($(Cy5)_1$ $(Cy3)_1$ $(FAM)_1$, $(Cy5)_1$ $(Cy3)_2$ $(FAM)_2$, $(Cy5)_1$ $(Cy3)_3$ $(FAM)_3$ and $(Cy5)_1$ $(Cy3)_4$ $(FAM)_4$). The normalized emission spectra for these light harvesting systems are shown in Fig. 2C. Here, the

fluorescence emission intensities of all fluorophores (Cy5, Cy3, FAM) increase with an increasing number of Cy3 and FAM (Fig. 2C). Due to a higher number of donor and transmitter molecules more light energy is transferred to the final acceptor. Therefore, the emission intensity of Cy5 at 665 nm increases gradually (Fig. 2C). Please note that the peak at 533 nm for $(Cy5)_1$ $(Cy3)_0$ $(FAM)_0$ is the water Raman peak as mentioned above and the emission peak of FAM for all light harvesting systems ($(Cy5)_1$ $(Cy3)_1$ $(FAM)_1$, $(Cy5)_1$ $(Cy3)_2$ $FAM)_2$, $(Cy5)_1$ $(Cy3)_3$ $(FAM)_3$ and $(Cy5)_1$ $(Cy3)_4$ $(FAM)_4$) is altered due to the water Raman peak. The light harvesting efficiency increases with higher numbers of Cy3 and FAM as shown in Fig. 2D (blue curve). The antenna effect increases again linearly but compared to $(Cy5)_1$ $(Cy3)_{0-4}$ $(FAM)_4$ the slope is steeper. This is attributed to the fact that for $(Cy5)_1$ $(Cy3)_{0-4}$ $(FAM)_4$ the direct energy transfer from FAM to Cy5 stays the same (number of FAM molecules is constant) and in $(Cy5)_1$ $(Cy3)_{0-4}$ $(FAM)_{0-4}$ the direct FAM-to-Cy5 FRET increases (increasing number of FAM molecules), which leads to a stronger increase of the light harvesting efficiency. Furthermore, the antenna effect is always smaller for $(Cy5)_1$ $(Cy3)_{0-4}$ $(FAM)_{0-4}$ when compared to $(Cy5)_1$ $(Cy3)_{0-4}$ $(FAM)_4$. This is again because of the direct FAM-Cy5 FRET which is always higher in $(Cy5)_1$ $(Cy3)_{0-4}$ $(FAM)_4$ (higher number of FAM molecules; 4 *vs.* 0–3). The AE1 for all paths and path combinations and the antenna effect 2 for $(Cy5)_1$ $(Cy3)_{1-4}$ $(FAM)_{1-4}$ are shown in the ESI (Fig S5E and S3B and C,† respectively). The AE2 values increase also linearly and range from 1.5 ± 0.1 in $(Cy5)_1$ $(Cy3)_1$ $(FAM)_1$ to 5.7 ± 0.3 in $(Cy5)_1$ $(Cy3)_4$ $(FAM)_4$. The overall behavior when comparing the AE2 values of $(Cy5)_1$ $(Cy3)_{1-4}$ $(FAM)_{1-4}$ and $(Cy5)_1$ $(Cy3)_{1-4}$ $(FAM)_4$ with each other is the same as for AE1 (slope is steeper and values are smaller for $(Cy5)_1$ $(Cy3)_{1-4}$ $(FAM)_{1-4}$). The reason for this has been discussed above.

FRET efficiency

After analyzing the steady-state fluorescence data we have also carried out time-resolved fluorescence measurements to further characterize the different light harvesting systems in terms of FRET efficiency (Fig. 3). The FAM fluorescence decay curves have been analyzed using a multi-exponential fit as explained in the ESI† (two-exponential for $(Cy5)_1$ $(Cy3)_0$ $(FAM)_{1-4}$ and three-exponential for $(Cy5)_1$ $(Cy3)_{0-4}$ $(FAM)_4$, $(Cy5)_1$ $(Cy3)_{1-4}$ $(FAM)_{1-4}$ and $(Cy5)_1$ $(Cy3)_4$ $(FAM)_8$). For all systems the last decay time component was set to the free FAM fluorescence decay time ($\bar{\tau}_D$ = 4.1–4.6 ns) (the FAM fluorescence decay time depends on the position of FAM on the DNA origami structure, an overview of FAM fluorescence decay times of the different positions and position combinations is shown in the ESI (Table S2†)).

The fluorescence decay curves for the two-color FRET system $(Cy5)_1$ $(Cy3)_0$ $(FAM)_{1-4}$ are depicted in Fig. 3A and the corresponding FRET efficiencies are plotted in Fig. 3D (black curve). The amplitude averaged decay time decreases from 4.3 ns in $(Cy5)_0$ $(Cy3)_0$ $(FAM)_4$ to 3.4 ns in $(Cy5)_1$ $(Cy3)_0$ $(FAM)_1$ due to direct FAM to Cy5 FRET. By increasing the number of FAM molecules stepwise the amplitude averaged decay time increases slightly ($(Cy5)_1$ $(Cy3)_0$ $(FAM)_1$: $\bar{\tau}_{DA}$ = (3.4 ± 0.5) ns; $(Cy5)_1$ $(Cy3)_0$ $(FAM)_2$: $\bar{\tau}_{DA}$ = (3.5 ± 0.2) ns; $(Cy5)_1$ $(Cy3)_0$ $(FAM)_3$: $\bar{\tau}_{DA}$ = (3.5 ± 0.1) ns; $(Cy5)_1$ $(Cy3)_0$ $(FAM)_4$: $\bar{\tau}_{DA}$ = (3.6 ± 0.1) ns). Thus, the FRET efficiency which has been calculated based on the FAM fluorescence decay times (amplitude averaged decay times) decreases slightly (Fig. 3D, black curve). The FRET efficiencies plotted in Fig. 3D are mean values of all paths and path combinations (see ESI, Fig. S5B†). Again, the error bars are the standard deviations of different paths and path combinations or the standard deviation of three separate measurements for $(Cy5)_1$ $(Cy3)_0$ $(FAM)_4$ and $(Cy5)_1$ $(Cy3)_4$ $(FAM)_4$ (Fig. 3D). The standard deviations of different paths and path combinations represent the structural heterogeneity (variations in donor/transmitter/acceptor distances and fluorophore orientations due to coupling to DNA) in the light harvesting design (see also ESI, Fig. S5†). The decrease in FRET efficiency can be explained by the manner of data analysis as follows: since we have determined the amplitude averaged fluorescence decay time, the decay time of unquenched FAM is taken into account. As we only increase the number of FAM molecules and FRET between FAM and Cy5 is rather weak, the amplitude of the decay time component for the free FAM increases (see also ESI, Fig. S7A†). This leads to an increase in the amplitude averaged decay time and therefore a decrease in FRET efficiency. The first decay time component belonging to the quenched FAM due to direct FAM-Cy5 FRET stays on average nearly the same for all cases (see also ESI, Fig. S7B†). The overall FRET efficiency is rather small ($E \approx$ 0.2) in this system because of the small spectral overlap between FAM and Cy5 (see ESI, Fig. S4A†) and the relatively long intermolecular distance (≈5–6 nm) as mentioned above. In general, this indicates that when FRET is of low efficiency the average FRET efficiency is further decreased upon increasing the number of D molecules. As we have seen above and will further discuss below, for high FRET efficiencies the average FRET efficiency is further increased upon increasing the number of D molecules.

Next, we consider the FRET efficiency for the three-color cascade (including Cy3). The FAM fluorescence decay curves for an increasing number of Cy3 molecules and a fixed number of Cy5 (1× Cy5) and FAM (4× FAM) molecules are shown in Fig. 3B. The FAM amplitude averaged fluorescence decay time decreases with an increasing amount of Cy3 ($(Cy5)_1$ $(Cy3)_0$ $(FAM)_4$: $\bar{\tau}_{DA}$ = (3.6 ± 0.1) ns; $(Cy5)_1$ $(Cy3)_1$ $(FAM)_4$: $\bar{\tau}_{DA}$ = (2.9 ± 0.2) ns; $(Cy5)_1$ $(Cy3)_2$ $(FAM)_4$: $\bar{\tau}_{DA}$ = (2.4 ± 0.4) ns; $(Cy5)_1$ $(Cy3)_3$ $(FAM)_4$: $\bar{\tau}_{DA}$ = (1.8 ± 0.5) ns; $(Cy5)_1$ $(Cy3)_4$ $(FAM)_4$: $\bar{\tau}_{DA}$ = (1.3 ± 0.2) ns). The corresponding FRET efficiencies plotted against the number of Cy3 molecules are shown in Fig. 3D (red curve). Please note that the FRET efficiencies are again mean values of different paths and path combinations (see ESI, Fig. S5D†). The FRET efficiency rises with an increasing amount of Cy3. For $(Cy5)_1$ $(Cy3)_1$ $(FAM)_4$ the FRET efficiency is still rather small (E = 0.32 ± 0.02) because one Cy3 molecule is not enough to transfer the light energy of four FAM molecules. The more Cy3 molecules are present the better the light energy is transferred (E increases). This is also in accordance with the antenna effect (Fig. 1D, red curve) discussed above. A stepwise addition of Cy3 molecules results in a linear increase of the FRET efficiency.

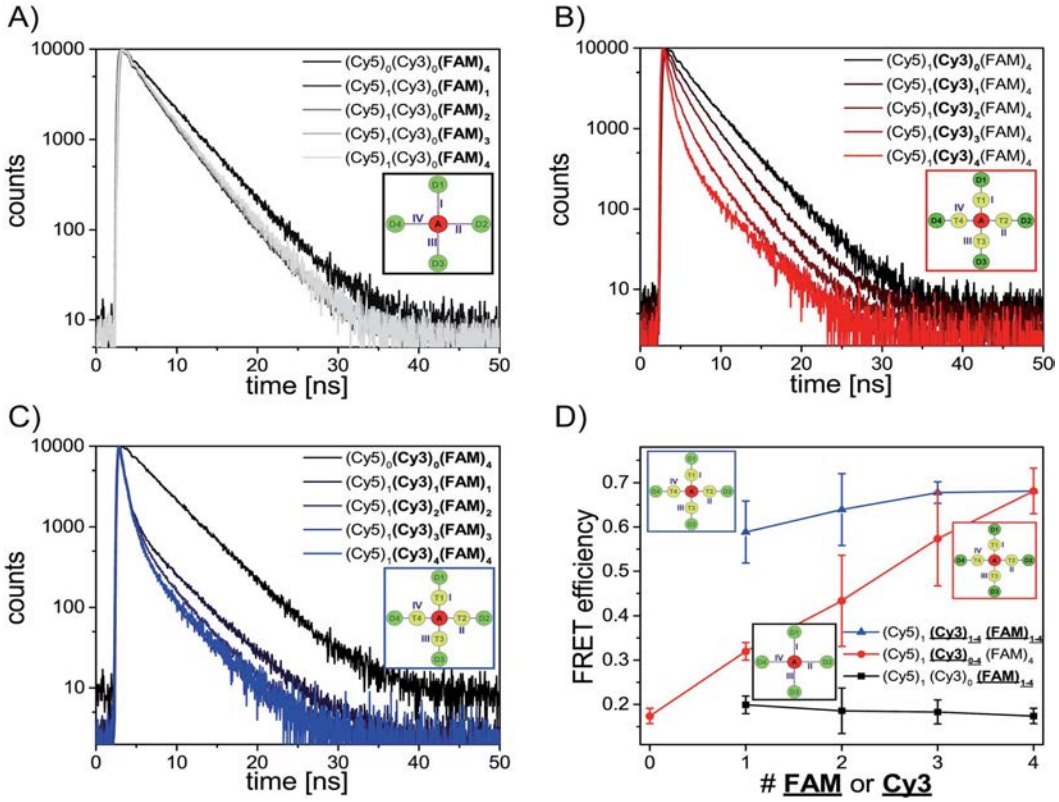

Fig. 3 FAM fluorescence decay curves ($\lambda_{ex} = 490$ nm, $\lambda_{em} = 520$ nm) and FRET efficiencies calculated based on amplitude averaged decay times for different light harvesting systems. (A) FAM fluorescence decay curves for the two-color FRET system with an increasing number of FAM molecules ($(Cy5)_1\,(Cy3)_0\,(FAM)_{1-4}$). (B) FAM fluorescence decay curves for the light harvesting system with a fixed number of Cy5 (1) and FAM (4) molecules and an increasing number of Cy3 molecules ($(Cy5)_1\,(Cy3)_{0-4}\,(FAM)_4$). The fluorescence decay time of FAM decreases with an increasing number of Cy3 molecules. (C) FAM fluorescence decay curves for the light harvesting system with an increasing amount of Cy3 and FAM molecules ($(Cy5)_1\,(Cy3)_{1-4}\,(FAM)_{1-4}$). The FAM fluorescence decay time decreases with increasing number of transmitter and donor molecules. (D) FRET efficiencies plotted against the number of FAM and Cy3, respectively (shown in bold letters). For the two-color FRET system, the FRET efficiency decreases slightly with an increasing number of FAM molecules (black). The FRET efficiency increases with an increasing number of FAM and Cy3 for the three-color light harvesting systems ($(Cy5)_1\,(Cy3)_{1-4}\,(FAM)_{1-4}$ (blue); $(Cy5)_1\,(Cy3)_{0-4}\,(FAM)_4$ (red)).

The FAM fluorescence decay curves for the light harvesting systems with increasing Cy3 and FAM molecules ($(Cy5)_1\,(Cy3)_{1-4}\,(FAM)_{1-4}$) are depicted in Fig. 3C. Again, the FAM fluorescence decay time decreases with an increasing amount of donor and transmitter molecules. Interestingly, the fluorescence decay time drops drastically from unquenched FAM ($(Cy5)_0\,(Cy3)_0\,(FAM)_4$: $\tau_D = 4.3$ ns) to the system with just one acceptor, transmitter and donor molecule ($(Cy5)_1\,(Cy3)_1\,(FAM)_1$: $\bar{\tau}_{DA} = (1.8 \pm 0.8)$ ns). This mono-molecular three-color FRET cascade $(Cy5)_1\,(Cy3)_1\,(FAM)_1$ is already very efficient because the spectral overlap of each FRET pair is large (see ESI, Fig S4B and D†) and the intermolecular distances are rather short (*ca.* 3–4 nm). The FAM fluorescence decay time decreases further with an increasing number of transmitter and donor molecules. It has to be noted that the decrease happens to a smaller extent compared to $(Cy5)_1\,(Cy3)_{0-4}\,(FAM)_4$ and it reaches a minimum value of (1.3 ± 0.2) ns ($(Cy5)_1\,(Cy3)_1\,(FAM)_1$: $\bar{\tau}_{DA} = (1.9 \pm 0.8)$ ns; $(Cy5)_1\,(Cy3)_2\,(FAM)_2$: $\bar{\tau}_{DA} = (1.5 \pm 0.4)$ ns; $(Cy5)_1\,(Cy3)_3\,(FAM)_3$: $\bar{\tau}_{DA} = (1.4 \pm 0.1)$ ns; $(Cy5)_1\,(Cy3)_4\,(FAM)_4$: $\bar{\tau}_{DA} = (1.3 \pm 0.2)$ ns). The FRET efficiency is plotted *versus* the number of Cy3 and FAM molecules and is shown in Fig. 3D (blue curve). The FRET efficiency rises with an increasing amount of Cy3 and FAM. The increase in FRET efficiency is not as strong as for $(Cy5)_1\,(Cy3)_{0-4}\,(FAM)_4$ and is at the beginning ($(Cy5)_1\,(Cy3)_1\,(FAM)_1$) already quite high. The reason has been explained above. Please note that the position of FAM molecules slightly influences the antenna effect (AE1 and AE2) and FRET efficiency when comparing $(Cy5)_1\,(Cy3)_4\,(FAM)_4$ (D1–D4) (AE1 = 0.96 ± 0.03, AE2 = 5.7 ± 0.4, $E = 0.68 \pm 0.05$) and $(Cy5)_1\,(Cy3)_4\,(FAM)_4$ (D5–D8) (AE1 = 0.81 ± 0.02, AE2 = 4.9 ± 0.1, $E = 0.53 \pm 0.07$) with each other as depicted in Fig. 4.

With these results we have shown that the FRET efficiency is not strongly dependent on the number of transmitter and donor molecules but rather on the spectral properties of the fluorophores (strong increase in FRET efficiency by addition of further transmitter molecules ($(Cy5)_1\,(Cy3)_{0-4}\,(FAM)_4$)). The

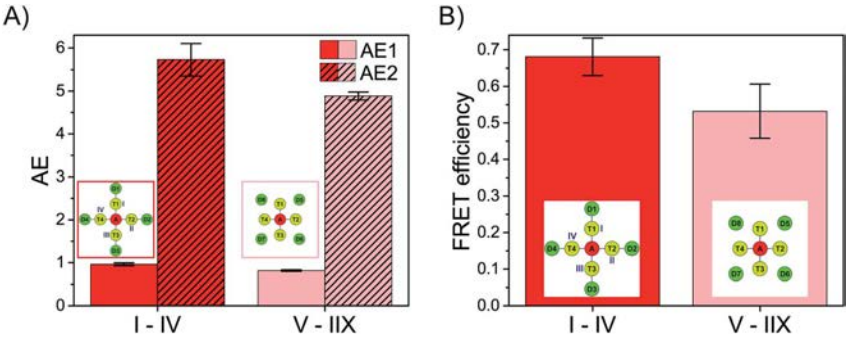

Fig. 4 AE1, AE2 and FRET efficiency for $(Cy5)_1$ $(Cy3)_4$ $(FAM)_4$ with different donor positions (D1–D4 (red), D5–D8 (rose)). (A) Both AE1 (solid) and AE2 (hatched) are slightly influenced by changing the positions of FAM. (B) The FRET efficiency is also slightly influenced by the position of FAM molecules. The error bars are the standard deviation of three separate measurements.

antenna effect (Fig. 2D) on the other hand highly depends on the number of fluorophores (it rises drastically with an increasing number of transmitter and donor molecules ($(Cy5)_1$ $(Cy3)_{1-4}$ $(FAM)_{1-4}$)). In contrast, the FRET efficiency describes the effectivity of donor quenching and the average FRET efficiency can even decrease although the antenna effect is enhanced. This is because the antenna effect only characterizes the enhancement of the acceptor emission, which is achieved by increasing the number of energy-delivering pathways.[45]

Optimization of the light harvesting system

These design rules can be used to rationally optimize the light harvesting efficiency of artificial antenna systems.

This is demonstrated in the following by further increasing the energy-delivering pathways. Thus, the number of donor molecules is further increased from four to eight. For this, four additional FAM molecules are introduced in such a way that each FAM molecule is placed between two transmitter molecules (see Fig. 1). Here, the distance between FAM and the neighboring Cy3 molecules is approximately the same as for the other positions ($R = 3.3$ nm). As shown in Fig. 5A the emission intensity of Cy3 (565 nm) and Cy5 (665 nm) increases drastically in presence of eight FAM molecules (gray spectrum) compared to a light harvesting system with only four FAM molecules (red spectrum). The antenna effect (AE1) has been calculated for both systems and is shown in Fig. 5B. With the addition of more FAM molecules the antenna effect 1 is further tuned from 0.96 ± 0.03 in $(Cy5)_1$ $(Cy3)_4$ $(FAM)_4$ to 1.58 ± 0.08 in $(Cy5)_1$ $(Cy3)_4$ $(FAM)_8$. The antenna effect 2 is also higher for $(Cy5)_1$ $(Cy3)_4$ $(FAM)_8$ ($AE2 = 8.6 \pm 0.2$) compared to $(Cy5)_1$ $(Cy3)_4$ $(FAM)_4$ ($AE2 = 5.7 \pm 0.4$) as shown in Fig. 5B. This is a remarkable result as it shows that also the second energy transfer step (AE2) is influenced by the presence of dyes emitting further in the blue part of the electromagnetic spectrum. The FAM fluorescence decay curves have been measured for both systems and are depicted in Fig. 5C. The FAM amplitude averaged fluorescence decay time decreases slightly with an increasing number of FAM molecules ($(Cy5)_1$ $(Cy3)_4$ $(FAM)_4$: $\bar{\tau}_{DA} = (1.3 \pm 0.2)$ ns; $(Cy5)_1$ $(Cy3)_4$ $(FAM)_8$: $\bar{\tau}_{DA} = (1.2 \pm 0.1)$ ns). Hence, the FRET efficiency increases also only slightly with an increasing number of FAM molecules as shown in Fig. 5D. Again, the antenna effect depends strongly on the number of fluorophores which are present in the light harvesting system. The emission intensity of the final acceptor (Cy5) can be enhanced by adding more and more donor molecules. The FRET efficiency on the other hand is only slightly influenced by further addition of donor molecules. The FRET efficiency as mentioned above describes the degree of donor quenching. Therefore, it is only slightly influenced by the addition of more donor molecules but rather by the addition of further transmitter molecules as shown for $(Cy5)_1$ $(Cy3)_{0-4}$ $(FAM)_4$.

To assess the overall light harvesting capability in terms of possible excitation wavelengths, we have measured the excitation spectra of selected light harvesting systems (see Fig. 6). By analyzing excitation spectra, we can determine specific wavelengths at which the light harvesting system is excitable. As shown in Fig. 6A the single acceptor Cy5 ($(Cy5)_1$ $(Cy3)_0$ $(FAM)_0$, black spectrum) can only be efficiently excited from *ca.* (570–700) nm (Cy5 excitation peak). By introducing four Cy3 molecules ($(Cy5)_1$ $(Cy3)_4$ $(FAM)_0$, Fig. 6A, green spectrum) the system can additionally be excited at wavelengths in the range of the excitation peak of Cy3 ((450–570) nm). By extending the light harvesting system even more (introducing FAM) the wavelength range for suitable excitation wavelengths can be further tuned. As shown in Fig. 6A a third excitation peak appears for the mono-molecular three-color FRET cascade ($(Cy5)_1$ $(Cy3)_1$ $(FAM)_1$, blue spectrum, FAM: 500 nm, Cy3: 550 nm, Cy5: 650 nm). Thus, the light harvesting complex can be excited at a broader wavelength range. Nevertheless, the overall intensity is rather weak for this dye configuration. This can be further improved by the addition of four FAM molecules ($(Cy5)_1$ $(Cy3)_1$ $(FAM)_4$, Fig. 6A, dark red spectrum). The intensity of the FAM excitation maximum increases due to a higher number of donor molecules. Again, the extent of excitation can be improved by adding more molecules $(Cy5)_1$ $(Cy3)_4$ $(FAM)_4$ (Fig. 6A, red spectrum). To finally optimize the light harvesting system eight donor molecules are introduced ($(Cy5)_1$ $(Cy3)_4$ $(FAM)_8$, Fig. 6A, gray spectrum). With such a light harvesting system the range of possible excitation wavelength is broadened ((425–700) nm) and the light energy can be absorbed to a higher extent. To summarize the light harvesting efficiency of the previously

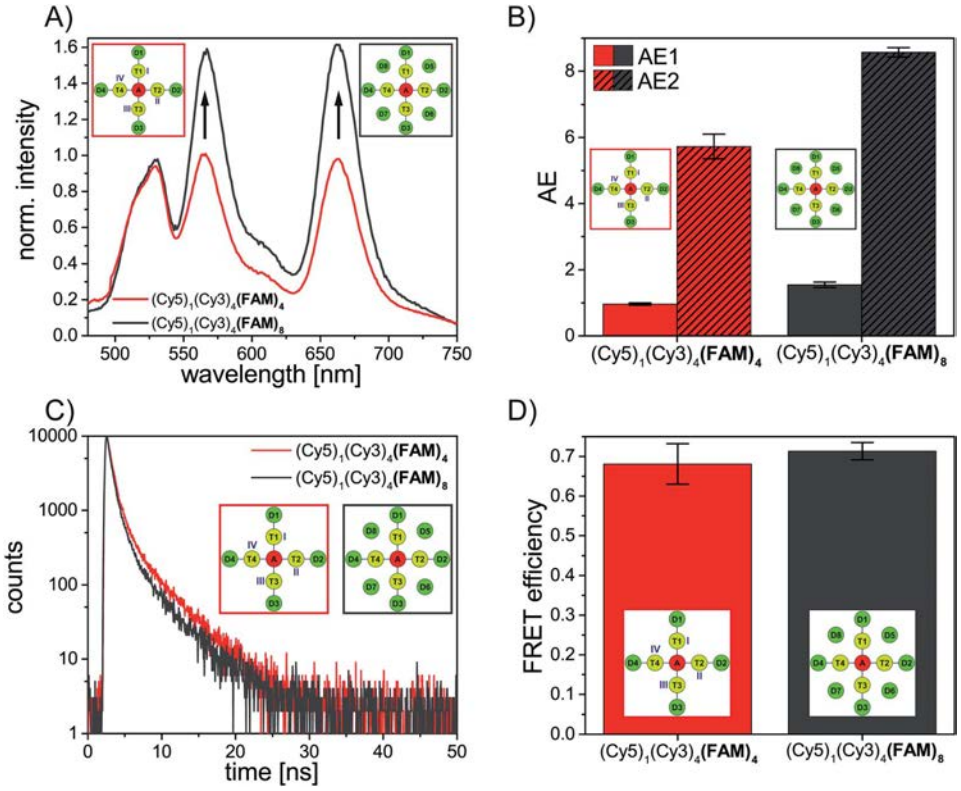

Fig. 5 Steady-state and time-resolved data for $(Cy5)_1$ $(Cy3)_4$ $(FAM)_4$ (red) and $(Cy5)_1$ $(Cy3)_4$ $(FAM)_8$ (gray). (A) Normalized emission spectra (λ_{ex} = 450 nm) for light harvesting systems with four (red) and eight donor molecules (gray). Emission intensities of Cy3 (565 nm) and Cy5 (665 nm) increase with increasing amount of FAM. (B) The antenna effects (AE1 (solid) and AE2 (hatched)) increase with increasing number of FAM molecules. (C) FAM fluorescence decay time (λ_{ex} = 490 nm, λ_{em} = 520 nm) decreases slightly with an increasing number of FAM molecules. (D) The FRET efficiency calculated based on the FAM fluorescence decay time is only slightly influenced by an additional number of FAM molecules. The error bars are the standard deviation of three individual measurements.

discussed light harvesting systems, the AE values (AE1 and AE2) are depicted in Fig. 6B. The AE2 value of a two-color FRET-based light harvesting system ($(Cy5)_1$ $(Cy3)_4$ $(FAM)_0$), which yields similar values compared to other studies (AE2 = 2.1 ± 0.2),[8] can be significantly improved by the addition of a third blue shifted dye such as FAM (AE2$(Cy5)_1$ $(Cy3)_4$ $(FAM)_4$ = 5.7 ± 0.4,

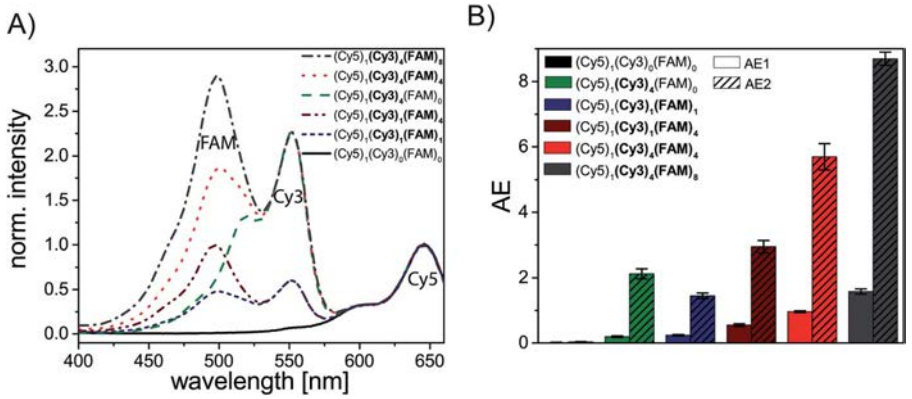

Fig. 6 (A) Excitation spectra (λ_{em} = 680 nm) for different light harvesting systems showing the impact of additional fluorophores on possible excitation wavelengths. (B) Overview of AE1 and AE2 values for light harvesting systems showing the significant increase due to additional fluorophores. The AE values of $(Cy5)_1$ $(Cy3)_0$ $(FAM)_0$ are rather small (AE1 = 0.02 ± 0.01, AE2 = 0.03 ± 0.01). The error bars are the standard deviations of different paths/path combinations and three separate measurements, respectively.

$AE2(Cy5)_1\ (Cy3)_4\ (FAM)_8 = 8.7 \pm 0.2$, Fig. 6B). Interestingly, even the system with just one Cy3 molecule and four FAM molecules lead to higher AE2 values compared to $(Cy5)_1\ (Cy3)_4\ (FAM)_0$ in which four Cy3 molecules are present ($AE2(Cy5)_1\ (Cy3)_4\ (FAM)_0 = 2.3 \pm 0.2$ *vs.* $AE2(Cy5)_1\ (Cy3)_1\ (FAM)_4 = 3.0 \pm 0.2$, Fig. 6B). In general, Fig. 6B shows that both antenna effects (AE1 and AE2) increase with an increasing number of dye molecules as thoroughly discussed above. This is also in good agreement with the excitation spectra (Fig. 6A) which show an increasing number and intensity of the excitation peaks for an increasing number of fluorophores.

Conclusion

In conclusion we have created different three-color FRET-based light harvesting systems by changing the amount and ratio of fluorophores (donor: FAM; transmitter: Cy3, acceptor: Cy5). The light harvesting efficiency expressed by the antenna effect and the overall FRET efficiency have been analyzed using steady-state and time-resolved fluorescence spectroscopy. We have shown that the light harvesting efficiency increases for a two color-FRET system by increasing the amount of donor molecules ($(Cy5)_1\ (Cy3)_0\ (FAM)_{0-4}$). The light harvesting efficiency can be further improved by introducing a transmitter dye and changing the transmitter/donor ratio ($(Cy5)_1\ (Cy3)_{0-4}\ (FAM)_4$) or by changing the amount of both transmitter and donor molecules to the same extent ($(Cy5)_1\ (Cy3)_{0-4}\ (FAM)_{0-4}$). Both approaches lead to a linear increase in the antenna effect. The overall FRET efficiency of the two-color FRET system is rather small and is tuned by introducing a transmitter molecule. We have shown that the FRET efficiency rises linearly for $(Cy5)_1\ (Cy3)_{0-4}\ (FAM)_4$ and only slightly for $(Cy5)_1\ (Cy3)_{1-4}\ (FAM)_{1-4}$. We have concluded that the antenna effect is highly dependent on the number of fluorophores involved in the light harvesting system whereas the FRET efficiency depends more on the spectral properties of used fluorophores. The antenna effect describes the efficiency of acceptor sensitization and the FRET efficiency characterizes the degree of donor quenching. Finally, we have shown that we can tune the antenna effect starting from 0.02 in $(Cy5)_1\ (Cy3)_0\ (FAM)_0$ to 1.58 in $(Cy5)_1\ (Cy3)_4\ (FAM)_8$. Thus, the overall light harvesting efficiency can be enhanced by a factor of almost 80 by changing the stoichiometry of donor and transmitter dyes when excited at 450 nm. For an excitation wavelength of 500 nm the light harvesting efficiency can be even improved by a factor of 200. We have shown that by using three different fluorophores in a light harvesting system the range for possible excitation wavelengths is significantly broadened and the light energy can be absorbed to a higher extent. In general, the light harvesting efficiency of a multichromophore system can be optimized based on the following design rules:

(1) To improve the antenna effect, the number of energy-delivering pathways must be increased by increasing the number of donor and transmitter molecules. Thus, a rosette-like design is best-suited.

(2) The FRET efficiency can only be increased by optimizing the spectral properties and making the intermolecular distances small. The number of D molecules barely changes the FRET efficiency.

(3) The final energy transfer step is also influenced by the number of dyes which are further blue shifted in the electromagnetic spectrum (addition of an extra donor).

(4) A variety of fluorophores resulting in multiple FRET steps leads to a broader range of possible excitation wavelength.

This can be exploited in artificial light harvesting systems used for instance in photosynthesis, photovoltaics in light harvesting chemical sensors.

Experimental methods

Materials and chemicals

Unmodified oligonucleotides (staple strands) have been acquired from Integrated DNA Technologies. The DNA strands have been purified by the manufacturer and dissolved in RNase-free water. The viral genome M13mp18 (7249 nb) has been purchased from tilibit nanosystems GmbH and dissolved in buffer containing 10 mM Tris and 1 mM EDTA by the manufacturer. The oligonucleotides modified with the organic dyes (FAM, Cy3 and Cy5) have been acquired from Metabion International AG (HPLC purified). All DNA strands have been used as delivered without further treatment. Magnesium chloride (≥98%) and Tris acetate-EDTA buffer (TAE buffer, 10× concentrated) have been acquired from Sigma Aldrich. The diluted TAE buffer (1× concentrated, in ultrapure water (Merck Millipore)) (pH = 8.2) contains 40 mM Tris-acetate and 1 mM EDTA. Mica has been purchased from Plano GmbH.

DNA origami preparation

The triangularly shaped DNA origami structures have been fabricated by mixing the viral genome M13mp18 (5 nM) together with 208 short single DNA strands (150 nM), TAE buffer (10× concentrated) containing 100 mM $MgCl_2$ and ultrapure water (Merck Millipore). Using a thermal cycler (PEQLAB/VWR), the solution has been heated up to 80 °C and then slowly cooled down to 8 °C in 2 hours with a defined temperature program (80 °C–66 °C: 1 °C every 30 s, 66 °C–25 °C: 1 °C every 2 min, 25 °C–8 °C: 1 °C every minute). Afterwards, the DNA origami structures have been purified using 100 kDa molecular weight cut-off centrifugal filters (Merck Millipore). For this, the samples have been washed four times with TAE buffer (1× concentrated) containing 10 mM $MgCl_2$ at 2655 g for 10 min. Fluorescence spectroscopy measurements have been performed after the DNA origami preparation at a concentration of approximately 5 nM.

AFM imaging

To investigate the correctly formed DNA origami structures, atomic force microscopy (AFM) has been performed for each sample (AFM image is shown in the ESI, Fig S1†). The samples have been adsorbed on freshly cleaved mica (Plano GmbH). For this, 2 μL of the purified sample (*ca.* 20 nM) and 33 μL of TAE buffer (1× concentrated) containing 10 mM $MgCl_2$ have been incubated for 30 s. After the incubation, the sample has been washed twice with 1 mL of ultrapure water (Merck Millipore). The fluid has been removed with compressed air. The measurements have been performed in air using the phase contrast mode. AFM

imaging has been performed with a Flex AFM from Nanosurf GmbH. A cantilever from Budget Sensors (Tap150 Al-G) with a resonance frequency of (125–160) kHz and a spring constant of 5 N m^{-1} has been used to visualize the DNA origami structures.

Steady-state fluorescence spectroscopy

Steady-state fluorescence spectroscopy measurements have been performed using a FluoromaxP spectrophotometer from HORIBA Jobin Yvon GmbH with 3 mm quartz cuvettes from Hellma Analytics. The measurements have been performed in a 90° angle acquisition using the system internal quantum correction. To record emission spectra, the excitation wavelength has been chosen according to the fluorophore which is directly excited (FAM: $\lambda_{ex} = 450$ nm, Cy3: $\lambda_{ex} = 500$ nm, Cy5: $\lambda_{ex} = 600$ nm). To measure excitation spectra, the emission wavelength has been set to $\lambda_{em} = 680$ nm. Following settings have been used for all measurements: increment = 1 nm, integration time = 0.2 s, bandpass(emission) = bandpass(excitation) = 5 nm.

Time-correlated single photon counting

Time-correlated single photon counting (TCSPC) measurements have been performed on a FLS920 fluorescence spectrophotometer from Edinburgh Instruments Ltd with the F900 software (Edinburgh Instruments Ltd) using 3 mm quartz cuvettes (Hellma Analytics). The samples have been measured in a 90° setup. As an excitation source a supercontinuum white light source SC-400-PP from Fianium/NKT Photonics A/S (0.5–20 MHz, 400 nm < λ < 24 000 nm, pulse width: *ca.* 30 ps) and as a detector a multi-channel-plate ELDY EM1-132/300 from Europhoton GmbH have been used. The excitation wavelength has been set to (490 ± 1) nm and emission wavelength to (520 ± 1) nm.

The measured fluorescence decay curves have been fitted using the FAST software (Edinburgh Instruments Ltd). The decay curves have been fitted multi-exponentially (bi- and tri-exponentially) with the following eqn S(1).

$$I(t) = \sum_{i=1}^{n} A_i e^{-\frac{t}{\tau_i}} \quad \text{(S1)}$$

Here, τ_i is the decay time and A_i is the amplitude characteristic for each decay time component. The amplitude averaged decay time $\bar{\tau}_{DA}$ is then calculated with eqn S(2).

$$\bar{\tau}_{DA} = \frac{\sum_{i=1}^{n} A_i \tau_i}{\sum_{i=1}^{n} A_i} \quad \text{(S2)}$$

The last decay time component has been fixed to the unquenched FAM decay time.

Acknowledgements

This research was supported by the Deutsche Forschungsgemeinschaft (DFG), a Marie Curie FP7 Integration Grant within the 7th European Union Framework Programme, by the University of Potsdam, the Federal Institute for Materials Research and Testing (BAM), and the DFG project GSC 1013 (SALSA).

References

1 B. Gobets and R. van Grondelle, *Biochim. Biophys. Acta*, 2001, **1507**, 80–99.
2 R. Emerson, *J. Gen. Physiol.*, 1932, **16**, 191–205.
3 G. McDermott, S. M. Prince, A. A. Freer, A. M. Hawthornthwaite-Lawless, M. Z. Papiz, R. J. Cogdell and N. W. Isaacs, *Nature*, 1995, **374**, 517–521.
4 X. Hu, A. Damjanović, T. Ritz and K. Schulten, *Proc. Natl. Acad. Sci. U. S. A.*, 1998, **95**, 5935–5941.
5 K. Kalyanasundaram and M. Graetzel, *Curr. Opin. Struct. Biol.*, 2010, **21**, 298–310.
6 B. Albinsson, J. K. Hannestad and K. Börjesson, *Coord. Chem. Rev.*, 2012, **256**, 2399–2413.
7 F. Garo and R. Häner, *Angew. Chem., Int. Ed.*, 2012, **51**, 916–919.
8 E. A. Hemmig, C. Creatore, B. Wunsch, L. Hecker, P. Mair, M. A. Parker, S. Emmott, P. Tinnefeld, U. F. Keyser and A. W. Chin, *Nano Lett.*, 2016, **16**, 2369–2374.
9 P. K. Dutta, S. Levenberg, A. Loskutov, D. Jun, R. Saer, J. T. Beatty, S. Lin, Y. Liu, N. W. Woodbury and H. Yan, *J. Am. Chem. Soc.*, 2014, **136**, 16618–16625.
10 P. K. Dutta, R. Varghese, J. Nangreave, S. Lin, H. Yan and Y. Liu, *J. Am. Chem. Soc.*, 2011, **133**, 11985–11993.
11 A. Ruiz-Carretero, P. G. A. Janssen, A. L. Stevens, M. Surin, L. M. Herz and A. P. H. Schenning, *Chem. Commun.*, 2011, **47**, 884–886.
12 A. L. Benvin, Y. Creeger, G. W. Fisher, B. Ballou, A. S. Waggoner and B. A. Armitage, *J. Am. Chem. Soc.*, 2007, **129**, 2025–2034.
13 H. Ozhalici-Unal and B. A. Armitage, *ACS Nano*, 2009, **3**, 425–433.
14 T. Mayr, S. M. Borisov, T. Abel, B. Enko, K. Waich, G. Mistlberger and I. Klimant, *Anal. Chem.*, 2009, **81**, 6541–6545.
15 L. Olejko, P. J. Cywinski and I. Bald, *Nanoscale*, 2016, **8**, 10339–10347.
16 S. Buckhout-White, C. M. Spillmann, W. R. Algar, A. Khachatrian, J. S. Melinger, E. R. Goldman, M. G. Ancona and I. L. Medintz, *Nat. Commun.*, 2014, **5**, 5615.
17 M. Heilemann, P. Tinnefeld, G. Sanchez Mosteiro, M. Garcia Parajo, N. F. van Hulst and M. Sauer, *J. Am. Chem. Soc.*, 2004, **126**, 6514–6515.
18 I. H. Stein, C. Steinhauer and P. Tinnefeld, *J. Am. Chem. Soc.*, 2011, **133**, 4193–4195.
19 C. M. Spillmann, S. Buckhout-White, E. Oh, E. R. Goldman, M. G. Ancona and I. L. Medintz, *Chem. Commun.*, 2014, **50**, 7246–7249.
20 P. W. K. Rothemund, *Nature*, 2006, **440**, 297–302.
21 F. Zhang, J. Nangreave, Y. Liu and H. Yan, *J. Am. Chem. Soc.*, 2014, **136**(32), 11198–11211.
22 I. Bald and A. Keller, *Molecules*, 2014, **19**, 13803–13823.

23 J. Prinz, B. Schreiber, L. Olejko, J. Oertel, J. Rackwitz, A. Keller and I. Bald, *J. Phys. Chem. Lett.*, 2013, **4**, 4140–4145.

24 J. Prinz, C. Heck, L. Ellerik, V. Merk and I. Bald, *Nanoscale*, 2016, **8**, 5612–5620.

25 J. Prinz, A. Matkovic, J. Pesic, R. Gajic and I. Bald, *Small*, 2016, **12**, 5458–5467.

26 A. Keller, J. Rackwitz, E. Cauët, J. Liévin, T. Körzdörfer, A. Rotaru, K. V. Gothelf, F. Besenbacher and I. Bald, *Sci. Rep.*, 2014, **4**, 7391.

27 J. Rackwitz, J. Kopyra, I. Dąbkowska, K. Ebel, M. L. Ranković, A. R. Milosavljević and I. Bald, *Angew. Chem., Int. Ed.*, 2016, **55**, 10248–10252.

28 S. Vogel, J. Rackwitz, R. Schürmann, J. Prinz, A. R. Milosavljevic, M. Refregiers, A. Giuliani and I. Bald, *J. Phys. Chem. Lett.*, 2015, **6**, 4589–4593.

29 Z. Deng, A. Samanta, J. Nangreave, H. Yan and Y. Liu, *J. Am. Chem. Soc.*, 2012, **134**, 17424–17427.

30 I. H. Stein, V. Schüller, P. Böhm, P. Tinnefeld and T. Liedl, *ChemPhysChem*, 2011, **12**, 689–695.

31 L. Olejko, P. J. Cywinski and I. Bald, *Angew. Chem., Int. Ed.*, 2015, **54**, 673–677.

32 Y. Ke, T. Meyer, W. M. Shih and G. Bellot, *Nat. Commun.*, 2016, **7**, 10935.

33 R. Tsukanov, T. E. Tomov, Y. Berger, M. Liber and E. Nir, *J. Phys. Chem. B*, 2013, **117**, 16105–16109.

34 B. Saccà, Y. Ishitsuka, R. Meyer, A. Sprengel, E.-C. Schöneweiß, G. U. Nienhaus and C. M. Niemeyer, *Angew. Chem., Int. Ed.*, 2015, **54**, 3592–3597.

35 B. L. Cannon, D. L. Kellis, P. H. Davis, J. Lee, W. Kuang, W. L. Hughes, E. Graugnard, B. Yurke and W. B. Knowlton, *ACS Photonics*, 2015, **2**, 398–404.

36 R. M. Zadegan, M. D. E. Jepsen, L. L. Hildebrandt, V. Birkedal and J. Kjems, *Small*, 2015, **11**, 1811–1817.

37 A. Adronov, S. L. Gilat, J. M. J. Fréchet, K. Ohta, F. V. R. Neuwahl and G. R. Fleming, *J. Am. Chem. Soc.*, 2000, **122**, 1175–1185.

38 R. A. Miller, A. D. Presley and M. B. Francis, *J. Am. Chem. Soc.*, 2007, **129**, 3104–3109.

39 F. Pu, L. Wu, X. Ran, J. Ren and X. Qu, *Angew. Chem., Int. Ed.*, 2015, **54**, 892–896.

40 S. L. Gilat, A. Adronov and J. M. Fréchet, *Angew. Chem., Int. Ed.*, 1999, **38**, 1422–1427.

41 L. Stryer and R. P. Haugland, *Proc. Natl. Acad. Sci. U. S. A.*, 1967, **58**, 719–726.

42 D. W. Brousmiche, J. M. Serin, J. M. J. Fréchet, G. S. He, T.-C. Lin, S.-J. Chung, P. N. Prasad, R. Kannan and L.-S. Tan, *J. Phys. Chem. B*, 2004, **108**, 8592–8600.

43 T. Förster, *Naturwissenschaften*, 1946, **33**, 166–175.

44 T. Förster, *Ann. Phys.*, 1948, **437**, 55–75.

45 B. Jana, S. Bhattacharyya and A. Patra, *Nanoscale*, 2016, **8**, 16034–16043.

Supporting Information

Lydia Olejko[a,b,c] and Ilko Bald[a,b]

[a] Department of Chemistry, Physical Chemistry, University of Potsdam, Karl-Liebknecht Str. 24-25, 14476 Potsdam, Germany

[b] BAM Federal Institute for Materials Research and Testing, Richard-Willstätter Str. 11, 12489 Berlin, Germany

[c] School of Analytical Sciences Adlershof, Humboldt-Universität zu Berlin, Unter den Linden 6, 10099 Berlin, Germany

AFM imaging

A typical AFM image of DNA origami structures adsorbed on freshly cleaved mica is shown in Figure S1.

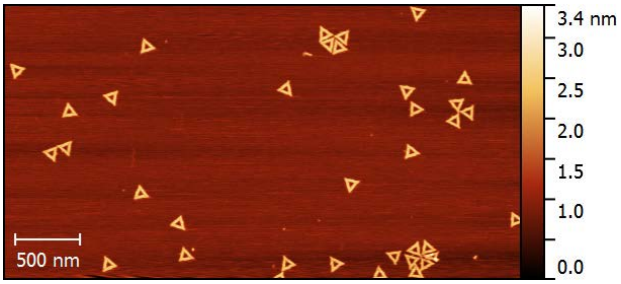

Figure S 1. Typical AFM image of triangularly shaped DNA origami structures on freshly cleaved mica.

Fluorophore orientation on DNA origami structure

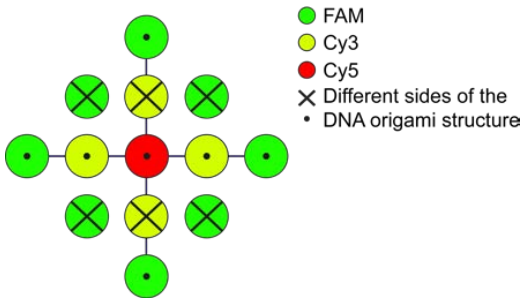

Figure S 2. Schematic illustration of different fluorophore orientations (green: FAM, yellow: Cy3, red: Cy5) showing that some fluorophores are on opposite sides of the DNA origami structure indicated by a cross or a dot.

Antenna effect 2 of $(Cy5)_1$ $(Cy3)_{1\text{-}4}$ $(FAM)_4$ and $(Cy5)_1$ $(Cy3)_{1\text{-}4}$ $(FAM)_{1\text{-}4}$

The antenna effect 2 (AE2) has been calculated for $(Cy5)_1$ **$(Cy3)_{1\text{-}4}$** $(FAM)_4$ and $(Cy5)_1$ **$(Cy3)_{1\text{-}4}$ $(FAM)_{1\text{-}4}$** using the following equation S3.

$$AE2 = \frac{I_{A(500\,nm)}}{I_{A(600\,nm)}} \qquad \text{(S1)}$$

AE2 is the ratio of the acceptor emission intensity when the transmitter dye is directly excited at 500 nm ($I_{A(500\,nm)}$) and the acceptor emission intensity upon direct Cy5 excitation at 600 nm ($I_{A(600\,nm)}$) of the same sample. Please note that AE2 is also dependent on the excitation wavelength of Cy5.[1]

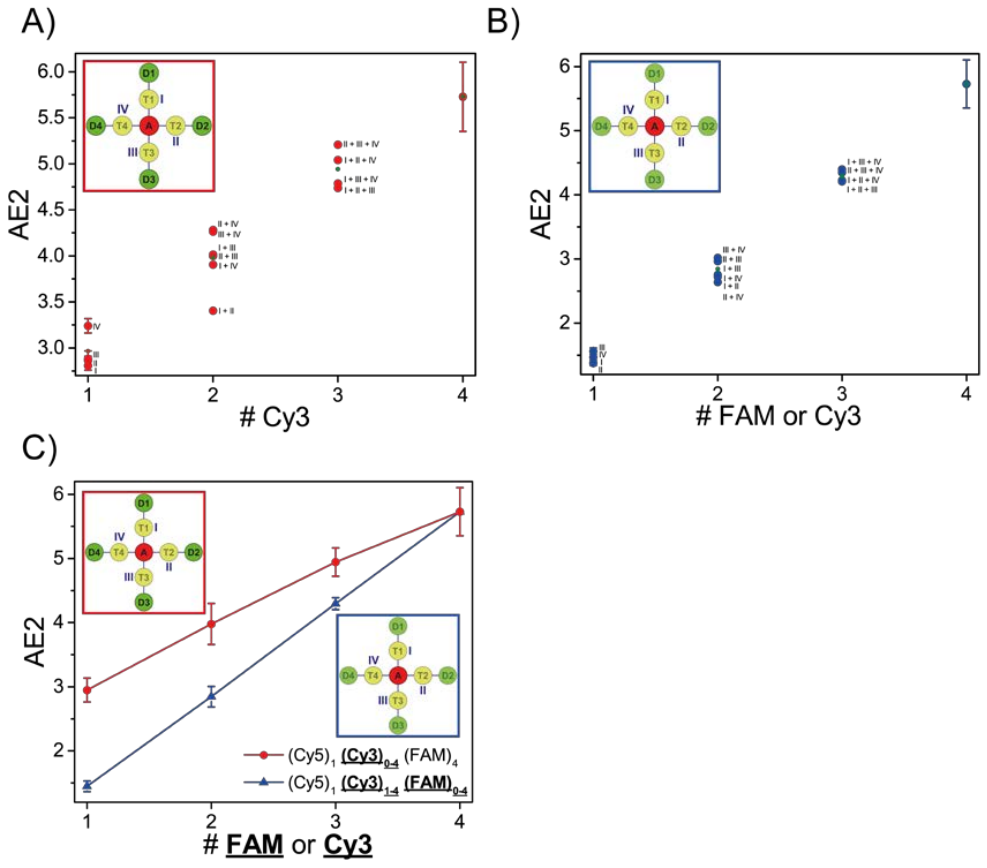

Figure S 3. Antenna effect 2 for different light harvesting systems. (A) AE2 for $(Cy5)_1$ **$(Cy3)_{1\text{-}4}$** $(FAM)_4$ for all paths and path combinations. The error bars are the standard deviation of three individual measurements. (B) AE2 increases with increasing amount of donor and transmitter molecules for $(Cy5)_1$ **$(Cy3)_{1\text{-}4}$ $(FAM)_{1\text{-}4}$**. The error bars are the standard deviation of three individual measurements. (C) Mean values of AE2 for both light-harvesting systems. AE2 increases linearly for both systems ($(Cy5)_1$ **$(Cy3)_{1\text{-}4}$ $(FAM)_4$** (blue) and $(Cy5)_1$ **$(Cy3)_{1\text{-}4}$ $(FAM)_{1\text{-}4}$** (red)). Number of FAM and Cy3 molecules on the x-axis refers to the number of fluorophores which are increased as indicated by bold letters in the caption. The error bars are the standard deviation of different paths and path combinations.

The calculated AE2 for $(Cy5)_1$ **$(Cy3)_{1\text{-}4}$** $(FAM)_4$ for all paths and path combinations and the mean values plotted versus the number of Cy3 molecules are shown in Figure S 2A and C. AE2 increases with an increasing number of Cy3 molecules. It is also visible that the values for different paths and path combinations vary. This can be attributed to slightly different intermolecular distances (paths I and III ≈ 4 nm; paths II and IV ≈ 3 nm) and different fluorophore orientations due to coupling to the DNA. The antenna effect 2 for $(Cy5)_1$ **$(Cy3)_{1\text{-}4}$ $(FAM)_{1\text{-}4}$** (all paths and path combinations) and the mean values are shown in Figure S 2B and C. Again, the antenna effect 2 increases with an increasing amount of donor and transmitter molecules. The variation of different paths and path combinations is again due to structural heterogeneity. Please note that the error bars for $(Cy5)_1$ **$(Cy3)_1$ $(FAM)_4$** (I, II, III, IV), $(Cy5)_1$ **$(Cy3)_1$ $(FAM)_1$** (I, II, III, IV) and $(Cy5)_1$ **$(Cy3)_4$ $(FAM)_4$** are the standard deviation of three separate measurements.

Spectral Properties of used fluorophores

In this study, we use three different fluorophores to create a three-color FRET cascade (donor: Fluorescein, FAM; transmitter: Cyanine3, Cy3; acceptor: Cynanine5, Cy5). The FRET efficiency highly depends on the spectral properties of used fluorophores and the donor-acceptor distance. For FRET to take place the emission spectrum of the donor molecule has to overlap with the absorption spectrum of the acceptor molecule.[2,3] The spectral overlap for each FRET pair is shown in Figures S 2A-C (A: FAM and Cy5, B: FAM and Cy3, C: Cy3 and Cy5). FRET between FAM and Cy5 is unlikely because the spectral overlap is relatively small. When Cy3 is introduced between these two fluorophores the light energy can be transferred from FAM over Cy3 to Cy5 as shown in Figure S 3D. The spectral overlap and the Förster radius of each FRET pair are summarized in Table S1. The Förster radius is the donor-acceptor distance at which the FRET efficiency is 50 % and it can be calculated using the following equation S4 and S5.

$$R_0^6 = \frac{9(ln10)\kappa^2 Q_D J}{128\pi^5 n^4 N_{AV}} \qquad \text{(S2)}$$

Here, κ^2 is the dipole orientation factor, Q_D is the fluorescence quantum yield of the donor molecule when the acceptor is absent, N_{AV} is Avogadro's number, n is the medium's refractive index and J is the spectral overlap integral representing the overlap of donor's emission and acceptor's absorption spectra.

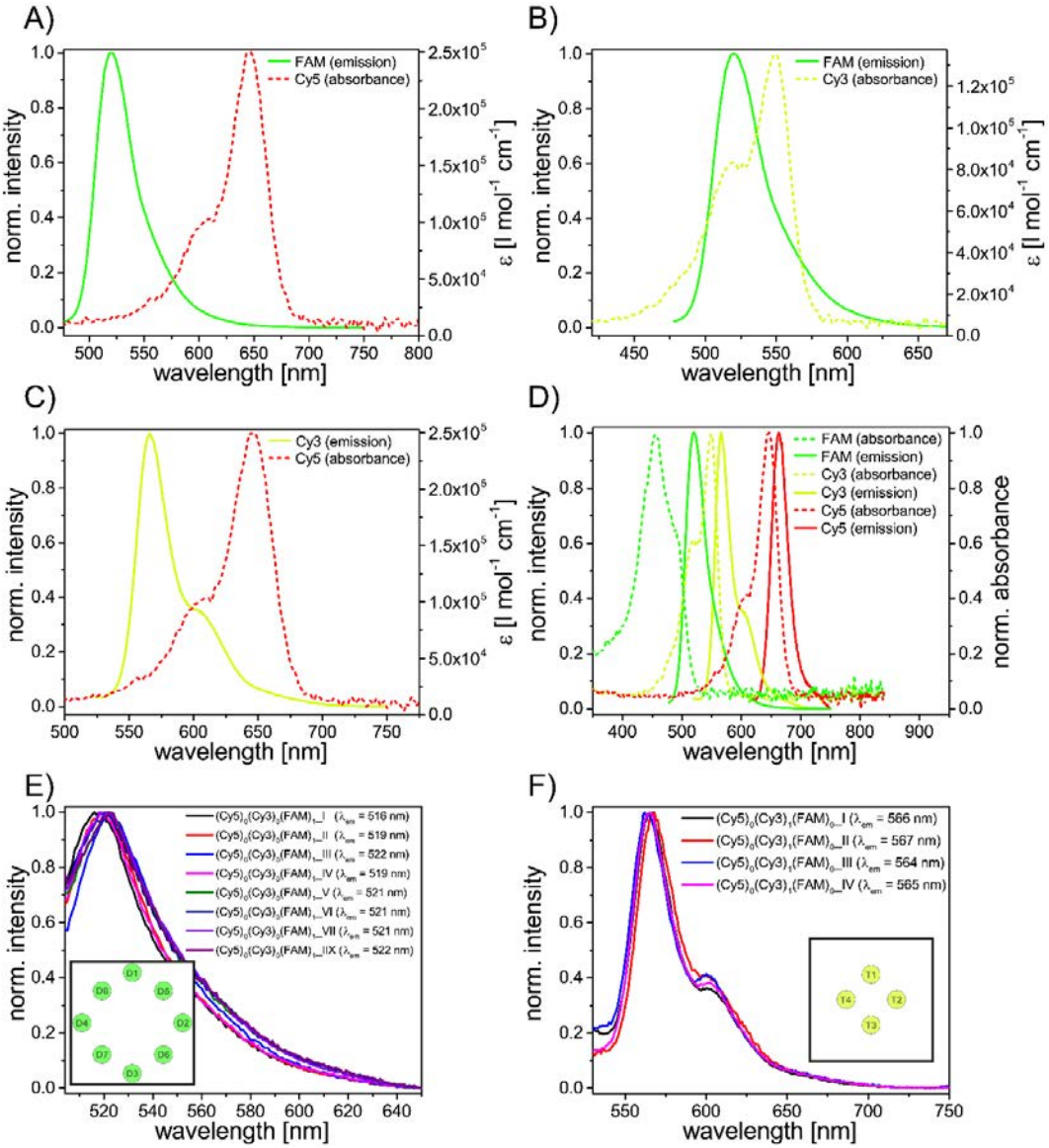

Figure S 4. Spectral overlap of different FRET pairs and emission spectra of FAM and Cy3 at different positions on the DNA origami structure. (A) Relatively small spectral overlap of FAM emission spectrum (solid line, green) and Cy5 absorption spectrum (dashed line, red). (B) Large spectral overlap between FAM emission spectrum (solid line, green) and Cy3 absorption spectrum (dashed line, yellow). (C) Relatively large spectral overlap between Cy3 emission spectrum (solid line, yellow) and Cy5 absorption spectrum (dashed line, red). (D) Emission and absorption spectra for the three-color FRET cascade (emission: solid line, absorption: dashed line, FAM: green, Cy3: yellow, Cy5: red). FAM is excited (450 nm) and transfers its energy over Cy3 (large spectral overlap) to Cy5 (emission maximum at 665 nm). (E) Normalized emission spectra of FAM at different positions on the DNA origami structure (λ_{ex} = 420 nm, int. time = 1 sec). The emission maximum ranges from 516 nm to 522 nm. (F) Normalized emission spectra (λ_{ex} = 500 nm, int. time = 0.2 sec) of Cy3 at different positions ($\lambda_{em,\,max.}$ = 564 – 567 nm).

The software PhotochemCAD 2.1 has been used to calculate the spectral overlap integrals J and the Förster radii R_0 for each FRET pair (FAM-Cy3, Cy3-Cy5, FAM-Cy5). The donor's emission and acceptor's absorption spectra for each FRET pair (acceptor's absorption spectrum in terms

of extinction coefficient) are imported and the dipole orientation factor (κ^2 = 2/3), the refractive index (n = 1.33) and the donor's quantum yield (*Q(FAM)* = 0.90; *Q(Cy3)* = 0.15)[6] are used as inputs in the software. The calculated Förster radii can be found in Table S1.

FAM and Cy3 have been placed on different positions on the DNA origami structures. The emission spectra for Cy3 and FAM for each position are shown in Figure 1E and F. The emission maximum of FAM varies slightly from 516 nm to 522 nm. The variation of the Cy3 emission maximum is also rather small (564 – 567 nm). The fluorescence decay time of FAM is also changing depending on the position on the DNA origami structure. The different FAM fluorescence decay times are summarized in Table S 2.

Table S 1. Overview of donor's quantum yields (Q_D), spectral overlap integral (J(λ)) and Förster radii (R_0) for the different FRET pairs.

FRET-pair	Q_D^6	$J(\lambda)$ [$nm^4 \cdot l \cdot mol^{-1}$]	R_0 [nm]
FAM-Cy5	0.90	$3.1 \cdot 10^{15}$	6.1
FAM-Cy3	0.90	$5.6 \cdot 10^{15}$	6.7
Cy3-Cy5	0.15	$7.4 \cdot 10^{15}$	5.2

Table S 2. Overview of different FAM fluorescence decay times τ_D (λ_{ex} = 490 nm, λ_{em} = 520 nm).

System	**Path**	τ_D [ns]
$(Cy5)_0(Cy3)_0(FAM)_1$	I	4.1
	II	4.3
	III	4.6
	IV	4.3
	V	4.6
	VI	4.4
	VII	4.3
	IIX	4.5
$(Cy5)_0(Cy3)_0(FAM)_2$	I + II	4.2
	I + III	4.3
	I + IV	4.2
	II + III	4.4

	II + IV	4.3
	III + IV	4.4
$(Cy5)_0(Cy3)_0(FAM)_3$	I + II + III	4.3
	I + II + IV	4.2
	I + III + IV	4.3
	II + III + IV	4.4
$(Cy5)_0(Cy3)_0(FAM)_4$	I + II + III + IV	4.3
	V + VI + VII + IIX	4.3
$(Cy5)_0(Cy3)_0(FAM)_8$	I + II + III + IV + V + VI + VII + IIX	4.1

Antenna effect 1 and FRET efficiency of different paths and path combinations

The antenna effect and the FRET efficiency vary depending on the path and path combination due to structural heterogeneity (variations in donor/ transmitter/ acceptor distances and fluorophore orientations due to coupling to DNA). AE1 and the FRET efficiency for every path and path combination (1x FAM or Cy3: I, II, III, IV; 2x FAM or Cy3: I + II, I + III, I+ IV, II + III, II+ IV, III + IV; 3x FAM or Cy3: I + II + III, I + II + IV, I + III + IV, II + III + IV) are shown in Figure S 4A-F. The error bars for the mono-molecular systems ($(Cy5)_1$ $(Cy3)_0$ **$(FAM)_1$**, $(Cy5)_1$ **$(Cy3)_1$ $(FAM)_4$** and $(Cy5)_1$ **$(Cy3)_1$ $(FAM)_1$**, for paths I - IV), **$(Cy5)_1$** $(Cy3)_0$ $(FAM)_0$, $(Cy5)_1$ $(Cy3)_0$ **$(FAM)_4$** and $(Cy5)_1$ **$(Cy3)_4$ $(FAM)_4$** are standard deviations of three separate measurements.

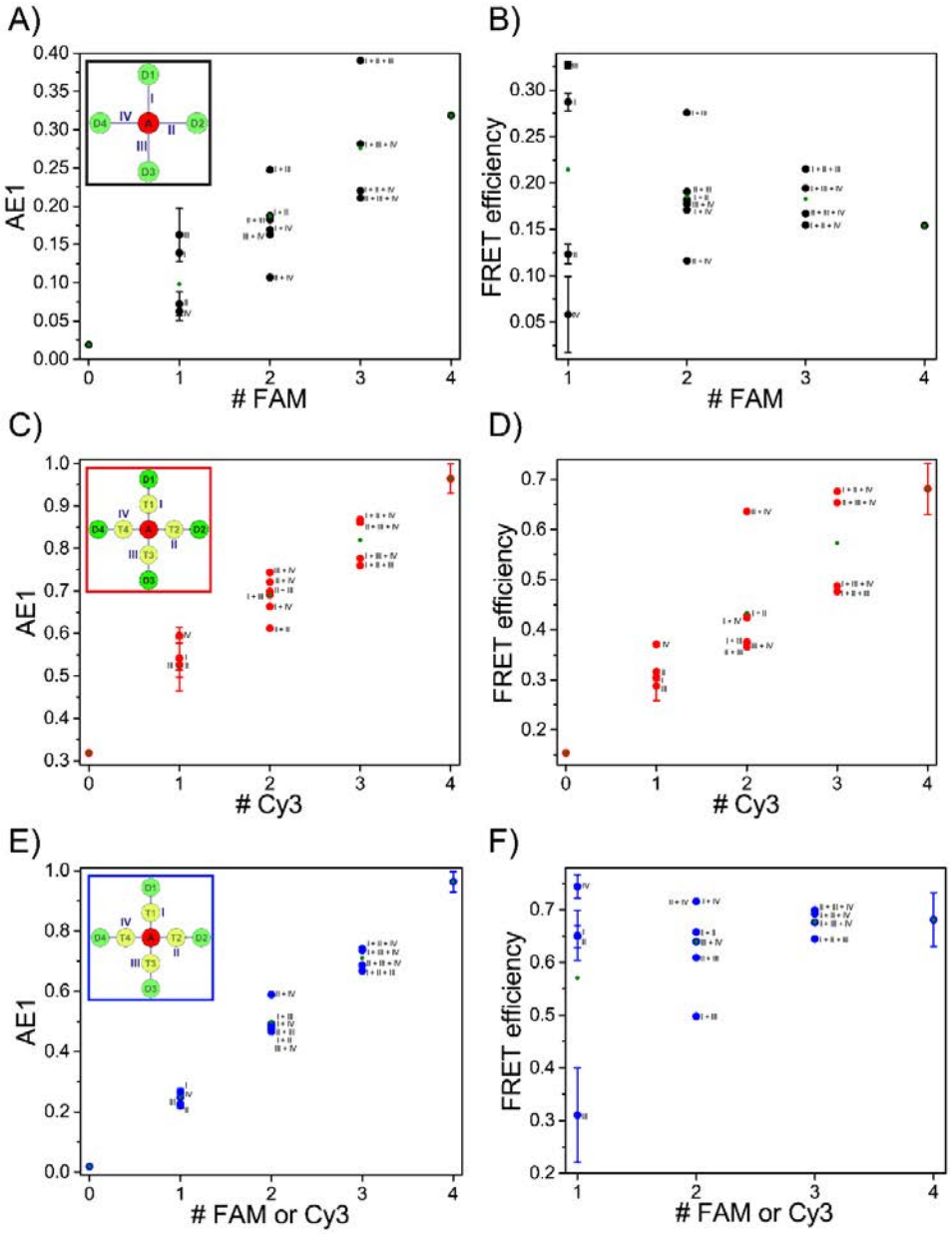

Figure S 5. AE1 and FRET efficiencies for $(Cy5)_1(Cy3)_0$**$(FAM)_{0\text{-}4}$** (A, B), $(Cy5)_1$**$(Cy3)_{0\text{-}4}$**$(FAM)_4$ (C, D) and $(Cy5)_1$**$(Cy3)_{0\text{-}4}$** **$(FAM)_{0\text{-}4}$** (E, F) for the different paths (I – IV) and path combinations (I + II, I + III, I + IV, II + III, II + IV, III + IV, I + II + III, I + II + IV, I + III + IV, II + III + IV). The error bars are the standard deviation from three separate measurements.

$(Cy5)_0(Cy3)_1(FAM)_0$ vs. $(Cy5)_0(Cy3)_4(FAM)_0$:

The emission intensity of Cy3 increases drastically from $(Cy5)_0$ **$(Cy3)_1$** $(FAM)_0$ to $(Cy5)_0$ **$(Cy3)_4$** $(FAM)_0$ when excited at both 450 nm (Figure S 5A) and 500 nm (Figure 5B) because the number of fluorophores per DNA origami structure increases.

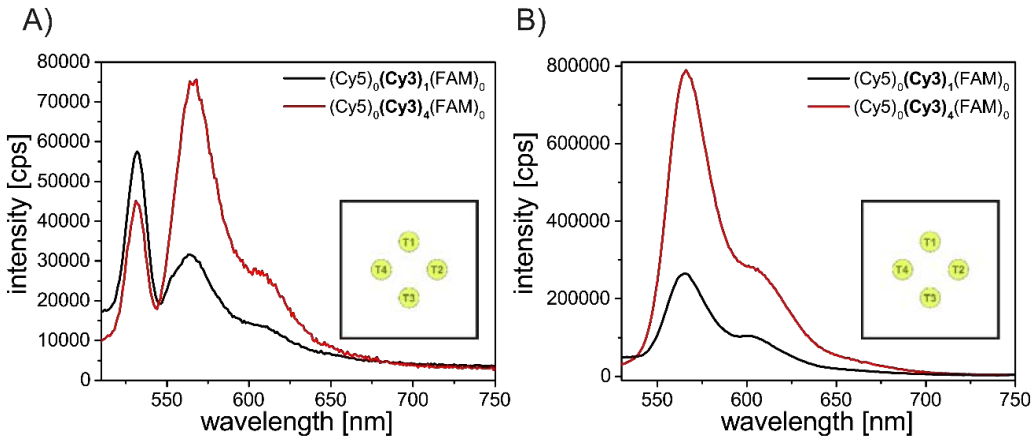

Figure S 6. Emission spectra of $(Cy5)_0$ **$(Cy3)_1$** $(FAM)_0$ (black) and $(Cy5)_0$ **$(Cy3)_4$** $(FAM)_0$ (red) showing that the Cy3 emission intensity increases with an increasing number of Cy3 molecules per DNA origami structure ((A) λ_{ex} = 450 nm, (B) λ_{ex} = 500 nm). The peak at 533 nm is the water Raman peak.

$(Cy5)_1(Cy3)_0(FAM)_{1\text{-}4}$: τ_D amplitudes and τ_1 values

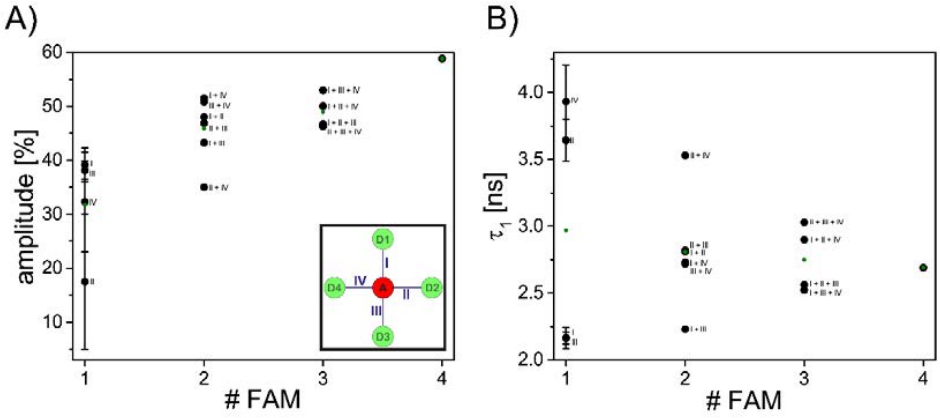

Figure S 7. (A) The amplitudes of τ_D for $(Cy5)_1$ $(Cy3)_0$ **$(FAM)_{1\text{-}4}$** increase with an increasing number of FAM molecules. The degree of unquenched FAM increases. (B) The values of the first decay time component τ_1 (quenched FAM fluorescence decay times) is almost unchanged with an increasing amount of FAM. The error bars are the standard deviation from three separate measurements.

The amplitudes of τ_D (unquenched FAM, Figure S 6A) increase with increasing FAM molecules whereas the values of τ_1 (quenched FAM due to FRET) are almost unchanged (Figure S 6B).

References

(1) Hemmig, E. A.; Creatore, C.; Wunsch, B.; Hecker, L.; Mair, P.; Parker, M. A.; Emmott, S.; Tinnefeld, P.; Keyser, U. F.; Chin, A. W. Programming Light-Harvesting Efficiency Using DNA Origami. *Nano Lett.* **2016**, *16* (4), 2369–2374. DOI: 10.1021/acs.nanolett.5b05139.

(2) Förster, T. Zwischenmolekulare Energiewanderung und Fluoreszenz. *Ann. Phys.* **1948**, *437* (1-2), 55–75. DOI: 10.1002/andp.19484370105.

(3) Förster, T. Energiewanderung und Fluoreszenz. *Naturwissenschaften* **1946**, *33* (6), 166–175. DOI: 10.1007/BF00585226.

(4) Lakowicz, J. R. *Principles of fluorescence spectroscopy*, 3rd ed; Springer: New York, 2006.

(5) Valeur, B.; Berberan-Santos, M. N. *Molecular Fluorescence: Principles and applications*, 2nd ed; Wiley-VCH: Weinheim, 2013.

(6) http://www.glenresearch.com//Technical/Extinctions.html.

Chapter 5

Discussion

DNA origami nanostructures are a perfect platform to assemble different molecules on the nanometer scale with a high local control to create for example a multitude of nanophotonic assemblies.[19,81,82,104] In these DNA origami structures, each staple strand can be modified individually making it possible to introduce a high variety of different molecules such as different fluorophores and biomolecules (*e.g.* DNA strands). Thus, it is possible to combine different molecules (fluorophores and DNA strands) on one nanostructure to study for example multi-color FRET arrays and additionally exploit the advantages of certain biomolecules to change their conformation induced by certain chemical inputs (*e.g.* G-quadruplex formation). Hence, controllable molecular switches with a fluorescence output signal can be generated. Furthermore, with the use of DNA origami structures 200 different positions on one structure are individually accessible. Thus, a variety of fluorophores can be attached without changing the specific structure of the DNA platform. This means, that starting from relatively simple systems (*e.g.* a two-color FRET system) more and more complex systems (*e.g.* photonic wires or multi-color light harvesting systems) can be established without changing the principle geometry of the used DNA template. Hence, possible influences on the FRET system by different parameters (flexibility and intermolecular distances) from different substrates (*e.g.* different arrangements of DNA double helices as shown by Buckhout-White *et al.*[176]) can be prevented.

In this section the development and analysis of such FRET arrays on DNA origami structures are discussed. Starting with the development of a two-color FRET system to study the conformational change of G rich DNA sequences from the random coil to the G-quadruplex structure. Here, the DNA origami structure does not only serve as a template phase to arrange the desired molecules but it also enables the development of an ion-selective FRET sensing scheme (manuscript "ion-selective FRET"[1]). This two-color FRET system has been further analyzed to study the reversibility of the G-quadruplex formation. Additionally, this two-color FRET system has been extended to create switchable photonic wire-like systems based on three- and four-color FRET

cascades (manuscript "switchable photonic wire"[2]). To utilize the multitude of possible attachment points on the DNA origami template even more, multi-color artificial light harvesting systems have been analyzed. In such systems, the number of fluorophores and the orientation to one another can be straightforwardly controlled by introducing or leaving out certain modified staple strands (manuscript "artificial light harvesting system"[3]).

Ion-selective FRET[1]

In the first studies of this work, the conformational change of G rich DNA strands induced by either K^+ or Na^+ has been analyzed for the free DNA sequence and for the DNA strand attached to DNA origami structures (the exact designs of both systems are discussed in detail in section 3.3.1). For this, RevHumTel has been analyzed ((5'-Cy3-TT $(GGG\ ATT)_4$)-FAM). The conformational change induced by monovalent cations has been studied using FRET. Here, the FRET efficiency increases due to the G-quadruplex formation because the donor (here: FAM, λ'_{em} = 515 nm) and acceptor molecule (here: Cy3, λ'_{em} = 565 nm) are in closer proximity in the compact G-quadruplex structure compared to the single strand. The emission spectra for the different systems after the addition of either NaCl or KCl are depicted in figure 5.1a-e. For the free telomeric DNA, the emission spectrum excited at 450 nm changes drastically upon both, KCl and NaCl addition (see figure 5.1a, b). The emission intensity of FAM decreases and at the same time the emission intensity of Cy3 becomes more pronounced after salt addition because of higher FRET. Please note that FRET also occurs when no salt is present (unfolded state) showing that FAM and Cy3 are already in close proximity in the random coil. Nevertheless, a change in FRET efficiency can still be recorded due to the G-quadruplex formation. Please note that the behavior of G-quadruplex formation in presence of KCl and NaCl is rather different. For KCl, an addition of ca. 1 mM leads to a change in the emission spectrum (G-quadruplex folds) whereas for NaCl a higher amount is needed (at least 25 mM). This can be ascribed to different association constants for KCl and NaCl.[17] The association constants for K^+ and Na^+ have been determined based on the emission intensities of FAM and Cy3 (see supporting information (SI) of the manuscript "ion-selective FRET", figure S3[1]) and found to be $1.5 \cdot 10^4$ M^{-2} for K^+ and 33.7 M^{-2} for Na^+. This shows that higher amounts of NaCl are needed to actually fold the G-quadruplex structure. This is an interesting aspect which can be exploited for selective K^+ sensing schemes.[17,154,158,197] Unfortunately, for the free telomeric DNA the discrimination between K^+ and Na^+ is only feasible at low salt concentrations. At higher salt concentrations (especially at physiological relevant Na^+ concentration of ca. 145 mM) the difference in the FRET efficiency (determined based on FAM fluorescence decay time) between KCl and NaCl is negligible (see figure 5.1f, gray and red curves). Thus, the free telomeric DNA is not

applicable for a selective K^+ sensing scheme. Nevertheless, by introducing RevHumTel on DNA origami structures a high ion-selectivity is achieved. As shown in figure 5.1c-e the emission spectra change (FAM emission intensity decreases and Cy3 emission intensity increases) after the addition of KCl (G-quadruplex formation) whereas after NaCl addition the emission spectra stay the same. Hence, the overall donor-acceptor distance does not change in presence of NaCl meaning that the G-quadruplex cannot fold on DNA origami structures which is additionally confirmed by the unchanged FRET efficiency shown in figure 5.1f (dark red curve).

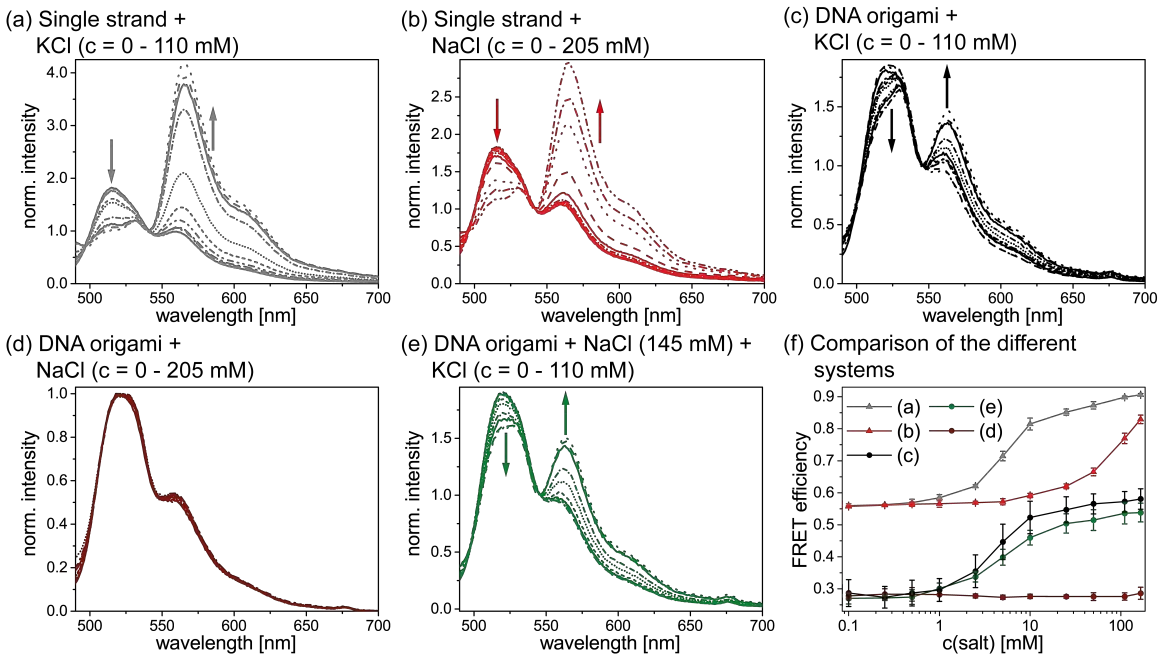

Figure 5.1: Emission spectra (λ_{ex} = 450 nm) for the free telomeric DNA (a, b) and telomeric DNA attached to DNA origami structures (c, d, e) (RevHumTel). (a, b) The addition of KCl (a) and NaCl (b) leads to a decrease in FAM emission and an increase in Cy3 emission due to G-quadruplex formation. (c, d, e) For RevHumTel on DNA origami structures, only KCl addition leads to a change of the emission spectrum (c) even in presence of 145 mM NaCl (e). The G-quadruplex does not fold in presence of NaCl (emission spectrum does not change, d). (f) FRET efficiency plotted *vs.* the salt concentration showing the difference between free RevHumTel (KCl (gray), NaCl (red)) and RevHumTel attached to DNA origami structures (KCl (black), KCl in presence of 145 mM NaCl (green), NaCl (dark red)). Selective K^+ sensing is possible even in presence of high amounts of Na^+ on DNA origami structures.

Advantageously, K^+ is still detectable in presence of high amounts of NaCl (145 mM, figure 5.1e, f, green curve). Additionally, this ion-selectivity is valid over a high variety of monovalent ions as shown in figure 5.2a (SI of the manuscript "switchable photonic wire", figure S2[2]). Only divalent ions such as Mg^{2+} and Ca^{2+} induce a change of the FRET signal although the signal is still not as strong as for K^+. The association constants for K^+ addition of RevHumTel on DNA origami structures have been calculated (see SI of the manuscript "ion-selective FRET", figure S3[1]) in absence of

additional NaCl ($2.6 \cdot 10^4$ M^{-2}) and presence of 145 mM NaCl ($1.4 \cdot 10^4$ M^{-2}). Since the determined association constants for KCl addition are nearly the same for all systems (free RevHumTel, RevHumTel on DNA origami structures in absence and presence of additional NaCl), the sensitivity towards K^+ is neither influenced by the DNA origami platform nor by the presence of additional Na^+ (for the DNA origami system). The FRET efficiencies which have been calculated based on the FAM fluorescence decay times for all systems are depicted in figure 5.1f. Please note that the difference of the FRET efficiency between free telomeric DNA and telomeric DNA on DNA origami structures is due to the different intermolecular distances which are discussed in detail in section 3.3.1.

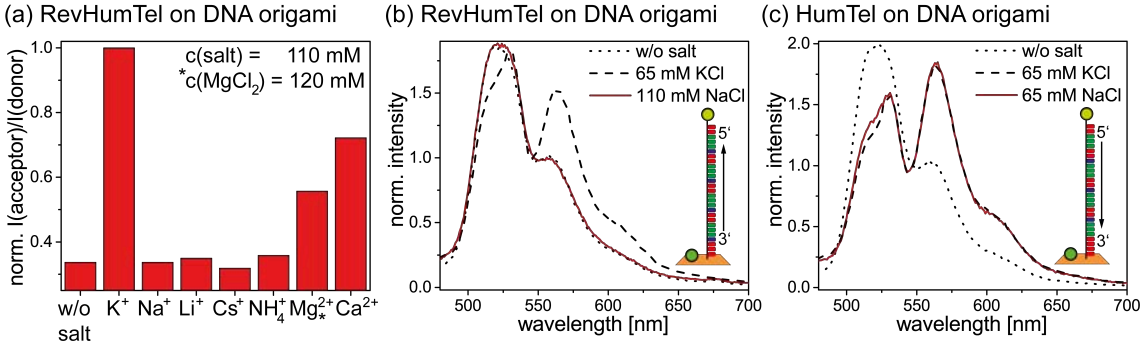

Figure 5.2: (a) Normalized acceptor-donor emission intensity ratio for RevHumTel on DNA origami structures after the addition of different cations showing the high ion-selectivity towards K^+. (b, c) Emission spectra (λ_{ex} = 450 nm) for RevHumTel (b) and HumTel (c) on DNA origami structures (red: T, green: G, blue: A). Only RevHumTel is selective for K^+ (b, dashed spectrum). The emission spectrum is not influenced by the addition of NaCl (b, red spectrum). For HumTel the emission spectrum changes after both, KCl (c, dashed spectrum) and NaCl addition (c, red spectrum).

Furthermore, not only the DNA origami structure makes sure that the FRET system is highly ion-selective but also the telomeric DNA sequence itself influences the ion-selectivity as depicted in figure 5.2b, c. By changing the direction of the telomeric DNA (RevHumTel (5'-TT (GGG ATT)$_4$ T) *vs.* HumTel (5'-TT (GGG TTA)$_3$ GGG TTT T)) the ion-selectivity for K^+ vanishes. The explanation for the K^+ selectivity of RevHumTel on DNA origami structures is not easily accessible. Two possible reasons for this ion-selectivity are discussed in the following paragraph. On the one hand, the DNA origami structure could sterically hinder the formation of certain G-quadruplex structures. As mentioned above the specific G-quadruplex structure can be influenced by an alteration of the DNA sequence or by different cations (see section 2.2.1). Hence, the formation of certain G-quadruplex structures (most likely those with diagonal or lateral loops) could be prevented due to the relatively large DNA origami structure. CD measurements of the unmodified G-quadruplex (without fluorophores and without the DNA origami platform) have shown that both, the DNA sequence (RevHumTel and HumTel) and the cation (K^+ and Na^+) have an influence on the CD signal and there-

fore induce different G-quadruplex structures (see figure 5.3a-d). By comparing the measured CD spectra with CD spectra reported in literature[131] certain G-quadruplex structures have been assigned to the telomeric DNA sequences in presence of KCl and NaCl, respectively. RevHumTel as depicted in figure 5.3a shows a negative peak at 240 nm and a positive peak at 288 nm. Additionally, a shoulder at ca. 275 nm is visible. This can be attributed to a "hybrid-type" G-quadruplex structure (one external and two lateral loops).[131] In presence of NaCl, the CD spectra of RevHumTel look entirely different (figure 5.3b). Here, two distinct positive peaks at 270 nm and 290 nm are observable. Unfortunately, the assignment of an exact G-quadruplex structure is rather difficult. The CD spectrum (figure 5.3b) indicates either a "hybrid-type" G-quadruplex (one external, one lateral and one diagonal loop) or a mixture of parallel and anti-parallel G-quadruplex structures.[131] Furthermore, the CD spectra show clearly that RevHumTel is more sensitive to KCl than to NaCl (G-quadruplex CD signals are visible at lower KCl concentration when compared to NaCl addition). The CD spectra for HumTel (figure 5.3c, d) are different compared to the CD spectra of RevHumTel showing that different G-quadruplex structures are folded.

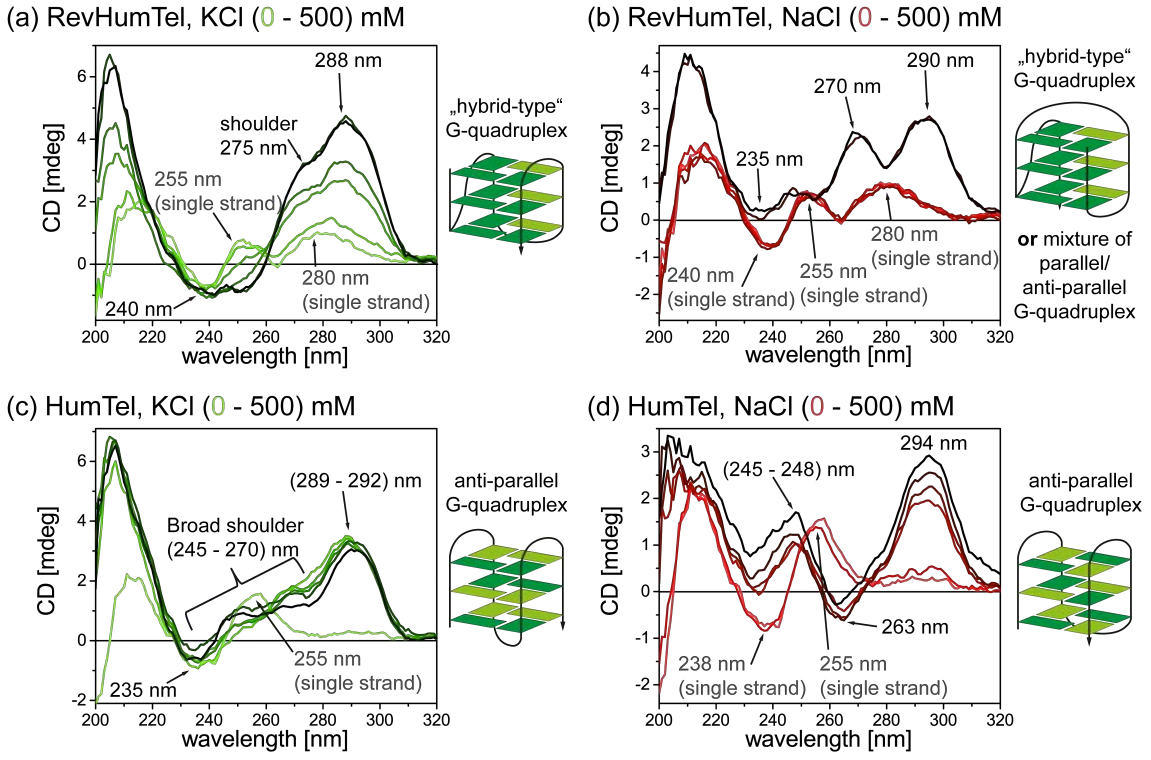

Figure 5.3: CD spectra of unmodified free telomeric DNA (c(DNA) = 8.5 µM). (a) RevHumTel (5'-TT (GGG ATT)$_4$) after KCl addition, (b) RevHumTel after NaCl addition, (c) HumTel (5'-TT (GGG TTA)$_3$GGG TTT) after KCl addition and (d) HumTel after NaCl addition. The salt concentration for all measurements range from 0 mM (light color) to 500 mM (darker color) (c(salt) = (2, 10, 20, 200, 500) mM). The CD spectra have been compared to CD spectra reported in literature to resolve the specific G-quadruplex structure.[131]

In presence of KCl, the CD spectra give rise to a positive peak at (289 - 292) nm and a broad shoulder ((245 - 270) nm, figure 5.3c). This indicates the formation of an anti-parallel G-quadruplex structure ("basket-type", one diagonal and two lateral loops).[131] Again, the G-quadruplex structure of HumTel is also influenced by the cation. In presence of NaCl, two positive peaks ((245 - 248) nm and 294 nm) and a negative peak at 263 nm are visible (figure 5.3d). This can be ascribed to an anti-parallel G-quadruplex structure ("chair-type", 3 lateral loops).[131] Similar to RevHumTel, HumTel also folds into G-quadruplexes at lower KCl than NaCl concentrations. Furthermore, HumTel folds into G-quadruplexes at lower salt concentrations than RevHumTel (HumTel, KCl: ca. 2 mM; HumTel, NaCl: ca. 10 mM; RevHumTel, KCl: ca. 10 mM; RevHumTel, NaCl: ca. 200 mM (data based on the measured salt concentrations, c = (2, 10, 20, 200, 500) mM)). Please note that the overall G-quadruplex structure for both, RevHumTel and HumTel (KCl and NaCl) is unaffected by the salt concentration. These results show that the specific G-quadruplex structure is immensely influenced by different parameters. Unfortunately, the G-quadruplex formation on DNA origami structures cannot be resolved using CD spectroscopy because the DNA origami itself leads to intense absorption signals which overlay the G-quadruplex signals. Hence, the exact G-quadruplex structure on DNA origami structures is not known (DNA origami could also influence the specific G-quadruplex structure) and therefore the assumption that only certain G-quadruplex structures fold on DNA origami substrates cannot be controlled by CD spectroscopy. On the other hand, the reason for the ion-selectivity of RevHumTel could be explained by the specific folding pathways. In this sense different intermediate states (hairpin, triplex or other G-quadruplex structures) could be formed in the different systems. It could be conceivable that RevHumTel in presence of NaCl passes through an intermediate state which cannot be formed on DNA origami structures leading to the ion-selectivity. Unfortunately, these explanations are only assumptions and could not be fully resolved in this work. Other structural and kinetics investigations (*e.g.* NMR, X-ray crystallography and molecular modeling) would be necessary to actually explain the reason for the ion-selectivity of RevHumTel on DNA origami structures but this is beyond the scope of this work.

Switchable photonic wire[2]

After analyzing the formation of G-quadruplexes the reversibility of this formation has been studied to develop different switchable FRET systems on DNA origami structures. The FRET switching has been thoroughly analyzed in the two-color FRET system discussed before (FAM/RevHumTel-Cy3). Because of the possibility to modify DNA origami structures relatively easy with different fluorophores, this two-color FRET system has been extended to create a three-color FRET cascade (FAM/RevHumTel-Cy3/Cy5) and furthermore to create a four-color FRET-based photonic wire (FAM/Rev-

HumTel-Cy3/Cy5/IRDye700). The different designs and structural properties of the studied FRET systems are discussed in section 3.3.2. The principle of the FRET switch on DNA origami structures is based on the G-quadruplex formation induced by K^+ (high FRET) with a subsequent unfolding of the G-quadruplex induced by cryptand addition (low FRET). Cryptand is a crown ether-like substance which encapsulates K^+ [198,199] and removes it from the core of the G-quadruplex which leads to an unfolding.

As a proof of principle for possible FRET switching the two-color FRET system discussed in the manuscript "ion-selective FRET"[1] (FAM/RevHumTel-Cy3 on DNA origami structures) has been analyzed at first. The emission spectra and FRET efficiencies (calculated based on FAM fluorescence decay times) are depicted in figure 5.4a, b. As shown in figure 5.4a (blue spectrum) the FAM emission intensity is dominant and the Cy3 emission intensity is rather low in the initial unfolded state. The overall FRET efficiency is relatively small in the unfolded state ($E = 0.42 \pm 0.01$, figure 5.4b) because of a long donor-acceptor distance. After KCl addition (G-quadruplex formation) the FRET efficiency increases ($E = 0.56 \pm 0.01$, figure 5.4b) which is also visible by a drop in FAM emission intensity and at the same time an increase in Cy3 emission intensity (figure 5.4a, black spectrum). The G-quadruplex unfolds subsequently when cryptand is added which is noticeable by a higher FAM emission intensity and a weaker Cy3 emission intensity (figure 5.4a, red spectrum). The overall FRET efficiency decreases again due to G-quadruplex unfolding ($E = 0.39 \pm 0.01$). Please note that the FAM emission intensity does not return to the initial value (visible through alteration of FAM emission peak due to the underlying water Raman peak) because cryptand quenches the FAM fluorescence (see SI of the manuscript "switchable photonic wire", figure S4[2]). The system can be restored after the removal of KCl and cryptand from the solution using centrifugal filters (figure 5.4a, green spectrum, $E = 0.42 \pm 0.01$). Thus, the switching between low and high FRET (unfolded and folded G-quadruplex) can be repeated several times on the DNA origami structure (figure 5.4b). It has to be noted that the overall DNA origami concentration decreases after each filtration step leading to a decrease in the overall emission intensity. To exploit the potential of the relatively simple modification of DNA origami structures, a third fluorophore (Cy5, $\lambda'_{em} = 665$ nm) has been introduced to create a switchable FRET cascade (figure 5.4c, d). In such a FRET cascade the light energy is transferred from FAM (donor) over Cy3 (transmitter) to Cy5 (acceptor). In the studied system, RevHumTel modified with Cy3 is placed in the middle of the FRET cascade. Hence, the FRET cascade is less efficient in the unfolded state (strong FAM emission and weak Cy3 and Cy5 emission, figure 5.4c, blue spectrum, $E = 0.41 \pm 0.01$) because FRET between FAM and Cy3 in this conformation is weak as mentioned above and direct FRET between FAM and Cy5 is highly unlikely (small spectral overlap and long donor-acceptor distance). Thus, the FRET cascade is only efficient when all

three fluorophores are in close proximity as in the case of the folded G-quadruplex. This is shown in figure 5.4c (black spectrum). Here, the FAM emission intensity decreases and the Cy3 and Cy5 emission intensities increase upon KCl addition. Again, the FRET efficiency increases due to the G-quadruplex formation (figure 5.4d, $E = 0.55 \pm 0.01$). Subsequently, the G-quadruplex unfolds upon cryptand addition leading to a low FRET signal once more (stronger FAM and weaker Cy3 and Cy5 emission intensities, figure 5.4c, red spectrum, $E = 0.40 \pm 0.01$). After the removal of KCl and cryptand from the solution the G-quadruplex formation can be repeated (figure 5.4d). Again, the formation of G-quadruplex structures can be repeated at least five times on DNA origami structures.

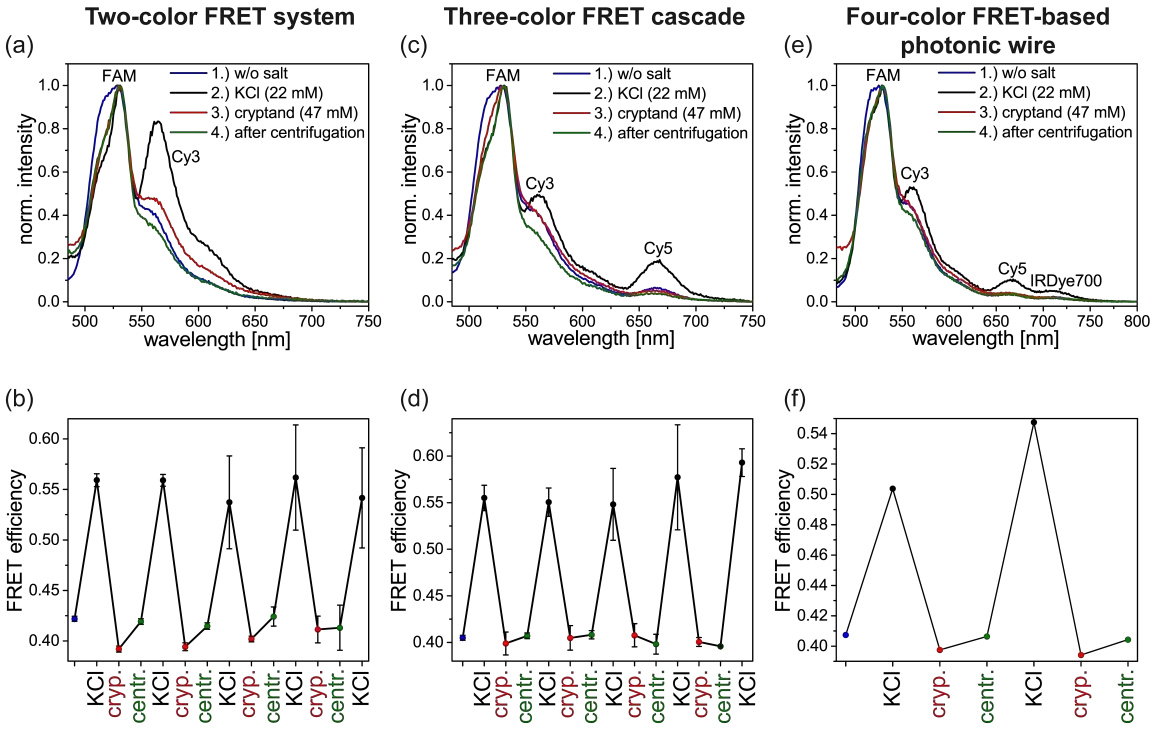

Figure 5.4: Normalized emission spectra (λ_{ex} = 450 nm, a, c and e) and FRET efficiencies (b, d and f) for the two-color FRET system (a, b), three-color FRET cascade (c, d) and four-color FRET-based photonic wire (e, f). The emission intensity of FAM decreases and the emission intensities of Cy3, Cy5 and IRDye700, respectively, increase after KCl addition (black) due to G-quadruplex formation (FRET efficiency increases). Subsequently, the G-quadruplex unfolds upon cryptand addition (red, FAM emission intensity increases; Cy3, Cy5 and IRDye700 emission intensities decrease, FRET efficiency decreases). The system is restored after a filtration step to remove KCl and cryptand (green). The switching is based on the folding and unfolding of G-quadruplex structures. The G-quadruplex formation can be repeated up to five times on DNA origami structures. For the four-color FRET system, only two folding steps are shown as a proof of principle.

To finally show the possibility to create switchable photonic wires on the nanometer scale on DNA origami structures, a fourth fluorophore (IRDye700, λ'_{em} = 710 nm) has been introduced (figure 5.4e, f). In this photonic wire the excitation energy is

transferred *via* three FRET steps from one end to the other, starting from the initial donor (FAM) over two transmitter molecules (Cy3 and Cy5) to the final acceptor (IRDye700). Again, RevHumTel modified with Cy3 has been placed in the middle of the photonic wire-like system to generate a FRET switch. In this way, a switchable photonic wire with a length of ca. 10 nm and a spectral range of ca. 200 nm has been created. As shown in figure 5.4e, the photonic wire is rather inefficient when the G-quadruplex is unfolded (blue spectrum, $E = 0.41$). Here, FAM emission is dominant and the emission intensities of Cy3, Cy5 and especially IRDye700 are rather weak. The signal transduction of the photonic wire can be turned on upon KCl addition. Due to the G-quadruplex formation the fluorophores are getting in closer proximity (FAM and Cy3, Cy3 and Cy5) leading to a more efficient signal transduction (IRDye700 emission becomes visible, figure 5.4e, black spectrum) and furthermore to a higher FRET efficiency ($E = 0.51$). As for the other switchable FRET systems, the G-quadruplex is unfolded after cryptand addition leading to a reduced FRET signal (figure 5.4e, red spectrum, $E = 0.40$). Again, the system is restored after a filtration step (figure 5.4e, green spectrum). The switching between "on" and "off" state of the photonic wire (signal transduction or no signal transduction) has been exemplary shown for two switching cycles (figure 5.4f).

In conclusion, in this study it has been shown that DNA origami structures can be used to assemble a variety of fluorophores and to create photonic wire-like systems with a relatively simple method. Furthermore, by using biomolecules which change their conformation based on chemical inputs an *in situ* switch has been created to change the photonic wire between an "on" and an "off" state.

Artificial light harvesting system[3]

As shown above, the overall acceptor emission intensity of a mono-molecular FRET cascade (one donor, one transmitter, one acceptor) is rather weak. Artificial light harvesting systems can be used to improve the brightness of the acceptor molecule. In such artificial light harvesting systems, the light energy is absorbed by many donor molecules and funneled to the acceptor molecule which is placed in the center of the system *via* one or multiple FRET steps depending on the number of fluorophores (see also section 2.3.3). By using multiple different fluorophores in one light harvesting system the range of possible excitation wavelength is broadened which is important in the field of artificial photosynthesis. Thus artificial light harvesting systems based on, for example, a three-color FRET cascade increase on the one hand the overall emission intensity of the acceptor molecule and on the other hand extend the excitation wavelength range. Here, artificial light harvesting systems based on a FAM/Cy3/Cy5 FRET cascade and assembled on DNA origami structures (detailed discussion of fluorophore arrangement and distances in section 3.3.3) have been analyzed in terms

of antenna effect ($AE1$ and $AE2$, see manuscript "artificial light harvesting system" equation 1 and 2, respectively[3]) and FRET efficiency.

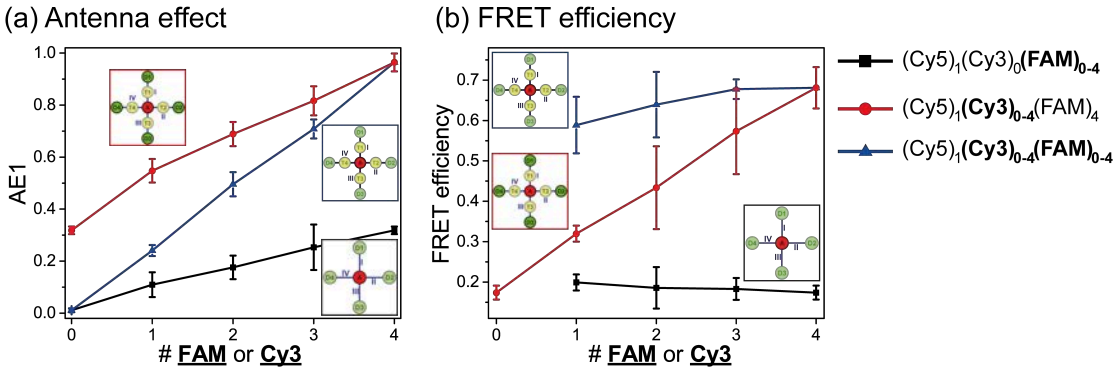

Figure 5.5: Antenna effect and FRET efficiency for different light harvesting systems on DNA origami structures. (a)$AE1$ plotted *vs.* the number of FAM and Cy3 molecules, respectively (number on the x-axis refers to the molecules which are increased indicated by highlighted letters) for different light harvesting systems. The $AE1$ increases for all analyzed systems ($(Cy5)_1$ $(Cy3)_0$ $\mathbf{(FAM)_{0\text{-}4}}$ (black), $(Cy5)_1$ $\mathbf{(Cy3)_{0\text{-}4}}$ $(FAM)_4$ (red), $(Cy5)_1$ $\mathbf{(Cy3)_{0\text{-}4}}$ $\mathbf{(FAM)_{0\text{-}4}}$ (blue)). The more fluorophores are present the brighter the Cy5 emission becomes. (b) The overall FRET efficiency is rather small for the two-color FRET system (FAM/Cy5) and decreases slightly with an increasing number of FAM molecules ($(Cy5)_1$ $(Cy3)_0$ $\mathbf{(FAM)_{1\text{-}4}}$ (black)). For $(Cy5)_1$ $\mathbf{(Cy3)_{0\text{-}4}}$ $(FAM)_4$ (red), the FRET efficiency increases linearly with an increasing number of transmitter molecules. Finally, for $(Cy5)_1$ $\mathbf{(Cy3)_{1\text{-}4}}$ $\mathbf{(FAM)_{1\text{-}4}}$ (blue), the overall FRET efficiency is high and increases slightly with an increasing number of fluorophores. The FRET efficiency depends on the fluorophores and their spectral overlap.

Firstly, the two-color FRET system using FAM as a donor molecule and Cy5 as an acceptor molecule has been analyzed. Please note that the overall light harvesting and FRET efficiency is rather low for this system because the spectral overlap between the FAM emission and Cy5 absorption spectra is rather small. Nevertheless, the AE can be tuned by increasing the number of FAM molecules ($(Cy5)_1$ $(Cy3)_0$ $\mathbf{(FAM)_{0\text{-}4}}$, $AE1$ = 0.02 - 0.32, number of fluorophore written in bold letters has been increased) as shown in figure 5.5a (black curve). The FRET efficiency (calculated based on FAM amplitude averaged fluorescence decay time) on the other hand decreases slightly when the number of FAM molecules increases (E = 0.21 - 0.15, figure 5.5b, black curve). This is attributed to the fact that the amplitude of unquenched FAM increases in a system with low FRET efficiency leading to an increase of the amplitude averaged fluorescence decay time (E decreases). To increase the AE and the FRET efficiency, a transmitter molecule (Cy3) is introduced to the two-color FRET system ($(Cy5)_1$ $\mathbf{(Cy3)_{0\text{-}4}}$ $(FAM)_4$). Here, the AE ($AE1$ = 0.32 - 0.96 $\pm$ 0.03) and the FRET efficiency (E = 0.15 - 0.68 $\pm$ 0.05) increase with an increasing number of Cy3 molecules as shown in figure 5.5a, b (red curve). The light energy can be transferred more efficiently from FAM to Cy5 when more and more Cy3 molecules

are present. Additionally, the number of FAM and Cy3 molecules has been increased to the same extent ((Cy5)$_1$ **(Cy3)$_{0\text{-}4}$ (FAM)$_{0\text{-}4}$**). The *AE* for such light harvesting systems increases linearly (*AE*1 = 0.02 - 0.96 ± 0.03) with an increasing number of fluorophores because more light energy is absorbed and subsequently transferred to the acceptor molecule (figure 5.5a, blue curve). The slope for (Cy5)$_1$ **(Cy3)$_{0\text{-}4}$ (FAM)$_{0\text{-}4}$** is steeper compared to (Cy5)$_1$ **(Cy3)$_{0\text{-}4}$** (FAM)$_4$. This is ascribed to the fact that for (Cy5)$_1$ **(Cy3)$_{0\text{-}4}$ (FAM)$_{0\text{-}4}$** the direct FAM-to-Cy5 FRET increases due to an increasing number of FAM molecules and for (Cy5)$_1$ **(Cy3)$_{0\text{-}4}$** (FAM)$_4$ it stays the same. The FRET efficiency for (Cy5)$_1$ **(Cy3)$_1$ (FAM)$_1$** is already high (*E* = 0.57) and increases slightly with the addition of Cy3 and FAM molecules (*E* = 0.57 - 0.68 ± 0.05) as shown in figure 5.5b (blue curve). These results show that the *AE* is highly dependent on the overall number of fluorophores assembled in a light harvesting system. It increases with more and more fluorophores arranged around the acceptor molecule. The FRET efficiency on the other hand depends on the spectral properties of the fluorophores. It is improved by a larger spectral overlap between the donor's emission and acceptor's absorption spectra. For the system (Cy5)$_1$ **(Cy3)$_4$ (FAM)$_4$**, *AE*1 (direct FAM excitation, involves two FRET steps) is tuned such that the emission of Cy5 is almost as high as when it is directly excited at 600 nm (*AE*1 is close to one). *AE*2 (direct Cy3 excitation, involves one FRET step) as shown in the SI of the manuscript "artificial light harvesting"[3] (figure S2) can be improved to a value of 5.7 ± 0.3 showing that the light harvesting system can be efficiently excited at 500 nm.

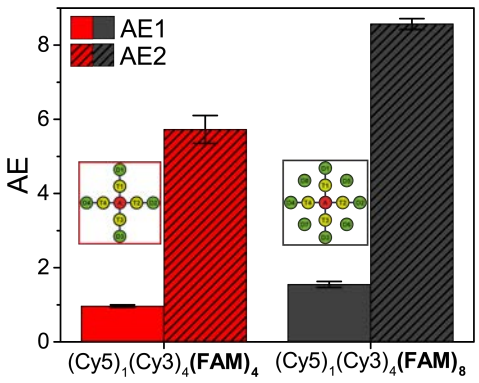

Figure 5.6: The antenna effect (*AE*1 (plain) and *AE*2 (hatched)) is optimized by adding additional FAM molecules ((Cy5)$_1$ (Cy3)$_4$ **(FAM)$_4$** (red) *vs.* (Cy5)$_1$ (Cy3)$_4$ **(FAM)$_8$** (gray)).

Finally, the artificial light harvesting system is optimized by introducing a total number of eight FAM molecules (the design of the system is shown in section 3.3.3). Both, *AE*1 and *AE*2 are significantly higher for (Cy5)$_1$ **(Cy3)$_4$ (FAM)$_8$** (*AE*1 = 1.58 ± 0.08, *AE*2 = 8.6 ± 0.2) than for (Cy5)$_1$ **(Cy3)$_4$ (FAM)$_4$** (*AE*1 = 0.96 ± 0.03, *AE*2 =

5.7 ± 0.4) as shown in figure 5.6. Please note that the FRET efficiency is only slightly influenced by additional FAM molecules ($E((\mathrm{Cy5})_1$ **$(\mathrm{Cy3})_4$ $(\mathrm{FAM})_8$**$) = 0.71 \pm 0.02$, $E((\mathrm{Cy5})_1$ **$(\mathrm{Cy3})_4$ $(\mathrm{FAM})_4$**$) = 0.68 \pm 0.05$, see figure 5d in the manuscript "artificial light harvesting system" [3]).

Fluorescence excitation spectra have been measured to evaluate the light harvesting capability in terms of the excitation wavelength range (see figure 5.7a). The single Cy5 molecule can only be efficiently excited in the range of its excitation peak (ca. (570 - 700) nm, figure 5.7a, black spectrum). When Cy5 is surrounded by four Cy3 molecules ($(\mathrm{Cy5})_1$ **$(\mathrm{Cy3})_4$** $(\mathrm{FAM})_0$, figure 5.7a, green spectrum) the range of possible excitation wavelengths is extended ((570 - 700) nm, Cy5 and Cy3 excitation peaks). This can be further extended by introducing FAM as an initial donor molecule. Already for the mono-molecular three-color FRET cascade, a third excitation peak appears ($(\mathrm{Cy5})_1$ **$(\mathrm{Cy3})_1$ $(\mathrm{FAM})_1$**, figure 5.7a, blue spectrum) meaning that the light harvesting complex can be excited at a broader wavelength range (ca. (425 - 700) nm). However, the overall intensity is rather weak for this arrangement. The intensity of the FAM excitation maximum can be increased by adding more FAM molecules ($(\mathrm{Cy5})_1$ **$(\mathrm{Cy3})_1$ $(\mathrm{FAM})_4$**, figure 5.7a, dark red spectrum) and the overall intensity of the excitation spectrum can be increased by the addition of both, Cy3 and FAM molecules ($(\mathrm{Cy5})_1$ **$(\mathrm{Cy3})_4$ $(\mathrm{FAM})_4$**, figure 5.7a, red spectrum). To finally optimize the artificial light harvesting system, the number of FAM molecules is increased to eight ($(\mathrm{Cy5})_1$ **$(\mathrm{Cy3})_4$ $(\mathrm{FAM})_8$**, figure 5.7a, gray spectrum). Now an artificial light harvesting system is created which can be efficiently excited in a wavelength range from 425 to 700 nm.

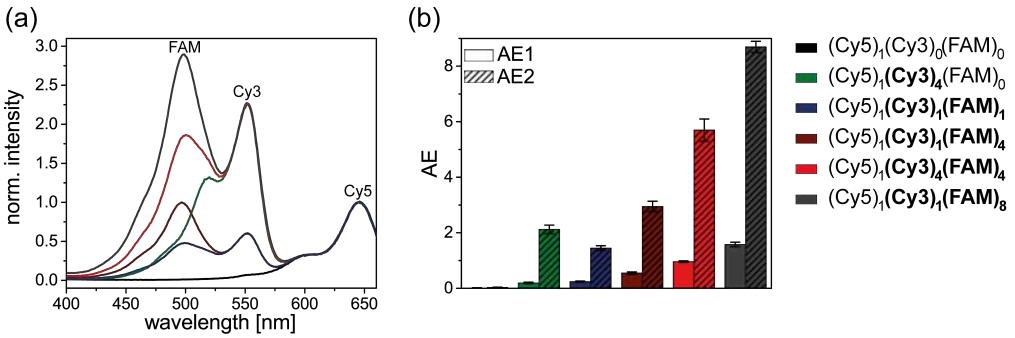

Figure 5.7: (a) Excitation spectra ($\lambda_{em} = 680$ nm) of different light harvesting systems. The range of possible excitation wavelengths is extended by using multiple fluorophores. (b) Overview of $AE1$ and $AE2$ values for different light harvesting systems showing the significant increase due to higher numbers of assembled fluorophores. The AE values for the single acceptor molecule ($(\mathrm{Cy5})_1$ $(\mathrm{Cy3})_0$ $(\mathrm{FAM})_0$) are rather small ($AE1 = 0.02$, $AE2 = 0.04$).

To summarize the findings of this study, the AE values ($AE1$ and $AE2$) of different artificial light harvesting systems on DNA origami structures are depicted in figure 5.7b. The $AE2$ value of the two color FRET system based on Cy3/Cy5-FRET ($(\mathrm{Cy5})_1$ **$(\mathrm{Cy3})_4$** $(\mathrm{FAM})_0$, $AE2 = 2.3$) increases substantially with the ad-

dition of a third blue shifted fluorophore such as FAM ($(Cy5)_1$ $\mathbf{(Cy3)_4}$ $\mathbf{(FAM)_4}$: $AE2 = 5.7 \pm 0.4$, $(Cy5)_1$ $\mathbf{(Cy3)_4}$ $\mathbf{(FAM)_8}$: $AE2 = 8.6 \pm 0.2$) as shown in figure 5.7b. Interestingly, even the system with just one Cy3 molecule and four FAM molecules leads to higher $AE2$ values compared to the two-color FRET system in which four Cy3 molecules are present ($(Cy5)_1$ $\mathbf{(Cy3)_4}$ $(FAM)_0$: $AE2 = 2.3$ *vs.* $(Cy5)_1$ $\mathbf{(Cy3)_1}$ $\mathbf{(FAM)_4}$: $AE2 = 3.0$, figure 5.7b).

In summary, DNA origami nanostructures can be used to arrange different fluorophores and create artificial light harvesting systems based on multiple fluorophores. The AE (light harvesting efficiency) can be optimized by the introduction of more and more fluorophores. The FRET efficiency on the other hand is tuned by optimizing the spectral properties of used fluorophores (large spectral overlap) and the range of possible excitation wavelengths can be extended by using multiple FRET steps.

Chapter 6

Summary and outlook

In this cumulative doctoral thesis, different FRET systems on triangular shaped DNA origami structures with different potential applications have been developed and analyzed. In the first investigations, the formation of G-quadruplex structures from telomeric DNA induced by monovalent cations using FRET between FAM and Cy3 has been studied. Here, the difference between the Na^+ and K^+ induced G-quadruplex formation for the reversed human telomeric DNA (Cy3-RevHumTel-FAM, 5'-Cy3-TT $(GGG\ ATT)_4$ T-FAM) has been examined. The fluorescence studies have shown that the association constant for K^+ is by several orders of magnitude higher than for Na^+. Thus, the G-quadruplex folds at lower K^+ concentrations compared to Na^+ which makes it a potential tool for K^+ sensing. However, at high ion concentrations (ca. 110 mM) a distinction between K^+ and Na^+ for free RevHumTel is no longer feasible. By attaching RevHumTel to DNA origami structures the difference between K^+ and Na^+ induced G-quadruplex structures becomes more pronounced. The G-quadruplex formation in presence of Na^+ is completely inhibited when RevHumTel is placed on DNA origami structures. Then again, the formation of K^+ induced G-quadruplex structures is unaffected on the DNA origami platform. Additionally and most importantly, K^+ induced G-quadruplex formation is still detectable in presence of high NaCl concentrations and the ion-selectivity for K^+ is maintained over a wide range of monovalent cations. Interestingly, by changing the direction of the telomeric DNA (RevHumTel, 5'-$(GGG\ ATT)_4$ *vs.* HumTel, 5'-$(TTA\ GGG)_4$) the ion-selectivity on DNA origami structures is revoked. The reason for the ion-selectivity of RevHumTel on DNA origami structures has been ascribed to either different G-quadruplex structures or to different folding pathways. In this study, a highly ion-selective K^+ sensing scheme on DNA origami structures has been developed.[1]

Afterwards, the reversibility of the G-quadruplex formation has been analyzed on DNA origami structures using FRET. For this, the G-quadruplex structures are folded upon KCl addition (high FRET) and subsequently unfolded after cryptand addition (low FRET). K^+ is removed by cryptand encapsulation leading to an unfolding of the G-

quadruplex. The G-quadruplex folding and unfolding can be repeated several times. The repeated switching between high and low FRET efficiencies has been analyzed for the two-color FRET system (FAM/RevHumTel-Cy3). Since the modification of DNA origami structures is relatively simple, the two-color FRET system has been extended to a three-color FRET cascade (FAM/RevHumTel-Cy3/Cy5) and furthermore to a four-color photonic wire (FAM/RevHumTel-Cy3/Cy5/IRDye700). In these FRET cascades, the light energy is transferred over several FRET steps from FAM (acceptor) over Cy3 (transmitter) to Cy5 (acceptor and transmitter, respectively) and finally to IRDye700 (acceptor). These FRET systems are only efficient when the G-quadruplex is folded and are not operative when the G-quadruplex is unfolded. In this sense, a switchable photonic wire on DNA origami structures with a signal transduction range over several nanometers and a spectral range of ca. 200 nm has been designed.[2]

In the last part, artificial light harvesting systems have been designed on DNA origami structures based on a three-color FRET cascade. Here, multiple donor (FAM) and transmitter (Cy3) molecules (light harvesting units) are placed around one single acceptor molecule (Cy5) in such way that they absorb the excitation energy and funnel the light energy efficiently to the acceptor. Thus, the acceptor absorption is amplified and the emission becomes brighter. With the help of DNA origami structures, the arrangement and number of fluorophores can be changed readily and the light harvesting efficiency expressed as the antenna effect and the FRET efficiency have been analyzed thoroughly. It has been shown that the antenna effect for a two-color FRET system with an overall low FRET efficiency (Cy5/FAM) increases with an increasing amount of donor molecules ($(Cy5)_1$ $(Cy3)_0$ $\mathbf{(FAM)_{0\text{-}4}}$). The FRET efficiency on the other hand decreases slightly with an increasing number of FAM molecules. To improve the light harvesting and FRET efficiencies, a transmitter molecule (Cy3) has been introduced. Here, the antenna effect and FRET efficiency increase linearly with an increasing number of Cy3 ($(Cy5)_1$ $\mathbf{(Cy3)_{0\text{-}4}}$ $(FAM)_4$). Since FRET is most efficient when all three fluorophores are present, the number of possible energy transfer pathways has been increased step wise. For this, the number of Cy3 and FAM has been increased to the same extent ($(Cy5)_1$ $\mathbf{(Cy3)_{0\text{-}4}}$ $\mathbf{(FAM)_{0\text{-}4}}$). The antenna effect increases linearly and also the FRET efficiency can be tuned with an increasing number of fluorophores. Finally, the light harvesting system has been optimized by increasing the number of FAM molecules up to eight ($(Cy5)_1$ $\mathbf{(Cy3)_4}$ $\mathbf{(FAM)_8}$). Based on the findings a general set of design rules for artificial light harvesting systems can be derived:[3]

1. The overall light harvesting efficiency is improved by increasing the number of donor and transmitter molecules.

2. The FRET efficiency is tuned by using fluorophores with large spectral overlaps.

3. The range of possible excitation wavelengths increases by the arrangement of several different fluorophores (multi-color FRET cascades).

In the present thesis, the fundamentals of different FRET assemblies on DNA origami structures have been examined. For future applications, the ion-selective FRET system on DNA origami structures could be immobilized on glass fibers to develop an optical K^+ sensor. Here, the advantage that DNA origami structures can be straightforwardly adsorbed on charged surfaces such as glass can be utilized. Additionally, the DNA origami structures can be modified with different environmentally sensitive fluorophores (*e.g.* pH- or O_2-sensitive fluorophores) to enable multiplexing.[200,201] However, it has to be noted that the emission intensity of one fluorophore per DNA origami structure is too weak for such optical sensors. Hence, several fluorophores need to be immobilized on one DNA origami structure. This can get rather expensive when a variety of staple strands are modified with different fluorophores. Therefore, other methods are needed to introduce the environmentally sensitive moieties. The K^+ selective RevHumTel for example could be introduced several times without a modification at the 5'-end. The folding of G-quadruplex structures can then be detected with G-quadruplex sensitive fluorophores.[155] Other environmentally sensitive fluorophores can be introduced by hybridization of modified DNA strands with complementary DNA strands which are attached as an extension of several staple strands. In this sense, only one DNA strand needs to be modified with the fluorophore.

Furthermore, the artificial light harvesting system can be advanced in such way that telomeric DNA strands are attached at the transmitter positions to achieve a switchable light harvesting system. Additionally, to decrease the overall costs for such a light harvesting system fluorophores can be introduced *via* hybridization. Here, different fluorophores can be attached to different DNA sequences so that the position of each fluorophore can still be precisely controlled.

To analyze the actual efficiency of this artificial light harvesting system for real applications in the field of artificial photosynthesis, the reaction center (RC) from for example the purple bacterium could be introduced in the middle of such multi-color light harvesting system. From literature it is known that the absorption spectrum of this particular RC overlaps with the emission spectrum of Cy5.[183] Thus, the multi-color light harvesting system analyzed in the present work would be suitable to test the real light harvesting efficiency with this RC. Here, the RC could be coupled to a staple strand and then be surrounded by Cy5, Cy3 and FAM on the DNA origami structure. According to literature the oxidation of for example cytochrome *c* (for this particular RC from the purple bacterium) is affected depending on the absorbed light energy in the RC (higher light absorption $\rightarrow$ faster cytochrome *c* oxidation).[202] Hence, by analyzing the cytochrome *c* oxidation one can assess the light harvesting efficiency of such artificial light harvesting complexes.

Bibliography

[1] a) L. Olejko, P. J. Cywinski, and I. Bald, "Ion-selective formation of a guanine quadruplex on DNA origami structures," *Angew. Chem., Int. Ed.* **54**(2), pp. 673–677, 2015;
b) L. Olejko, P. J. Cywinski, and I. Bald, "Ionenselektive Guanin-Quadruplex-Faltung auf DNA-Origami-Strukturen," *Angew. Chem.* **127**(2), pp. 683–687, 2015.

[2] L. Olejko, P. J. Cywinski, and I. Bald, "An ion-controlled four-color fluorescent telomeric switch on DNA origami structures," *Nanoscale* **8**(19), pp. 10339–10347, 2016.

[3] L. Olejko and I. Bald, "FRET efficiency and antenna effect in multi-color DNA origami-based light harvesting systems," *RSC Adv.* **7**, pp. 23924–23934, 2017.

[4] N. C. Seeman, "Nucleic acid junctions and lattices," *J. Theor. Biol.* **99**(2), pp. 237–247, 1982.

[5] N. C. Seeman, *Structural DNA nanotechnology*, Cambridge University Press, Cambridge, United Kingdom, 2015.

[6] P. W. K. Rothemund, "Folding DNA to create nanoscale shapes and patterns," *Nature* **440**, pp. 297–302, 2006.

[7] J. A. Liddle and G. M. Gallatin, "Nanomanufacturing: A Perspective," *ACS nano* **10**(3), pp. 2995–3014, 2016.

[8] R. Thiruvengadathan, V. Korampally, A. Ghosh, N. Chanda, K. Gangopadhyay, and S. Gangopadhyay, "Nanomaterial processing using self-assembly-bottom-up chemical and biological approaches," *Rep. Prog. Phys.* **76**(6), pp. 066501–066556, 2013.

[9] A. A. Rempel, "Nanotechnologies. Properties and applications of nanostructured materials," *Russ. Chem. Rev.* **76**(5), pp. 435–461, 2007.

[10] T. J. Fu and N. C. Seeman, "DNA double-crossover molecules," *Biochemistry* **32**(13), pp. 3211–3220, 1993.

[11] E. Winfree, F. Liu, L. A. Wenzler, and N. C. Seeman, "Design and self-assembly of two-dimensional DNA crystals," *Nature* **394**, pp. 539–544, 1998.

[12] J. H. Chen and N. C. Seeman, "Synthesis from DNA of a molecule with the connectivity of a cube," *Nature* **350**, pp. 631–633, 1991.

[13] Y. Zhang and N. C. Seeman, "Construction of a DNA-Truncated Octahedron," *J. Am. Chem. Soc.* **116**(5), pp. 1661–1669, 1994.

[14] F. C. Simmel, "DNA-Nanotechnologie," *Chem. unserer Zeit* **47**(3), pp. 164–173, 2013.

[15] T. Förster, "Energiewanderung und Fluoreszenz," *Naturwissenschaften* **33**(6), pp. 166–175, 1946.

[16] T. Förster, "Zwischenmolekulare Energiewanderung und Fluoreszenz," *Ann. Phys.* **437**(1-2), pp. 55–75, 1948.

[17] H. Ueyama, M. Takagi, and S. Takenaka, "A Novel Potassium Sensing in Aqueous Media with a Synthetic Oligonucleotide Derivative. Fluorescence Resonance Energy Transfer Associated with Guanine Quartet−Potassium Ion Complex Formation," *J. Am. Chem. Soc.* **124**(48), pp. 14286–14287, 2002.

[18] P. J. Cywiński, L. Olejko, and H.-G. Löhmannsröben, "A time-resolved luminescent competitive assay to detect L-selectin using aptamers as recognition elements," *Anal. Chim. Acta* **887**, pp. 209–215, 2015.

[19] I. H. Stein, C. Steinhauer, and P. Tinnefeld, "Single-molecule four-color FRET visualizes energy-transfer paths on DNA origami," *J. Am. Chem. Soc.* **133**(12), pp. 4193–4195, 2011.

[20] B. Albinsson, J. K. Hannestad, and K. Börjesson, "Functionalized DNA nanostructures for light harvesting and charge separation," *Coord. Chem. Rev.* **256**(21-22), pp. 2399–2413, 2012.

[21] F. Wang, X. Liu, and I. Willner, "DNA switches: from principles to applications," *Angew. Chem., Int. Ed.* **54**(4), pp. 1098–1129, 2015.

[22] S. Neidle and S. Balasubramanian, *Quadruplex nucleic acids*, RSC Publishing, Cambridge, United Kingdom, 2006.

[23] S. Burge, G. N. Parkinson, P. Hazel, A. K. Todd, and S. Neidle, "Quadruplex DNA: sequence, topology and structure," *Nucleic Acids Res.* **34**(19), pp. 5402–5415, 2006.

[24] I. L. Medintz and N. Hildebrandt, *FRET - Förster resonance energy transfer: From theory to applications*, Wiley-VCH, Weinheim, Germany, 1. ed., 2014.

[25] W. Su, V. Bonnard, and G. A. Burley, "DNA-templated photonic arrays and assemblies: design principles and future opportunities," *Chem. Eur. J.* **17**(29), pp. 7982–7991, 2011.

[26] S. Neidle, *Therapeutic applications of quadruplex nucleic acids*, Elsevier/Academic Press, London, United Kindom and Waltham, U.S.A. and San Diego, U.S.A., 1. ed., 2012.

[27] N. C. Seeman, "Nanomaterials based on DNA," *Annu. Rev. Biochem.* **79**, pp. 65–87, 2010.

[28] J. M. Berg, L. Stryer, and J. L. Tymoczko, *Biochemie*, Springer Spektrum, Berlin, Germany, 7. ed., 2013.

[29] J. D. Watson and F. H. C. Crick, "Molecular Structure of Nucleic Acids: A Structure for Deoxyribose Nucleic Acid," *Nature* **171**, pp. 737–738, 1953.

[30] J. Kjems, E. Ferapontova, and K. V. Gothelf, *Nucleic Acid Nanotechnology*, vol. 29, Springer, Berlin Heidelberg, Germany, 2014.

[31] T. H. LaBean, H. Yan, J. Kopatsch, F. Liu, E. Winfree, J. H. Reif, and N. C. Seeman, "Construction, Analysis, Ligation, and Self-Assembly of DNA Triple Crossover Complexes," *J. Am. Chem. Soc.* **122**(9), pp. 1848–1860, 2000.

[32] H. Yan, S. H. Park, G. Finkelstein, J. H. Reif, and T. H. LaBean, "DNA-templated self-assembly of protein arrays and highly conductive nanowires," *Science* **301**(5641), pp. 1882–1884, 2003.

[33] Y. He, Y. Chen, H. Liu, A. E. Ribbe, and C. Mao, "Self-assembly of hexagonal DNA two-dimensional (2D) arrays," *J. Am. Chem. Soc.* **127**(35), pp. 12202–12203, 2005.

[34] Y. He, Y. Tian, Y. Chen, Z. Deng, A. E. Ribbe, and C. Mao, "Sequence symmetry as a tool for designing DNA nanostructures," *Angew. Chem., Int. Ed.* **44**(41), pp. 6694–6696, 2005.

[35] Y. He, Y. Tian, A. E. Ribbe, and C. Mao, "Highly connected two-dimensional crystals of DNA six-point-stars," *J. Am. Chem. Soc.* **128**(50), pp. 15978–15979, 2006.

[36] S. H. Park, R. Barish, H. Li, J. H. Reif, G. Finkelstein, H. Yan, and T. H. LaBean, "Three-helix bundle DNA tiles self-assemble into 2D lattice or 1D templates for silver nanowires," *Nano Lett.* **5**(4), pp. 693–696, 2005.

[37] A. Rangnekar, K. V. Gothelf, and T. H. LaBean, "Design and synthesis of DNA four-helix bundles," *Nanotechnology* **22**(23), pp. 235601–235609, 2011.

[38] F. Mathieu, S. Liao, J. Kopatsch, T. Wang, C. Mao, and N. C. Seeman, "Six-helix bundles designed from DNA," *Nano Lett.* **5**(4), pp. 661–665, 2005.

[39] M. N. Hansen, A. M. Zhang, A. Rangnekar, K. M. Bompiani, J. D. Carter, K. V. Gothelf, and T. H. LaBean, "Weave tile architecture construction strategy for DNA nanotechnology," *J. Am. Chem. Soc.* **132**(41), pp. 14481–14486, 2010.

[40] W. M. Shih, J. D. Quispe, and G. F. Joyce, "A 1.7-kilobase single-stranded DNA that folds into a nanoscale octahedron," *Nature* **427**, pp. 618–621, 2004.

[41] J. Zheng, J. J. Birktoft, Y. Chen, T. Wang, R. Sha, P. E. Constantinou, S. L. Ginell, C. Mao, and N. C. Seeman, "From molecular to macroscopic via the rational design of a self-assembled 3D DNA crystal," *Nature* **461**, pp. 74–77, 2009.

[42] R. Jungmann, T. Liedl, T. L. Sobey, W. Shih, and F. C. Simmel, "Isothermal assembly of DNA origami structures using denaturing agents," *J. Am. Chem. Soc.* **130**(31), pp. 10062–10063, 2008.

[43] I. Bald and A. Keller, "Molecular Processes Studied at a Single-Molecule Level Using DNA Origami Nanostructures and Atomic Force Microscopy," *Molecules* **19**(9), pp. 13803–13823, 2014.

[44] C. E. Castro, F. Kilchherr, D.-N. Kim, E. L. Shiao, T. Wauer, P. Wortmann, M. Bathe, and H. Dietz, "A primer to scaffolded DNA origami," *Nat. Methods* **8**(3), pp. 221–229, 2011.

[45] E. S. Andersen, M. Dong, M. M. Nielsen, K. Jahn, R. Subramani, W. Mamdouh, M. M. Golas, B. Sander, H. Stark, C. L. P. Oliveira, J. S. Pedersen, V. Birkedal, F. Besenbacher, K. V. Gothelf, and J. Kjems, "Self-assembly of a nanoscale DNA box with a controllable lid," *Nature* **459**, pp. 73–76, 2009.

[46] Y. Ke, J. Sharma, M. Liu, K. Jahn, Y. Liu, and H. Yan, "Scaffolded DNA origami of a DNA tetrahedron molecular container," *Nano Lett.* **9**(6), pp. 2445–2447, 2009.

[47] S. M. Douglas, H. Dietz, T. Liedl, B. Hogberg, F. Graf, and W. M. Shih, "Self-assembly of DNA into nanoscale three-dimensional shapes," *Nature* **459**(7245), pp. 414–418, 2009.

[48] H. Dietz, S. M. Douglas, and W. M. Shih, "Folding DNA into twisted and curved nanoscale shapes," *Science* **325**(5941), pp. 725–730, 2009.

[49] D. Han, S. Pal, J. Nangreave, Z. Deng, Y. Liu, and H. Yan, "DNA origami with complex curvatures in three-dimensional space," *Science* **332**(6027), pp. 342–346, 2011.

[50] D. Wei, G. N. Parkinson, A. P. Reszka, and S. Neidle, "Crystal structure of a c-kit promoter quadruplex reveals the structural role of metal ions and water molecules in maintaining loop conformation," *Nucleic Acids Res.* **40**(10), pp. 4691–4700, 2012.

[51] Y. Ke, L. L. Ong, W. M. Shih, and P. Yin, "Three-dimensional structures self-assembled from DNA bricks," *Science* **338**(6111), pp. 1177–1183, 2012.

[52] S. Williams, K. Lund, C. Lin, P. Wonka, S. Lindsay, and H. Yan, "Tiamat: A Three-Dimensional Editing Tool for Complex DNA Structures," in *DNA Computing (DNA 14)*, **5347**, pp. 90–101, Springer, Berlin Heidelberg, Germany, 2009.

[53] E. S. Andersen, A. Lind-Thomsen, B. Knudsen, S. E. Kristensen, J. H. Havgaard, E. Torarinsson, N. Larsen, C. Zwieb, P. Sestoft, J. Kjems, and J. Gorodkin, "Semiautomated improvement of RNA alignments," *RNA* **13**(11), pp. 1850–1859, 2007.

[54] E. S. Andersen, M. Dong, M. M. Nielsen, K. Jahn, A. Lind-Thomsen, W. Mamdouh, K. V. Gothelf, F. Besenbacher, and J. Kjems, "DNA origami design of dolphin-shaped structures with flexible tails," *ACS nano* **2**(6), pp. 1213–1218, 2008.

[55] S. M. Douglas, A. H. Marblestone, S. Teerapittayanon, A. Vazquez, G. M. Church, and W. M. Shih, "Rapid prototyping of 3D DNA-origami shapes with caDNAno," *Nucleic Acids Res.* **37**(15), pp. 5001–5006, 2009.

[56] A. Gietl, P. Holzmeister, D. Grohmann, and P. Tinnefeld, "DNA origami as biocompatible surface to match single-molecule and ensemble experiments," *Nucleic Acids Res.* **40**(14), p. e110, 2012.

[57] T. Tørring, N. V. Voigt, J. Nangreave, H. Yan, and K. V. Gothelf, "DNA origami: a quantum leap for self-assembly of complex structures," *Chem. Soc. Rev.* **40**(12), pp. 5636–5646, 2011.

[58] H. Li, J. D. Carter, and T. H. LaBean, "Nanofabrication by DNA self-assembly," *Mater. Today* **12**(5), pp. 24–32, 2009.

[59] L. Wang, Y. Sun, Z. Li, A. Wu, and G. Wei, "Bottom-Up Synthesis and Sensor Applications of Biomimetic Nanostructures," *Materials* **9**(1), pp. 53–81, 2016.

[60] W. Pfeifer and B. Saccà, "From Nano to Macro through Hierarchical Self–Assembly: The DNA Paradigm," *ChemBioChem* **17**(12), pp. 1063–1080, 2016.

[61] A. R. Chandrasekaran, N. Anderson, M. Kizer, K. Halvorsen, and X. Wang, "Beyond the Fold: Emerging Biological Applications of DNA Origami," *ChemBioChem* **17**(12), pp. 1081–1089, 2016.

[62] Y. R. Yang, Y. Liu, and H. Yan, "DNA Nanostructures as Programmable Biomolecular Scaffolds," *Bioconjugate Chem.* **26**(8), pp. 1381–1395, 2015.

[63] M. Endo, Y. Yang, and H. Sugiyama, "DNA origami technology for biomaterials applications," *Biomater. Sci.* **1**(4), pp. 347–360, 2013.

[64] A. Rajendran, M. Endo, and H. Sugiyama, "Single-molecule analysis using DNA origami," *Angew. Chem., Int. Ed.* **51**(4), pp. 874–890, 2012.

[65] J. Nangreave, D. Han, Y. Liu, and H. Yan, "DNA origami: a history and current perspective," *Curr. Opin. Struct. Biol.* **14**(5), pp. 608–615, 2010.

[66] F. Zhang, J. Nangreave, Y. Liu, and H. Yan, "Structural DNA nanotechnology: state of the art and future perspective," *J. Am. Chem. Soc.* **136**(32), pp. 11198–11211, 2014.

[67] J. Prinz, B. Schreiber, L. Olejko, J. Oertel, J. Rackwitz, A. Keller, and I. Bald, "DNA Origami Substrates for Highly Sensitive Surface-Enhanced Raman Scattering," *J. Phys. Chem. Lett.* **4**(23), pp. 4140–4145, 2013.

[68] J. Prinz, C. Heck, L. Ellerik, V. Merk, and I. Bald, "DNA origami based Au–Ag-core–shell nanoparticle dimers with single-molecule SERS sensitivity," *Nanoscale* **8**(10), pp. 5612–5620, 2016.

[69] S. Helmi, C. Ziegler, D. J. Kauert, and R. Seidel, "Shape-controlled synthesis of gold nanostructures using DNA origami molds," *Nano Lett.* **14**(11), pp. 6693–6698, 2014.

[70] Y. Ke, T. Meyer, W. M. Shih, and G. Bellot, "Regulation at a distance of biomolecular interactions using a DNA origami nanoactuator," *Nat. Commun.* **7**, p. 10935, 2016.

[71] E.-M. Roller, C. Argyropoulos, A. Hogele, T. Liedl, and M. Pilo-Pais, "Plasmon-Exciton Coupling Using DNA Templates," *Nano Lett.* **16**(9), pp. 5962–5966, 2016.

[72] A. Samanta, Y. Zhou, S. Zou, H. Yan, and Y. Liu, "Fluorescence Quenching of Quantum Dots by Gold Nanoparticles: A Potential Long Range Spectroscopic Ruler," *Nano Lett.* **14**(9), pp. 5052–5057, 2014.

[73] R. Schreiber, J. Do, E.-M. Roller, T. Zhang, V. J. Schüller, P. C. Nickels, J. Feldmann, and T. Liedl, "Hierarchical assembly of metal nanoparticles, quantum dots and organic dyes using DNA origami scaffolds," *Nat. Nanotechnol.* **9**(1), pp. 74–78, 2014.

[74] Y. Zhang, J. Chao, H. Liu, F. Wang, S. Su, B. Liu, L. Zhang, J. Shi, L. Wang, W. Huang, L. Wang, and C. Fan, "Transfer of Two-Dimensional Oligonucleotide Patterns onto Stereocontrolled Plasmonic Nanostructures through DNA-Origami-Based Nanoimprinting Lithography," *Angew. Chem., Int. Ed.* **55**(28), pp. 8036–8040, 2016.

[75] J. Sharma, R. Chhabra, C. S. Andersen, K. V. Gothelf, H. Yan, and Y. Liu, "Toward reliable gold nanoparticle patterning on self-assembled DNA nanoscaffold," *J. Am. Chem. Soc.* **130**(25), pp. 7820–7821, 2008.

[76] L. Weller, V. V. Thacker, L. O. Herrmann, E. A. Hemmig, A. Lombardi, U. F. Keyser, and J. J. Baumberg, "Gap-Dependent Coupling of Ag–Au Nanoparticle Heterodimers Using DNA Origami-Based Self-Assembly," *ACS photonics* **3**(9), pp. 1589–1595, 2016.

[77] P. Zhan, P. K. Dutta, P. Wang, G. Song, M. Dai, S.-X. Zhao, Z.-G. Wang, P. Yin, W. Zhang, B. Ding, and Y. Ke, "Reconfigurable Three-Dimensional Gold Nanorod Plasmonic Nanostructures Organized on DNA Origami Tripod," *ACS nano* , 2017.

[78] S. Pal, Z. Deng, B. Ding, H. Yan, and Y. Liu, "DNA-origami-directed self-assembly of discrete silver-nanoparticle architectures," *Angew. Chem., Int. Ed.* **49**(15), pp. 2700–2704, 2010.

[79] Z. Deng, A. Samanta, J. Nangreave, H. Yan, and Y. Liu, "Robust DNA-Functionalized Core/Shell Quantum Dots with Fluorescent Emission Spanning from UV–vis to Near-IR and Compatible with DNA-Directed Self-Assembly," *J. Am. Chem. Soc.* **134**(42), pp. 17424–17427, 2012.

[80] T. L. Doane, R. Alam, and M. M. Maye, "Functionalization of quantum rods with oligonucleotides for programmable assembly with DNA origami," *Nanoscale* **7**(7), pp. 2883–2888, 2015.

[81] I. H. Stein, V. Schüller, P. Böhm, P. Tinnefeld, and T. Liedl, "Single-molecule FRET ruler based on rigid DNA origami blocks," *ChemPhysChem* **12**(3), pp. 689–695, 2011.

[82] E. A. Hemmig, C. Creatore, B. Wunsch, L. Hecker, P. Mair, M. A. Parker, S. Emmott, P. Tinnefeld, U. F. Keyser, and A. W. Chin, "Programming Light-

Harvesting Efficiency Using DNA Origami," *Nano Lett.* **16**(4), pp. 2369–2374, 2016.

[83] N. Aissaoui, K. Moth-Poulsen, M. Kall, P. Johansson, L. M. Wilhelmsson, and B. Albinsson, "FRET enhancement close to gold nanoparticles positioned in DNA origami constructs," *Nanoscale* **9**(2), pp. 673–683, 2017.

[84] C. Steinhauer, R. Jungmann, T. L. Sobey, F. C. Simmel, and P. Tinnefeld, "DNA origami as a nanoscopic ruler for super-resolution microscopy," *Angew. Chem., Int. Ed.* **48**(47), pp. 8870–8873, 2009.

[85] J. J. Schmied, A. Gietl, P. Holzmeister, C. Forthmann, C. Steinhauer, T. Dammeyer, and P. Tinnefeld, "Fluorescence and super-resolution standards based on DNA origami," *Nat. Methods* **9**(12), pp. 1133–1134, 2012.

[86] J. J. Schmied, M. Raab, C. Forthmann, E. Pibiri, B. Wunsch, T. Dammeyer, and P. Tinnefeld, "DNA origami-based standards for quantitative fluorescence microscopy," *Nat. Protoc.* **9**(6), pp. 1367–1391, 2014.

[87] D. Koirala, P. Shrestha, T. Emura, K. Hidaka, S. Mandal, M. Endo, H. Sugiyama, and H. Mao, "Single-Molecule Mechanochemical Sensing Using DNA Origami Nanostructures," *Angew. Chem., Int. Ed.* **53**(31), pp. 8137–8141, 2014.

[88] Y. Ke, S. Lindsay, Y. Chang, Y. Liu, and H. Yan, "Self-assembled water-soluble nucleic acid probe tiles for label-free RNA hybridization assays," *Science* **319**(5860), pp. 180–183, 2008.

[89] S. Vogel, J. Rackwitz, R. Schürmann, J. Prinz, A. R. Milosavljevic, M. Refregiers, A. Giuliani, and I. Bald, "Using DNA Origami Nanostructures to Determine Absolute Cross Sections for UV Photon-Induced DNA Strand Breakage," *J. Phys. Chem. Lett.* **6**(22), pp. 4589–4593, 2015.

[90] J. Rackwitz, J. Kopyra, I. Dąbkowska, K. Ebel, M. L. Ranković, A. R. Milosavljević, and I. Bald, "Sensitizing DNA Towards Low-Energy Electrons with 2-Fluoroadenine," *Angew. Chem., Int. Ed.* **55**(35), pp. 10248–10252, 2016.

[91] A. Keller, I. Bald, A. Rotaru, E. Cauët, K. V. Gothelf, and F. Besenbacher, "Probing electron-induced bond cleavage at the single-molecule level using DNA origami templates," *ACS nano* **6**(5), pp. 4392–4399, 2012.

[92] A. Keller, J. Rackwitz, E. Cauët, J. Liévin, T. Körzdörfer, A. Rotaru, K. V. Gothelf, F. Besenbacher, and I. Bald, "Sequence dependence of electron-induced DNA strand breakage revealed by DNA nanoarrays," *Sci. Rep.* **4**, p. 7391, 2014.

[93] N. V. Voigt, T. Tørring, A. Rotaru, M. F. Jacobsen, J. B. Ravnsbaek, R. Subramani, W. Mamdouh, J. Kjems, A. Mokhir, F. Besenbacher, and K. V. Gothelf, "Single-molecule chemical reactions on DNA origami," *Nat. Nanotechnol.* **5**(3), pp. 200–203, 2010.

[94] A. Kuzyk, K. T. Laitinen, and P. Torma, "DNA origami as a nanoscale template for protein assembly," *Nanotechnology* **20**(23), pp. 235305–235309, 2009.

[95] A. Kuzuya, M. Kimura, K. Numajiri, N. Koshi, T. Ohnishi, F. Okada, and M. Komiyama, "Precisely programmed and robust 2D streptavidin nanoarrays by using periodical nanometer-scale wells embedded in DNA origami assembly," *ChemBioChem* **10**(11), pp. 1811–1815, 2009.

[96] K. Numajiri, M. Kimura, A. Kuzuya, and M. Komiyama, "Stepwise and reversible nanopatterning of proteins on a DNA origami scaffold," *Chem. Commun.* **46**(28), pp. 5127–5129, 2010.

[97] K. Gopfrich, C.-Y. Li, M. Ricci, S. P. Bhamidimarri, J. Yoo, B. Gyenes, A. Ohmann, M. Winterhalter, A. Aksimentiev, and U. F. Keyser, "Large-Conductance Transmembrane Porin Made from DNA Origami," *ACS nano* **10**(9), pp. 8207–8214, 2016.

[98] S. Helmig, A. Rotaru, D. Arian, L. Kovbasyuk, J. Arnbjerg, P. R. Ogilby, J. Kjems, A. Mokhir, F. Besenbacher, and K. V. Gothelf, "Single molecule atomic force microscopy studies of photosensitized singlet oxygen behavior on a DNA origami template," *ACS nano* **4**(12), pp. 7475–7480, 2010.

[99] J. Prinz, A. Matkovic, J. Pesic, R. Gajic, and I. Bald, "Hybrid Structures for Surface-Enhanced Raman Scattering: DNA Origami/Gold Nanoparticle Dimer/Graphene," *Small* **12**(39), pp. 5458–5467, 2016.

[100] A. Matković, B. Vasić, J. Pešić, J. Prinz, I. Bald, A. R. Milosavljević, and R. Gajić, "Enhanced structural stability of DNA origami nanostructures by graphene encapsulation," *New J. Phys.* **18**(2), pp. 025016–025025, 2016.

[101] B. Saccà, Y. Ishitsuka, R. Meyer, A. Sprengel, E.-C. Schöneweiß, G. U. Nienhaus, and C. M. Niemeyer, "Reversible reconfiguration of DNA origami nanochambers monitored by single-molecule FRET," *Angew. Chem., Int. Ed.* **54**(12), pp. 3592–3597, 2015.

[102] R. Tsukanov, T. E. Tomov, Y. Berger, M. Liber, and E. Nir, "Conformational dynamics of DNA hairpins at millisecond resolution obtained from analysis of single-molecule FRET histograms," *J. Phys. Chem. B* **117**(50), pp. 16105–16109, 2013.

[103] R. Tsukanov, T. E. Tomov, R. Masoud, H. Drory, N. Plavner, M. Liber, and E. Nir, "Detailed study of DNA hairpin dynamics using single-molecule fluorescence assisted by DNA origami," *J. Phys. Chem. B* **117**(40), pp. 11932–11942, 2013.

[104] P. K. Dutta, R. Varghese, J. Nangreave, S. Lin, H. Yan, and Y. Liu, "DNA-directed artificial light-harvesting antenna," *J. Am. Chem. Soc.* **133**(31), pp. 11985–11993, 2011.

[105] E. H. Blackburn, "The molecular structure of centromeres and telomeres," *Annu. Rev. Biochem.* **53**, pp. 163–194, 1984.

[106] W. I. Sundquist and A. Klug, "Telomeric DNA dimerizes by formation of guanine tetrads between hairpin loops," *Nature* **342**, pp. 825–829, 1989.

[107] D. Sen and W. Gilbert, "Formation of parallel four-stranded complexes by guanine-rich motifs in DNA and its implications for meiosis," *Nature* **334**, pp. 364–366, 1988.

[108] T. Evans, E. Schon, G. Gora-Maslak, J. Patterson, and A. Efstratiadis, "S1-hypersensitive sites in eukaryotic promoter regions," *Nucleic Acids Res.* **12**(21), pp. 8043–8058, 1984.

[109] J. L. Huppert, "Hunting G-quadruplexes," *Biochimie* **90**(8), pp. 1140–1148, 2008.

[110] A. K. Todd, M. Johnston, and S. Neidle, "Highly prevalent putative quadruplex sequence motifs in human DNA," *Nucleic Acids Res.* **33**(9), pp. 2901–2907, 2005.

[111] J. L. Huppert and S. Balasubramanian, "Prevalence of quadruplexes in the human genome," *Nucleic Acids Res.* **33**(9), pp. 2908–2916, 2005.

[112] I. Bang, "Untersuchungen über die Guanylsäure," *Biochem. Z.* **26**, pp. 293–311, 1910.

[113] M. Gellert, M. N. Lipsett, and D. R. Davies, "Helix formation by guanylic acid," *Proc. Natl. Acad. Sci. U.S.A.* **48**, pp. 2013–2018, 1962.

[114] P. Balagurumoorthy, S. K. Brahmachari, D. Mohanty, M. Bansal, and V. Sasisekharan, "Hairpin and parallel quartet structures for telomeric sequences," *Nucleic Acids Res.* **20**(15), pp. 4061–4067, 1992.

[115] T. Li, S. Dong, and E. Wang, "A lead(II)-driven DNA molecular device for turn-on fluorescence detection of lead(II) ion with high selectivity and sensitivity," *J. Am. Chem. Soc.* **132**(38), pp. 13156–13157, 2010.

[116] B. Y. Won, C. Jung, K. S. Park, and H. G. Park, "An electrochemically reversible DNA switch," *Electrochem. Commun.* **27**, pp. 100–103, 2013.

[117] R. Tippana, W. Xiao, and S. Myong, "G-quadruplex conformation and dynamics are determined by loop length and sequence," *Nucleic Acids Res.* **42**(12), pp. 8106–8114, 2014.

[118] M. Marušič and J. Plavec, "The Effect of DNA Sequence Directionality on G–Quadruplex Folding," *Angew. Chem., Int. Ed.* **54**(40), pp. 11716–11719, 2015.

[119] A. T. Phan, "Human telomeric G-quadruplex: structures of DNA and RNA sequences," *FEBS J.* **277**(5), pp. 1107–1117, 2010.

[120] D. Renciuk, I. Kejnovska, P. Skolakova, K. Bednarova, J. Motlova, and M. Vorlickova, "Arrangements of human telomere DNA quadruplex in physiologically relevant K+ solutions," *Nucleic Acids Res.* **37**(19), pp. 6625–6634, 2009.

[121] A. Marchand and V. Gabelica, "Folding and misfolding pathways of G-quadruplex DNA," *Nucleic Acids Res.* **44**(22), pp. 10999–11012, 2016.

[122] M. Kaushik, A. Bansal, S. Saxena, and S. Kukreti, "Possibility of an antiparallel (tetramer) quadruplex exhibited by the double repeat of the human telomere," *Biochemistry* **46**(24), pp. 7119–7131, 2007.

[123] G. N. Parkinson, M. P. H. Lee, and S. Neidle, "Crystal structure of parallel quadruplexes from human telomeric DNA," *Nature* **417**(6891), pp. 876–880, 2002.

[124] Y. Wang and D. J. Patel, "Solution structure of the human telomeric repeat d[AG3(T2AG3)3] G-tetraplex," *Structure* **1**(4), pp. 263–282, 1993.

[125] D. Miyoshi, A. Nakao, T. Toda, and N. Sugimoto, "Effect of divalent cations on antiparallel G-quartet structure of d(G4T4G4)," *FEBS Lett.* **496**, pp. 128–133, 2001.

[126] A. Ambrus, D. Chen, J. Dai, T. Bialis, R. A. Jones, and D. Yang, "Human telomeric sequence forms a hybrid-type intramolecular G-quadruplex structure with mixed parallel/antiparallel strands in potassium solution," *Nucleic Acids Res.* **34**(9), pp. 2723–2735, 2006.

[127] J. Palacký, M. Vorlíčková, I. Kejnovská, and P. Mojzeš, "Polymorphism of human telomeric quadruplex structure controlled by DNA concentration: a Raman study," *Nucleic Acids Res.* **41**(2), pp. 1005–1016, 2013.

[128] B. Heddi and A. T. Phan, "Structure of human telomeric DNA in crowded solution," *J. Am. Chem. Soc.* **133**(25), pp. 9824–9833, 2011.

[129] J. Y. Lee, B. Okumus, D. S. Kim, and T. Ha, "Extreme conformational diversity in human telomeric DNA," *Proc. Natl. Acad. Sci. U.S.A.* **102**(52), pp. 18938–18943, 2005.

[130] A. I. S. Holm, B. Kohler, S. V. Hoffmann, and S. Brøndsted Nielsen, "Synchrotron radiation circular dichroism of various G-quadruplex structures," *Biopolymers* **93**(5), pp. 429–433, 2010.

[131] A. I. Karsisiotis, N. M. Hessari, E. Novellino, G. P. Spada, A. Randazzo, and M. W. D. Silva, "Topological characterization of nucleic acid G-quadruplexes by UV absorption and circular dichroism," *Angew. Chem., Int. Ed.* **50**(45), pp. 10645–10648, 2011.

[132] C. V. Pagba, S. M. Lane, and S. Wachsmann-Hogiu, "Conformational changes in quadruplex oligonucleotide structures probed by Raman spectroscopy," *Biomed. Opt. Express* **2**(2), pp. 207–217, 2010.

[133] R. D. Gray, J. O. Trent, and J. B. Chaires, "Folding and unfolding pathways of the human telomeric G-quadruplex," *J. Mol. Biol.* **426**(8), pp. 1629–1650, 2014.

[134] R. Jin, B. L. Gaffney, C. Wang, R. A. Jones, and K. J. Breslauer, "Thermodynamics and structure of a DNA tetraplex: A spectroscopic and calorimetric study of the tetramolecular complexes of d(TG3T) and d(TG3T2G3T)," *Proc. Natl. Acad. Sci. U.S.A.* **89**(18), pp. 8832–8836, 1992.

[135] J.-L. Mergny, A.-T. Phan, and L. Lacroix, "Following G–quartet formation by UV–spectroscopy," *FEBS Lett.* **435**, pp. 74–78, 1998.

[136] T. Mashimo and H. Sugiyama, "Folding pathways of human telomeric hybrid G-quadruplex structure," *Nucleic Acids Symp. Ser. (2007)* (51), pp. 239–240, 2007.

[137] T. Mashimo, Y. Sannohe, H. Yagi, and H. Sugiyama, "Folding pathways of hybrid-1 and hybrid-2 G-quadruplex structures," *Nucleic Acids Symp. Ser. (2008)* (52), pp. 409–410, 2008.

[138] A. Rajendran, M. Endo, K. Hidaka, and H. Sugiyama, "Direct and Single-Molecule Visualization of the Solution-State Structures of G-Hairpin and G-Triplex Intermediates," *Angew. Chem., Int. Ed.* **53**(16), pp. 4107–4112, 2014.

[139] T. R. Cech, "Life at the End of the Chromosome: Telomeres and Telomerase," *Angew. Chem., Int. Ed.* **39**(1), pp. 34–43, 2000.

[140] C. W. Greider and E. H. Blackburn, "Identification of a specific telomere terminal transferase activity in tetrahymena extracts," *Cell* **43**(2), pp. 405–413, 1985.

[141] A. M. Zahler, J. R. Williamson, T. R. Cech, and D. M. Prescott, "Inhibition of telomerase by G-quartet DNA structures," *Nature* **350**, pp. 718–720, 1991.

[142] J. Bidzinska, G. Cimino-Reale, N. Zaffaroni, and M. Folini, "G-quadruplex structures in the human genome as novel therapeutic targets," *Molecules* **18**(10), pp. 12368–12395, 2013.

[143] P. Alberti, A. Bourdoncle, B. Sacca, L. Lacroix, and J.-L. Mergny, "DNA nanomachines and nanostructures involving quadruplexes," *Org. Biomol. Chem.* **4**(18), pp. 3383–3391, 2006.

[144] Y. Krishnan and F. C. Simmel, "Nucleic acid based molecular devices," *Angew. Chem. Int. Ed.* **50**(14), pp. 3124–3156, 2011.

[145] B. Ge, Y. C. Huang, D. Sen, and H.-Z. Yu, "A robust electronic switch made of immobilized duplex/quadruplex DNA," *Angew. Chem., Int. Ed.* **49**(51), pp. 9965–9967, 2010.

[146] Y. Hu, F. Wang, C.-H. Lu, J. Girsh, E. Golub, and I. Willner, "Switchable enzyme/DNAzyme cascades by the reconfiguration of DNA nanostructures," *Chem. Eur. J.* **20**(49), pp. 16203–16209, 2014.

[147] X. Wang, J. Huang, Y. Zhou, S. Yan, X. Weng, X. Wu, M. Deng, and X. Zhou, "Conformational switching of G-quadruplex DNA by photoregulation," *Angew. Chem., Int. Ed.* **49**(31), pp. 5305–5309, 2010.

[148] P. Alberti and J.-L. Mergny, "DNA duplex-quadruplex exchange as the basis for a nanomolecular machine," *Proc. Natl. Acad. Sci. U.S.A.* **100**(4), pp. 1569–1573, 2003.

[149] M. Endo, X. Xing, X. Zhou, T. Emura, K. Hidaka, B. Tuesuwan, and H. Sugiyama, "Single-Molecule Manipulation of the Duplex Formation and Dissociation at the G-Quadruplex/i-Motif Site in the DNA Nanostructure," *ACS nano* **9**(10), pp. 9922–9929, 2015.

[150] A. Kuzuya, Y. Sakai, T. Yamazaki, Y. Xu, and M. Komiyama, "Nanomechanical DNA origami 'single-molecule beacons' directly imaged by atomic force microscopy," *Nat. Commun.* **2**, pp. 449–457, 2011.

[151] Y. Sannohe, M. Endo, Y. Katsuda, K. Hidaka, and H. Sugiyama, "Visualization of dynamic conformational switching of the G-quadruplex in a DNA nanostructure," *J. Am. Chem. Soc.* **132**(46), pp. 16311–16313, 2010.

[152] A. Rajendran, M. Endo, K. Hidaka, P. L. T. Tran, J.-L. Mergny, and H. Sugiyama, "Controlling the stoichiometry and strand polarity of a tetramolecular G-quadruplex structure by using a DNA origami frame," *Nucleic Acids Res.* **41**(18), pp. 8738–8747, 2013.

[153] B. Juskowiak, E. Galezowska, A. Zawadzka, A. Gluszynska, and S. Takenaka, "Fluorescence anisotropy and FRET studies of G-quadruplex formation in presence of different cations," *Spectrochim. Acta, Part A* **64**(4), pp. 835–843, 2006.

[154] S. Nagatoishi, T. Nojima, E. Galezowska, B. Juskowiak, and S. Takenaka, "G quadruplex-based FRET probes with the thrombin-binding aptamer (TBA) sequence designed for the efficient fluorometric detection of the potassium ion," *ChemBioChem* **7**(11), pp. 1730–1737, 2006.

[155] D.-M. Kong, Y.-E. Ma, J. Wu, and H.-X. Shen, "Discrimination of G-quadruplexes from duplex and single-stranded DNAs with fluorescence and energy-transfer fluorescence spectra of crystal violet," *Chem. Eur. J.* **15**(4), pp. 901–909, 2009.

[156] J. Zhang, Y. Wan, L. Wang, S. Song, D. Li, and C. Fan, "Switchable charge transport path via a potassium ions promoted conformational change of G-quadruplex probe monolayer," *Electrochem. Commun.* **10**(9), pp. 1258–1260, 2008.

[157] L. Zhang, H. Liu, Y. Shao, C. Lin, H. Jia, G. Chen, D. Yang, and Y. Wang, "Selective Lighting Up of Epiberberine Alkaloid Fluorescence by Fluorophore-Switching Aptamer and Stoichiometric Targeting of Human Telomeric DNA G-Quadruplex Multimer," *Anal. Chem.* **87**(1), pp. 730–737, 2015.

[158] B. Ruttkay-Nedecky, J. Kudr, L. Nejdl, D. Maskova, R. Kizek, and V. Adam, "G-quadruplexes as sensing probes," *Molecules* **18**(12), pp. 14760–14779, 2013.

[159] L. Zhang, J. Zhu, J. Ai, Z. Zhou, X. Jia, and E. Wang, "Label-free G-quadruplex-specific fluorescent probe for sensitive detection of copper(II) ion," *Biosens. Bioelectron.* **39**(1), pp. 268–273, 2013.

[160] J. S. Kahn, A. Trifonov, A. Cecconello, W. Guo, C. Fan, and I. Willner, "Integration of Switchable DNA-Based Hydrogels with Surfaces by the Hybridization Chain Reaction," *Nano Lett.* **15**(11), pp. 7773–7778, 2015.

[161] X. Yu, Y. Hu, J. S. Kahn, A. Cecconello, and I. Willner, "Orthogonal Dual–Triggered Shape–Memory DNA–Based Hydrogels," *Chem. - Eur. J.* **22**(41), pp. 14504–14507, 2016.

[162] W. U. Dittmer, A. Reuter, and F. C. Simmel, "A DNA-based machine that can cyclically bind and release thrombin," *Angew. Chem., Int. Ed.* **43**(27), pp. 3550–3553, 2004.

[163] J. R. Lakowicz, *Principles of fluorescence spectroscopy*, Springer, New York, U.S.A., 3. ed., 2006.

[164] B. Valeur and M. N. Berberan-Santos, *Molecular Fluorescence: Principles and applications*, Wiley-VCH, Weinheim, Germany, 2. ed., 2013.

[165] A. Jabłoński, "Über den Mechanismus der Photolumineszenz von Farbstoffphosphoren," *Z. Phys.* **94**, pp. 38–46, 1935.

[166] P. W. Atkins and J. de Paula, *Physikalische Chemie*, Wiley-VCH, Weinheim, Germany, 4., vollst. überarb. ed., 2006.

[167] R. W. Wagner and J. S. Lindsey, "A molecular photonic wire," *J. Am. Chem. Soc.* **116**(21), pp. 9759–9760, 1994.

[168] Y. Ohya, K. Yabuki, M. Hashimoto, A. Nakajima, and T. Ouchi, "Multistep fluorescence resonance energy transfer in sequential chromophore array constructed on oligo-DNA assemblies," *Bioconjugate Chem.* **14**(6), pp. 1057–1066, 2003.

[169] S. Vyawahare, S. Eyal, K. D. Mathews, and S. R. Quake, "Nanometer-scale Fluorescence Resonance Optical Waveguides," *Nano Lett.* **4**(6), pp. 1035–1039, 2004.

[170] M. Bälter, M. Hammarson, P. Remón, S. Li, N. Gale, T. Brown, and J. Andréasson, "Reversible energy-transfer switching on a DNA scaffold," *J. Am. Chem. Soc.* **137**(7), pp. 2444–2447, 2015.

[171] J. K. Hannestad, P. Sandin, and B. Albinsson, "Self-assembled DNA photonic wire for long-range energy transfer," *J. Am. Chem. Soc.* **130**(47), pp. 15889–15895, 2008.

[172] M. Heilemann, P. Tinnefeld, G. Sanchez Mosteiro, M. Garcia Parajo, N. F. van Hulst, and M. Sauer, "Multistep energy transfer in single molecular photonic wires," *J. Am. Chem. Soc.* **126**(21), pp. 6514–6515, 2004.

[173] M. Heilemann, R. Kasper, P. Tinnefeld, and M. Sauer, "Dissecting and reducing the heterogeneity of excited-state energy transport in DNA-based photonic wires," *J. Am. Chem. Soc.* **128**(51), pp. 16864–16875, 2006.

[174] C. M. Spillmann, S. Buckhout-White, E. Oh, E. R. Goldman, M. G. Ancona, and I. L. Medintz, "Extending FRET cascades on linear DNA photonic wires," *Chem. Commun.* **50**(55), pp. 7246–7249, 2014.

[175] K. Boeneman, D. E. Prasuhn, J. B. Blanco-Canosa, P. E. Dawson, J. S. Melinger, M. Ancona, M. H. Stewart, K. Susumu, A. Huston, and I. L. Medintz, "Self-assembled quantum dot-sensitized multivalent DNA photonic wires," *J. Am. Chem. Soc.* **132**(51), pp. 18177–18190, 2010.

[176] S. Buckhout-White, C. M. Spillmann, W. R. Algar, A. Khachatrian, J. S. Melinger, E. R. Goldman, M. G. Ancona, and I. L. Medintz, "Assembling programmable FRET-based photonic networks using designer DNA scaffolds," *Nat. Commun.* **5**, p. 5615, 2014.

[177] C. L. Dwyer, S. A. Díaz, S. A. Walper, A. Samanta, K. Susumu, E. Oh, S. Buckhout-White, and I. L. Medintz, "Chemoenzymatic Sensitization of DNA Photonic Wires Mediated through Quantum Dot Energy Transfer Relays," *Chem. Mater.* **27**(19), pp. 6490–6494, 2015.

[178] M. Massey, M. G. Ancona, I. L. Medintz, and W. R. Algar, "Time-Gated DNA Photonic Wires with Förster Resonance Energy Transfer Cascades Initiated by a Luminescent Terbium Donor," *ACS photonics* **2**(5), pp. 639–652, 2015.

[179] C. M. Spillmann, M. G. Ancona, S. Buckhout-White, W. R. Algar, M. H. Stewart, K. Susumu, A. L. Huston, E. R. Goldman, and I. L. Medintz, "Achieving Effective Terminal Exciton Delivery in Quantum Dot Antenna-Sensitized Multistep DNA Photonic Wires," *ACS nano* **7**(8), pp. 7101–7118, 2013.

[180] X. Hu, A. Damjanović, T. Ritz, and K. Schulten, "Architecture and mechanism of the light-harvesting apparatus of purple bacteria," *Proc. Natl. Acad. Sci. U.S.A.* **95**(11), pp. 5935–5941, 1998.

[181] G. McDermott, S. M. Prince, A. A. Freer, A. M. Hawthornthwaite-Lawless, M. Z. Papiz, R. J. Cogdell, and N. W. Isaacs, "Crystal structure of an integral membrane light-harvesting complex from photosynthetic bacteria," *Nature* **374**, pp. 517–521, 1995.

[182] R. Emerson, "The Photochemical Reaction in Photosynthesis," *J. Gen. Physiol.* **16**(2), pp. 191–205, 1932.

[183] P. K. Dutta, S. Levenberg, A. Loskutov, D. Jun, R. Saer, J. T. Beatty, S. Lin, Y. Liu, N. W. Woodbury, and H. Yan, "A DNA-directed light-harvesting/reaction center system," *J. Am. Chem. Soc.* **136**(47), pp. 16618–16625, 2014.

[184] B. Gobets and R. van Grondelle, "Energy transfer and trapping in photosystem I," *Biochim. Biophys. Acta* **1507**, pp. 80–99, 2001.

[185] T. Mayr, S. M. Borisov, T. Abel, B. Enko, K. Waich, G. Mistlberger, and I. Klimant, "Light Harvesting as a Simple and Versatile Way to Enhance Brightness of Luminescent Sensors," *Anal. Chem.* **81**(15), pp. 6541–6545, 2009.

[186] F. Garo and R. Häner, "A DNA–Based Light–Harvesting Antenna," *Angew. Chem., Int. Ed.* **51**(4), pp. 916–919, 2012.

[187] R. A. Miller, A. D. Presley, and M. B. Francis, "Self-assembling light-harvesting systems from synthetically modified tobacco mosaic virus coat proteins," *J. Am. Chem. Soc.* **129**(11), pp. 3104–3109, 2007.

[188] A. Ruiz-Carretero, P. G. A. Janssen, A. L. Stevens, M. Surin, L. M. Herz, and A. P. H. J. Schenning, "Directing energy transfer in discrete one-dimensional oligonucleotide-templated assemblies," *Chem. Commun.* **47**(3), pp. 884–886, 2011.

[189] A. L. Benvin, Y. Creeger, G. W. Fisher, B. Ballou, A. S. Waggoner, and B. A. Armitage, "Fluorescent DNA nanotags: supramolecular fluorescent labels based on intercalating dye arrays assembled on nanostructured DNA templates," *J. Am. Chem. Soc.* **129**(7), pp. 2025–2034, 2007.

[190] H. Ozhalici-Unal and B. A. Armitage, "Fluorescent DNA nanotags based on a self-assembled DNA tetrahedron," *ACS nano* **3**(2), pp. 425–433, 2009.

[191] F. Pu, L. Wu, X. Ran, J. Ren, and X. Qu, "G-quartet-based nanostructure for mimicking light-harvesting antenna," *Angew. Chem., Int. Ed.* **54**(3), pp. 892–896, 2015.

[192] C. V. Kumar and M. R. Duff, JR, "DNA-based supramolecular artificial light harvesting complexes," *J. Am. Chem. Soc.* **131**(44), pp. 16024–16026, 2009.

[193] J. G. Woller, J. K. Hannestad, and B. Albinsson, "Self-assembled nanoscale DNA-porphyrin complex for artificial light harvesting," *J. Am. Chem. Soc.* **135**(7), pp. 2759–2768, 2013.

[194] A. Dietrich, V. Buschmann, C. Müller, and M. Sauer, "Fluorescence resonance energy transfer (FRET) and competing processes in donor–acceptor substituted DNA strands: A comparative study of ensemble and single-molecule data," *Rev. Mol. Biotechnol.* **82**(3), pp. 211–231, 2002.

[195] D. M. Gray, J.-D. Wen, C. W. Gray, R. Repges, C. Repges, G. Raabe, and J. Fleischhauer, "Measured and calculated CD spectra of G-quartets stacked with the same or opposite polarities," *Chirality* **20**, pp. 431–440, 2008.

[196] J. Kypr, I. Kejnovska, D. Renciuk, and M. Vorlickova, "Circular dichroism and conformational polymorphism of DNA," *Nucleic Acids Res.* **37**(6), pp. 1713–1725, 2009.

[197] Le Ying, N. Xie, Y. Yang, X. Yang, Q. Zhou, B.-C. Yin, J. Huang, and K. Wang, "A Cell-Surface-Anchored Ratiometric I-Motif Sensor for Extracellular pH Detection," *Chem. Commun.* **52**, pp. 7818–7821, 2016.

[198] B. G. Cox, D. Knop, and H. Schneider, "Thermodynamics and kinetics of alkali metal ion complexes with 5,6-benzo-4,7,13,16,21,24-hexaoxa-1,10-diazabicyclo[8.8.8]hexacosane in methanol," *J. Phys. Chem.* **84**(3), pp. 320–323, 1980.

[199] K. E. Krakowiak, J. S. Bradshaw, H.-Y. An, and R. M. Izatt, "Simple methods for the preparation of cryptands," *Pure Appl. Chem* **65**(3), pp. 511–514, 1993.

[200] T. Schwarze, H. Müller, S. Ast, D. Steinbrück, S. Eidner, F. Geissler, M. U. Kumke, and H.-J. Holdt, "Fluorescence lifetime-based sensing of sodium by an optode," *Chem. Commun.* **50**(91), pp. 14167–14170, 2014.

[201] X.-D. Wang and O. S. Wolfbeis, "Fiber-Optic Chemical Sensors and Biosensors (2013-2015)," *Anal. Chem.* **88**(1), pp. 203–227, 2016.

[202] P. K. Dutta, S. Lin, A. Loskutov, S. Levenberg, D. Jun, R. Saer, J. T. Beatty, Y. Liu, H. Yan, and N. W. Woodbury, "Reengineering the optical absorption cross-section of photosynthetic reaction centers," *J. Am. Chem. Soc.* **136**(12), pp. 4599–4604, 2014.

Appendix

Table A.1: Overview of all staple strands used for the DNA origami triangle.

notation	**sequence (5' → 3')**
t8s27g	CGC GAA CTA AAA CAG AGG TGA GGC TTA GAA GTA TT
t8s7g	AGC CAT TTA AAC GTC ACC AAT GAA CAC CAG AAC CA
t9s10h	TAT CTT ACC GAA GCC CAA ACG CAA TAAT AAC GAA AAT CAC CAG
t9s16e	ACT AAA GTA CGG TGT CGA ATA TAA
t9s18g	TGC TGT AGA TCC CCC TCA AAT GCT GCG AGA GGC TTT TGC A
t9s20h	AAA GAA GTT TTG CCA GCA TAA ATA TTC ATT GAC TCA ACA TGT T
t9s26e	ACC ACC AGC AGA AGA TGA TAG CCC
t9s28g	TAA AAC ATT AGA AGA ACT CAA ACT TTT TAT AAT CAG TGA G
t9s30h	GCC ACC GAG TAA AAG AAC ATC ACT TGC CTG AGC GCC ATT AAA A
t9s6e	CCA TTA GCA AGG CCG GGG GAA TTA
t9s8g	GAG CCA GCG AAT ACC CAA AAG AAC ATG AAA TAG CAA TAG C
t-10s17h	ACC AAC CTA AAA AAT CAA CGT AAC AAA TAA ATT GGG CTT GAG A
t-10s27h	AAC TCA CAT TAT TGA GTG TTG TTC CAG AAA CCG TCT ATC AGG G
t-10s7h	ACG ACA ATA AAT CCC GAC TTG CGG GAG ATC CTG AAT CTT ACC A
t-12s19h	CCT GAC GAG AAA CAC CAG AAC GAG TAG GCT GCT CAT TCA GTG A
t-12s29h	ACG TGG ACT CCA ACG TCA AAG GGC GAA TTT GGA ACA AGA GTC C

notation	sequence (5' → 3')
t-12s9h	TGC TAT TTT GCA CCC AGC TAC AAT TTT GTT TTG AAG CCT TAA A
t-1s10e	AGA GAA TAA CAT AAA AAC AGG GAA GCG CAT TA
t-1s12i	AGG GAT AGC TCA GAG CCA CCA CCC CAT GTC AA
t-1s14e	ATT TTC TGT CAG CGG AGT GAG AAT ACC GAT AT
t-1s14i	CAA CAG TTT ATG GGA TTT TGC TAA TCA AAA GG
t-1s16e	ATT CGG TCT GCG GGA TCG TCA CCC GAA ATC CG
t-1s16i	GCC GCT TTG CTG AGG CTT GCA GGG GAA AAG GT
t-1s18g	CGA CCT GCG GTC AAT CAT AAG GGA ACG GAA CAA CAT TAT T
t-1s18i	GCG CAG ACT CCA TGT TAC TTA GCC CGT TTT AA
t-1s20e	ACA GGT AGA AAG ATT CAT CAG TTG AGA TTT AG
t-1s22i	CGC GTC TGA TAG GAA CGC CAT CAA CTT TTA CA
t-1s24e	CAG TTT GAC GCA CTC CAG CCA GCT AAA CGA CG
t-1s24i	AGG AAG ATG GGG ACG ACG ACA GTA ATC ATA TT
t-1s26e	GCC AGT GCG ATC CCC GGG TAC CGA GTT TTT CT
t-1s26i	CTC TAG AGC AAG CTT GCA TGC CTG GTC AGT TG
t-1s28g	TTT CAC CAG CCT GGC CCT GAG AGA AAG CCG GCG AAC GTG G
t-1s28i	CCT TCA CCG TGA GAC GGG CAA CAG CAG TCA CA
t-1s2i	CCT TTT TTC ATT TAA CAA TTT CAT AGG ATT AG
t-1s30e	CGA GAA AGG AAG GGA AGC GTA CTA TGG TTG CT
t-1s4e	TTA TCA AAC CGG CTT AGG TTG GGT AAG CCT GT
t-1s4i	TTT AAC CTA TCA TAG GTC TGA GAG TTC CAG TA
t-1s6e	TTA GTA TCG CCA ACG CTC AAC AGT CGG CTG TC
t-1s6i	AGT ATA AAA TAT GCG TTA TAC AAA GCC ATC TT
t-1s8g	TTT CCT TAG CAC TCA TCG AGA ACA ATA GCA GCC TTT ACA G
t-1s8i	CAA GTA CCT CAT TCC AAG AAC GGG AAA TTC AT
t-2s11g	CCT CAG AAC CGC CAC CCA AGC CCA ATA GGA ACG TAA ATG A
t-2s13g	AGA CGT TAC CAT GTA CCG TAA CAC CCC TCA GAA CCG CCA C
t-2s15f	CAC GCA TAA GAA AGG AAC AAC TAA GTC TTT CC
t-2s17f	ATT GTG TCT CAG CAG CGA AAG ACA CCA TCG CC

notation	**sequence (5' → 3')**
t-2s1g	AAA ACA AAA TTA ATT AAA TGG AAA CAG TAC ATT AGT GAA T
t-2s21g	GCT CAT TTT TTA ACC AGC CTT CCT GTA GCC AGG CAT CTG C
t-2s23g	GTA ACC GTC TTT CAT CAA CAT TAA AAT TTT TGT TAA ATC A
t-2s25f	ACG TTG TAT TCC GGC ACC GCT TCT GGC GCA TC
t-2s27f	CCA GGG TGG CTC GAA TTC GTA ATC CAG TCA CG
t-2s3g	AGA GTC AAA AAT CAA TAT ATG TGA TGA AAC AAA CAT CAA G
t-2s5f	ACT AGA AAT ATA TAA CTA TAT GTA CGC TGA GA
t-2s7f	TCA ATA ATA GGG CTT AAT TGA GAA TCA TAA TT
t-3s10g	AAC GTC AAA AAT GAA AAG CAA GCC GTT TTT ATG AAA CCA A
t-3s14e	GTT TTG TCA GGA ATT GCG AAT AAT CCG ACA AT
t-3s16e	GAC AAC AAG CAT CGG AAC GAG GGT GAG ATT TG
t-3s18g	TAT CAT CGT TGA AAG AGG ACA GAT GGA AGA AAA ATC TAC G
t-3s20g	TTA ATA AAA CGA ACT AAC CGA ACT GAC CAA CTC CTG ATA A
t-3s24e	TGT AGA TGG GTG CCG GAA ACC AGG AAC GCC AG
t-3s26e	GGT TTT CCA TGG TCA TAG CTG TTT GAG AGG CG
t-3s28g	GTT TGC GTC ACG CTG GTT TGC CCC AAG GGA GCC CCC GAT T
t-3s30g	TAG AGC TTG ACG GGG AGT TGC AGC AAG CGG TCA TTG GGC G
t-3s4e	GAT TAA GAA ATG CTG ATG CAA ATC AGA ATA AA
t-3s6e	CAC CGG AAT CGC CAT ATT TAA CAA AAT TTA CG
t-3s8g	AGC ATG TAT TTC ATC GTA GGA ATC AAA CGA TTT TTT GTT T
t-4s11g	AGG TTT AGT ACC GCC ATG AGT TTC GTC ACC AGG ATC TAA A
t-4s13g	AGC GTA ACT ACA AAC TAC AAC GCC TAT CAC CGT ACT CAG G
t-4s15f	TAG TTG CGA ATT TTT TCA CGT TGA TCA TAG TT

notation	sequence (5' → 3')
t-4s17f	GTA CAA CGA GCA ACG GCT ACA GAG GAT ACC GA
t-4s1g	GAG CAA AAG AAG ATG AGT GAA TAA CCT TGC TTA TAG CTT A
t-4s21g	GTT AAA ATT CGC ATT AAT GTG AGC GAG TAA CAC ACG TTG G
t-4s23g	GGA TAG GTA CCC GTC GGA TTC TCC TAA ACG TTA ATA TTT T
t-4s25f	AGT TGG GTC AAA GCG CCA TTC GCC CCG TAA TG
t-4s27f	CGC GCG GGC CTG TGT GAA ATT GTT GGC GAT TA
t-4s3g	ACA TAG CGC TGT AAA TCG TCG CTA TTC ATT TCA ATT ACC T
t-4s5f	GTT AAA TAC AAT CGC AAG ACA AAG CCT TGA AA
t-4s7f	CCC ATC CTC GCC AAC ATG TAA TTT AAT AAG GC
t-5s10g	TCC CAA TCC AAA TAA GAT TAC CGC GCC CAA TAA ATA ATA T
t-5s16e	AAC AGC TTG CTT TGA GGA CTA AAG CGA TTA TA
t-5s18g	CCA AGC GCA GGC GCA TAG GCT GGC AGA ACT GGC TCA TTA T
t-5s20g	ACC AGT CAG GAC GTT GGA ACG GTG TAC AGA CCG AAA CAA A
t-5s26e	TGC TGC AAA TCC GCT CAC AAT TCC CAG CTG CA
t-5s28g	TTA ATG AAG TTT GAT GGT GGT TCC GAG GTG CCG TAA AGC A
t-5s30g	CTA AAT CGG AAC CCT AAG CAG GCG AAA ATC CTT CGG CCA A
t-5s6e	GTG TGA TAA GGC AGA GGC ATT TTC AGT CCT GA
t-5s8g	ACA AGA AAG CAA GCA AAT CAG ATA ACA GCC ATA TTA TTT A
t-6s13f	ACA GAC AGC CCA AAT CTC CAA AAA AAA ATT TCT TA
t-6s15c	CGA GGT GAG GCT CCA AAA GGA GCC
t-6s17f	ACC CCC AGA CTT TTT CAT GAG GAA CTT GCT TT
t-6s23f	CGG CGG ATT GAA TTC AGG CTG CGC AAC GGG GGA TG
t-6s25c	TGG CGA AAT GTT GGG AAG GGC GAT

notation	**sequence (5' → 3')**
t-6s27f	TGT CGT GCA CAC AAC ATA CGA GCC ACG CCA GC
t-6s3f	TCC CTT AGA ATA ACG CGA GAA AAC TTT TAC CGA CC
t-6s5c	GTT TGA AAT TCA AAT ATA TTT TAG
t-6s7f	AAT AGA TAG AGC CAG TAA TAA GAG ATT TAA TG
t-7s10g	GCC AGT TAC AAA ATA ATA GAA GGC TTA TCC GGT TAT CAA C
t-7s18g	AAA ACA CTT AAT CTT GAC AAG AAC TTA ATC ATT GTG AAT T
t-7s20g	ACC TTA TGC GAT TTT ATG ACC TTC ATC AAG AGC ATC TTT G
t-7s28g	TTC CAG TCC TTA TAA ATC AAA AGA GAA CCA TCA CCC AAA T
t-7s30g	CAA GTT TTT TGG GGT CGA AAT CGG CAA AAT CCG GGA AAC C
t-7s8g	GCG CCT GTT ATT CTA AGA ACG CGA TTC CAG AGC CTA ATT T
t-8s15f	CGG TTT ATC AGG TTT CCA TTA AAC GGG AAT ACA CT
t-8s17c	GGC AAA AGT AAA ATA CGT AAT GCC
t-8s25f	TCT TCG CTA TTG GAA GCA TAA AGT GTA TGC CCG CT
t-8s27c	GCG CTC ACA AGC CTG GGG TGC CTA
t-8s5	TTC TGA CCT AAA ATA TAA AGT ACC GAC TGC AGA AC
t-8s7c	TCA GCT AAA AAA GGT AAA GTA ATT
t-9s10g	ACG CTA ACG AGC GTC TGG CGT TTT AGC GAA CCC AAC ATG T
t-9s20g	TGG TTT AAT TTC AAC TCG GAT ATT CAT TAC CCA CGA AAG A
t-9s30g	CGA TGG CCC ACT ACG TAT AGC CCG AGA TAG GGA TTG CGT T
ts-rem1	GCG CTT AAT GCG CCG CTA CAG GGC
t-5s2e-t6s23c	TTA ATT AAT TTT TTA CCA TAT CAA A
t-7s4e-t8s25c	TTA ATT TCA TCT TAG ACT TTA CAA
t-9s6e-t10s27c	CTG TCC AGA CGT ATA CCG AAC GA
t-11s8e-t12s29c	TCA AGA TTA GTG TAG CAA TAC T
t-5s12e-t6s3c	TGT AGC ATT CCT TTT ATA AAC AGT T
t-7s14e-t8s5c	TTT AAT TGT ATT TCC ACC AGA GCC

notation	sequence (5' → 3')
t-9s16e-t10s7c	ACT ACG AAG GCT TAG CAC CAT TA
t-11s18e-t12s9c	ATA AGG CTT GCA ACA AAG TTA C
t-5s22e-t6s13c	GTG GGA ACA AAT TTC TAT TTT TGA G
t-7s24e-t8s15c	CGG TGC GGG CCT TCC AAA AAC ATT
t-9s26e-t10s17c	ATG AGT GAG CTT TTA AAT ATG CA
t-11s28e-t12s19c	ACT ATT AAA GAG GAT AGC GTC C
t11s18h	AAT ACT GCG GAA TCG TAG GGG GTA ATA GTA AAA TGT TTA GAC T
t11s28h	TCT TTG ATT AGT AAT AGT CTG TCC ATC ACG CAA ATT AAC CGT T
t11s8h	CAG AAG GAA ACC GAG GTT TTT AAG AAA AGT AAG CAG ATA GCC G
t1s10g	GAC GGG AGA ATT AAC TCG GAA TAA GTT TAT TTC CAG CGC C
t1s12i	TCA TAT GTG TAA TCG TAA AAC TAG TCA TTT TC
t1s14i	GTG AGA AAA TGT GTA GGT AAA GAT ACA ACT TT
t1s16i	GGC ATC AAA TTT GGG GCG CGA GCT AGT TAA AG
t1s18i	TTC GAG CTA AGA CTT CAA ATA TCG GGA ACG AG
t1s20g	GAA TAC CAC ATT CAA CTT AAG AGG AAG CCC GAT CAA AGC G
t1s22i	TCG GGA GAT ATA CAG TAA CAG TAC AAA TAA TT
t1s24i	CCT GAT TAA AGG AGC GGA ATT ATC TCG GCC TC
t1s26i	GCA AAT CAC CTC AAT CAA TAT CTG CAG GTC GA
t1s28i	CGA CCA GTA CAT TGG CAG ATT CAC CTG ATT GC
t1s2i	CGG GGT TTC CTC AAG AGA AGG ATT TTG AAT TA
t1s30g	TTG ACG AGC ACG TAT ACT GAA ATG GAT TAT TTA ATA AAA G
t1s4i	AGC GTC ATG TCT CTG AAT TTA CCG ACT ACC TT
t1s6i	TTC ATA ATC CCC TTA TTA GCG TTT TTC TTA CC
t1s8i	ATG GTT TAT GTC ACA ATC AAT AGA TAT TAA AC
t2s11g	AGA AAA GCC CCA AAA AGA GTC TGG AGC AAA CAA TCA CCA T
t2s13g	ACA GTC AAA GAG AAT CGA TGA ACG ACC CCG GTT GAT AAT C
t2s15f	ATA GTA GTA TGC AAT GCC TGA GTA GGC CGG AG
t2s17f	AAC CAG ACG TTT AGC TAT ATT TTC TTC TAC TA

notation	**sequence (5' → 3')**
t2s1g	GAT AAG TGC CGT CGA GCT GAA ACA TGA AAG TAT ACA GGA G
t2s21g	CCT GAT TGC TTT GAA TTG CGT AGA TTT TCA GGC ATC AAT A
t2s23g	TGG CAA TTT TTA ACG TCA GAT GAA AAC AAT AAC GGA TTC G
t2s25f	AAG GAA TTA CAA AGA AAC CAC CAG TCA GAT GA
t2s27f	GGA CAT TCA CCT CAA ATA TCA AAC ACA GTT GA
t2s3g	TTT GAT GAT TAA GAG GCT GAG ACT TGC TCA GTA CCA GGC G
t2s5f	CCG GAA CCC AGA ATG GAA AGC GCA ACA TGG CT
t2s7f	AAA GAC AAC ATT TTC GGT CAT AGC CAA AAT CA
t3s10g	GTC AGA GGG TAA TTG ATG GCA ACA TAT AAA AGC GAT TGA G
t3s14e	CAA TAT GAC CCT CAT ATA TTT TAA AGC ATT AA
t3s16e	CAT CCA ATA AAT GGT CAA TAA CCT CGG AAG CA
t3s18g	AAC TCC AAG ATT GCA TCA AAA AGA TAA TGC AGA TAC ATA A
t3s20g	CGC CAA AAG GAA TTA CAG TCA GAA GCA AAG CGC AGG TCA G
t3s24e	TAA TCC TGA TTA TCA TTT TGC GGA GAG GAA GG
t3s26e	TTA TCT AAA GCA TCA CCT TGC TGA TGG CCA AC
t3s28g	AGA GAT AGT TTG ACG CTC AAT CGT ACG TGC TTT CCT CGT T
t3s30g	AGA ATC AGA GCG GGA GAT GGA AAT ACC TAC ATA ACC CTT C
t3s4e	TGT ACT GGA AAT CCT CAT TAA AGC AGA GCC AC
t3s6e	CAC CGG AAA GCG CGT TTT CAT CGG AAG GGC GA
t3s8g	CAT TCA ACA AAC GCA AAG ACA CCA GAA CAC CCT GAA CAA A
t4s11g	GCA AAT ATT TAA ATT GAG ATC TAC AAA GGC TAC TGA TAA A
t4s13g	CGT TCT AGT CAG GTC ATT GCC TGA CAG GAA GAT TGT ATA A
t4s15f	CAG GCA AGA TAA AAA TTT TTA GAA TAT TCA AC
t4s17f	GAT TAG AGA TTA GAT ACA TTT CGC AAA TCA TA

notation	sequence (5' → 3')
t4s1g	TAG CCC GGA ATA GGT GAA TGC CCC CTG CCT ATG GTC AGT G
t4s21g	GCG CAG AGG CGA ATT AAT TAT TTG CAC GTA AAT TCT GAA T
t4s23g	GAT TAT ACA CAG AAA TAA AGA AAT ACC AAG TTA CAA AAT C
t4s25f	TAG GAG CAT AAA AGT TTG AGT AAC ATT GTT TG
t4s27f	TGA CCT GAC AAA TGA AAA ATC TAA AAT ATC TT
t4s3g	TTT AAC GGT TCG GAA CCT ATT ATT AGG GTT GAT ATA AGT A
t4s5f	CTC AGA GCA TAT TCA CAA ACA AAT TAA TAA GT
t4s7f	GGA GGG AAT TTA GCG TCA GAC TGT CCG CCT CC
t5s10g	GAT AAC CCA CAA GAA TGT TAG CAA ACG TAG AAA ATT ATT C
t5s14e	TTA ATG CCT TAT TTC AAC GCA AGG GCA AAG AA
t5s16e	TTA GCA AAT AGA TTT AGT TTG ACC AGT ACC TT
t5s18g	TAA TTG CTT TAC CCT GAC TAT TAT GAG GCA TAG TAA GAG C
t5s20g	AAC ACT ATC ATA ACC CAT CAA AAA TCA GGT CTC CTT TTG A
t5s24e	AAT GGA AGC GAA CGT TAT TAA TTT CTA ACA AC
t5s26e	TAA TAG ATC GCT GAG AGC CAG CAG AAG CGT AA
t5s28g	GAA TAC GTA ACA GGA AAA ACG CTC CTA AAC AGG AGG CCG A
t5s30g	TTA AAG GGA TTT TAG ATA CCG CCA GCC ATT GCG GCA CAG A
t5s4e	CCT TGA GTC AGA CGA TTG GCC TTG CGC CAC CC
t5s6e	TCA GAA CCC AGA ATC AAG TTT GCC GGT AAA TA
t5s8g	TTG ACG GAA ATA CAT ACA TAA AGG GCG CTA ATA TCA GAG A
t6s15g	ATA AAG CCT TTG CGG GAG AAG CCT GGA GAG GGT AG
t6s17f	TAA GAG GTC AAT TCT GCG AAC GAG ATT AAG CA
t6s25g	TCA ATA GAT ATT AAA TCC TTT GCC GGT TAG AAC CT
t6s27f	CAA TAT TTG CCT GCA ACA GTG CCA TAG AGC CG
t6s5g	CAG AGC CAG GAG GTT GAG GCA GGT AAC AGT GCC CG
t6s7f	ATT AAA GGC CGT AAT CAG TAG CGA GCC ACC CT

notation	**sequence (5' → 3')**
t7s10g	ATA AGA GCA AGA AAC ATG GCA TGA TTA AGA CTC CGA CTT G
t7s14e	ATG ACC CTG TAA TAC TTC AGA GCA
t7s16e	TAA AGC TAT ATA ACA GTT GAT TCC CAT TTT TG
t7s18g	CGG ATG GCA CGA GAA TGA CCA TAA TCG TTT ACC AGA CGA C
t7s20g	GAT AAA AAC CAA AAT ATT AAA CAG TTC AGA AAT TAG AGC T
t7s24e	ACA ATT CGA CAA CTC GTA ATA CAT
t7s26e	TTG AGG ATG GTC AGT ATT AAC ACC TTG AAT GG
t7s28g	CTA TTA GTA TAT CCA GAA CAA TAT CAG GAA CGG TAC GCC A
t7s30g	GAA TCC TGA GAA GTG TAT CGG CCT TGC TGG TAC TTT AAT G
t7s4e	GCC GCC AGC ATT GAC ACC ACC CTC
t7s6e	AGA GCC GCA CCA TCG ATA GCA GCA TGA ATT AT
t7s8g	CAC CGT CAC CTT ATT ACG CAG TAT TGA GTT AAG CCC AAT A
t8s17g	TAA TTG CTT GGA AGT TTC ATT CCA AAT CGG TTG TA

Table A.2: Overview of modified staple strands and studied telomeric DNA sequences (modified and unmodified). Fluorophores which are internally introduced to the DNA sequence are coupled to a uracil base. The oligonucleotides have been acquired from Metabion International AG.

notation	**sequence (5' → 3')**	**ref.**
Cy3-RevHumTel-FAM	**Cy3**-TTG GGA TTG GGA TTG GGA TTG GGA TT-**FAM**	[1]
Cy3-RevHumTel	**Cy3**-TTG GGA TTG GGA TTG GGA TTG GGA TT	[1]
RevHumTel-FAM	TTG GGA TTG GGA TTG GGA TTG GGA TT-**FAM**	[1]
Cy3-RevHumTel-t1s6i	**Cy3**-TTG GGA TTG GGA TTG GGA TTG GGA TTT TTC ATA ATC CCC TTA TTA GCG TTT TTC TTA CC	[1,2]
FAM-t-1s6i	AGT ATA AAA TAT GCG TTA TAC A (**FAM**) A GCC ATC TT	[1,2]
Cy5-RevHumTel-t1s8i	**Cy5**-TTG GGA TTG GGA TTG GGA TTG GGA TTT ATG GTT TAT GTC ACA ATC AAT AGA TAT TAA AC	[1]
Cy3-t-1s8i	CAA GTA CCT CAT TCC AAG AAC GGG AAA TTC AT-**Cy3**	[1]
RevHumTel	TTG GGA TTG GGA TTG GGA TTG GGA TT	
HumTel	TTG GGT TAG GGT TAG GGT TAG GGT TT	
Cy3-HumTel-t1s6i	**Cy3**-TTG GGT TAG GGT TAG GGT TAG GGT TTT TCA TAA TCC CCT TAT TAG CGT TTT TCT TAC C	[2]
Cy5-t2s7f	AAA GAC AAC ATT TTC GGT CAT AGC CA (**Cy5**) AAT CA	[2]
IRDye700-t2s5f	CCG GAA (**IRDye700**) CCC AGA ATG GAA AGC GCA ACA TGG CT	[2]
Cy5-t-2s5f_II	**Cy5**-TAT ATG TAC GCT GAG A	[3]
t-2s5f_II	TAT ATG TAC GCT GAG A	[3]
Cy3-t-2s3g_I (**T1**)	**Cy3**-AGA GTC AAA AAT CAA T	[3]
t-2s3g_I	AGA GTC AAA AAT CAA T	[3]
FAM-t-2s3g_II (**D1**)	**FAM**-ATA TGT GAT GAA ACA AAC ATC AAG	[3]
t-2s3g_II	ATA TGT GAT GAA ACA AAC ATC AAG	[3]

notation	**sequence (5' → 3')**	**ref.**
Cy3-t-1s4e_II-t-1s6e (**T2**)	**Cy3**-GTA AGC CTG TTT AGT ATC GCC AAC GCT CAA CAG TCG GCT GTC	[3]
t-1s4e_II-t-1s6e	GTA AGC CTG TTT AGT ATC GCC AAC GCT CAA CAG TCG GCT GTC	[3]
FAM-t-1s4e_I (**D2**)	TTA TCA AAC CGG C (**FAM**) TT AGG TTG G	[3]
t-1s4e_I	TTA TCA AAC CGG CTT AGG TTG G	[3]
Cy3-t-2s5f_I (**T3**)	**Cy3**-ACT AGA AAT ATA TAA C	[3]
t-2s5f_I	ACT AGA AAT ATA TAA C	[3]
FAM-t-2s7f (**D3**)	TCA ATA ATA GGG CTT A (**FAM**) AT TGA GAA TCA TAA TT	[3]
Cy3-FAM-t-3s4e_II (**T4, D4**)	**Cy3**-ATG CTG ATG CA (**FAM**) A ATC AGA ATA AA	[3]
Cy3-t-3s4e_II (**T4**)	**Cy3**-ATG CTG ATG CAA ATC AGA ATA AA	[3]
FAM-t-3s4e_II (**D4**)	ATG CTG ATG CA (**FAM**) A ATC AGA ATA AA	[3]
FAM-t-2s1g (**D5**)	AAA ACA AAA TTA ATT AAA TGG AAA CAG TAC ATT (**FAM**) AGT GAA T	[3]
Cy3-FAM-t-1s4e_II-t-1s6e (**T4, D6**)	**Cy3**-CAC CGG AA (**FAM**) T CGC CAT ATT TAA CAA AAT TTA CG	[3]
FAM-t-1s4e_II-t-1s6e (**D6**)	GTA (**FAM**) AGC CTG TTT AGT ATC GCC AAC GCT CAA CAG TCG GCT GTC	[3]
FAM-t-3s6e (**D7**)	CAC CGG AA (**FAM**) T CGC CAT ATT TAA CAA AAT TTA CG	[3]
FAM-t-4s1g-t-3s4e_I (**D8**)	GAG CAA AAG AAG ATG AGT GAA TAA CCT TGC TTA TAG CTT AGA TTA AGA (**FAM**) A	[3]
t-4s1g-t-3s4e_I	GAG CAA AAG AAG ATG AGT GAA TAA CCT TGC TTA TAG CTT AGAT TAA GAA	[3]

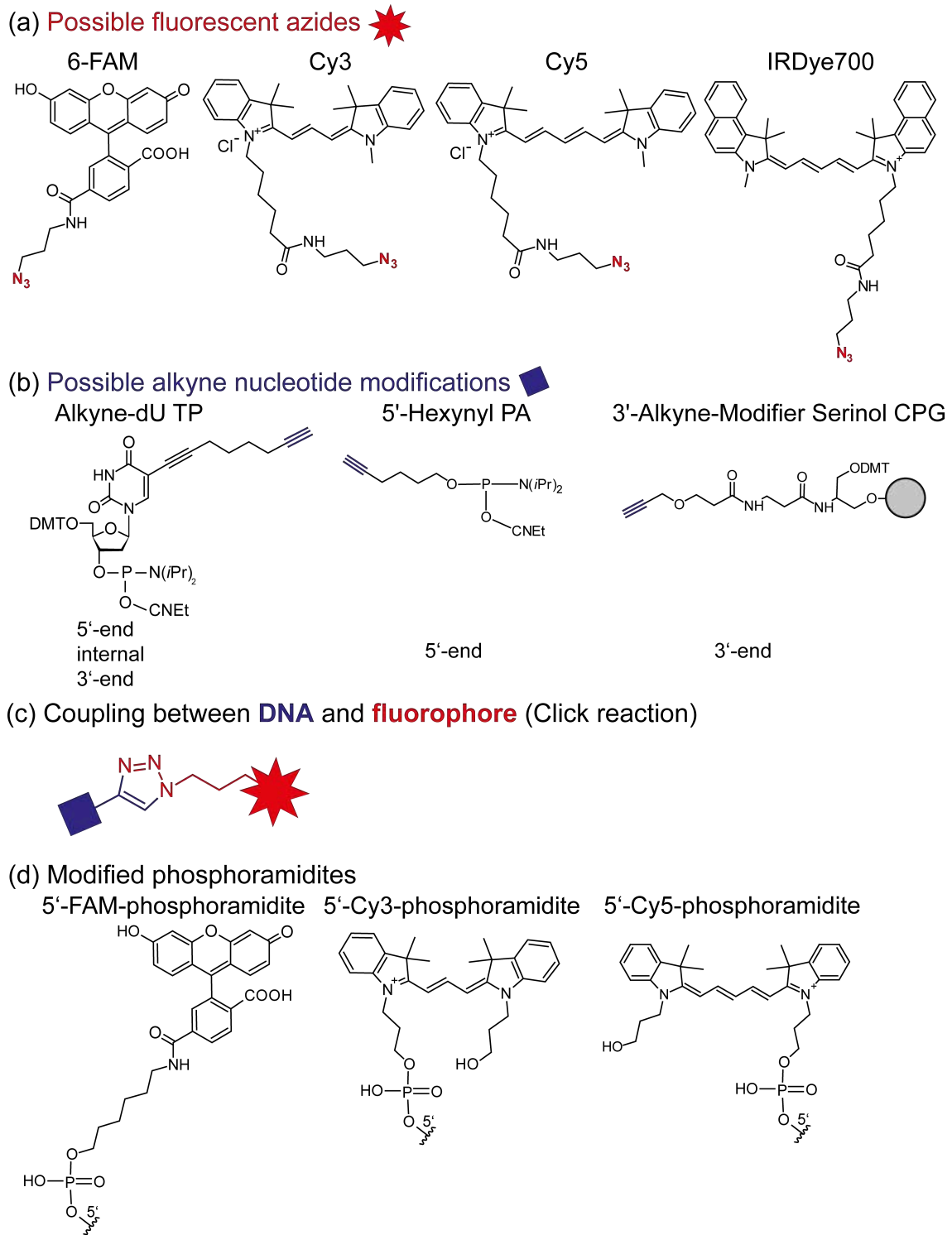

Figure A.1: (a-c) Detailed chemical structures for DNA modification using Click-chemistry according to the manufacturer (Metabion International AG, baseclick GmbH (Munich, Germany), Glen Research (Sterling, U.S.A.). (a) Chemical structures of different fluorophores which have been used in this work (FAM, Cy3, Cy5 and IRDye700) modified with an external azide (red). The exact structure of the fluorophore (linker between fluorophore and azide) can vary depending on the position in the DNA strand. (b) Possible alkyne modified DNA building blocks. Uracil or cytosine triphosphate (TP) modified with an external alkyne group can be used to couple fluorophores at

the 5'-end, internally and at the 3'-end (chemical structure exemplary shown for uracil, Alkyne-dU TP). If the last base of the DNA sequence (5'- or 3'-end) is neither a thymine nor a cytosine, fluorophores can be either attached using 5'-hexynyl phosphoramidite (PA) (5'-modification, 5'-Hexynyl PA) or a 3'-alkyne-modifier attached to the solid support material *e.g.* controlled pore glass (CPG, gray circle, 3'-Alkyne-Modifier Serinol CPG)). (c) After the click reaction the DNA building block (blue square) and the fluorophore (red star) are connected *via* a 1,2,3-triazole group. (d) The fluorophores can also be introduced through directly modified PA. This is often done for modifications at the 5'-end.

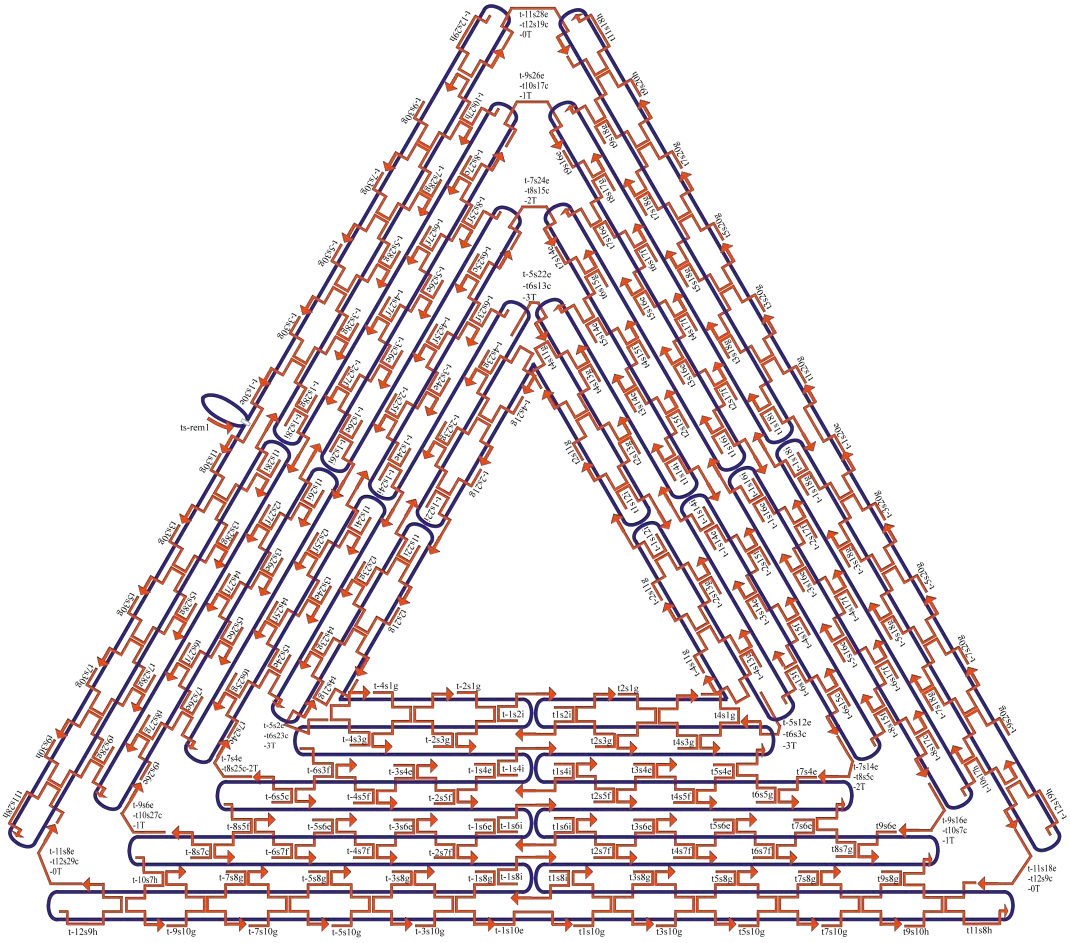

Figure A.2: Detailed map of the DNA origami triangle with all staple strands (red) and the scaffold strand (blue). The 3'-ends of the staple strands are indicated with an arrow.

List of abbreviations

List of abbreviations is sorted alphabetically (Latin letters first, Greek letters last) and refers to the main text. Abbreviations found in the manuscripts are not necessarily found in this list but are explained in the manuscript itself.

abbreviation	**meaning**
2D	two-dimensional
3D	three-dimensional
18-crown-6	1,4,7,10,13,16-hexaoxacyclooctadecane
A	adenine
A	absorbance
$A(260\ nm)$	absorbance at 260 nm
Ac	acceptor
Ac*	excited acceptor
AE	antenna effect
$AE1$	antenna effect 1, excitation at 450 nm, $AE1 = \frac{I(A,\lambda_{450nm})}{I(A,\lambda_{600nm})}$
$AE2$	antenna effect 2, excitation at 500 nm, $AE2 = \frac{I(A,\lambda_{500nm})}{I(A,\lambda_{600nm})}$
AFM	atomic force microscopy
A_i	amplitude of decay time component (data analysis)
AuNPs	gold nanoparticles
bzw.	*German:* beziehungsweise
C	cytosine
c	molar concentration
c'	concentration in $\left[\frac{ng}{\mu L}\right]$
ca.	circa
Ca^{2+}	calcium ion
$CaCl_2$	calcium chloride
CD	circular dichroism
CFD	constant function discriminator
CPG	controlled pore glass (solid support material)
cryptand	4,7,13,16,21,24-hexaoxa-1,10-diazabicyclo[8.8.8]hexacosane
Cs^+	cesium ion

abbreviation	**meaning**
CsCl	cesium chloride
Cy3	Cyanine3
Cy5	Cyanine5
D(1 - 8)	donor (1 - 8)
DMT	4,4'-dimethoxytrityl group
DNA	deoxyribonucleic acid
DNS	*German:* Desoxyribonukleinsäure
Do	donor
Do*	excited donor
DOTA	1,4,7,10-tetraazacyclododecane-1,4,7,10-tetraacetic acid
dsDNA	double stranded DNA
DX tile	double crossover tile
E	FRET efficiency
EDTA	ethylenediaminetetraacetic acid
e.g.	for example (Latin: *exempli gratia*)
E_I	FRET efficiency based on fluorescence intensity
engl.	Englis(c)h
Et	ethyl group
etc.	et cetera
E_τ	FRET efficiency based on fluorescence decay time
FAM	Fluorescein
$F_D(\lambda)$	donor's emission spectrum
Fl.	fluorescence
FRET	Förster resonance energy transfer
G	guanine
g	gravitational acceleration
G_m	any number of guanines of length m
GMP	guanylic acid, guanosine monophosphate
H	hydrogen
HOMO	highest occupied molecular orbital
HPLC	high-performance liquid chromatography
HumTel	human telomeric DNA
$I(A, \lambda_{ex}(A))$	acceptor emission intensity due to direct excitation
$I(A, \lambda_{ex}(D))$	acceptor emission intensity due to donor excitation
IC	internal conversion
I_D	donor's emission intensity in absence of the acceptor
I_{DA}	donor's emission intensity in presence of the acceptor
iPr	isopropyl group

abbreviation	**meaning**
IR	internal relaxation
IRDye®700	IRDye700
IRF	instrument response function
ISC	intersystem crossing
$I(t)$	intensity-time-function
$J(\lambda)$	spectral overlap integral
K^+	potassium ion
KCl	potassium chloride
k_D	donor's emission rate constant
k_{FRET}	rate constant for FRET
k_{nr}	rate constant for non-radiative deactivation
k_r	rate constant for radiative deactivation
l	absorption path length
Li^+	lithium ion
LiCl	lithium chloride
LUMO	lowest unoccupied molecular orbital
M	molecular mass
MCA	multichannel analyzer
Mg^{2+}	magnesium ion
$MgCl_2$	magnesium chloride
N	nitrogen
n	refractive index
Na^+	sodium ion
NaCl	sodium chloride
N_{Av}	Avogadro's constant ($6.02 \cdot 10^{23}$ mol^{-1})
nb	nucleobase(s)
NH_4^+	ammonium ion
NH_4Cl	ammonium chloride
NMR	nuclear magnetic resonance
nt	nucleotide(s)
O	oxygen
P	phosphorous
PA	phosphoramidite(s)
PGA	programmable gain amplifier
R	donor-acceptor distance
R_0	Förster distance
$\vec{r}_A$	acceptor's absorption transition moment
Rb^+	rubidium ion

abbreviation	**meaning**
RC	reaction center
$\vec{r}_D$	donor's emission transition moment
ref.	reference
RevHumTel	reversed human telomeric DNA
RT	room temperature
S	sulfur
S_0	electronic ground state
S_1, S_2	higher electronic singlet states
SERS	surface-enhanced Raman scattering
SI	supporting information
ssDNA	single stranded DNA
T	thymine
T(1 - 4)	transmitter (1 - 4)
T_1, T_2	higher electronic triplet states
TAC	time-to-amplitude converter
TAE	tris acetate-EDTA
TAMRA	Tetramethylrhodamine
TCSPC	time-correlated single photon counting
TP	triphosphate
Tris	tris(hydroxymethyl)aminomethane
TX tile	triple crossover tile
U	uracil
UV	ultra-violet
Vis	visible
vs.	*versus*
WD	window discriminator
X_n	any nucleotide of length n
X_o	any nucleotide of length o
α	angle between donor's emission and acceptor's absorption transition moments
β	angle between donor-acceptor linkage and donor's emission transition moment
γ	angle between donor-acceptor linkage and acceptor's absorption transition moment
ΔG	Gibbs energy
ΔH	enthalpy
ΔS	entropy
ε	extinction coefficient

abbreviation	**meaning**
$\varepsilon_A(\lambda)$	acceptor's extinction coefficient spectrum
κ^2	dipole orientation factor
λ	wavelength
λ'_{em}	emission maximum
λ_{abs}	absorption maximum
λ_{em}	emission wavelength
λ_{ex}	excitation wavelength
τ_D	donor's fluorescence decay time in absence of the acceptor
τ_{DA}	donor's fluorescence decay time in presence of the acceptor
$\bar{\tau}_{DA}$	amplitude averaged fluorescence decay time
τ_F	fluorescence decay time
τ_I	decay time component (data analysis)
Φ_D	donor's quantum yield
Φ_F	fluorescence quantum yield

Declaration

Hiermit versichere ich, dass ich die vorliegende Arbeit selbst verfasst und keine anderen Quellen und Hilfsmittel als die hier angegebenen verwendet habe.
Ich versichere, dass diese Arbeit bisher nicht an anderer Stelle zur Erlangung des Doktorgrades eingereicht wurde.

Potsdam, Januar 2017 Lydia Olejko